Design and Development of AlGaN/GaN HEMT Based Electrochemical Biosensors

Ph.D. Thesis

NIKETA SHARMA

(ID. No.: 2014REC9023)

DEPARTMENT OF ELECTRONICS & COMMUNICATION ENGINEERING
MALAVIYA NATIONAL INSTITUTE OF TECHNOLOGY, JAIPUR, INDIA

OCTOBER 2019

Design and Development of AlGaN/GaN HEMT Based Electrochemical Biosensors

Submitted in

fulfillment of the requirements for the degree of

Doctor of Philosophy

by

NIKETA SHARMA

ID. No.: 2014REC9023

Under the Supervision of

Dr. C. Periasamy

Assistant Professor, Dept. of ECE, MNIT Jaipur

Dr.-Ing N. Chaturvedi

(External Co-Supervisor)

Sr. Principal Scientist, Smart Sensor Area, CSIR-CEERI, Pilani

DEPARTMENT OF ELECTRONICS & COMMUNICATION ENGINEERING

MALAVIYA NATIONAL INSTITUTE OF TECHNOLOGY JAIPUR

OCTOBER 2019

DECLARATION

I, Niketa Sharma, declare that this thesis titled, ‘Design and Development of AlGaN/GaN HEMT based Electrochemical Biosensors’ and the work presented in it are my own. I confirm that:

- This work was done wholly or mainly while in candidature for a research degree at this University.
- Where any part of this thesis has previously been submitted for a degree or any other qualification at this University or any other institution, this has been clearly stated.
- Where I have consulted the published work of others, this is always clearly attributed.
- Where I have quoted from the work of others, the source is always given. With the exception of such quotations, this thesis is entirely my own work.
- I have acknowledged all main sources of help.
- Where the thesis is based on work done by myself jointly with others, I have made clear exactly what was done by others and what I have contributed myself.

Date:

Niketa Sharma
(2014REC9023)

CERTIFICATE

This is to certify that the thesis entitled "**Design and Development of AlGaN/GaN HEMT based Electrochemical Bioensors**" being submitted by **Niketa Sharma (2014REC9023)** is a bonafide research work carried out under my supervision and guidance in fulfillment of the requirement for the award of the degree of **Doctor of Philosophy** in the Department of Electronics & Communication Engineering, Malaviya National Institute of Technology, Jaipur. The matter embodied in this thesis is original and has not been submitted to any other University or Institute for the award of any other degree.

Dr. C. Periasamy
Assistant Professor
Department of ECE
MNIT, Jaipur

Dr. Nidhi Chaturvedi
Senior Principal Scientist,
Professor ACSiR, IP Manager
Smart Sensor Area
CSIR-CEERI Pilani

Place: Jaipur
Date: 15-10-2019

Effort and hard work construct the bridge that connects your dreams to reality

-- Daisaku Ikeda

ACKNOWLEDGEMENT

The satisfaction that accompanies the successful completion of this thesis would be incomplete without making mention of the people who made it possible, whose constant guidance and encouragement crown all the efforts. Truly, words are not enough to express my gratitude to all of them.

First and foremost, I would like to express my deep and sincere gratitude to my research supervisor, Dr. C. Periasamy, Department of Electronics & Communication Engineering, Malaviya National Institute of Technology, Jaipur, India, for supporting me during these past four years through his guidance and consistent encouragement. His painstaking guidance despite of very busy schedule, inspiring supervision, invaluable and tireless devotion, scientific approach and brilliant technological acumen has been a source of tremendous help and motivation throughout my research period. His critical comments during the discussions enabled me to overcome my weaknesses and make valuable improvements. Thanks for your belief in my abilities and to direct my passion towards the right direction!

I would also like to express my sincere gratitude towards Dr.-Ing. Nidhi Chaturvedi, Senior Principal Scientist, CSIR-Central Electronics Engineering Research Institute, Pilani, for agreeing to serve as my co-supervisor at CEERI, Pilani and for extending her tremendous support and encouragement during last six years. Her patience, flexibility, genuine caring, concern, and faith in me during the dissertation process, hold me boosted. Thanks for all experimental work and discussions, motivational talks, guidance and listening to me all the times.

I would like to thanks members of Departmental Research Evaluation Committee (DREC) members, Prof. Vineet Sahula, Prof. D. Boolchandani, Prof. Lava Bhargava and Dr Chitrakant Sahu for their scholarly guidance, encouragement, and constructive criticisms that contributed immensely to the successful completion of this work. I am thankful to Prof. K.K. Sharma, Head, Department of Electronics & Communication Engineering, MNIT, Jaipur and all other faculty members for their kind support during entire period of my work. I am also thankful to all the office staff of the department for their help and co-operation.

I would also like to extend thanks to my fellow labmates Sandeep Kumar Dhakad, Saurabh Bhardwaj, Rakesh Saini, Shivanshu Mishra and Tanushri at ODG, CEERI for the sleepless nights we were working together before deadlines, and for all the fun we have had in the last four years. I am really thankful to Mr. Ashok Chauhan (Senior Scientist, CEERI, Pilani), Mr. Kuldeep Singh (Senior Scientist, CEERI, Pilani), Dr. Manish Mathew (Senior Scientist, CEERI, Pilani), Mr. Ashok Kumar Gupta (Principal Technical Officer), Dr. Suchandan Pal (Senior Principal Scientist, CEERI, Pilani) and Technical Staff (Mr. Priyvrat, Mr. Arvind Kumar, Mr. B.C Pathak, Mr. Prateek Kothari, Mr. Pawan Kumar and Mr. Bhupendra Kushwaha, ODG, MEMS and SNTG, CEERI, Pilani for their kind co-operation and support at different stages of my experimental work.

It is my pleasure to acknowledge my senior mates and colleagues in the department: Mrs. Sapna Khandelwal , Dr. Shashikant Sharma, Dr. Lokesh Garg, Mr Ashish Sharma , Dr. Lintu Rajan, Mr Shailendra, Shanky, Ramakrishna, Yogendra, for their guidance and support in a very special way. I have gained a lot from them, through their personal and scholarly interactions, their suggestions at various points of my research programme. My heartfelt thanks to my loving juniors: Arun, Arjun, Raju, Gaurav, Rachna, Nawaz, Aarthy, Bharat, Prateek, Sidharth and Vikas with whom I spent countless relaxing, hilarious and pleasant moments. The discussions, experiments, evening tea at Annapurna, paper acceptance celebrations, birthday parties, lunches, dinners, memorable trips and all other cherishable moments which we all spent together will always remain memorable for me. !! I Will Miss You All !!

I sincerely thank Mr Sanjay Agheda and Mrs Hina Agheda for their invaluable helps in language editing of my manuscripts.

Lastly, I would like to express my deepest love and gratitude towards my both the families. The people, who instilled inspiring in my life are those who brought me up, nurtured and imparted me the real virtues of humanities, empathy and kindness. They are my real motivators to bring me at the present position and blessed me with their grace and affection. I record my deep and utmost gratitude to my father Mr. Bal Kishan Sharma and my mother Mrs. Urmila Sharma, for their devotion, sacrifices, encouragement, support, and prayers for my whole life. I can say, this small space is not enough to acknowledge your contributions in my life. Endless thank to my lovely sister Madhuri and my brother Harish for their love and affection in every aspect of my life. My niece Sanvi is twinkle of my eyes. Though I didn't find too much time to spend with her, but listening about their kiddish acts and seeing their pics, re-energized and given me a much-needed reprieve from work. Thank you!

Words in this universe are not enough to express my love and gratitude towards my husband, Mr. Mohit Kapoor, my pillar of support for his patience, and deep understanding. He has supported me throughout this process and has constantly encouraged me when the tasks seemed arduous and insurmountable.

Above all, I owe it all to Almighty God for granting me the wisdom, health and strength to undertake this research task and enabling me to its completion. Thank you God!

(Niketa Sharma)

ABSTRACT

With the commendable progress in science and technology, miniaturized, highly sensitive and reliable biosensors have turned into a reality. Still the requirement for cost-effective, sophisticated, dependable, robust biosensors that can be utilized to detect various kinds of biomolecules continues a technological issue to be solved.

GaN-based high electron mobility transistor (HEMT) possess remarkable properties like wide bandgap (3.4 eV), high breakdown voltage (3 MV/cm), high operating temperature (750^{o}C) low toxicity, chemical stability, chemical inertness, biocompatibility and superior thermal conductivity provides the high saturation velocity, high mobility, and high sheet carrier concentration of the two-dimensional electron gas (2DEG) layer in the AlGaN/GaN heterostructure have drawn a great interest of researchers in recent years. Based on all these fascinating properties, GaN-based HEMT devices excelled over their silicon counterparts and emerged as a potential candidate for power electronics, optoelectronics, bioelectronics, gas, chemical, and biosensing applications. Therefore, our objective in this study was to investigate the potentiality of GaN-based HEMT for biosensing devices that can be very useful in a variety of biomedical applications.

This work presents a systematic study of simulation, fabrication, and characterization of AlGaN/GaN HEMTs and their application in pH detection and as salinity sensor. First, electrical properties of AlGaN/GaN HEMT device have been studied using ATLAS device simulator from Silvaco international so that the performance of the device can be optimized over the tool itself with reduced fabrication cost and efforts. This simulation study presents a systematic investigation on various important device parameters such as electric field distribution, electron concentration, electron mobility, output drain current, transconductance, transfer characteristics, energy band diagram and gate leakage current. Effect of parameter variations (such as AlGaN thickness, GaN Cap layer thickness, gate length, source-gate length and source-drain length) followed by a closer look at the high temperature and trapping effects on the performance of the HEMT device has also been studied. Then, HEMT devices have been fabricated on AlGaN/GaN epitaxial structure grown by metal organic chemical vapor deposition (MOCVD) technique. Various device processing steps such as mesa isolation, the formation of ohmic and schottky contact have been optimized in order to achieve high-performance HEMT devices. AlGaN/GaN heterostructures have been characterized to determine the electrical characteristics and surface properties using Keithley 4200-SCS semiconductor characterization system and Scanning Electron Microscopy (SEM) respectively. Subsequently, the fabricated devices have been tested for the potential applications as pH sensor.

AlGaN/GaN HEMTs based pH sensor was fabricated and characterized. We observe the linear change of current when devices were exposed to the PBS solution of different pH values. The sensitivity of GaN HEMT in different pH solutions has been investigated. These GaN HEMT structures demonstrated a quick response to the pH changes. Finally, we also fabricated AlGaN/GaN HEMT based salinity sensor and evaluate the change in output current while changing molar concentrations of the aqueous salt solution (NaCl + DI). These devices also show the change in current with the very small concentration (Femotolevel Molar concentration) of NaCl present in water. On the basis of obtained outcomes, we proposed a model of surface chemical reaction associated with the difference in H^+ and OH^+ ions concentration and their interaction with AlGaN surface.

In this work, demonstration of high sensitivity AlGaN/GaN HEMT based sensor suggest that GaN heterostructure based devices and technologies do have a promising potential to get extended from research labs to commercial future market.

Table of Contents

List of Figures

List of Tables

List of Abbreviations

2-DEG	Two Dimensional Electron Gas
III-Nitride	GaN, InN, AlN and ternary and quaternary alloys
III-N	Bond between group third element and N atom
AFM	Atomic Force Microscope
AlGaN	Aluminum Gallium Nitrides
AlN	Aluminum Nitride
BioFET	Biosensing ISFET
CAD	Computer Aided Design
CVD	Chemical Vapor Deposition
FET	Field Effect Transistor
GaAs	Gallium Arsenide
GaN	Gallium Nitrides
HBT	Hetero-junction bipolar transistors
HEMT	High Electron Mobility Transistors
HFET	Hetero-junction FET
HR-XRD	High resolution X-ray diffraction
ICP-RIE	Inductively Coupled Plasma Reactive Ion Etching
I.I	Ion Implantation
ISFET	Ion Sensitive Field Effect Transistor
I-V	Current Voltage
MBE	Molecular Beam Epitaxy
MESFET	Metal Semiconductor FET
MMIC	Microwave monolithic integrated circuits
MOCVD	Metal Organic Chemical Vapor Deposition
MODFET	Modulation doped FET
MS	Metal Semiconductor
PAE	Power added efficiency
PECVD	Plasma enhanced Chemical Vapor Deposition
PL	Photoluminescence
RIE	Reactive Ion Etching
SEM	Scanning Electron Microscopy
SiC	Silicon Carbide
TEM	Transmission Electron Microscopy
TLM	Transmission Line Method

CHAPTER 1

Introduction

In this chapter, general background of contributed work has been presented. The fundamental structural and electrical properties of GaN as a semiconductor material and AlGaN/GaN HEMTs have been explained. The different applications of GaN HEMTs in high power electronics and electrochemical biosensing have been presented. The objectives and organization of the thesis have been elaborated at the end.

1.1 General Background

The interest for detection and screening of chemical substances along with biomolecular analytes are expanding step by step. High-speed, consistent, susceptible, compact sensor frameworks are of most extreme significance for distinguishing these analytes. Mainly, electrochemical biosensors exhibit relative simplicity, convey ability, compactness, minimal expense and minimal power requisite which make them an outstanding contender for distinguishing an extensive variety of genus counting proteins, nucleic acids, viruses and different liquids. In light of the current pattern of the purpose of bio-care application, this category of biosensors is quickly turning into a vital analytic device. With the assistance of integrated systems, optimally improved functionality of sensor could be sustained through allied electronics, fluidics and separation technology. The prospect for a massive achievement of electrochemical biosensor technology is a substantial probability.

Sensors employing semiconducting material can be developed by means of established practices from the Si commerce as well as new nanotechnology methods. In 1991, another span of biosensing was propelled by the incorporation of field effect transistor

(FET) as a sensing component rather than the earlier employed basic metal electrodes [1]. In the beginning, Si-based field effect transistors were utilized for chemical sensing. From the time when Bergveld in 1970 [2] initiated the concept of Si-based ISFET the area related to solid state sensing resoluted by material excerption to enhance the accomplishment of ISFETs in support of pH and specific ion detecting applications. A standout amid the most used pH measurement electrochemical sensor is the ISFET based sensors [3], [4]. A historical overview, which is additionally, underlines potential challenges and outcomes, which is given by Bergveld [5]. The Si-based biosensing ISFETs are also named as BioFETs. The detection was acknowledged via conductivity modulation in the channel area because of chemical sensitivity of the metal-oxide gate contact. Regrettably, devices fabricated from Si material were experienced chemical instability and reaction when in contact with fluid. Likewise, ideally outlined Si devices are normally-off, that is why it's necessary to supply reference electrode. It facilitates gate biasing above of threshold voltage to enable minority carriers to move in the conductive channel. In spite of the fact that Si-based transistor is able to work excluding reference terminal while fabricated on highly doped Si wafers (normally-on), such substantial doping cause diminished device outcomes (e.g., low electron mobility) and amplifies production costs. As a consequence, the majority of Si-basedsISFETs utilizes a reference anode, a portion of the sensor which introduces cumbersomeness and delicacy within the framework. Nevertheless, these sensing devices are not suitable for function in severe conditions. For example, high temperature, high pressure or destructive ambient deteriorate the sensor performance. Si gets etched from the portion come into the contact of acidic or basic aqueous solutions for biological detection. These challenges triggered the search for novel material, and together with passivating layers these are fulfilling the requirement for commercially accessible devices utilizing BioFETs. Due to differences from Si, GaN material isn‘t etched by any chemicals at temperatures below a couple of hundred degrees. For that reason, wide band-gap III-Nitride semiconductors are elective choices to complement Si in applications as mentioned earlier on account of chemical resistance, high temperature/high power capability, high electron saturation velocity and simple incorporation through existing GaN-based UV light-emitting diode, UV detectors, and wireless communication chips. A potential electrochemical biosensing technology has employed using GaN-based high electron mobility transistors (HEMTs) as a sensing device. AlGaN/GaN-based high electron mobility transistor (HEMT) has been enormously proficient for chemical, gas, liquid and biosensing application [6]–[8] because of its remarkable properties like low toxicity, chemical stability, and superior conductivity on account of the high saturation velocity and high sheet carrier concentration of the two-dimensional electron gas (2DEG) layer in the AlGaN/GaN heterostructure [9]–[12]. GaN-based wide band semiconductors can be used at an elevated temperature of 750^{o}C without degradation in performance. These devices have an ability to detect even lower current values than traditional Si-based devices. Moreover, electrochemical biosensors fabricated from the GaN material are mainly of great importance in various biomedical applications where pure DI and salt-free water is required [13].

This chapter discuss the overview, motivation and objective of the research and give a brief statement of the outline of thesis.

1.2 Motivation of Research

All the applications of GaN HEMTs mentioned in above section originate from its material properties.

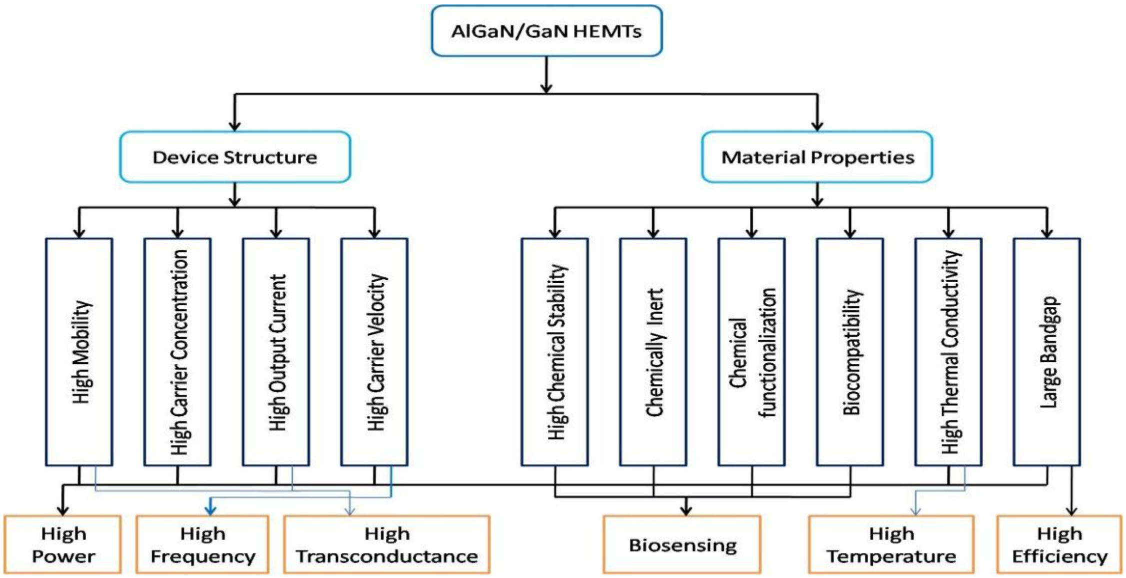

Figure 1.1: Factors influencing the performance of the AlGaN/GaN HEMT

Therefore, it is vital to discuss the material and electrical properties of GaN. This section explains the various features of GaN and device structure that makes it a favorite candidate for a variety of applications. Fig. 1.1 describes the key factors influencing the performance of the AlGaN/GaN HEMT.

1.2.1. Material Properties of III-N Semiconductors

GaN possess exceptionally large band-gap 3.4 eV in contrast to Silicon (Si) having bandgap 1.12 eV, and Gallium Arsenide (GaAs) has 1.42 eV, provide significantly high breakdown voltage about 3 MV/cm.

Table 1.1: Semiconductor material properties

Material properties	**Si**	**GaAs**	**SiC**	**GaN**	**AlN**
Band gap (eV)	1.1	1.4	3.25	3.4	6.2
Electron mobility (cm ^{2}/Vs)	1500	8500	500	1300	300
Breakdown voltage (MV/cm)	0.3	0.4	2.0	3.0	11.7
Saturation velocity (x10^7 cm /s)	1.0	0.8	2.0	2.7	2.0
Thermal conductivity (W/cm-K)	1.5	0.5	3.5	1.3	2.5
Operating temperature (°C)	300	300	> 500	750	> 500
Melting temperature (°K)	1690	1510	> 2100	>1700	3000
Johnson figure of merit($\alpha\mu E_{br}^2 V^2_{sat}$)	1	11	400	760	5100

GaN-based devices attained high speed owing to high carrier velocity. These devices are capable of withstanding at very high temperatures (750°C) because GaN material possess high thermal conductivity (1.3 W/cm-K) [9], [14]–[16], which makes these devices thermally stable. All these factors altogether make GaN a solid contender in the field of applications such as satellite communication, mobile base stations, radars, missiles, communication networks, and biosensing. The material properties of GaN along with its other counterparts are listed in Table 1.1.

1.2.1.1 Structure

III-Nitride semiconductor crystallized in wurtzite and zinc blende phase as shown in Fig. 1.2. Both aspects are epitaxially grown, as a thin film [17], [18]. Wurtzite phase is the thermodynamically stable state.

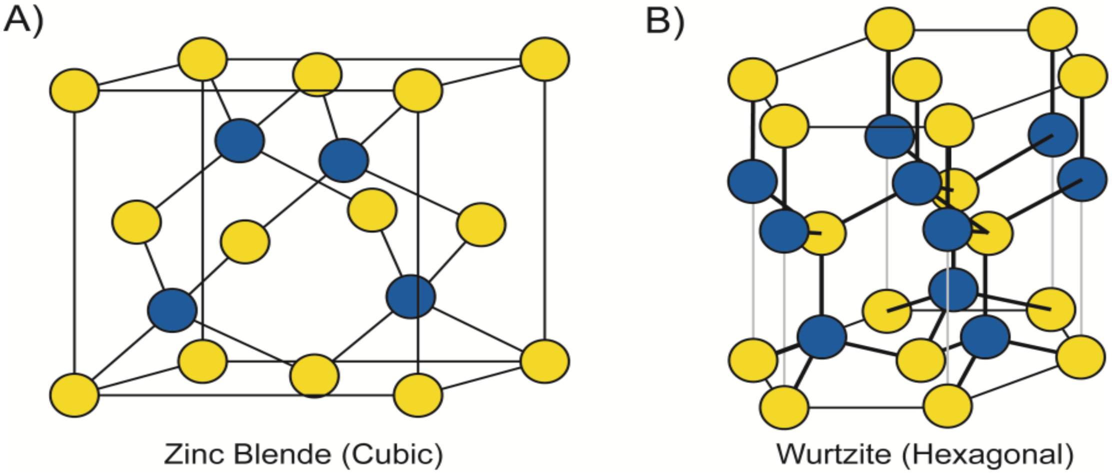

Figure 1.2: Example diagrams of both Zinc Blende and Wurtzite structures seen in III-nitride compounds [19]

a) Zinc Blende Structure

Zinc blende structures consist of two interpenetrating f.c.c. lattices, one displaced from another by a translation along the body diagonal (a/4 a/4 a/4). Lattice constant (a) for zinc blende GaN is 4.5 Ǻ and the bandgap is 3.2 eV at room temperature [20]. Zinc blende structure of III-Nitride semiconductors is readily cleaved and etched.

b) Wurtzite Structure

Wurtzite is the thermodynamically steady structure of III-Nitride semiconductor materials. It compose of two interpenetrating hexagonal close-packed lattices, offset in relation to each other by 3/8c. Lattices are defined by a, c and u (u=b/c, and b is the bond length in c direction) parameters. Lattice constant (c) describes the distance between two indistinguishable hexagonal lattice planes, and the lattice parameter (a) illustrates the range of atoms in the hexagonal lattice plane. u characterize the bond length alongside the c-axis, and provide details of the deformation of the element cell. Miller's index of wurtzite materials is generally written as (h k i l), where h, k and l are normal miller index terms and i (= -h-k) is called redundant index [19].

1.2.1.2 Band Gap

New measurements show a much smaller band gap of InN which varies from 0.65 to 0.9 eV [21], earlier it was taken as 1.89 eV. Fig. 1.3 illustrates the bandgap versus lattice parameter (a) for III-Nitride material systems. The bandgap of III-Nitride materials is continuously varied as of 6.2 eV (AlN) to 0.7 eV (InN).

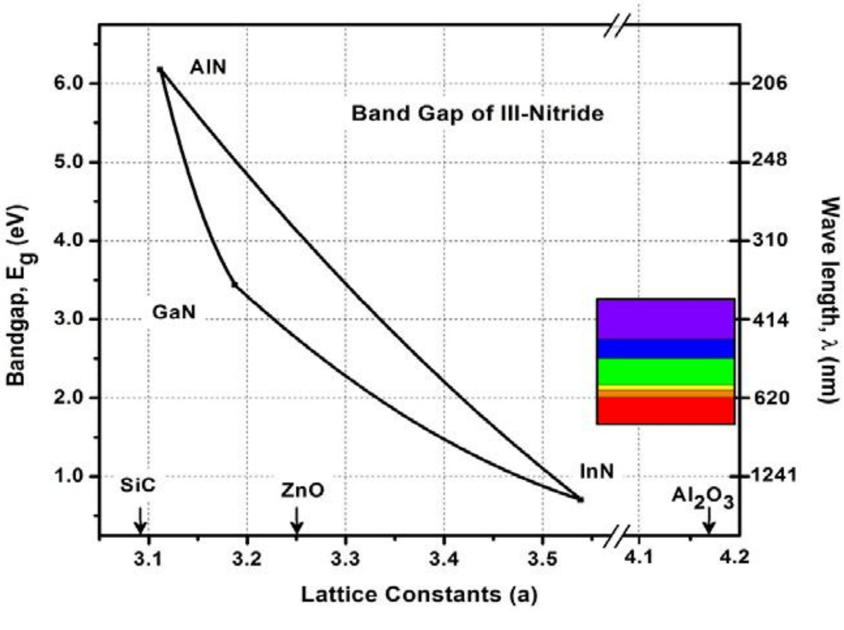

Figure 1.3: Bandgap of III-Nitride semiconductor versus lattice constant

a) Band offset

In III-Nitride materials band alignment of Type-1 are found, as shown in Fig 1.4. Conduction band offset (ΔE_c), and valence band offset (ΔE_v) is related to band gap different (ΔE_g) as,

$$\Delta E_g = \Delta E_{g1} + \Delta E_{g2} = \Delta E_c + \Delta E_c \tag{1.1}$$

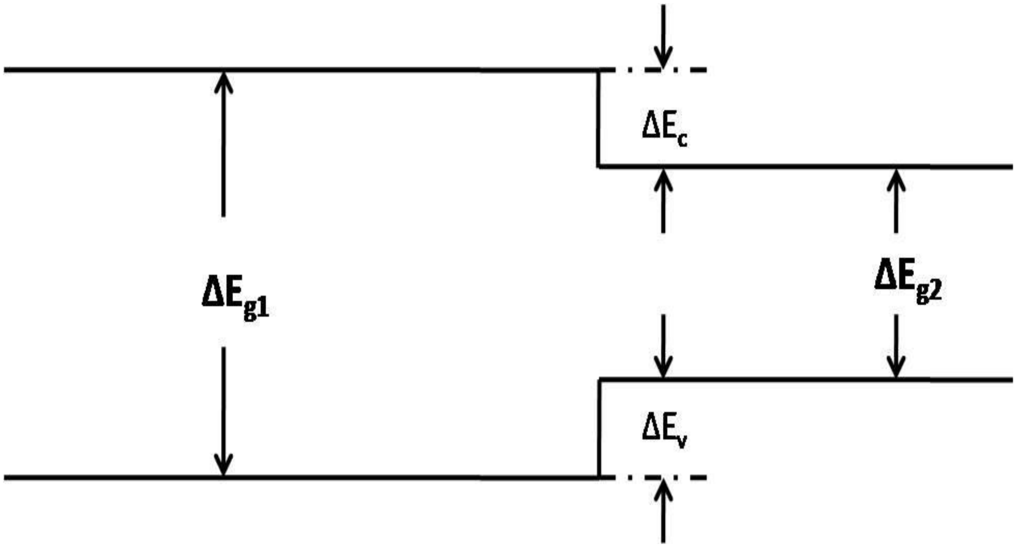

Figure 1.4: Type-1 band alignment in III-Nitride semiconductors

There are considerable disagreements in the value of conduction band offsets and valence band offsets, between AlGaN/GaN [22].

1.2.1.3 Polarity

Wurtzite III-Nitride materials don’t have inversion symmetry by the side of the c-axis. So there are two different patterns of atomic layers, in two opposite direction parallel x-axis (illustrated in Fig. 1.5). With regard to GaN, if the nitrogen particles are put over the group III atoms, the film is labeled as Ga-or [0001] polar. The group III atoms are over N particles, the film is termed as N-or $[000\bar{1}]$ polar.

N-face crystal can be etched chemically and has low threading dislocations [23], whereas Ga-face III-Material shows better transport properties [24].GaN epitaxial layer developed with Molecular Beam Epitaxy (MBE) technique over c-plane sapphire are N-faced [25], and with the help of Metal Organic Chemical Vapour deposition (MOCVD) technique, the Ga-faced epitaxial layer is obtained [26].

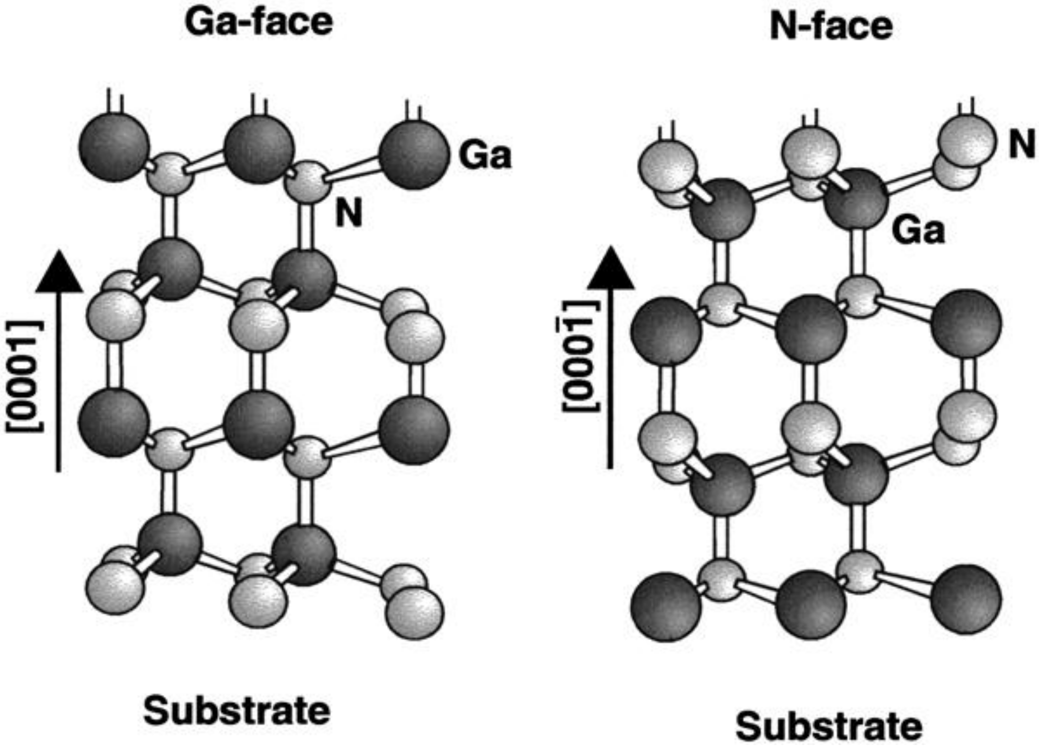

Figure 1.5: Ga-face and N-face Wurtzite GaN structure [9]

1.2.1.4 Ideality

The ideal c/a ratio and u parameter of wurtzite structures are 1.633 Ǻ and 0.375 Ǻ respectively. Wurtzite structures with c/a proportion less than the ideal value are stable. The lattice parameters of wurtzite III-Nitride materials are given in Table 1.2 [27].

Table 1.2: Lattice and other parameters of wurtzite InN, GaN and AlN

Parameter	**Units**	**AlN**	**GaN**	**InN**	**Ideal Case**
Lattice constant, a	Å	3.112	3.189	3.540	Na
Lattice constant, c	Å	4.982	5.185	5.705	Na
c/a ratio		1.601	1.625	1.611	1.633
Cell Parameter, u	Å	0.380	0.376	0.377	0.375
Band gap, E_g	eV	6.180	3.400	0.700	Na

If c/a declines, at that point u increments such that the four tetrahedral separations stay almost constant and in that case the tetrahedral inclines get deformed. The lattice constants a(x) and c(x) of ternary wurtzite Nitride materials are calculated by Vegard's laws.

1.2.1.5 Polarization

The deflection of the unit cell is commencing the standard hexagonal wurtzite structure. The robust ionic nature of the III-N bond results in a strong polarization field in wurtzite III-Nitride semiconductor materials. There are two kinds of polarization fields exist in Nitride materials: Spontaneous polarization and piezoelectric polarization.

a) *Spontaneous Polarization*

Due to large electro-negativity of the nitrogen atom, the electron in III-N bond is strongly attracted to the substantial coulomb potential of nitrogen nuclei. So in III-Nitride materials, covalent bond comprises a preferred measure of ionicity in contrast to other III-V covalent bonds. These materials don't retain inversion symmetry along the c-axis. Hence, strong ionicity of the III-N bonding causes significant polarization along the [0001] crystal direction, termed as spontaneous polarization (Psp). The extent of non-ideality of crystal lattice regulates the intensity of spontaneous polarization. As the c/a ratio decreases, the three back bond angle gets broader with respect to the c-axis. Consequently, the inherent polarization reduces and providing augmentation to macroscopic P_{sp}. As non-ideality in lattice increases the magnitude of P_{sp} step up, that is start with GaN to InN then to AlN as given in Table 1.3.

b) *Piezoelectric Polarization*

If, the c/a ratio changes externally, the further added polarization in III-Nitride materials is known as piezoelectric polarization (P_{pz}). The piezoelectric constants of III-Nitride materials are 5 to 20 times larger than InAs, GaAs and AlAs materials. During or after pseudo-morphic growth, the lattice constant of top layer increases or go down to complement the in-plane lattice constants of the underneath layer. Under bi-axial compressive stress, lattice constant (a) within a plane in wurtzite crystal decreases. The c/a ratio increases concerning the ideal lattice, so net polarization in crystal decreases.Conversely, if the epitaxial layers are in tensile stress, the in-plane constant escalates and lowers c/a fraction different as of the standard value. These factors boost the net polarization in crystal, in this case, the P_{pz} and the P_{sp} proceed onto the similar path. Strength of Piezoelectric polarization for both cases is given by [27], [28]:

$$P_z = E_{ij} \otimes E_{kl}$$

(1.2)

Where, E_{ij} is piezoelectric tensor and E_{kl} is strain sensor. The above equation for wurtzite symmetry reduces to,

Table 1.3: Polarizations in III-Nitride semiconductors [29], [30]

Parameter	**Units**	**AlN**	**GaN**	**$Al_xGa_{1-x}N$**
Lattice Constant, a	Å	3.112	3.189	3.189-0.077x
Lattice Constant, c	Å	4.982	5.185	5.185-0.232x
Cell Parameter, u		0.382	0.377	0.382x + 0.377(1-x) – 0.0032x(1-x)
Energy Gap, Eg (300 K)	eV	6.28	3.42	6.28x + 3.42(1-x) – 1.00x(1-x)
Dielectric Constant, ε_r		9	9.5	-0.5x+9.5
Spontaneous Polarization, P_{sp}	C/m^2	-0.090	-0.034	-0.090x – 0.034(1-x) + 0.021x(1-x)
Piezoelectric Coefficients, E_{31}	C/m^2	-0.60	-0.49	-0.11x-0.49
Piezoelectric Coefficients, E_{33}	C/m^2	1.46	0.73	0.73x+0.73
Elastic Constant, C_{13}	GPa	108	103	5x+103
Elastic constant, C_{33}	GPa	373	405	-32x+405

$$P_z = 2\frac{a_s - a_0}{a_0}\left(E_{31} - \frac{E_{33}C_{13}}{C_{33}}\right) \tag{1.3}$$

Where, a_0 is the equilibrium lattice constant, a_s is the actual lattice constant, E_{31} and E_{33} are the piezoelectric coefficients, and C_{13} and C_{33} are the elastic constants.

For wurtzite

E_{31} is –ve

E_{33} is +ve

C_{13} is +ve

C_{33} is +ve

So, $E_{31} - \left(\frac{E_{33}C_{13}}{C_{33}}\right)$ is –Ve.

P_{pz} in III-Nitride materials indicates negative biasing for layers under the tensile stress ($a > a_0$) and positive in support of layers having compressive stress ($a < a_0$). So in Ga-face polarization P_{sp} vector is pointing toward the substrate while in N-face GaN this vector point upward. For ternary and quaternary spontaneous polarization is calculated by Vegard law.

1.3 Basics of AlGaN/GaN HEMT Devices

1.3.1 AlGaN/GaN HEMT Structure

A typical GaN HEMT structure shown in Fig. 1.6 consists of a Sapphire semi-insulating substrate, AlN nucleation, undoped GaN buffer, undoped AlGaN spacer, doped AlGaN donor with doping $n_d = 5\text{x}10^{18}\ \text{cm}^{-3}$ and undoped AlGaN barrier layer.

1.3.2 Two Dimensional Electron Gas (2-DEG)

III-Nitride semiconductors have a unique material property that distinguishes it from SiC, is the formation of heterostructures.

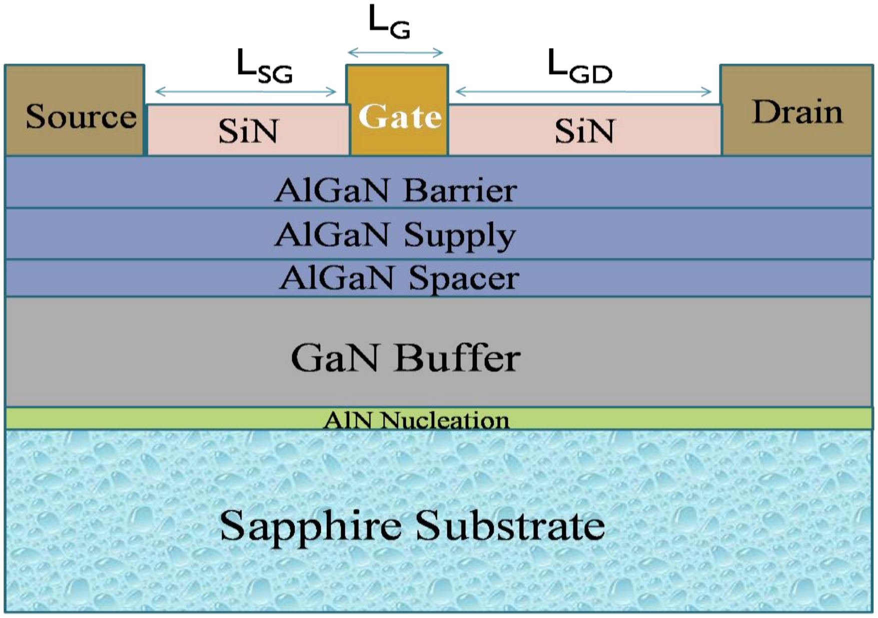

Figure 1.6: Schematic of AlGaN/GaN HEMT on sapphire

When a high band gap material is deposited on low bandgap material, due to the difference in electron affinities, an inversion layer (Quantum Well) is formed at hetero-junction, in low band gap material. Electrons are able to travel liberally in this plane of the hetero-interface, whereas the movement in the perpendicular direction is constrained to a limited region with characteristic energy levels, momentum, and wave function quantization. Thus an electron in the inversion layer are said to form a two-dimensional electron gas (2-DEG). The thickness of inversion layer is of the order of of 2-3 nm. Silicon-doped aluminum gallium nitride (AlGaN-Supply) is grown over the GaN buffer layer at an exceptionally high doping level. High doping in AlGaN/GaN HEMTs provides high sheet charge density across channel area. AlGaN has a significantly larger energy gap than GaN. The silicon impurities bestow electrons to the crystal having tendency to amass in the region of lowest potential – forming a quantum well underneath the AlGaN/GaN crossing point where the electrons can move quickly and freely. This creates a channel of highly mobile electrons with very high concentration. This channel confines electrons in a triangular quantum well. This develops a sheet of electrons, which comprises two-dimensional electron gas (2DEG). Besides, owing to modulation doping, carriers in the un-doped hetero-interface (GaN-Buffer) are spatially separated from the originally doped region or AlGaN-Supply layer by undoped AlGaN-Spacer and have enormously high mobility since there is no impurity scattering. The AlGaN barrier spatially separates the supply layer from schottky gate metal to prevent conduction. Undoped GaN buffer is primarily used to provide high mobility by reducing scattering in this region. This layer also provides fine isolation between devices due to high resistivity. In AlGaN/GaN HEMT there is a thin layer of (~ 1-3 nm) of AlN amid the AlGaN and GaN layers. The idea behind this version of a HEMT structure is to minimize a scattering phenomenon called alloy scattering.

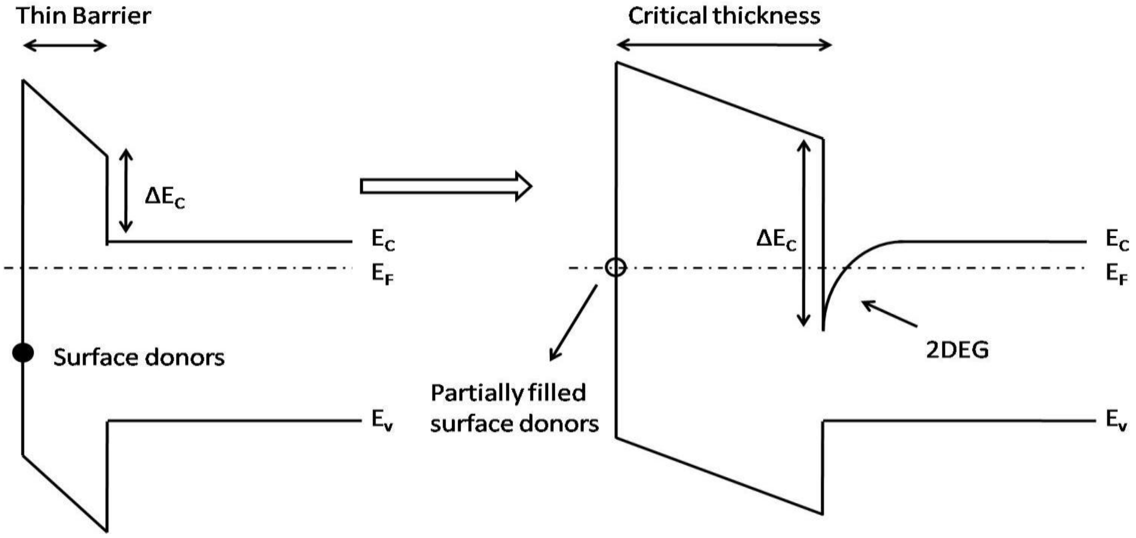

Figure 1.7: Schematic outline demonstrating the expansion of barrier thickness and the relating vitality of the trapping state levels [31].

As said beforehand, the materials which grow these heterostructures are undoped thus the starting point of the `free' electrons that compenste the positive charge along the interface like was anticipated in [9]. Hence, the 2DEG is formed and possibly will emerge from surface trap levels [31]. These appeared traps perhaps the cause of formation of 2DEG and the previously mentioned positive charge that compensate the negative polarization-stimulated charge over the surface of AlGaN layer. Traps allude to energy states within bandgap of the semiconductor, arising from crystal imperfections, separation and the nearness of contaminations. As shown in Fig. 1.7 we can say that these traps are donor like surface states (i.e. unbiased when charged and positive when discharge) and are found somewhere down in the AlGaN bandgap The site of the conduction band regarding Fermi level ought to be recorded for every situation.

In case of thin AlGaN barrier, the surface traps are beneath the Fermi level and the complete states would be engaged with electrons that are neutral in consequence. Since the AlGaN boundary thickness builds, the Fermi level on the surface lowers down moving toward the innate donor sites. About a specific critical thickness t_{cr} the electrons get sufficient energy to depart the traps thus presence of free electrons impelled by solid polarization-instigated electric fields in the AlGaN layer to develop the 2DEG. These traps become vacant and turn out to be positively charged. The observed trapping energy levels are 1.65 eV (through MBE growth technique) [31] and 1.42 eV [32] (by MOCVD growth technique) beneath the conduction band edge (E_C) all together for a 2DEG formation. An additional increment in AlGaN barrier causes dense electrons in the 2DEG, in spite of the fact that this will immerse as the estimation of the polarization-induced charge is revived.

1.3.3 AlGaN/GaN Heterostructures

The spontaneous polarizations in Ga-face III-Nitride materials are always negative, so Psp vector points towards the substrate in relaxed AlGaN and GaN materials as depicted in Fig 1.8 (a). As a result of lattice mismatch, strained AlGaN epitaxial layer on GaN experienced tensile stress. Under tensile stress, P_{pz} vector in AlGaN layer is –ve. In this case +ve (+σ) charge, are stimulated at the boundary, as a result of difference in polarization values at the interface. If the polarity turn from Ga-face to N-face, P_{sp} and P_{pz} change sign as expressed in Fig 1.8 (d) and Fig 1.8 (e) and a –ve (-σ) is induced at the interface. If strained GaN is grown on relaxed AlGaN layer, then the GaN layer experiences compressive stress.

The charges caused at the interface, in this case depend upon the polarity. For Ga-face +ve charge is induced at the interface while in N-face –ve charge is induced at the interface as shown in Fig.1.8 (c) and Fig. 1.8 (f).

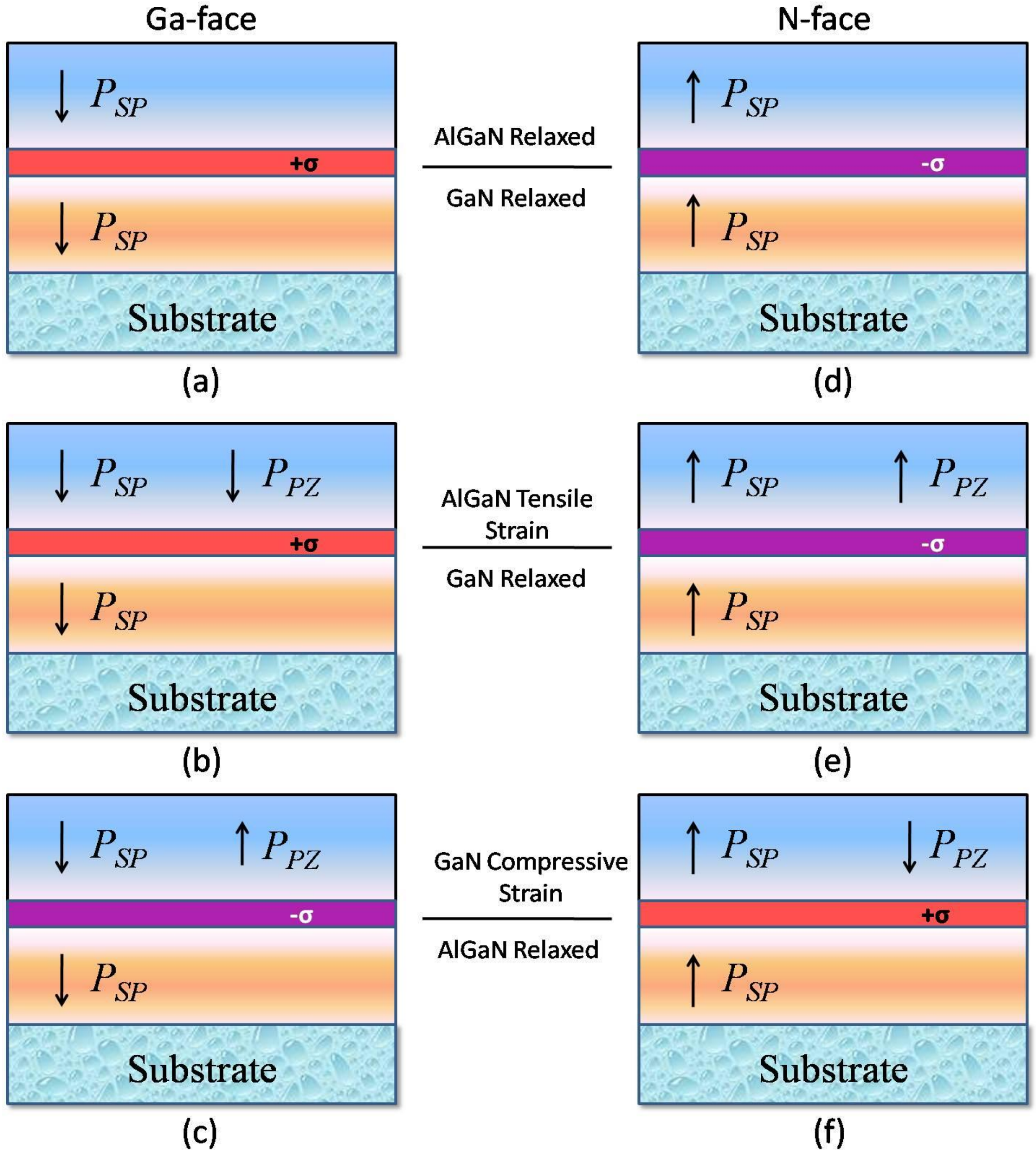

Figure 1.8: (a)-(f) Spontaneous and piezoelectric polarization bound interface charges[9]

The polarization-induced charge density is determined by [9]:

$$\sigma = P(AlGaN) - P(GaN) = P_{SP}(AlGaN) + P_{PZ}(AlGaN) - P_{SP}(GaN) \qquad (1.4)$$

Where, P_{SP} is the spontaneous polarizations and P_{PE} is the piezoelectric polarizations.

According to Gauss’s law, this polarization induced charges at the interface will give rise to the field. Electrons and holes present in the material will try to rearrange themselves to cancel these fields. For Ga-face AlGaN/GaN heterostructure the bounded charge at the interface is +ve. This +ve bounded charge attracts equal numbers of electrons from AlGaN/surface traps to an interface. Hence, a 2-DEG is developed at the interface. The carrier density in 2-DEG (n_s) is ordered of $10^{13}/cm^2$ for AlGaN/GaN structures. In N-face AlGaN/GaN heterostructures the bounded charge is –ve, so same no of holes is attracted towards the interface and 2 Dimensional Hole Gas (2-DHG) is created at the interface.

1.3.4 Device Operation

The fundamental motivation behind a HEMT is to either turn on the electrical signals or to open up them (as an independent device or an element of bigger amplifier circuit). The drain current versus drain voltage characteristics for depletion mode HEMT is demonstrated in Fig.1.9. It is intended for descriptive objectives and utilized as a guide for portraying the HEMT operation. In depletion mode, turning off necessitates the use of a negative bias to diminish the charge carrier in channel causes an exceptionally resistive channel area and this is acknowledged as `pinch-off'. The representation concerns the quantity of electrons present in channel to the employed bias voltage is specified by (modelling of 2DEG - metal gate as a capacitor) [33]:

$$n_s = \frac{\epsilon_{AlGaN}}{q(d_{AlGaN}+\Delta d)}(V_{GS} - V_T) \tag{1.5}$$

where n_s express charge density per unit area of the 2DEG, q is the electronic charge, ϵ_{AlGaN} is relative permittivity of AlGaN, d_{AlGaN} shows thickness of the AlGaN barrier layer, Δd represent the effective distance of the 2DEG from the hetero interface, V_{gs} is the gate voltage and V_T, is the threshold voltage, is the negative value of gate voltage at which device initiates to conduction of current. At the point while V_{gs} is equal to V_T it bringing about n_s to be zero and the device goes turned off. As V_{gs} become zero the channel heavily occupied by electrons and the implication of a drain voltage will prompt flow of current amid source and drain.

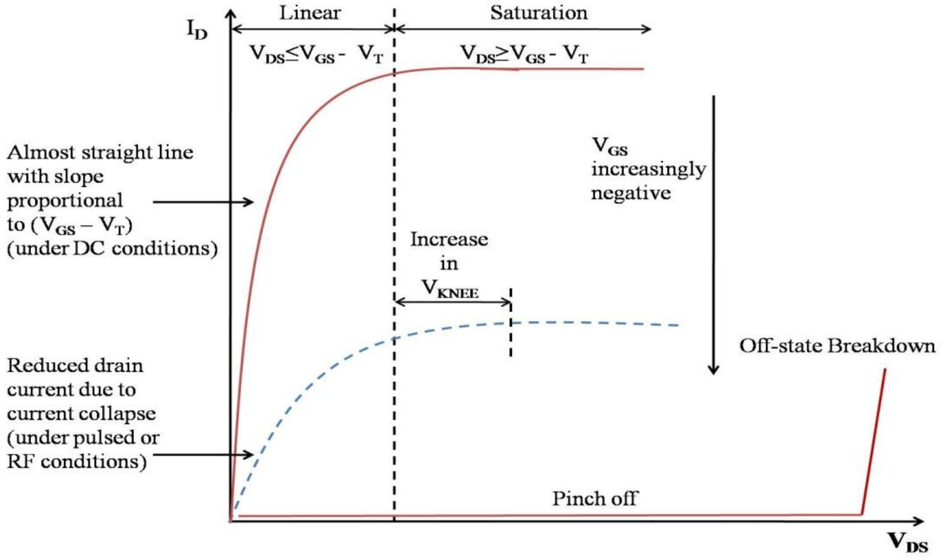

Figure 1.9: Depiction of I-V characteristic of AlGaN/GaN HEMTs

Relating to Fig. 1.9 and Eqn. (1.4), for $V_D < V_{gs} - V_T$ the device is thought to work in the linear region. The electron velocity in the channel region is corresponding to the employed electric field. Thus the current will increment with the electric field. The current in between the source and drain now is specified by:

$$I_D = qn_sV_{eff}W_G \tag{1.6}$$

where, q is the charge of electron, n_s is sheet carrier density, v_{eff} is the effective velocity of the electrons in the channel and W_G is the width of the gate. The velocity of the electrons in the channel relies upon their mobility and the electric field applied and is given by the relationship [34]:

$$v = \mu_n E \tag{1.7}$$

where, μ_n is the electron mobility and E is the applied electric field. The mobility of the charge carriers within 2DEG of an AlGaN/GaN HEMT is influenced via carrier scattering due to defects and dislocations within semiconductor crystal and alloy disorder scattering [35]. As per Eqn. (1.7) the electron velocity raises linearly with the applied field and thus utilizing this value in Eqn. (1.6) the current is appeared to increment linearly for $V_D < V_{gs}$

- V_T . Expanding the applied field with the goal that the drain bias is $V_D > V_{gs} - V_T$, the electron rate starts to saturate and turn out to be not dependent on the applied field.

Since the drain voltage goes up likewise $V_D > V_{gs} - V_T$, the lateral voltage below gate contact (because of the drain voltage) starts to pinch the channel off towards the drain side of the gate. This proceeds till to the extent where the carrier flow within the channel is narrower and restrains the measure of carrier flow to the drain terminal. Now the devices tend to shifts in saturation region and additional increment in the drain voltage not result any improvement in drain current (as shown in Fig. 2.5). Here, the output drain current can be communicated by:

$$I_{DS} = \frac{\epsilon_{AlGaN} V_{sat} W_G}{(d_{AlGaN} + \Delta_d)} (V_{GS} - V_T) \tag{1.8}$$

where, v_{sat} is the saturated electron velocity. Any changes in the gate width W_G would straightforwardly affect the variation in current.

1.3.5 Surface States

Carrier density (n_d) in GaN buffer is ordered of 10^{16} cm^{-3}, and for 2 μm GaN buffer, total carriers in GaN buffer are 2×10^{12} cm^{-2}. These values are less than the observed value of n_s (= 10^{13} cm^{-2}), so what are sources of the carrier at the interface (2-DEG). Ibbetson et al. predicted that the surface donor like traps is the basis of the carrier in 2-DEG at the interface [31]. Some assumptions for characterizing surface states are:

1) Surface states are characterized by a charge neutrality level (Φ_{CNL}), state above Φ_{CNL} are acceptor and below are donor states.
2) Occupations of the surface state are defined by Fermi level.
3) Surface states are negatively charged if they are occupied and positively charged if they are empty.
4) Density function is constant, and at zero Kelvin it is used to calculate the electron distribution over the states as,

$$\sigma_{ss} = D_s(\emptyset_{CNL} - E_F) \tag{1.9}$$

If surface states are very large, then Φ_{CNL} lie closer to Fermi level, and in that case the Fermi level gets pinned (Fermi level pinning) to Φ_{CNL} [36]. In that situation, all metal contacts to the semiconductor show same contact properties independent to work function. At AlGaN/GaN interface the polarization charge ($+q\sigma_{int}$) is shielded by accumulated electron ($-q\sigma_{2DEG}$). At Air/AlGaN interface, the surface charge ($-q\sigma_{surf}$) is larger than $+q\sigma_{int}$. Hence, a compensating positive charge at the surface is needed, to maintain the distinction in the charges as shown in Fig. 1.10. This indicates that electrons are transferred from the surface to the interface.

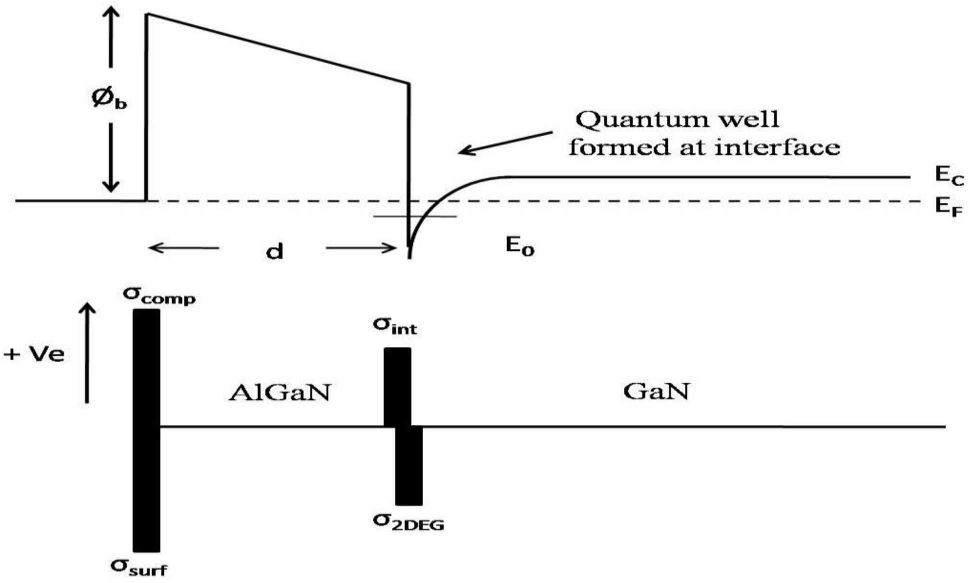

Figure 1.10: Charges at AlGaN/GaN hetero-interface

1.3.6 Surface State Passivation

In AlGaAs/GaAs system surface passivation is done, to reduce surface state density. The maximum channel current of the device degrades with surface passivation. But in AlGaN/GaN system, the performance of the device significantly improves by surface passivation [37]. A lot of view points, concerning the physical mechanism due to which surface passivation advances AlGaN/GaN HFET performance are proposed, but the main theme is that the surface passivation,

1. It lessens the density of dynamic surface states, as well as,

2. It diminishes the negative charge density at the surface, instigating 2-DEG to rise, and a surface barrier to drop off.

1.3.7 Electron Mobility

Mobility in semiconductor materials depends on various scattering mechanisms and mainly limited by different scattering mechanism and defects in the structure. Mathematically, mobility is defined as,

$$V_d = \mu_n \times E \tag{1.10}$$

In semiconductor devices, doping is done, to achieve higher charge carriers, for better current transport. High doping in semiconductor materials results in high ionized impurity scattering and thus reduces the carrier mobility. In 1978 Dingle et al., proposed modulation doping in semiconductors to improve the carrier densities and motilities simultaneously [38]. In this, carriers are separated from the ionized doped region [38]. Coulomb scattering from ionized donor atoms can further decrease by using an un-doped spacer layer, which is sandwiched in between the un-doped channel layer and the doped barrier layer.

1.3.8 Degradation of HEMT Performance

The theoretical maximum output power extracted from a HEMT could be evaluated via I-V characteristics [39]:

$$P_{OUT} = \frac{1}{8} I_{MAX} \times (V_{BR} - V_{KNEE}) \tag{1.11}$$

Where, I_{MAX} is the maximum drain current, V_{BR} is the breakdown voltage of the device and V_{KNEE} is the knee voltage at which the I-V curves changeover from the linear to the saturation region.

It is demonstrated through experimentation, nevertheless, that in RF or pulsed settings; for the time being drain current is lessened [39] (see Fig. 1.9). The reduction in output current is an immediate after-effect of traps which present near the surface and in deep sites which decrease the quantity of electrons accessible in the channel [40]. This impact likewise commence outcome of expanding the knee voltage as shown in Fig. 1.9 while the effective on-resistance is rising in channel. This occurrence is usually named as dispersion or current collapse.

Referring to Fig. 1.11, Current collapse falls originates with the implication of considerable negative gate voltage. Electrons can spill as of gate contact and pile up trapping sites beneath in between gate and drain zones forming a `virtual gate' - basically a region of negative charge over the exercised surface.  The `virtual gate' has the impact of regulating the depletion regime and thusly moderately diminishes the channel similarly like the actual gate carry out after applying negative voltage. This heads to decrease in whole output current of the device. This is commonly believed that the charge carrier would trap in donor states over the surface and their transient time constant relies on the trapping energy levels [41]. To limit the effect of the surface states growing this virtual gate, passivation with silicon nitride (Si_3N_4) has been appeared as a blocking method [39] (shown in Fig. 1.12). The Si_3N_4 blocks the virtual gate by present verifies the surface states are certainly accountable for its development. The Si_3N_4 perform exceptionally sound in comparison to other dielectrics due to the presence of Si atoms as shallow donors in trapping locations over the surface of the AlGaN.

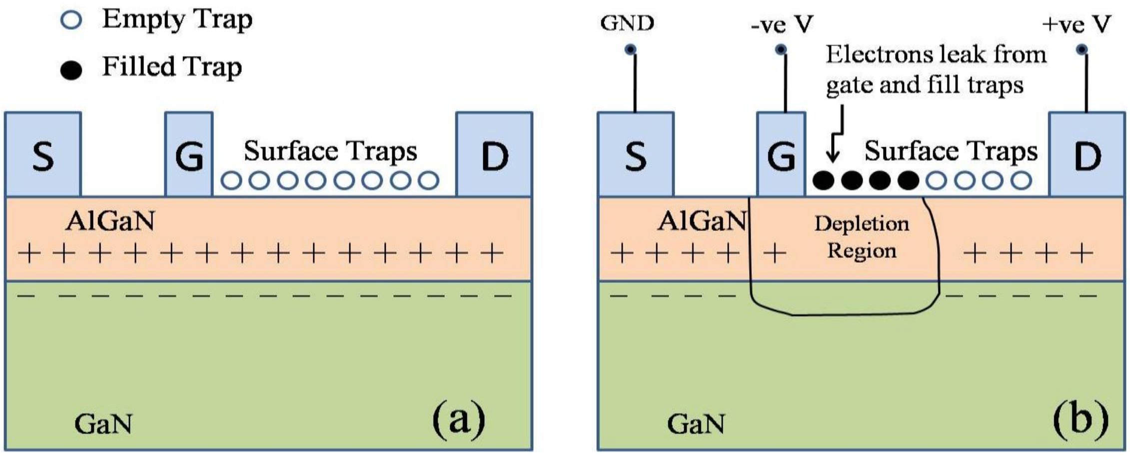

Figure 1.11: a) AlGaN/GaN HEMT device without biasing, b) AlGaN/GaN HEMT with biasing (negative voltage on the gate)

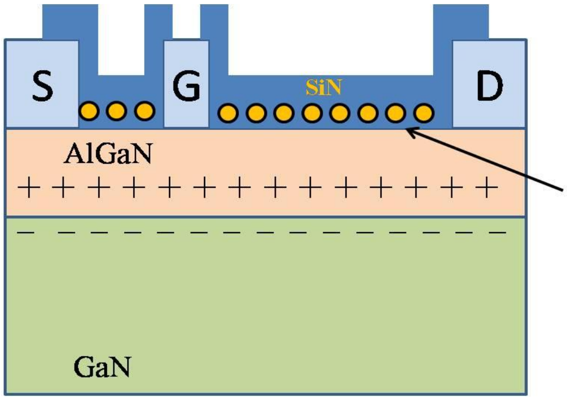

Si atoms from Si_3N_4 act as shallow donors in trap sites on AlGaN surface which prevents virtual gate forming

Figure 1.12: Passivation of HEMT device using Si_3N_4 blocks formation of virtual gate

This showed combat outcomes of reducing the impact of electrons leaking from the gate and growing the virtual gate and additionally allows to improve the 2DEG and consequently allows high drain currents.

1.4 AlGaN/GaN HEMT based Sensor

A biosensor is basically a chemical sensing device in which a biologically derived recognition entity is coupled to a transducer, to allow the quantitative development of some complex biochemical parameter.

1.4.1 Basic Concept of Biosensor

Biosensor is an arrangement of two sections: Bioelement and a sensor component. A particular bioelement, for example, a chemical, perceives a particular analyte and the sensor component transduces the adjustment in the biomolecule which converted in electrical flag. The bioelement is certain to the analyte to which it is delicate or sensitive. It doesn't perceive different analytes. Particular communications between the objective analyte and the correlative biorecognition layer create a physico-chemical change which is distinguished and might be estimated by the transducer. The bioelement and the sensor components can be joined together utilizing immobilization strategy. (as shown in Fig. 1.13). These devices are incorporated with physicochemical transducers (optical, electrochemical, piezoelectric, thermometric), a predetermined organic receptor layer (proteins, microorganisms, immunogents, chemo receptors, tissue, organelles, biomimetic impetuses, cells or partiality based mixes (antibodies, DNA, synthetic or common receptors)) and a keen signal assessment. The main aim of a biosensor is to produce discrete or continual automated electronic signals that corresponds to a solitary analyte or a related gathering of analytes (see figure 1.14) [41], [42].

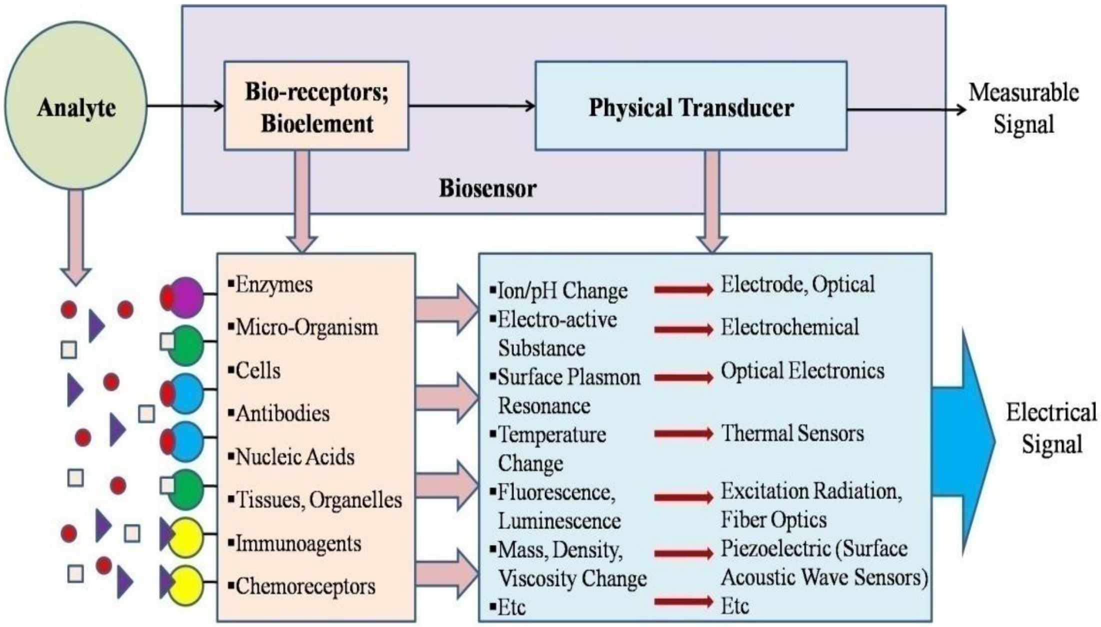

Figure 1.13: Components of a biosensor

These devices are incorporated with physicochemical transducers (optical, electrochemical, piezoelectric, thermometric), a predetermined organic receptor layer (proteins, microorganisms, immunogents, chemo receptors, tissue, organelles, biomimetic impetuses, cells or partiality based mixes (antibodies, DNA, synthetic or common receptors)) and a keen signal assessment. The biological sensory system employed in biosensor development is the centre component of the sensor as the novel organic identification framework can be utilized for investigative purposes to enhance selectivity and sensitivity. Biosensors can be classified in various ways: it is feasible to cluster biosensors as indicated by the method of data used for transduction (e.g., optical, thermometric, piezoelectric and electrochemical) or as per the biomolecule utilized (e.g. biocatalytic or liking based) [43].

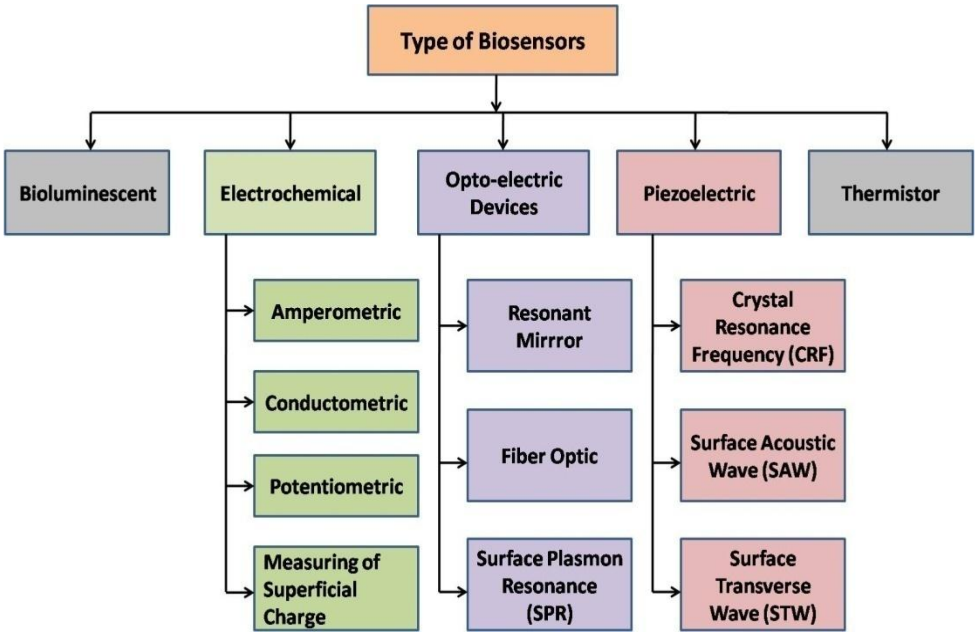

Figure 1.14: Types of biosensor

In **optical biosensors**, the yield is transduced signal that is estimated in light. A biosensor could be constructed in light of optical diffraction or electrochemiluminescence. Optical-diffraction sensors designe includes silicon wafer covered via protein through covalent bonds. The wafer is presented to UV light utilizing a mask, and the antibodies end up idle in the uncovered areas. At the point when the diced wafer chips are brooded in an analyte, antigen-antibody acting agent ties are shaped in the dynamic districts, in this manner making a diffraction grating. This grating generates a diffraction flag when enlightened with a light source, for example, a laser. The subsequent flag can be estimated or additionally opened up before estimating for enhanced affectability.

In **thermometric biosensors**, the yield transduced data that is estimated is light. Thermal exposure biosensors misuse one of the essential attributes of biological responses, specifically ingestion or generation of heat, which thus alters the temperature of the transitional in which the response happens. These biosensors are developed by joining immobilized protein atoms with temperature sensors. At the point when the analyte interacts with the protein, the warmth response of the chemical is estimated and adjusted against the analyte fixation. The aggregate warmth delivered or ingested is relative to the molar enthalpy and the aggregate number of molecules in the response. The estimation of the temperature is regularly proficient by means of a thermistor, and such gadgets are known as chemical thermistors. Their high sensitivity to thermal variations formulates thermistors perfect for such applications. Not at all like different transducers, thermal biosensors don't require visit recalibration and are uncaring to the optical and electrochemical properties of the example. General uses of this kind of biosensor incorporate the recognition of pesticides and pathogenic microbes.

In **piezoelectric biosensors**, the generated transduced signal which is estimation of variation in frequency relative to the mass alteration Piezo-electric crystals (e.g. quartz) tremble affected by an electric field. The frequency of this oscillation (f) relies upon their thickness and cut, every crystal having a trademark resonant frequency. This frequency varies as particles adsorb or desorbs from the surface of the crystal, complying with the connections[44] :

$$\Delta f = \frac{Kf^2 \Delta m}{A} \tag{1.12}$$

Where f is the change in resonant frequency (Hz), m is the adjustment in mass of adsorbed material (g), K is a constant for the specific crystal subject to such factors as its thickness and cut, and A is the adsorbing surface area (cm^2). For any piezoelectric crystal, the adjustment in frequency is corresponding to the mass of consumed material, up to around a 2% variation. This frequency variation is effortlessly recognized by generally unsophisticated electronic circuits. A straightforward utilization of such a transducer is a formaldehyde biosensor, using a formaldehyde dehydrogenase covering immobilized to a quartz crystal and sensitive to vaporous formaldehyde.

In **electrochemical biosensors**, the estimated transduced signal is current, voltage or impedance. The basic rule for this category of biosensors is that numerous chemical responses create or consume particles or electrons, causing some modification in the electrical properties of the solution that can be detected out and utilized as an estimating parameter. Electrochemical biosensors can be categorized in view of the estimating electrical parameters as shown in Table 1.4 [43]:

a. **Conductimetric** (Computed constraint is electrical conductance or resistance) - When electrochemical responses deliver particles or electrons, the general conductivity or resistivity of the solution alters. This variation is estimated and adjusted to a legitimate scale. Conductance estimations have moderately low sensitivity. The electric field is caused utilizing a sinusoidal voltage, which assists in limiting bothersome impacts, for example, Faradaic forms, double layer charging, and concentration polarization.
b. **Amperometric** (Estimated constraint is current) - Amperometric is a high sensitivity biosensor that can recognize electroactive species display in organic test investigation. Since the organic test trials may not be characteristically electro dynamic, chemicals are expected to catalyze the creation of radioactive species. For this situation, the deliberate parameter is present. Amperometric Biosensors deliver a current corresponding to the grouping of the substance to be identified. The most well-known amperometric biosensors utilize the Clark Oxygen anode.
c. **Potentiometric** (Estimated constraint is potential) - In the potentiometric kind of sensor, the deliberate parameter is the oxidation or decrease capability of an electrochemical response. The working guideline depends on the way that when a slope voltage is connected to a terminal in solution, a current stream happens in view of electrochemical responses. The voltage at which these responses happen shows a specific response and specific species. Kinds of potentiometric: ISEs, FETs, ISFETs, m-electrodes.

Electrochemical biosensors are mainly used for the detection of hybridized DNA, DNA-binding drugs, pH and glucose concentration. Electrochemical-based biosensors offer favorable position in the zones of sensitivity and quantization. They experience the ill effects of the drawback that it is important to give intends to electron exchange between the biomolecule and the electrode whereupon they are upheld, for the most part by giving an electrically conducting substrate to the biomolecule, for example, a metal or carbon, their utilize is restricted to a fluid, by and large watery, condition. Different issues are obstructions, identified with electrochemical response of species other than the one(s) of intrigue, and fouling.

Table 1.4: Different electrochemical sensing characteristics

	Electrochemical Sensing		
	Conductimetric	**Amperometric**	**Potentiometric**
Measured Parameter	Conductance/Resistance	Current	Potential/Voltage
Applied Voltage	Sinusidal (AC)	Constant Potential (DC)	Ramp Voltage
Sensitivity	Low	High	
Governing Equation	Incremental Resistance	Cottrell Equation	Nernst Equation
Fabrication	FET+Enzyme	FET+Enzyme	FET+Enzyme
		2 electrodes	Oxide electrodes

The inherent points of interest of electrochemical biosensors are their strength, simple scaling down, phenomenal detection limits, additionally with small analyte volumes, and capacity to be utilized as a part of turbid biofluids with optically absorbing and fluorescing compounds.

1.4.2 Characteristics of Biosensor

With respect to any sensor in view of molecular recognition [45], it is critical to portray a biosensor response: it is significantly more essential here since working parameters may demonstrate the idea of the rate-constraining advances (transport or reaction) and encourage biosensor improvement in a given framework. This section will briefly list principle execution criteria and talk about their connection to properties of the receptor and transducer parts of the electrochemical biosensors. At the point when execution criteria are not specific to biosensors but rather regular to most sorts of chemical sensors or scientific strategies, e.g. accuracy, precision, inter laboratory and interpersonal reproducibility, it is suggested that standard IUPAC definitions be followed [46]. The fast expansion of biosensors and their assorted variety has prompted an absence of meticulousness in defining execution criteria. While every sensor can just really be assessed for a specific application, it is as yet helpful to build up standard conventions for assessment of execution criteria, as per standard IUPAC conventions or definitions [46].

a. **Linearity** of a sensor defined as unit of its capability to follow rapid transformations in the input parameter

b. **Sensitivity** can be expresse as minimum input of physical parameter that causes a measurable output change.

c. **Response time**: Sensors do not alter output state instantly with variation in input parameter. However, it will modify to the new state over a period of time, expressed as response time. The response time is describe as the time requisite for a sensor outcome to transform from its previous state to a final settled value within a tolerance band of the correct new value.

d. **Reproducibility** is a measure of the scatter or the drift in a series of observations or results performed over a period of time. It is generally determined for the analyte concentrations within the usable range.

e. **Selectivity** is expressed as the ratio of the signal output with the analyte alone to that with the interfering substance alone, at the same concentration as that of the analyte.

f. **Reliability** of biosensors for given samples depends both on their selectivity and their reproducibility. It has to be determined under actual operating conditions, i.e. in the presence of possible interfering substances. In order to be reliable for an analyst, the biosensor response should be directly related to the analyte concentration and should not vary with fluctuations of concentrations of interfering substances within the sample matrix.

g. **Limits of detection (LOD)** and of **quantification** (LOQ) take into account the blank and the signal fluctuation (noise).

h. **Steady-state response time** is calculated for each analyte addition to experimental unit. Also determined as time taken to attain 90% of the steady-state value [47].

i. **Transient response time** corresponds to the time needed for the first derivative of the output signal to attain its maximum value (dR/dt)max following the analyte addition.

j. **Lifetime (t_L)**, as the storage or operational time necessary for the sensitivity, within the linear concentration range, to decrease by a factor of 10% (t_{L10}) or 50% (t_{L50}).

k. **Stability** may also be quantified as the drift, when the sensitivity evolution is monitored during either storage or operational conditions.

Calibration characteristics of a sensor is sensitivity, working and linear concentration range, detection and quantitative determination limits.

1.5 HEMT-based Sensor and Its Representative Fabrication Process

The HEMT-based sensor (Fig. 1.15) comprises the HEMT structure and the functionalization layer to make it selective to specific species or parameters. The HEMT structure [48], [49] typically consists of a sapphire (or silicon or 4H-SiC) substrate, an undoped GaN buffer layer (typically 2-3 μm thick), an AlGaN spacer layer (20 A° thickness), and a Si-doped GaN cap layer (200 A° thickness). The cap layer, not shown in the figure, reduces the surface states and provides a homogeneous surface chemistry for functionalization, as well as improves the ohmic contacts for source and drain without adversely affecting the Schottky contact.

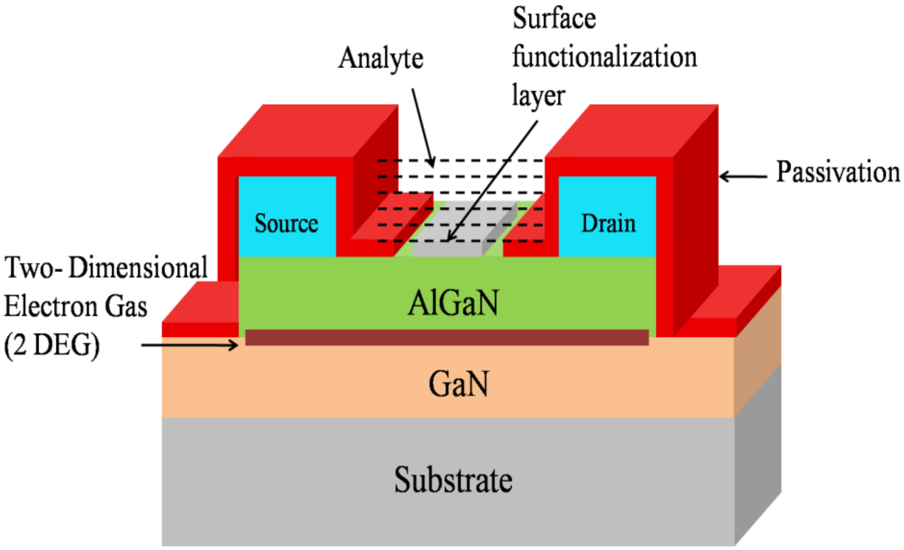

Figure 1.15: Schematic view of AlGaN/GaN HEMT Sensor

The epitaxial layers are developed by means of molecular beam epitaxy (MBE) or metal-organic chemical vapour deposition (MOCVD). Mesa isolation is performed via inductively-coupled plasma etching. For ohmic contacts, Ti/Al/Pt/Au metallization is done using electron- beam evaporation with the pattern defined by lift-off process. The contacts are annealed at 850°C for 45 s. For Schottky contact, Ni/Au is deposited by sputtering. The source and drain regions are encapsulated using polymethyl methacrylate (PMMA). Only the gate area is left exposed for interaction with the analyte.

Polydimethylsiloxane (PDMS) and polyimide are also used as encapsulants. The exposed gate area may be either gold-coated or left unmetallized. It is subsequently coated with the appropriate functionalization layer, depending on the intended application.

1.6 Applications of AlGaN/GaN HEMT Devices

The sudden increase of the web interactive media interchanges has quickly widened around the world, which critically calls for the expansion of transmission network limit. GaN HEMTs devices considered as the mainly appealing alternatives for getting through speed bounds, high gain, and low noise system. Distinctive organizations overall create and produce HEMT devices, and numerous conceivable areas have been proposed for these devices. Electronic biosensors exploration has lately strengthened owing to significant development in growth and fabrication of semiconductors, in addition to approaches for the surface functionalization [50], [51]. Several reports have revealed that the complexity of the bioanalytes with clinical significance can be most excellently addressed by HEMT devices composed of compound semiconductors. Agreed to their remarkable steadiness in the air, water, and blood environments; exceptional biocompatibility [52]; and fine control of electrical, structural, and surface properties, III-nitride-based HEMTs demonstrate the potential candidate for compound semiconductor biosensors [53]. Without taking into account those conceivable outcomes, some major applications are outlined in this segment, also depicted in Fig.1.16.

a) Power Electronics and Microwave Monolithic Integrated Circuits (MMICs) Applications

GaN HEMTs operated at high voltages are a very promising device in support of high power, high temperature and microwave applications. In mobile communication as the numbers of users are increasing daily, so more base-stations and sub-stations are needed [54]. To increase the power density from base- or sub-station, large no of power amplifier units will be required. The GaN HEMT was initially produced for high-speed applications.

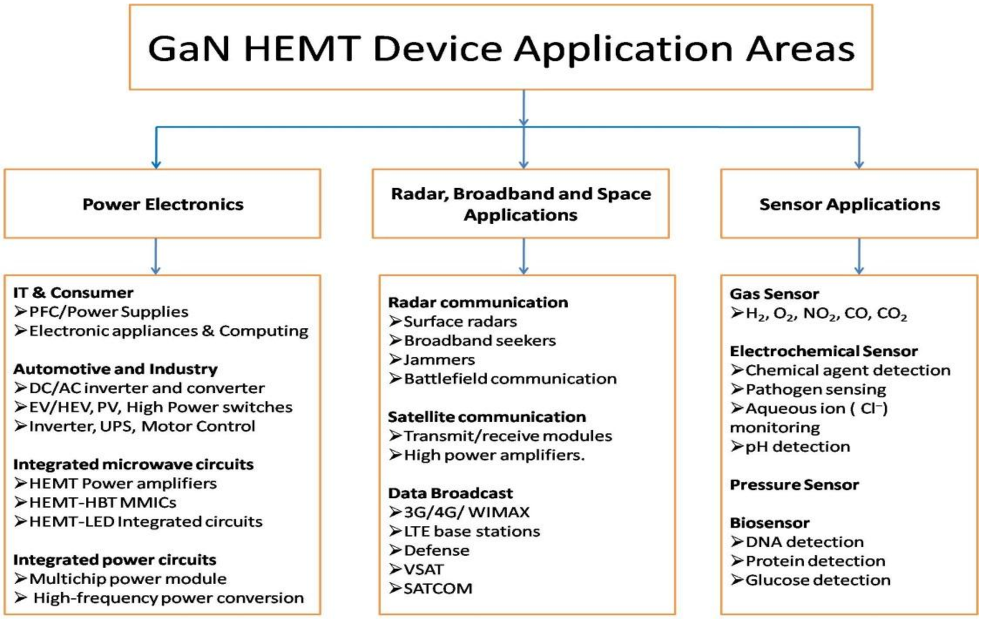

Figure 1.16: Application areas of GaN-based HEMT devices

The innovative points of interest of GaN/AlGaN HEMT result from the combined attributes of the wide bandgap of III-Nitride and the accessibility of AlGaN/GaN heterostructure where high voltage, high current and low on-resistance can be all the while accomplished, bringing about high power-high effectiveness operation. Besides, the wide-bandgap presents a robust and reliable innovation prepared to drive at high voltage and high-temperature functions. These points of interest proclaim numerous commercial, automotive and aircraft functioning areas similar to high power voltage rectifiers - converters. GaN HEMT devices are utilized as a part of an extensive variety of RF applications together with cellular communications, direct broadcast receivers - DBS, radar, radio stargazing, and RF attention that need a blend of low noise and high-frequency operation. HEMTs are produced through numerous semiconductor device developers over the globe. They might be as discrete transistors, yet these days they are all the more customarily fused into incorporated circuits. The particular Monolithic Microwave Integrated Circuit (MMICs) are generally utilized for RF plan applications. The HEMT based MMICs are broadly employed to give the requisite amount of execution in numerous fields. As regards the production of integrated devices, the monolithic integration of chemical sensors with III-nitride materials in support of collective spectroscopic investigation, HEMTs representing on-chip signal handling, and surface acoustic wave devices [55] in favor of similar signal filtering are feasible. Wireless sensor networks by means of radio frequency identification (RFID) have additionally recommended [56].

b) Radar, Broadband and Space Applications

Mobile communication comprises the major vital nonmilitary uses of HEMT devices through substituting Si transistors. In favor of such broadband/multiband communication usage, we acquire a considerable measure of points of interest. The expansion in comparative transmission capacity intended to a specified power limit is one of those innovative circuit and framework ideas give transfer speed with expanded efficiency. Linearity has been enhanced for a similar yield control. The decrease of memory impacts is likewise found by utilizing GaN HEMT devices [57]. High gain and low noise amplifiers are the fundamental attributes for producing radar parts. GaN HEMTs are the primary alternatives for such module. Active electronic sensor arrays are worked from GaN HEMTs, which are utilized for airborne radars, ground-based air safeguard radars, and maritime radars [58]. Ka-band rocket applications at 35 GHz are additionally being examined in writings [59]. Discrete HEMTs are quite often utilized as the preamplifier in a conventional DBS receiver, trailed by at least one GaAs MESFET monolithic microwave integrated circuits (MMICs) because of their amazing low-noise attributes. The utilization of low-noise HEMT preamplifier has brought about considerable enhancements in framework execution at a minimal extra cost [60]. Microwave hardware utilized in space applications are exceptionally costly since they require additional safeguard as of severe condition in space to outlive. Additionally, rocket might be propelled, and this suggests the hardware ought to likewise manage without harm at elevated amounts of vibrations and stuns. HEMTs can be fabricated to outlast this situation and have been widely utilized as a part of different fields.

c) Sensor Applications

A less observed promising usage of the GaN HEMT structure is sensors. A short while ago, electrochemical sensors have picked up significance for utilization that incorporates land security, medicinal and environmental observing, and food well-being. The attractive objective is the ability to concurrently investigate a broad range of environmental, biological gases and liquids in the area possess the capacity to selectively distinguish an intended analyte through eminent specificity and sensitivity. In the HEMTs, 2DEG region provides conducting path near the interface which is extremely sensitive to a chemical constituent that is undergoing analysis. Subsequently, HEMT sensors could be a decent option for identifying gases, ions, and chemicals [61]. Benefitting from distinction to the exploration of HEMTs using the essential HEMT structure, electrochemical sensors for gases and liquids are fabricated which got expanded consideration over the most recent time [56], [62]. Because of their wide bandgap and robust bond qualities, GaN material has decent chemical stability while found in resistance from wet etching methods [12], [63], and their biocompatibility [64], [65]. III-nitrides are anticipated as a standout amongst the utmost encouraging materials used for biosensing gadgets because of wide bandgap [66], low noise and high sensitivity towards variation in the surface charge [67], [68]. In addition, the straightforwardness in the visible range of light drives the likelihood to join typical optical and electrical estimations.

1.7 Outline of Research

The fundamental objective of this thesis is to make a systematic investigation of GaN-based HEMT devices for electrochemical sensing for space and biomedical applications. First, the comprehensive simulation study of AlGaN/GaN HEMTs incorporating optimization of AlGaN and GaN Cap thicknesses, high temperature and trapping effects on the device performance has been presented via SILVACO-ATLAS. These simulation studies can be beneficial to reduce the fabrication cost and efforts by optimizing various device parameters over the simulation tool itself before moving for the actual device fabrication. Then, GaN HEMTs were fabricated over MOCVD grown HEMT epitaxies on a sapphire substrate. Various physical and design parameters were optimized during the fabrication to achieve high-performance HEMT devices. A detailed investigation of electrical properties of GaN HEMTs has been done, and the output characteristics of these fabricated HEMT devices after dicing and packaging at room temperature has also been tested. The scope of the work has further been extended to characterize the pH, and salt detection properties of these GaN-based HEMT sensors for a various biomedical and space applications. The thesis consists of six chapters including the present one entitled as “Introduction”. The remaining chapters are organized as follows:

Chapter -2 compiles some important state-of-the-art work in this area. The major work done in this field by various research groups is presented in brief. A detailed review of latest trends in the field of III-Nitride semiconductors, GaN-based HEMTs, and their applications in electrochemical sensing has been presented. Based on the literature survey, various research gaps in this area have been identified. Finally, the motivation behind this study has been outlined at the end of the chapter.

Chapter-3 presents simulation course and performance examination of AlGaN/GaN HEMTs using simulation software ATLAS™ from SILVACO International. Different electrical parameters for example, electric field distribution, electron concentration, electron mobility, energy band diagram, output characteristics, transfer curve, transconductance and leakage current of GaN-based HEMTs have been simulated. A detailed simulation of GaN HEMT devices for the optimization of AlGaN and GaN Cap layer thicknesses, followed by a closer look at the high temperature and trapping effects on the device performance is also executed.

Chapter-4 is devoted to the fabrication and characterization of GaN HEMTs devices on the 2 inch wafer. Device processing includes wafer cleaning, device isolation, the formation of ohmic and schottky contacts, metal interconnects, surface passivation, dicing and device packaging. Different isolation techniques including Mesa etching and Ion implantation is also investigated Optimization of Ohmic contacts on both thin (18 nm) and thick (25 nm) AlGaN/GaN HEMTs devices has been examined in detail so that high-quality ohmic contacts along with low contact resistance and smooth surface morphology can be achieved. We also performed a comparative study of AlGaN/GaN with and without passivated HEMT devices with two different dielectrics, SiO_2 and Si_3N_4 .In this study, we used similar device dimensions on the identical epi-layer configuration with similar fabrication techniques. The methods used for dicing and packaging of HEMT devices have been discussed. Finally, the AlGaN/GaN heterostructures have been characterized to calculate the electrical characteristics and surface properties using Keithley 4200-SCS Semiconductor Characterization System and Scanning Electron Microscopy (SEM) respectively.

Chapter-5 deals with fabrication and characterization of GaN HEMT based electrochemical biosensor for pH and salinity sensing. . We examined the linear change of current when devices are exposed to the PBS solution of different pH values and the aqueous salt solution of NaCl + DI water. The sensitivity of GaN HEMT in different pH solutions and various molar concentrations of aqueous solution have been investigated. On account of obtained outcomes, a model has been proposed to explain surface chemical reaction associated with the difference in H^+ and OH^+ ions concentration and their interaction with AlGaN surface.

Chapter-6 concludes some major findings and outcomes of the thesis. The chapter summarizes all the results presented in previous chapters of the thesis. Finally, the future scope of the work is outlined in the end.

CHAPTER 2

AlGaN/GaN HEMTs for sensing applications: A General Review

This chapter builds the background and context for the research addressed in this thesis and presents state-of-the-art work reported by various research institutions in the area of GaN HEMTs based electrochemical sensors.

2.1 Introduction

Literature survey plays a significant role in any kind of research. A thorough knowledge of the state of the art work in any research area can only be predicted by the future trends in that particular research area. Therefore, this chapter is dedicated to present some important state of the art work addressed by various research experts in the area of AlGaN/GaN HEMTs. This chapter primarily focuses on some important investigations that have been done in the area of GaN based HEMT devices over the last decade. Simulation and fabrication of AlGaN/GaN HEMTs and their applications as a biosensor has been reviewed in detail.

Due to the constraint of the Silicon MOSFET (Metal-Oxide-Semiconductor Field-Effect Transistor) and III-V forerunner MESFET (Metal–Semiconductor Field-Effect Transistor) are advances as the stimulus for the HEMT (High Electron Mobility Transistor). The steadfast functioning of wide-bandgap HEMT devices at elevated temperatures up to 400°C, alongside their less susceptibility to thermal or optical stimulation, together with the more noteworthy protection from chemical deterioration using acids and soluble bases, has urged scientists to make attempts concerning the advancement of a group of sensors in severe situations, a field where traditional silicon MOSFET and ISFET (Ion-Sensitive Field-Effect Transistor) devices are found to be ineffectual. Also, the closeness of the conducting 2DEG (two-dimensional electron gas)

HEMT channel to the surface gives improved sensitivity to adsorption of substances, while the scaling down and high-recurrence activity ability of HEMT-based micro-sensors empowers their consistent reconciliation into remote sensor systems for remote checking of patient's wellbeing through bedside or handheld instrumentation.The word 'HEMT' infers the prospect of a high-frequency and high-power device utilized as a part of microwave media communications. An additional utilization of HEMT, which is no less vital, however regularly neglected, is 'sensing operation'. This key uses of HEMT frame an extension, connecting the patient at home with the specialist in a far away centre or doctor's facility, or other comparative modern computerization tool. An extra quill in the top of HEMT device is its capacity to endure in harsh or unpleasant circumstances. The previously mentioned attributes of HEMTs, alongside their non-toxicity to living cells, have empowered HEMT-based sensors to carve out an exceptional role for themselves, finding their ways into areas where Si-based devices have until now unable to make the grade.

2.2 GaN HEMT TCAD Simulation

Computer simulation has turned out to be a flexible and important apparatus for engineering design and investigation. Up till now, the Silvaco software applications draw closer to the front line of design and investigation of semiconductor devices. Instead of this, GaN-based devices necessitate unusual interest for computer modelling and simulation because of their innate piezoelectric (PZ) and spontaneous (PS) polarization, characteristics. Extensive research concentration has been given toward these nitride-based devices, to develop accurate model for the various properties and other associated impacts. Device simulation and modelling are vital in the advancement of any innovation enabling researchers to optimise device designs and process flows prior to placing them into fabrication. This is especially valid for GaN based devices while concerning about the expansive cost of the material.

In this work, Silvaco International device simulation software was used for the device simulation. Silvaco-ATLAS^{TM} tool carried out the general device simulation[69]. Whereas BLAZE^{TM}, GIGA^{TM}, and C-INTERPRETER^{TM} executed specific capacities requisite for III-V heterojunction devices, thermal counts, and user defined equations, respectively. To control and adjust the models, Silvaco's VWF Interactive Tools (particularly DECKBUILD^{TM}, TONYPLOT^{TM}, and DEVEDIT^{TM}) were used. The Silvaco programming utilizes physically based simulation as opposed to empirical modelling. While empirical modelling generates formulas that agree with present information, while physically based simulation calculate device execution in view of physical structure and predisposition conditions. The Silvaco programming symbolize a device on a two dimensional mesh. At each meshing point the program simulate carrier transport by methods for differential equations got from Maxwell's laws. To accomplish exactness, the program must fuse the fitting material physics through numerical methods.

This section presents some recent state-of-the-art work regarding different issues related to device design and technology while simulating the devices.

Eimers *et al.* [70] gave theory to consolidate piezoelectric (PZ) conditions in the Silvaco Atlas programming for demonstrating GaN/AlGaN structures. The PZ impact improves 2DEG at the GaN/AIGaN interface because of stress instigated polarization. This impact brings about an anticipated measure of electron sheet charge at the heterojunction giving outstanding conductivity of electron current. The software changes utilize that outcome and recreate embedding a proper measure of donor concentration influences in the best 10 nanometers of GaN material that positioned specifically underneath the AlGaN layer.

Holmes *et al.* [71] endeavoured to include the impacts of piezoelectric and spontaneous polarization onto the HEMT display using a C-interpreter strategy. This work gets a satisfactory I-V curve for a HEMT device using a C- interpreter schedule. Nevertheless, this model should have been rectified to all the more intently coordinate the general task of the HEMT device.

Salm *et al.* [72] modelled the impact with an interface charge with the piezoelectric model, and his outcomes were satisfactory and all the more precisely demonstrated the coveted qualities of a HEMT device. His proposal likewise examined the thermal characteristics of the device using the GIGA™ module. The GIGA™ module is equipped for giving a numerical, and in addition illustrative, portrayal of device heating. Salm's outcomes demonstrated a significant change in device heating because of an adjustment in substrate material.

Albrecht *et al.* [73] investigated that the minor irregularity in the lateral temperature distribution amid contacts might be originated by variations in the electrical field distribution and charge trapping and infusion in GaN based high power devices. Analysis of thermal profile in HEMT provided improved consideration of local variations.

Littlejohn *et al.* [74] was first time reported on the Monte Carlo simulation of the electron transport in GaN with repect to electric field at different temperatures and doping concentration in 1976. Authors considered a two valley model and included scattering by acoustic phonons, polar optical phonons, ionized impurities, and piezoelectric charge to predict a peak in the electron drift velocity of ~2 x 10^7 ms^{-1} at a field of ~ 2 x 10^5 Vcm^{-1} for an electron concentration of 10^{18} cm^{-3}, which is considerably larger than that found in Si or GaAs.

Karmalkar *et al.* [75] research the breakdown upgrade capability of the field plate (FP) method with regards to GaN power HEMTs. A deliberate methodology was given by the authors for outlining a FP device, utilizing two dimensional (2-D) simulations, to get the most extreme frequency response. The FPs more equally scatters the electric field in the channel. The procedure of this paper can be extended to the outline of FP structures in other FETs, for example, MESFETs and LD-MOSFETs.

Smith *et al.* [76] performed two-dimensional hydrodynamic simulations. This electron transport model attained maximum accuracy together with computational efficiency. The charge transport models were typically achieved by employing approximations and improvements to the Boltzmann Transport Equation. Since the drift-diffusion turned out to be less exact for smaller component sizes, the hydrodynamic arrangement was attained by captivating the following two higher instants of the Boltzmann condition over that in support of the drift-diffusion elucidation. Thus, the hydrodynamic reproduction gives a feasible trade off flanked by these two strategies.

Russo *et al.* [77] demonstrated that a reduction the source–gate separation could enhance device operations, upgrading the output current furthermore, the device transconductance. The primary explanation behind this impact is identified with the unusual dynamic of electrons in the GaN-based HEMTs, which prompts a non-saturated speed routine in the source entry area, notwithstanding for high drain voltages.

Miller *et al.* [78] examined broadly the gate leakage current estimations through 2D computations demonstrate that vertical tunnelling is the predominant component for gate leakage current in the typical barrier HFET and with the aim to improve barrier structure blocking this system so as to accomplish a lessened leakage current. An analytical representation of vertical tunnelling in a reverse-biased HFET gate-drain diode is created to assess the credibility of this accomplishment.

Pérez-Tomás *et al*. [79] addressed a frequency based on conductance examination to describe the gate traps and demonstrated an profusion of surface states and interface traps in the Schottky gate AlGaN/GaN HEMTs.

Sathaiya *et al.* [80] addressed the reliability issues included non-linear source resistance which degrades the device performance under high RF drive and DC/RF breakdown due to impact ionization in the 2DEG channel.

Glasstone *et al.* [81] investigated the gate leakage, an essential reliability concern which restrains the device performance by affecting the DC characteristics of the device. The surface of the device in the drain access region facilitates leakage current flow due to the presence of shallow traps.

Kuang *et al.* [82] explored traps in the AlGaN barrier which assists in the trap assisted tunnelling mechanism from the gate to the 2DEG which forms a secondary path for the gate leakage current flow. The gate leakage current degrades the performance of the device by increasing the pinchoff current and by degrading the sub-threshold characteristic.

2.3 GaN HEMT Device Fabrication

Khan *et al.* [83] were among the first few investigators to fabricate GaN MESFETs developed on sapphire utilizing low-pressure MOCVD. A thin film AlN buffer layer was utilized to upgrade the nature of GaN films. The gate length and width for the MESFETs were 4 and 100 µm, respectively. The reverse leakage current density at a gate bias of -5 V was measured to be ~1 mA/cm^2. For such MESFET the transconductance was 23 mS/mm at gate bias of - 1V. The calculated carrier density and low-field mobility for a channel of thickness 0.6 µm thicknesses were 10^{17} cm^{-3} and 350 cm^2/Vs respectively. The extracted drift velocity of carriers commencing these values was 5 x 10^6 cm^2/s.

Dingle *et al.* [38] proposed the n-type modulation doped semiconductor heterostructure in 1978, to simultaneously improve the carrier density and the mobility, and spatially isolate the carriers to the ionized scatter.

Khan *et al.* [84] reported an exciting development, establishment of a 2DEG in the quantum wells at the interface of an AlGaN/GaN heterostructure. It was formed by depositing 3000 Å thick unintentionally doped GaN on AlN buffer, capped by 500 A^o undoped $Al_{0.09}Ga_{0.91}N$. The sheet carrier density in the quantum well was 5 x 10^{12} cm^{-2}, and the carrier mobility was 620 cm^2/Vs at 300 K, 1600 cm^2/Vs at 77 K.

Takeshi *et al.* [85], in their device a 2 DEG mobility 12000 cm^2/Vs with a sheet carrier density of 2.8 x 10^{12} cm^{-2} was observed at 8.9 K. The recessed gate HEMT structure demonstrated maximum extrinsic transconductance of 181 mS/mm and drain-source current 1120 mA/mm for a gate length 1.5 µm at 25 ^{o}C with a recess depth of 30 nm and a recess width of 6 nm. The observed transconductance of this recessed device is much larger in comparison to basic HEMTs as expected.

Wang *et al.* [86] provides a comparative study between recessed and conventional AlGaN/GaN HEMTs. The use of n-GaN cap layer considerably reduced the contact and channel resistance and increased the RF and microwave power performance of the device. A lower knee voltage, a higher transconductance (223 mS/mm), a higher current density

(1.104 A/mm), and a higher microwave output power (4 W/mm) was accomplished in recessed AlGaN/GaN HEMTs.

Farahmand *et al.* [11] worked on to accomplish a high sheet carrier density with high carrier mobility with the designs concerning a high Al content of gating layer. The subsequent higher band discontinuity ought to advance the carrier confinement, and stronger spontaneous polarization and the piezoelectric effects caused a improved sheet charge density in the channel. Additionally, a higher band gap of the AlGaN layer provides a higher composite breakdown field. Transport attributes of nitride semiconductor are concisely reported by the authors.

Mishra *et al.* [87] anticipated the impact of the gate width on the power performance utilzing $Al_{0.5}Ga_{0.5}N$ HEMTs with 0.25 μm gate length. Expanding the gate width from 100 to 500 μm, a consistent increment of aggregate output from 0.35 to 1W at 8GHz was examined, though the power density reduced from 3.3 to 2 W/mm, individually. This conduct was credited to self-heating impact for bigger devices.

Kumar *et al.* [88] reported on the high performance 0.25 μm gate length AlGaN/GaN HEMT on sapphire substrate with transconductance of over 400mS/mm with f_T of 85 GHz and f_{max} of 151 GHz.

Wu *et al.* [89] proposed the devices on SiC substrate with 0.12 μm displayed an extrinsic transconductance of 217 mS/mm and current drive capability 1.19mA/mm and a record high unity current gain cut-off frequency of 101 GHz and maximum oscillation frequency of 155 GHz.

Han *et al.* [90] **and Wu *et al.*** [91] compared the surface morphology of GaN/AlGaN heterostructures after Cl_2 /H_2, Cl_2 /Ar, and Cl_2 /BCl_3 ICP etching, and concluded that the surface morphology could be improved by the addition of BCl_3 to chlorine plasmas. But their etch conditions are not favourable to the fabrication of optoelectronic devices due to the lower etch rate and selective etching of GaN over AlGaN.

Jenkins *et al.* [92] **and Scheitz *et al.*** [93] are supposed that TiN be able to simply develop Ohmic contact to the wide band gap GaN or AlGaN. In the situation where TiN development is instigated, the rest of the layer has N-deficient *n*-type doping at the metal/GaN interface which is adequately large enough for tunnelling contact mechanism to be influenced. Ti additionally perform the function of oxide getter from the surface of the epilayer. Consequently, when it is combined with metals with high conductivity, for example Al, it can facilitate direct Ohmic contact deposition.

Ruvimov *et al.* [94] reported that amid the numerous contact metallization methods reported in the literature, Ti/Al-based contacts are the most widely utilized. Ti based metallization schemes reduce contact resistance by forming an inter-metallic alloy with a low work function on GaN and AlGaN surfaces.

Hilsenbeck *et al.* [95] found that, it is usually easier to get low contact resistance using the more conventional high temperature sintering approach and WSiN cap can help to improve the morphology of the Ohmic contacts after high temperature sintering significantly.

Chaturvedi *et al.* [96] stated some edge non-uniformity in the Ti/Al/Ti/Au/WSiN Ohmic contact metalization. The fundamental cause of this edge non-uniformity is correlated with the way that the Ohmic contacts were developed through a lift-off method and Ti/Al/Ti/ Au was deposited by electron beam evaporation however WSiN deposited using sputtering procedure. Amid WSiN sputtering, there is some WSiN deposited on the photoresist sidewall. While liftoff, the WSiN film may break in a non-uniform manner doe to non-uniform WSiN film thickness on the photoresist sidewall, ensuing in edge non-uniformity. Hence there is a solid motivation to improve the basic Ti/Al/Ti/Au Ohmic contact process without using WSiN.

2.4 GaN HEMT based Sensors

2.4.1 HEMT based Chemical Sensors

Since the first demonstration of a fluid monitoring sensor based on AlGaN/GaN hetero structures by Neuberger[97], the application of AlGaN/GaN HEMTs as liquid sensors has been a subject of intense research. Neuberger et al. have expressed that the sensing mechanism for chemical absorbates originated from the compensation of the polarization induced bound surface charge by interaction with polar molecules in the fluids. The time dependence of changes in source-drain current of gateless HEMTs exposed to polar liquids (isopropanol, acetone, methanol) with different dipole moments using GaN/AlGaN hetero-interfaces was also reported. In particular, it was possible to distinguish liquids with different polarities. The HEMT sensors at a glance are shown in Table 2.1.

Mercury (II) Ion Sensor

Wang *et al.* [98] detected Hg^{2+} ions in as low as 10^{-7} M concentrations using bare Au-gated and thioglycolic acid functionalized AlGaN/GaN HEMTs. The latter sensors had 2.5 times larger sensitivity than the former, and also responded in <5 s. Selectivity of mercury detection over sodium or magnesium ions was >100.

Potassium Ion CHEM HEMT

Alifragis *et al.* [99] proposed the Valinomycin-doped PVC membrane build upon the non-metallized gate of AlGaN/GaN HEMT helped in achieving a K^+-ion sensitivity of 52.4 mV/pK^+ in the concentration range 10^{-5} to 10^{-2} M of a lesser exposure boundary of 3.1×10^{-6} M. The drain-source current increased linearly with log [K^+].

pH Sensor

Kang *et al.* [100] Ungated AlGaN/GaN HEMTs using Sc_2O_3 gate dielectric illustrate a change in drain-source current of 37 μA for each decade pH variation in the pH range 3 to 8, with a resolution of 0.1 pH.

Abidin *et al.* [101] investigated the sensing response of an open-gated pH sensor fabricated on AlGaN/GaN HEMT configuration. High sensitivity of 1.9 mA/pH at drain-source voltage = 5 V was obtained.

Steinhoff *et al.* [102] suggested that the native oxide on the nitride surface was responsible for the *p*H sensitivity of the response of gateless GaN based heterostructure transistors to electrolyte solutions. The linear response of nonmetallized GaN gate region using different *p*H valued electrolyte solutions and sensitivity with a resolution better than 0.05 *p*H from *p*H = 2 to *p*H = 12 were shown.

Ammonium Ion Sensor

Alifragis *et al.* [103] proposed the HEMT device with non-metallized gate and coated with nonactin-enriched PVC membrane showed sensitivity of 55.5 mV/p NH_4^+ mm ammonium ions in the range 10-5 to 10-2 M.

Oxygen Sensor

Wang *et al.* [104] studied that the Indium zinc oxide (IZO)-gated AlGaN/GaN HEMTs showed a strong response to the oxygen gas at 120°C; in addition, IZO was deposited by cosputtering from ZnO and In_2O_3 targets.

Hung *et al.* [105] suggested that the Hydrothermally-grown SnO_2 gate electrode with AlGaN/GaN HEMT sensor provided detection of 1% oxygen in nitrogen at 100°C.

Chloride Ion Sensor

Chu *et al.* [61] proposed the AgCl thin film on ZnO-nanorod gated AlGaN/GaN HEMT could detect up to 10^{-8} M concentration.

Nitrate Ion Sensor

Myers *et al.* [106] explored that a plasticized PVC-based membrane containing a nitrate–selective ionophore was deposited on the HEMT gate, resulting in a nitrate ion sensor with a working range from 1×10^{-6} to 1×10^{-2} M, and a lower detection limit of 1×10^{-7} M.

Hydrogen Sensor

Cheng *et al.* [107] studied Pd/Oxide/$Al_{0.24}Ga_{0.76}As$ HEMT-based sensor which showed low hydrogen detection limit (4.3 ppm H_2/air) with a short response time.

Hung *et al.* [108] investigated synthesized SnO_2 dispersion by hydrothermal method, deposited it selectively on Au gate of HEMT by photolithography, and annealed it at 200-400°C. They studied the time dependence of the sensitivity on cycling between 1% H_2 in

N_2 and pure N_2 gas at temperatures of 150°C, 200°C and 300°C. Fast and reversible hydrogen sensing was observed at low temperature.

Guo *et al.* [109] reported an AlGaN/GaN HEMT-based hydrogen sensor which showed response variation of 25.8 % upon 10-fold change of hydrogen concentration at 130°C.

Cl_2 gas and HCl Vapor Sensor

Son *et al.* [110] addressed the HEMTs for detecting corrosive and caustic chemicals. Exposure of Pt-gated HEMT to an oxidizing gas (1% Cl_2 gas) resulted in an increase in drain-source current I_{DS} whereas its exposure to a reducing gas (1% HCl vapour) caused a decrease in drain-source current, showing the ability of HEMT to differentiate between oxidizing and reducing agents. Cl_2 gas withdraws electrons from the Pt-gate leading to a less negative effective gate voltage and producing a larger I_{DS}. The HCl vapour has the opposite effect.

2.4.2 HEMT based Physical Sensors

Strain Sensor

Yilmazoglu *et al.* [111] Piezoresistance of $Al_{0.3}Ga_{0.7}N$/GaN HEMT channel was investigated, who measured a gauge factor between 19 and 350 under defined biasing conditions. Thus HEMTs are employed as strain sensing elements.

Eliza *et al.* [112] analytically modelled and studied the performance of GaN HEMT device for the induced strain.

Pressure Sensor

Kang *et al.* [113] determined the variations in the capacitance of the channel of an AlGaN/GaN HEMT membrane formation developed over the Si substrate.

Hung *et al.* [114] coated the gate area of AlGaN/GaN HEMT with PVDF film using an inkjet plotter, polarized the PVDF film by the appliance of a high voltage (10 kV at 70°C) between a copper electrode positioned 2 mm over the film and the grounded chuck on which the HEMT was mounted, and subjected the polarized PVDF-gated HEMT to pressure changes of 1 atm to 1 psi. They observed appreciable variations in channel conductance of HEMT, indicating its usability to measure pressure differences ~ 1 psi.

Edwards et al. [115] studied the electromechanical behaviour of a sapphire/GaN-based diaphragm structure.

Brezeanu et al. [116] revealed a HEMT sensor for measuring pressures in harsh environments.

Hall Magnetic Field Sensor

Koide *et al.* [117] AlGaN/GaN HEMT-based micro HEMT-based sensors exhibit stable operation from room temperature to 400°C with current-related magnetic sensitivity of 77 $VA^{-1}T^{-1}$.

Terahertz Sensor

Lü and Shur *et al.* [118] demonstrated AlGaAs/GaAs terahertz HEMT sensor derived at 2.5 THz and reported a system of activity of such HEMT terahertz indicators which enabled them to build the responsivity in excess of a order of extent.

Fatimy *et al.* [119] fabricated ultra-short-gate (50 nm) InGaAs/InP devices and observed efficient THz detection.

Watanabe *et al.* [120] investigated dual-grating-gate (DGG)-HEMT structures for broadband detection of THz radiations, and showed ultra-sensitive THz imaging with the InP-based asymmetric DGG-HEMTs.

Esfhani *et al.* [121] reported changes in channel conductance for potential applications in chip-scale frequency-agile detectors, scalable to mid-THz frequencies.

2.4.3 HEMT based Biosensors

Prostate specific Antigen (Prostate Cancer Marker) Sensor

Kang *et al.* [122] explored PSA antibody was fixed to Au-gated HEMT through carboxylate succinimdyl ester bonds with immobilized thioglycolic acid. After PSA incubation, the drain-source current decreased with detection limit of 10 pg/ml. The PSA concentrations up to 1 μg/ml were measured, and the response time was less than 5 s.

KIM-1 (Kidney Injury Disease Biomarker) Sensor

Wang *et al.* [48] proposed a self-assembled monolayer of thioglycolic acid which was absorbed on the Au gate of the HEMT. Kidney injury molecule-1 (KIM-1) antibody was immobilized through reaction between amine group of the antibody and carboxyl group of thioglycolic acid. On exposure to KIM-1, the drain-source current changed, and the change was nonlinearly proportional to KIM-1 concentration. The detection limit was 1 ng/ml in PBS buffer.

Botulinum Toxin Sensor

Wang et al. [123] detected Botulinum toxin in the range from 1 to 10 ng/ml by botulinum antibody functionalized Au-gated HEMT.

Lactic Acid Sensor

Chu *et al.* [124] was grown the ZnO nanorods on the gate of the HEMT to provide a large surface area with a high surface-area-to volume ratio. Lactate oxidase enzyme was immobilized on the nanorod array. The biosensor could detect lactic acid from 167 nM to 139 μM.

c-erb-2 (Breast Cancer Marker) Sensor

Chen *et al.* [125] was attached the antibody to the Au-gated HEMT through immobilized thioglycolic acid. When c-erb-2 antigen was introduced, the drain-source current decreased in <5 s. The change was nonlinearly related to the antigen concentration. The detection range was from 16.7 to 0.25 μg/ml.

Perkisus Marinus Sensor

Wang *et al.* [126] explained the antibody coating of the protozoan pathogen was applied on the thioglycolic acid immobilized on Au-gated HEMT. The presence of P. Marinus in water was seen through drain-source current changes within 5-20 s.

Glucose Sensor

Chu *et al.* [127] investigated the Glucose oxidase enzyme which was immobilized on zinc oxide nanorod-gated HEMT. The sensor could detect glucose concentrations from 0.5 nM to 125 μM in pH=7.4 buffer in <5 s.

Uric Acid Sensor

Song et al. [128] constructed uric acid biosensor by uniformly distributing ZnO nanotetrapods on the HEMT gate and immobilizing uricase enzyme upon it. This sensor could detect uric acid concentrations from 0.2 nM to 0.2mM with the detection limit of 0.2 nM.

DNA Sensor

Thapa *et al.* [49] fabricated a highly specific HEMT DNA sensor by immobilizing amine-modified single strand DNA upon the self-assembled monolayers of 11-mercaptoundecanoic acid on the Au gate. The drain-source current decreased by about 100 μA at 1 V bias, when hybridization with complementary DNA took place.

Makowski *et al.* [129] developed Au nanoparticle/HEMT sensors for detection of analytes such as specific DNA sequences, proteins, or other metabolites. Au NPs provide a proven system for detection of such analyte-receptor interactions.

2.5 Summary and Concluding Remarks

This chapter presents some important state-of-the-art research on III-V semiconductor, AlGaN/GaN HEMTs and their application in sensing. The literature survey presented in the above sections can be summarized as follows:

- These devices do extremely well over their silicon correspondent as a consequence of their innate properties for example chemically stable bulk and surface properties and the availability of high-density two-dimensional electron gas (2DEG) at the hetero-interface which let a highly sensitive detection of the surface charge related phenomena.

Table 2.1: GaN HEMT-based sensors at a glance

Sensor Category	Sensed quantity	Gate Surface	Surface coating	Transduction mechanism	References
HEMT-based Chemical sensors	Mercury ion	Au	Thioglycolic acid	Chelation	[98]
	Potassium ion	GaN cap	Valinomycin-doped PVC	Selective binding of K^+ ions to valinomycin	[99]
	pH	AlGaN	Sc_2O_3	Action between polarization-induced surface charges and ions in the electrolyte	[100]
	Ammonium ion	Gan cap	PVC enriched with nonactin	Selective binding of ammonium ions by ionophore	[103]
	Oxygen gas	GaN	Indium zinc oxide	Oxidation	[104]
	Chloride ion	ZnO nanorods	AgCl thin film	Anodization	[61]
	Nitrate ion	GaN Cap	Nitrate ionophore in PVC	Selective binding of nitrate ions by ionophore	[106]
	Hydrogen gas	Pd-MOS Schottky structure	None	Catalytic dissociation	[107], [108]
	Cl_2 gas and HCl vapor	Pt	None	Actions of oxidizing and reducing gases on Pt-gate	[49]
HEMT-based Physical sensors	Strain	----------	---------	Variation in 2DEG channel conduction by external forces	[111]
	Pressure	PVDF film	None	Changes in the charge of polarized PVDF film	[114]
	Magnetic field	Cross pattern of Ti/Al/Ni/Au electrodes	None	Hall voltage generation from magnetic field between probes on AlGaN/GaN heterostructure having 2DEG at the heterointerface.	[117]
	Terahertz waves	----------	---------	Rectification of plasma waves	[118]–[120]
HEMT-based Biosensors	PSA	Au	Ab-PSA	Ab-Ag binding	[122]
	KIM-1	Au	Ab-KIM-1	Ab-Ag binding	[48]
	Botulinum	Au	Ab-Botulinum	Ab-Ag binding	[123]
	Lactic acid	ZnO nanorods	LO_X	Enzyme promoted reaction	[124]
	c-erb-2	Au	Antibody (Ab)- c-eb-2	Antibody (Ab)-Antigen (Ag) binding	[125]
	P. Marinus	Au	Ab-P.Marinus	Ab-Ag binding	[126]
	Glucose	ZnO nanorods	Go_X	Enzyme promoted reaction	[127]
	Uric acid	ZnO nanotetrapods	Uricase	Enzyme promoted reaction	[128]
	DNA	Au	Thiolated ssDNA	Hybridization	[49]

- An extensive discussion on the fundamental device structure, semiconductor material parameters and the simulation set-up is much needed. It reduces time as well as cut down the improvement cost required in extensive development and handling steps and furthermore helped in understanding the fundamental material science engaged with the device and create new insights and logics. Very few reports are available on the simulation and modelling of the HEMT device design for the biosensing applications. There is plenty of room for the researchers to investigate in this domain.
- Benefitting from the study on HEMT devices and using the fundamental HEMT structure, chemical sensors for gases and liquids was product which got extended consideration over the most recent couple of years. Inferable from their wide band gaps and strong bond strengths, GaN material system has an improved chemical stability as found in their resistance to wet etching methods and their biocompatibility.
- Difficulty in achieving reliable, small, robust, reliable and compatible with on-chip development of GaN HEMT sensor has made an unsolved problem. In order to put a superior comprehension of the chemical processes, which happen near the sensor surface and a more profound chemical analysis of the sensor active area while each estimation, encourage alignment analyzes in characterized electrolytes are vital. By functionalization the ionic species, which add to the signal generation ought to be recognized explicitly. Many efforts are going on by various research groups to improve the performance of GaN HEMT based sensors. However, a little work is available on GaN HEMT based sensors in literature. The ungated HEMTs with Sc_2O_3 in the gate region exhibited a linear change in current between pH 3-10 of 37μA/pH were reported by Kang et al. Could be the best performing HEMT sensor till date[100]. To the best of our knowledge GaN HEMT based Salinity Sensor has been reported to date. It is important to investigate the sensitivity and response time of GaN HEMT based sensor devices so that the usability of these structures can be ensured in variety of biomedical applications. It is apparent that there is enough scope left for the researchers to work in this area.

Finally, the literature survey presented in this chapter concludes that there is enough scope to study III-Nitrides, GaN HEMTs and its application in electrochemical sensing. All these research gaps have motivated us to study AlGaN/GaN HEMT devices for pH and salinity detection applications.

CHAPTER 3

Performance Analysis of AlGaN/GaN HEMT: A Simulation Study

In this chapter, we are reporting the simulation results obtained by ATLAS for AlGaN/GaN HEMT devices, specifically to validate our simulation results with the reported ones.

3.1 Introduction

An accurate simulation of the AlGaN/GaN HEMT entails a good comprehension of the underlying material physics as well as a precise knowledge of the material parameters used for the simulation. To adapt with current rivalry in semiconductor enterprises, Computer Aided Design (TCAD) tools are widely utilized for the device design and expedite the device development and optimization process for new technology. TCAD is a profitable system for investigating semiconductor device structures. It spares time as well as diminishes the improvement cost required in extensive development and handling steps and furthermore helped in understanding the fundamental material science engaged with the device and create new thoughts and logic. A few inquiries amid operation of the device can be tended to by CAD tools. Computer-aided design tools are actively utilized for foreseeing the attributes of devices from numerous years.

Till now, several softwares have come into the picture for the cutting edge engineering design and investigation of semiconductor devices and processes. Different commercial accessible simulation software like ATLAS (Silvaco) [69], MEDICI (Synopsis) [130], SEANTAURUS (Synopsis) [131], DESIS (ISE Integrated System Engineering) [132], APSYS (Crosslight) [133], BIPOLE3 (Bipsim) [134], and G-PISCES (Gateway Modeling) [135] are accessible. Many simulators designed by universities like PISCES

(Stanford University) [136], MINIMOS [137], FLOODS [138], GALENE, DEVICE [139], Nextnano3 [140] and PROSA [141] are also utilized as device simulators. The TCAD tool utilized in this work was ATLAS, a PISCES based two-dimensional numerical device simulator from Silvaco [69]. Silvaco-ATLAS is a widely used for III-Nitride semiconductor devices and utilized for tending to various issues in III-Nitride HEMTs [142], [143]. It is a physical two-dimensional or three-dimensional device simulator, which foresees the electrical attributes related to predefined physical structures and bias conditions, by approximating the functionality of a device onto the 2D/3D framework, comprising of various mesh points. Using differential equations, resulting via Maxwell's equations, onto this framework electrical characteristic of indicated semiconductor structures can be anticipated.

In this chapter, the TCAD simulation results for the AlGaN/GaN HEMTs are presented. The chapter starts off with a discussion of the fundamental device structure, semiconductor material parameters and the simulation set-up. Next, we simulated GaN HEMT devices for the optimization of AlGaN and GaN Cap thicknesses, followed by a closer look at the high temperature and trapping effects on the performance of AlGaN/GaN HEMTs.

3.2 Device Description Under Investigation and Simulation Setup

A single gate finger device of 100 µm unit gate width was used for simulation. The epitaxial structure comprised of a 25 nm $Al_{0.25}Ga_{0.75}N$ layer, 2.7 µm GaN buffer and an AlN layer with sapphire as a substrate. The gate length (L_G), source-to-gate length (L_{SG}), and gate-to-drain length (L_{GD}) parameters that were set for the device are 1 µm, 1 µm, and 2 µm respectively as shown in Fig. 3.1.

3.2.1 Input Material Parameter

In the AlGaN/GaN HEMTs, a high-density 2DEG was formed at the interface, as a consequence of spontaneous and piezoelectric polarization effects with no intentional doping in the AlGaN barrier layer. In order to account for the 2DEG in the TCAD model, a simple approach can be used where a layer of fixed positive sheet charge is defined at the AlGaN/GaN interface.

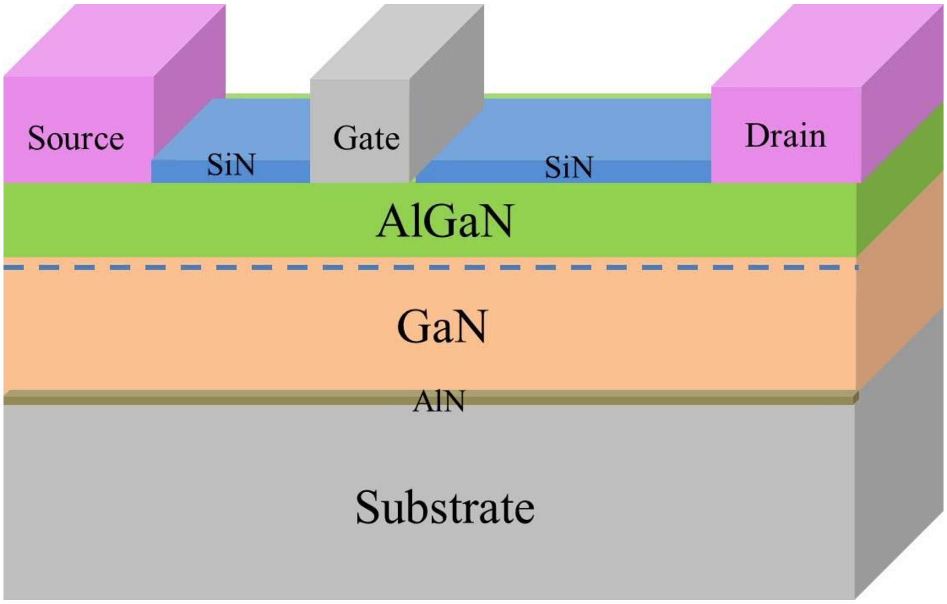

Figure 3.1: Schematic representation of simulated device

Nevertheless, this simple method can even now be utilized to prompt a precise measure of channel electrons and effectively anticipate the drain current characteristics of the device.

Many input parameters are taken from ATLAS library. However, polarization values in GaN and AlGaN are considered by the interface charge density. High field electron mobility is incorporated through C-interpreter. Input material parameters used for AlGaN/GaN HEMT in the study are given in Table 3.1.

3.2.2 Material Model Specification

In order to accomplish more realistic outcomes, several models were initiated in simulations. Similar device dimension were used by Treidel *et al.* for high power application [144]. AUGER, SRH and CONSRH models of recombination mechanism have been taken into account for drain current evaluation. Material properties, such as band energies, carrier mobility, carrier relaxation times, and densities of polarization charges at the channel/barrier interface were accurately modeled. Parallel field dependent electron mobility model (FLDMOB) accounted for velocity saturation.

Table 3.1: Input material parameters used in simulation of AlGaN/GaN HEMTs

Parameters	**Units**	**AlGaN**	**GaN**
Band gap (300 K), Eg	eV	3.96	3.4
Permittivity		9.5	9.5
Betan		2	2
Betap		1	1
Saturation Velocity for electron, V_{satn}	cm/s	$1x10^7$	$1x10^7$
Saturation Velocity for hole, V_{satp}	cm/s	$1x10^7$	$1x10^7$
Conduction band density of states, NC300	cm^{-3}	$3.3x10^{18}$	$2.3x10^{18}$
Valence band density of states, NV300	cm^{-3}	$1.5x10^{20}$	$0.4x10^{20}$
Align		0.65	0.65
Thermal Conductivity, TCON.CONST	W/cm.K	2.85	1.5
Richardson constant for electron, ARICHN	$A/cm^2/K^2$		24
Richardson constant for holes, ARICHP	$A/cm^2/K^2$		96
Donor energy level, Edb	eV		0.025
Acceptor energy level, Eab	eV		0.160
Piezoelectric Constant	c/m^2	-0.729	-1.0

The concentration dependent analytical model (CONMOB) has been used for mobility calculation. Shockley-Read-Hall model (SRH), Fermi-Dirac model (FERMI), polarization model (SPONTANEOUS) and (PIEZOELECTRIC) also used for device modelling. Band to band tunnelling model has been considered for tunnelling mechanism. Low ohmic distributed contact resistivity of 1.6 x 10^{-6} Ω-cm^2 is considered. Uniform doping of the regions has been taken into account for the simulation. We performed two-dimensional hydrodynamic electro thermal Simulations [76], [145]. Our selection of electron transport model aimed to attain most extreme precision alongside computational effectiveness. The current density equations or charge transport models were typically attained through employing approximations and simplifications to the Boltzmann Transport Equation. Since the drift-diffusion estimation became less accurate for smaller feature sizes, the hydrodynamic solution was obtained by taking the next two higher moments of the Boltzmann equation over the drift-diffusion solution. As a result, the hydrodynamic simulation provided a practical compromise between these two methods [146]. Self-heating effects were represented the lattice heat flow equation. It was acquired by the stationary energy flux balance resulting as of the second moment solving the Boltzmann transport equation and the carrier continuity equation.

3.3 Optimization of AlGaN/GaN HEMT Performance

By optimizing the device dimensions like GaN Cap layer thicknesses, AlGaN thicknesses and the gate length (L_G), source to gate length (L_{SG}), gate to drain length (L_{GD}) one can enhance the performance of the device.

3.3.1 GaN Cap Layer Thickness

A single gate finger device of 100µmμm unit gate width was used for simulation (shown in Fig. 3.2 (a) and (b)). In order to study the effects of variation of GaN cap layer and AlGaN layer thicknesses on the device electrical characteristics, we performed two sets of simulations. The first set consisted of a GaN/$Al_{0.25}Ga_{0.75}N$/GaN heterostructure with a 25 nm thick AlGaN barrier, 2.7µm GaN buffer and a GaN capping layer that varied in thickness from 0 to 100 nm. The second set comprised of an $Al_{0.25}Ga_{0.75}N$/GaN heterostructure with a 2.7µm GaN buffer and an AlGaN layer that differed in thickness from 5 to 30 nm.

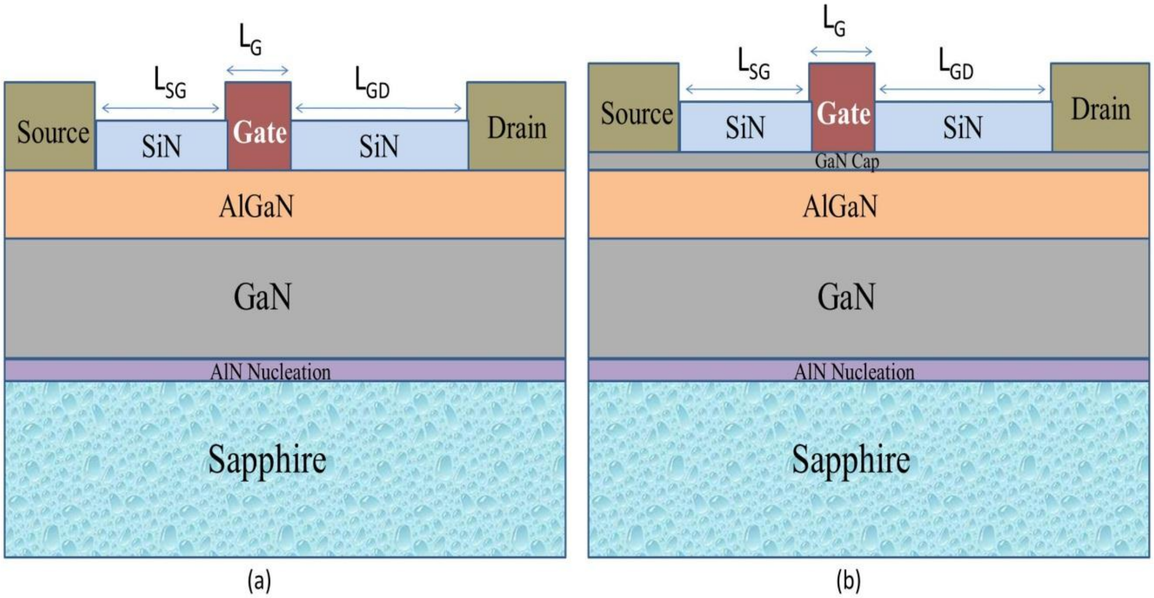

Figure 3.2: Schematic representation of (a) standard and (b) GaN capped HEMT device

The output characteristics as a function of GaN capping layer thickness had been estimated for the above first set of heterostructures, which are accessible in Fig. 3.3. It demonstrates the resulting depth distribution of electron concentration and drain current (I_{ds}), as a function of the GaN cap layer thickness. Drain current was increased rapidly from 0.39 A/mm to 1.83 A/mm for cap layer thickness varied from 1 nm to 20 nm which later got saturated after 20 nm. The peak in the profile corresponds to the position of hetero interface, indicating the confinement of electrons, which was the formation of 2DEG. The occurrence of the GaN cap layer resulted in a decrement of the peak electron concentration, from 1.30 x 10^{19} cm^{-3} with no GaN cap, down to 6.84 x 10^{18} cm^{-3} with a 2 nm cap layer. Between 1 nm and 20 nm, the electron concentration increased rapidly from 1.8 x 10^{18} cm^{-3} to 1.48 x 10^{19} cm^{-3}. However, beyond 20 nm, the electron concentration increased slowly, reaching 1.56 x 10^{19} cm^{-3} for a thickness of 50 nm and after that decreased and saturated at 1.4 x 10^{19} cm^{-3} for cap layer thickness more than 70 nm.

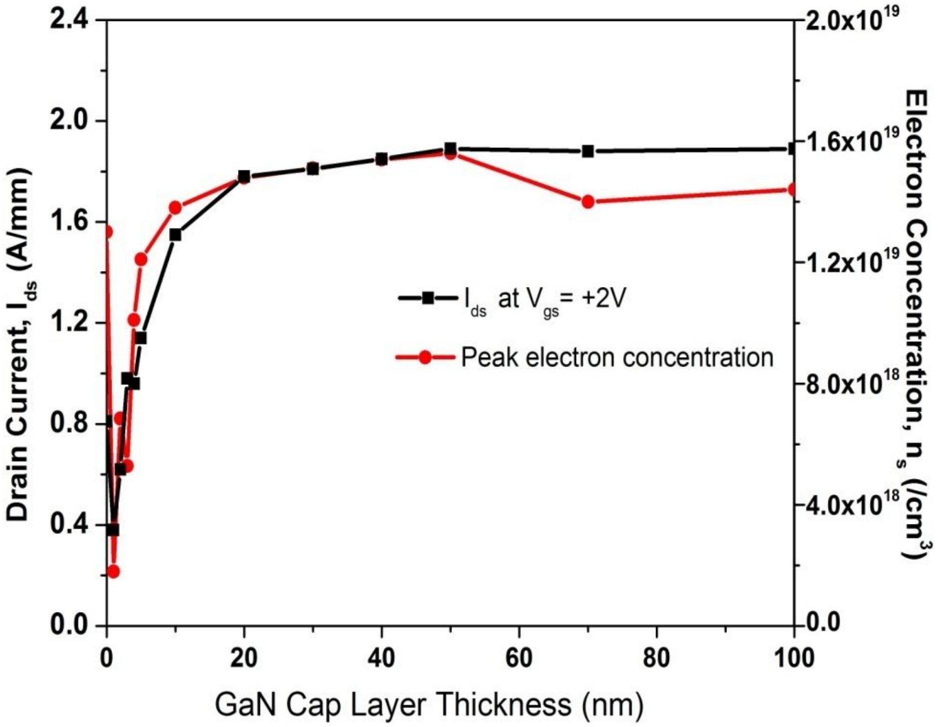

Figure 3.3: An impact of GaN cap layer thickness on drain current and profile of electron concentration, for a GaN/AlGaN/GaN heterostructure with a fixed AlGaN layer thickness of 25 nm at V_{ds} =+10 V and V_{gs} = +2 V

Results obtained for the effect of cap layer thickness on AlGaN/GaN heterostructure were in good agreement with the results stated by S. Heikman et al [147]. The decline in 2DEG sheet density with expanding distance between the 2DEG carriers and the AlGaN/GaN interface causes an adjustment of the electron scattering mechanisms and also on the 2D-electron mobility. The electron mobility indicated an opposite trend to the electron concentration, for the cap layer thickness above 10 nm, with magnitude falling from 1200 cm^2/Vs at 10 nm, down to 770 cm^2/Vs at 100 nm. Fig. 3.4 displays the subsequent electron mobility, as a function of the GaN cap layer thickness. To understand the observed trends in detail, the electric field distributions, and band bending of all the structures were simulated. Introduction of GaN cap layer at HEMT structure created a negative polarization charge over the upper hetero interface, causing increased electric fields in the AlGaN.

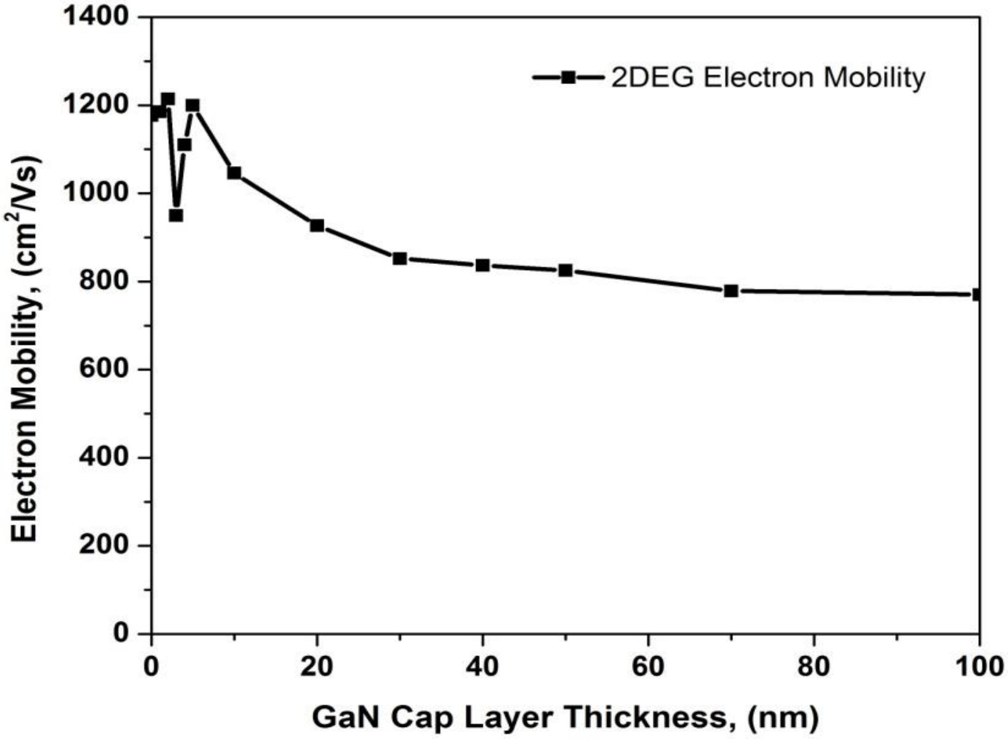

Figure 3.4: An impact of GaN cap layer thickness on electron mobility, for a GaN/AlGaN/GaN heterostructure with a fixed AlGaN layer thickness of 25 nm.

Density of electric field fringes at the upper hetero interface increased with the cap layer thickness. For thick cap layers, electric field fringes became denser in the spacer region. The order of the electric field used for the calculation of the mobility is 2.0 MV/cm. Electron mobility decreases with increase in GaN Cap Layer and as the GaN cap layer thickness increases, the valence-band shifts upward, eventually reaching the Fermi level. At this point, a 2DHG formed at the upper GaN/AlGaN interface, pinning the valence band, hindering any further increase of the electric field in the AlGaN layer.

As an effect of which scattering could be high in this region and thus mobility was reduced. We also simulated band bending at the hetero interface of the GaN capped structures (illustrated in Fig. 3.5) to investigate the carrier confinement in quantum well. GaN capped designs showed higher carrier concentrations and deeper band bending due to which they delivered higher I_{ds}. Thick capped design had a higher band bending and conduction band minimum values in comparison to thin Capped design. AlGaN/GaN

HEMTs devices required low gate leakage current for low noise and improved reliability [78].

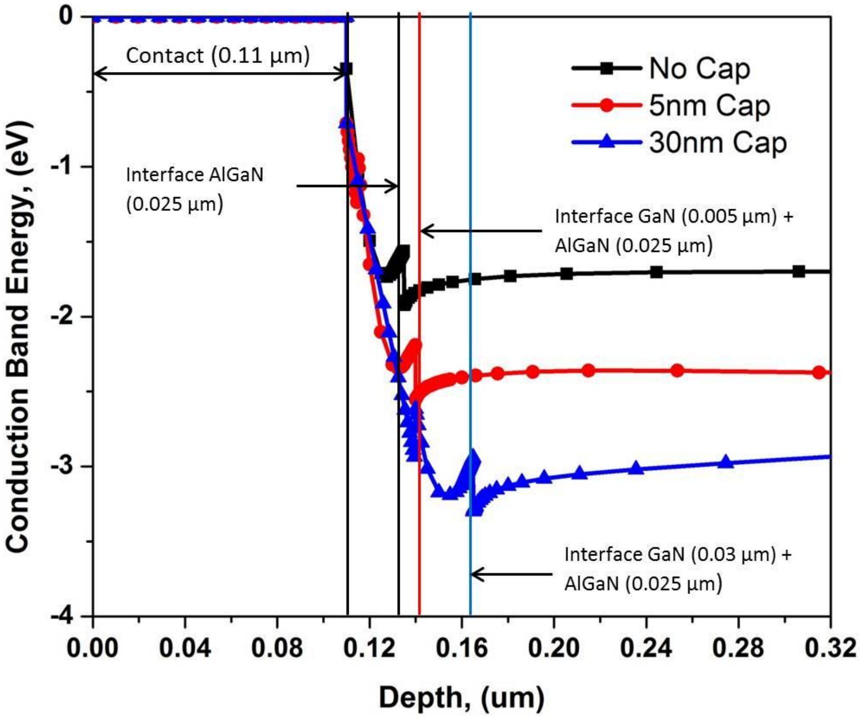

Figure 3.5: Energy band bending of GaN HEMTs at the heterointerfaces: AlGaN/GaN (No Cap layer) and GaN/AlGaN/GaN (5 nm, 30 nm) GaN Cap layer

3.3.2 AlGaN Thickness

In the second series of simulations, single $Al_{0.25}Ga_{0.75}N$ layers were deposited on semi-insulating GaN base layers and the AlGaN thickness varied between 5 nm and 30 nm. Fig. 3.6 demonstrates the resulting output characteristics as an element of the AlGaN thickness. Drain current was somewhat decreased in between AlGaN thickness of 5 nm and 7 nm and then bit increased for 10 nm. However, beyond 10nm, there was a rapid increase in drain current from 0.298 A/mm to 1.106 A/mm.. To analyze these results, we studied peak electron concentration, band bending and electron mobility distribution in detail, which can be seen in Fig. 3.7 (a), (b), and Fig. 3.8.

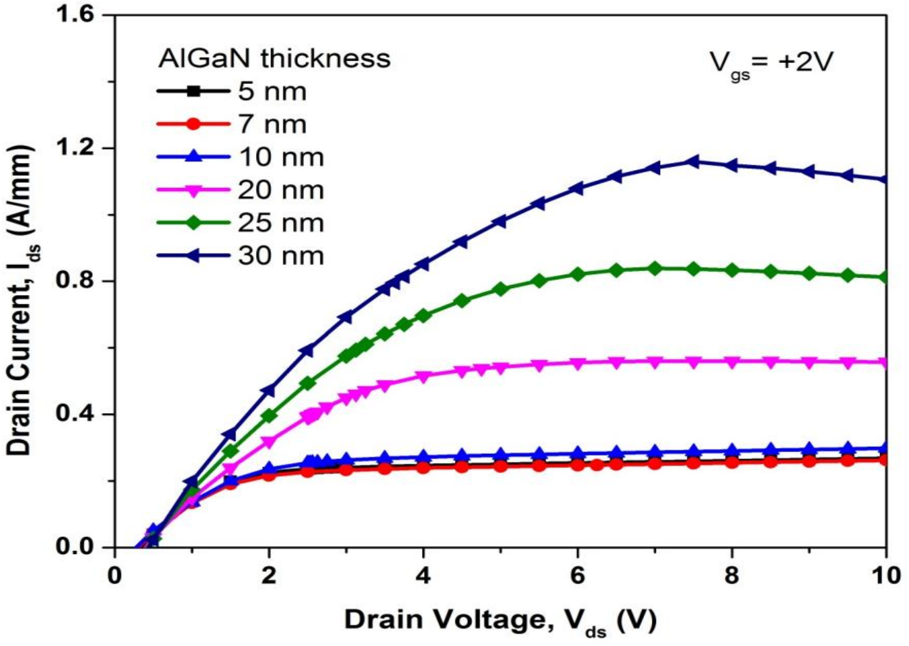

Figure 3.6: An impact of variation in AlGaN layer thickness on drain current at V_{gs} = +2V

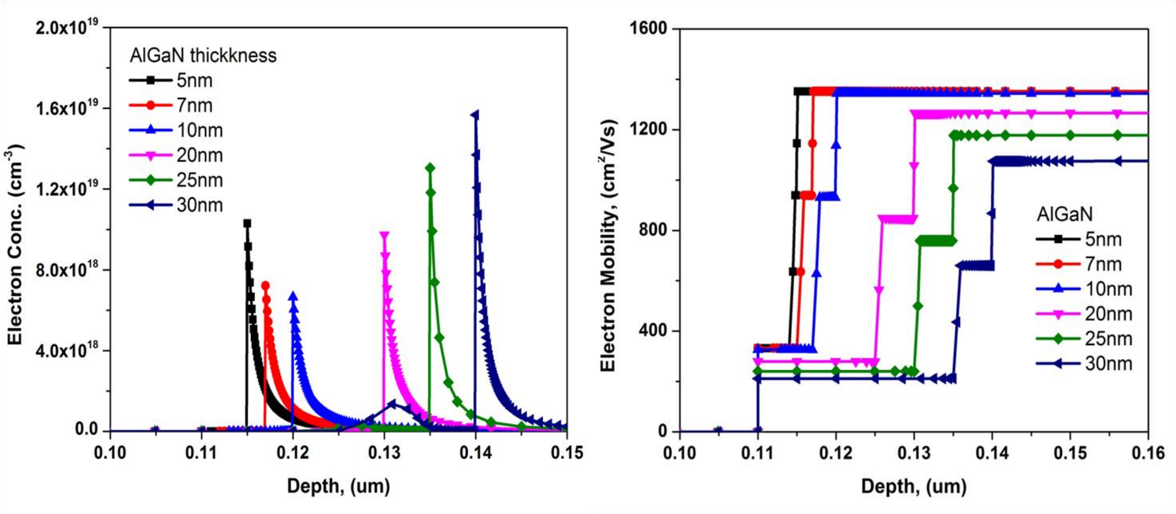

Figure 3.7: (a) and (b) An impact of variation in AlGaN layer thickness on electron mobility at V_{ds} =+10 V and V_{gs} = +2 V

Between 5 nm and 10 nm, the peak electron concentration confinement decreased from 1 x 10^{19} cm^{-3} to 6.65 x 10^{18} cm^{-3}. However, beyond 10 nm, the electron concentration increased rapidly reaching 1.57 x 10^{19} cm-^{3} for a thickness of 40 nm.

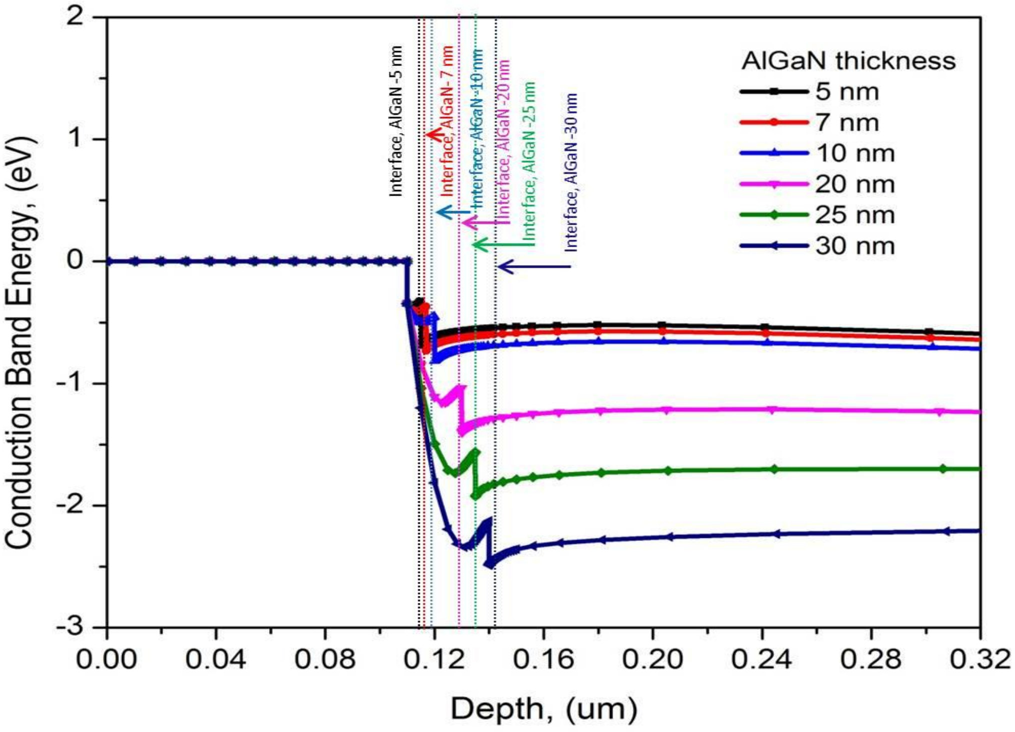

Figure. 3.8: Energy band bending of GaN HEMTs at the hetero interface: for different AlGaN thickness

In the electron mobility an opposite trend has been noticed to the electron concentration for AlGaN thicknesses above 5 nm, with values decreasing from 1354 cm^2/Vs at 5 nm, down to 1076.5 cm^2/Vs at 30 nm. To analyze these results in more depth, we simulated band bending at hetero interface and electric field distributions. AlGaN layer thickness greater than 10 nm indicated higher carrier concentrations and deeper band bending (shown in Fig. 3.8) due to which they delivered higher drain current. Electric field distributions under the gate edge of drain side were increased with the AlGaN layer thickness.

Peak of electric field under the gate was 4.2×10^5 V/cm for the AlGaN thickness layer of 30 nm and lowest 3.2×10^5 V/cm for the 10 nm AlGaN thickness. These trends were similar to the variation in drain current with AlGaN thickness. Reverse tunnelling of electrons from the gate to semiconductor surface was resulting in high gate leakage current. That could have happened due to high electric field at the gate edge of drain side.

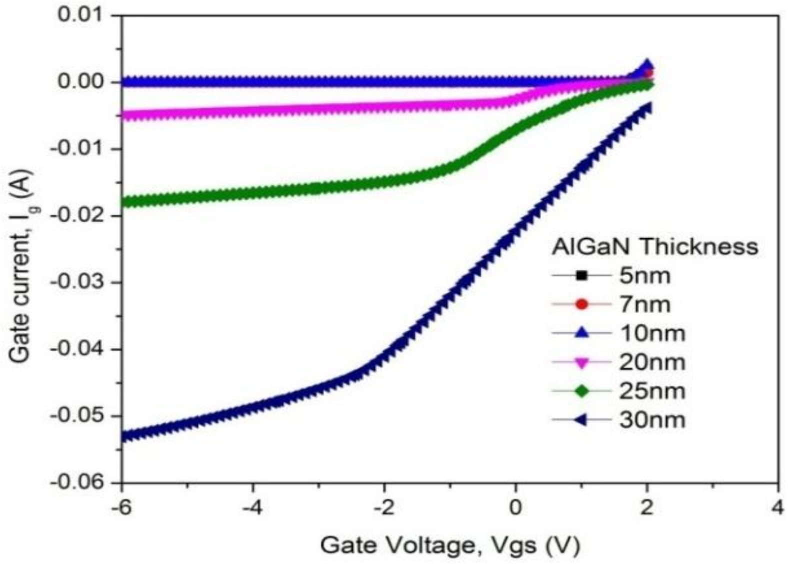

Figure 3.9: Comparison of leakage current with different AlGaN thickness

Gate leakage current was increased with the AlGaN layer thickness as shown in Fig. 3.9. Thin AlGaN layer was reduced gate leakage current component because electric field was also lesser at the gate edge of drain side. An increment in the gate to channel length with an AlGaN layer thickness could have been a probable reason for high gate leakage current in the thick AlGaN layer.

3.3.3 Gate Length, Source to Gate Length and Source to Drain Length

Scaling of gate length and source to gate length played a key role in the performance of biosensor as it directly influences the device transconductance and hence the sensitivity and response time of biosensors. Transconductance (g_m) in these devices strongly influenced the sensitivity of a biosensor. In a biosensor, it is required to have a large gate area as well as area between source-gate to immobilize bio-functional units uniformly for bio-chemical reactions to occur. However, increasing gate length adversely affects the device performance, but it is beneficial for bio-functionalization. In this work, we investigated the effect of variations in gate length (1µm to 5µm) and source to gate length (1µm to 3µm) to choose the most suitable one for bio sensing applications. Downscaling of gate length (L_G) and source to gate length (L_{SG}) improved the device performance, enhancing the drain-current (I_{ds}) and device transconductance. In order to study the effects of downscaling the contact distances the sensitivity and response time of bio sensing device, we performed two sets of simulations. In the first set of simulation, L_{SD} and L_G were kept constant to the value of 7.0 µm and 1.0 µm respectively with L_{SG} varied from 1 µm to 3 µm. In the second case, L_{SD} and L_{SG} were kept constant to the value of 7.0 µm and 1.0 µm respectively and L_G varied from 1 µm to 5 µm. Downscaling of gate length (L_G) and source to gate length (L_{SG}) enhanced the drain-current and transconductance. Therefore, firstly we checked the value of electric field under the gate region. Output current for L_{SG}=1µm, L_G=1µm was higher (1.01 A/mm) due to highest recorded electric field (4.36 x 10^5 V/cm), where as it was lowest for L_{SD}7µm_L_G 5µm_L_{SG}1µm configuration as shown in Fig. 3.10. These results fitted to the relationship of I_{dmax} and L_{SG} +L_G, that could be expressed by $I_{dmax} \alpha (L_{SG} + L_G)^{-0.25}$ [148].

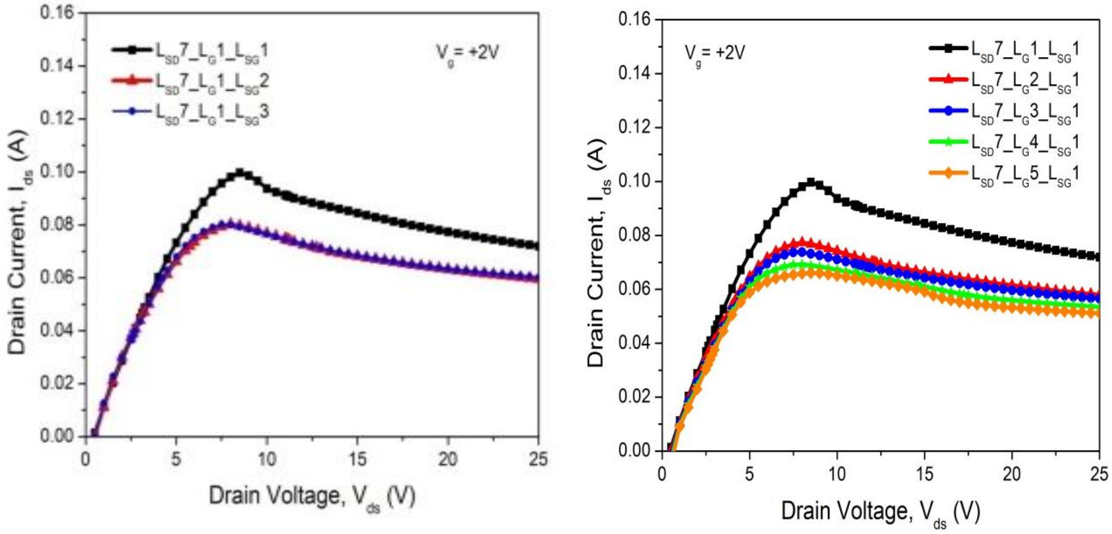

Figure 3.10: Comparison of drain current with different L_{SG} and L_G

In the first set of simulation, g_m decreases from (211mS/mm to 135mS/mm) with increased L_{SG} 1 to 3 µm. In order to know the reasons behind these results, we checked mobility and parasitic capacitances. Here, the mobility reduced from 1151.5cm²/V-s 745.63 cm²/V-s with up scaling of L_{SG}. To extract parasitic capacitances, a small signal parameter extraction was done at 50GHz with method adopted in [149], which showed an increment in source to gate capacitance C_{GS} (10.210pF - 7.393 pF) with downscaling of L_{SG}.

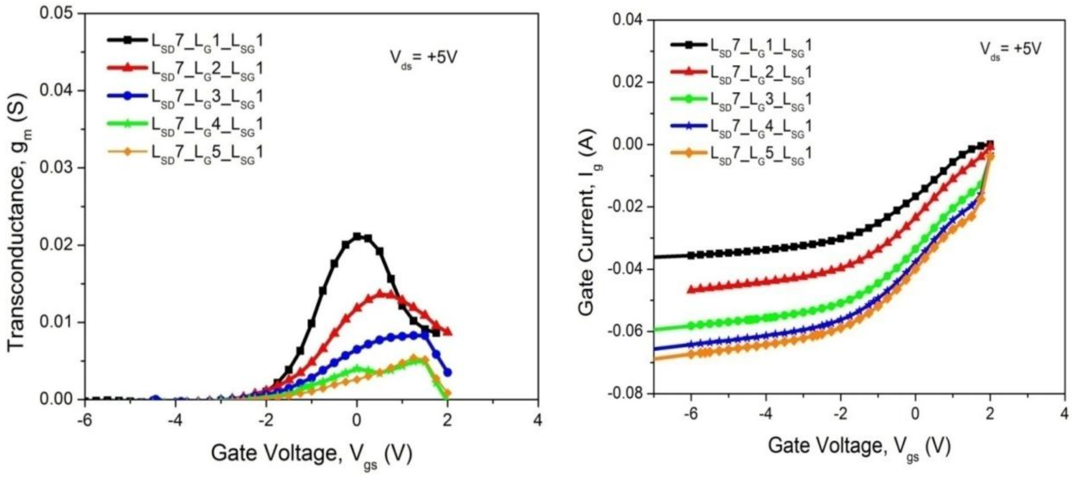

(a) **(b)**

Figure 3.11: Comparison of (a) transconductance and (b) leakage current with different L_G.

Fig. 3.11 (a) shows corresponding changes in g_m characteristics for the second set of simulation which follows the same trend as in case of first set. Here g_m decreases from (211 mS/mm–48 mS/mm) with increased L_G from 1µm to 5µm due to decrement in the gate capacitance. An increment in L_G resulted in drain current reduction irrespective of any variations in the L_{SG} value. Reduction in L_G was more effective than the reduction in L_{SG} to influence the Biosensors performance. Fig. 3.11 (b) shows the comparison of gate leakage current. Lowest value of gate leakage current was found with a decrement in L_G. Different configurations related to L_G and L_{SG} variations were simulated and compared to choose the most suitable design for GaN HEMTs based bio-sensors. I_{ds} and g_m values were notably decease with increase in L_G and L_{SG}. An increment in L_G was resulted in drain current reduction irrespective of any variations in the L_{SG} value. Configuration L_{SD}7µm_L_G1µm_L_{SG}1µm was chosen as the best combination due to highest attainable value of g_m (211 mS/mm) and I_{ds} (1.01 A/mm). That was the result of highest extracted value of C_{gs} (10.210 pF), mobility (1151.5 cm^2/Vs) and electric field (4.36 x 10^5 V/cm) with lowest value of gate leakage current among all these simulated designs. However, the high value of parasitic capacitances may adversely affect the response time, though they could be good for the sensitivity. Hence a compromise must be made in between response time and sensitivity while selecting gate lengths and hence the resulting capacitances.

3.4 High-Temperature Effects on the Performance of AlGaN/GaN HEMTs

As various working domains necessitate the GaN devices to be operated at elevated temperatures, a systematic investigation of temperature dependences of the device parameter is vital. In comparison to others III-V semiconductor material, GaN material devices can operate at much higher temperature (750^{o}C), without degradation in performance. The capability to operate at high-temperature facilitate the device to be effective in the applications at extreme environments [150]. An assortment of chemical, gas and biosensor in view of HEMT technology has been operated at elevated temperatures [151]–[153]. Long term stability and high-temperature operation are the significant prerequisite for a gas sensor. For instance, in a hydrogen gas sensor hydrocarbons are dissociated by catalytic metals merely at elevated temperatures. The Si based gas sensor has a point of confinement to be operated underneath 250^{o}C, prohibiting them from being utilized as hydrocarbon detectors or for other applications requiring a high-temperature operation. Therefore, semiconductor devices based on AlGaN/GaN heterostructure have a great potential for sensor application in harsh environments. Various simulations were conducted on different mechanisms of GaN-based HEMTs such as transport and mobility properties [154], [155], self- heating effects [156], carrier lifetime, etc. Temperature dependent models for some physical characteristics have been stated by Islam and Huq [157]. An integrated simulation study of GaN-based devices was greatly required for their performance at high temperatures. This section deals with performance evaluation of the AlGaN/GaN HEMTs at higher ambient temperatures, between 300 K and 600 K. The device was analyzed by means of two-dimensional hydrodynamic simulations [76], [145] using Silvaco-ATLAS to characterize the various electrical properties of the instrument [69]. Further, we evaluated the temperature dependence of the drain current and transconductance on the source to gate length, gate length and gate recessing structures.An extensive theoretical outline was done to attain the most overall values for GaN and AlGaN properties. Energy band gap, the density of states, saturation velocities, surface traps, polarization effects, carrier lifetime and mobility, permittivity, effective Richardson’s constant donor, and acceptor energy levels were considered as critical parameters for predicting the temperature effects in

AlGaN/GaN HEMTs. The three differential equations have material-specific parameters, such as band gap energy, electron mobility, thermal conductivity, etc. The dependence of these parameters on temperature was expressed through models which are discussed in the following.

1) Band Gap Energy

The most significant parameter of any semiconductor material is bandgap. Temperature dependence of the energy bandgap (E_g) of a semiconductor can be articulated by the following empirical Varshni equation [158]:

$$E_g = E_{g,0} - \frac{\alpha_g {T_L}^2}{\beta_g + T_L} \tag{3.1}$$

where, $E_{g,\ 0}$ is the energy band gap at 0 K, α_g and β_g are empirical varshni constants. Energy band gap for ternary semiconductor was estimated via the magnitude of binary compounds and their mole fraction in accordance with given equation:

$$E_g^{AlGaN} = E_g^{AlN}\mathrm{x} + E_g^{GaN}(1-x) + C_g(1-x)x \tag{3.2}$$

here C_g is the bowing parameter, x is the Al composition. These fitting parameters were calculated commencing various empirical calculations. The typical values employed in this analysis for GaN and AlN are sum up in Table 3.2.

Table 3.2: Fitting parameters for temperature dependent energy band gap calculation

Material	**$E_{g,0}$ (eV)**	**α_g(eV/K)**	**B_g(K)**
GaN	3.4	$9.09\text{x } 10^{-4}$	830 [44]
AlN	6.2	$18\text{x } 10^{-4}$	1462 [45]

The effect of variation in energy bandgap for GaN, AlN and AlGaN with temperature could be explained by Fig. 3.12.

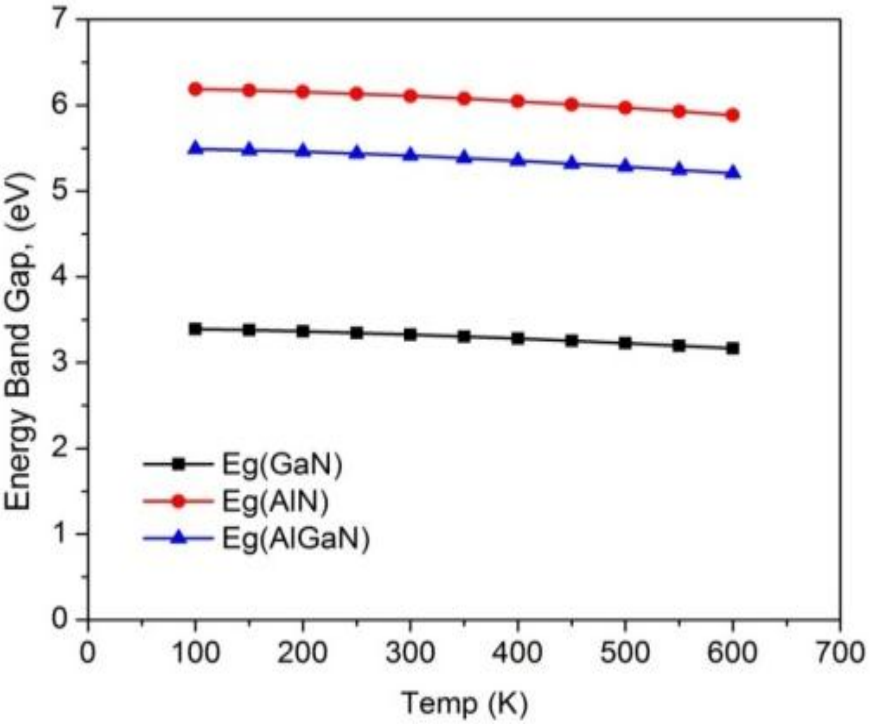

Figure. 3.12: Energy bandgap as a function of temperature

2) Thermal Conductivity

The thermal conductivity is modelled by a power law [159]:

$$k(T_L) = k_{300}\left(\frac{T_L}{300K}\right)^{\alpha} \tag{3.3}$$

where, k_{300} is the value at 300 K, T_L is the lattice temperature and α is the fitting parameter. For bulk GaN k_{300}=130 W/mK was extracted [160] from earlier experiments. GaN was grown over the sapphire substrate by the method of vapor phase epitaxial growth technique. However, later experiments of epitaxial structures gave higher values of k_{300}= 220W/mK and strong dependence on dislocation density using hybrid vapor phase epitaxy growth technique [161]. From two studies [160], [161]we extracted two parameter material model sets for GaN summarizes in Table 3.3. Fig. 3.13 compares the two model sets of analytical as well as ATLAS simulations (model set1 was used for the simulations).

Table 3.3: Fitting parameter for thermal conductivity

Material	**K_{300} (W/m K)**	**A**
GaN Model set 1	130	-0.43 [160]
GaN Model set 2	220	-1.2 [161]
AlN	350	-1.7 [162]

In case of AlN, the deviation of the extracted digits of the thermal conductivity as a component of temperature is expressed in Fig. 3.14. We assume a $k_{300}$of 350 W/mK, which was near enough the value stated by [162]. The parameter α, which modeled the decline with temperature, was calibrated alongside calculated data [162]–[164].

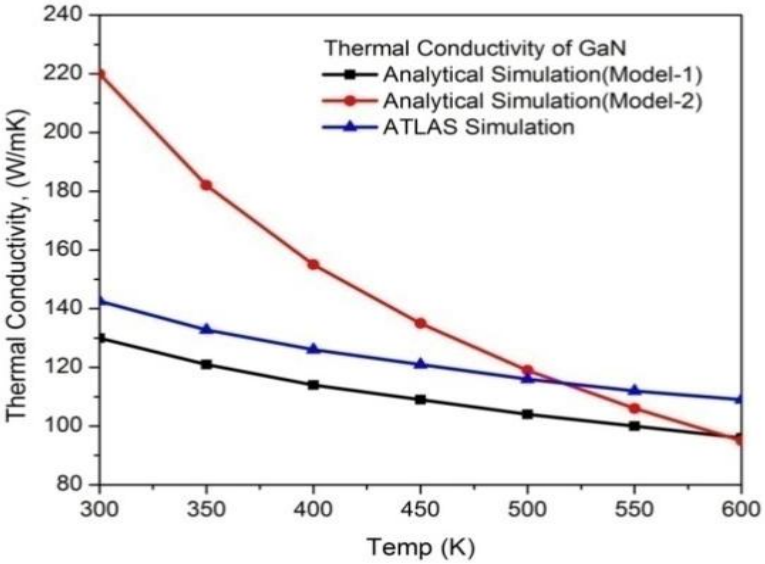

Figure. 3.13: The comparison between the analytical approximation and ATLAS simulation outcomes of the GaN thermal conductivity as a function of Temp from T=300 K to 600 K

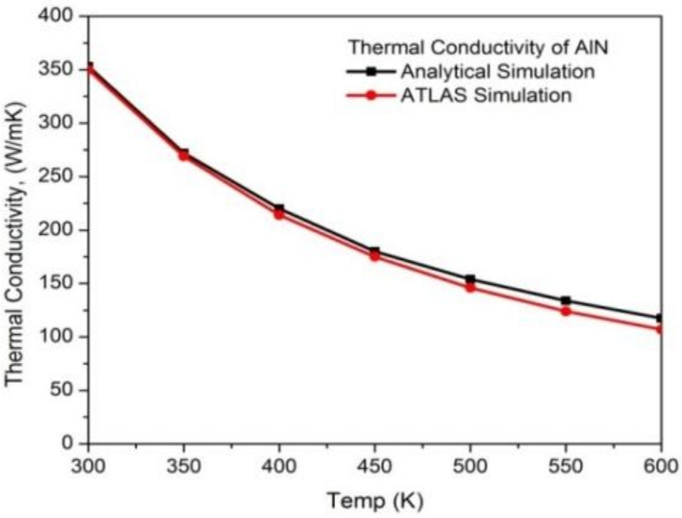

Figure 3.14: The comparison between the analytical approximation and ATLAS simulation outcomes of the AlN thermal conductivity as a function of Temp from T=300 K to 600 K.

3) Electron Mobility

The low-field mobility can be modelled by an expression [165]

$$\mu_0(T,N) = \mu_{min}\left(\frac{T}{300}\right)^{\beta 1} + \frac{(\mu_{max}-\mu_{min})\cdot\left(\frac{T}{300}\right)^{\beta 2}}{1+\left[\frac{N}{Nref\left(\frac{T}{300}\right)^{\beta 3}}\right]^{\alpha\left(\frac{T}{300}\right)^{\beta 4}}} \tag{3.4}$$

where, T is the temperature, N is the total doping density, and α, β_1, β_2, β_3, β_4, μ_{min}, $\mu_{max,}$ and N_{ref} are parameters that can be determined either from experiment or Monte Carlo simulation. Table 3.4 Summarizes low-field mobility model parameters for GaN.

Table 3. 4: Summary of low-field mobility model parameters for GaN

μ_{min}	**μ_{max}**	**α**	**β_1**	**β_2**	**β_3**	**β_4**
312.1	1401.3	0.74	-6.51	-2.31	7.07	-0.86 [165]

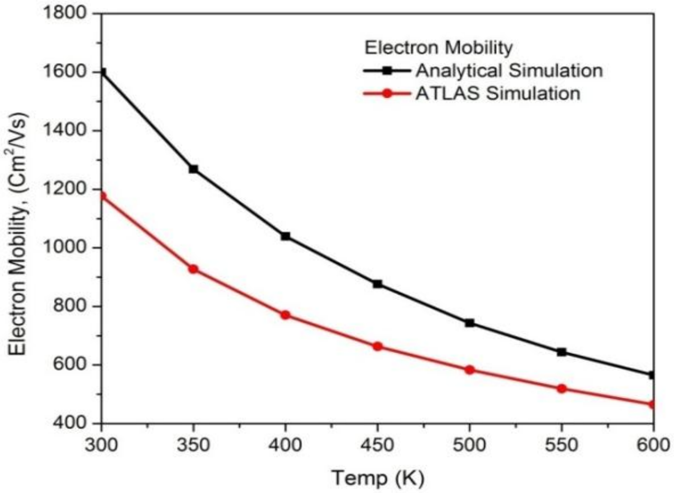

Figure 3.15: Comparison between the analytical approximation and ATLAS simulation of the Low-field bulk mobility in GaN as a function of Temp from T=300 K to 600 K

The electron mobility dropped monotonically with rising in temperature because of the improved scattering rate, as shown in Fig. 3.15. Results obtained from analytical modelling have been compared with those obtained from ATLAS^{TM} from SILVACO International. A close fit between the results obtained from numerical simulation and ATLAS software simulations have been observed. The variation in the results might be due to the boundary conditions applied during simulation in sub nanometer region. Hydrodynamic models has been applied which gives precise results upto 4th order of simulation results.

3.4.1 Temperature Dependency on Output Characteristics

The temperature dependence of the maximum current and transconductance of different devices were also investigated. The I_{ds}-V_{ds} curve for gate bias V_{gs}= +2 V of the simulated AlGaN/GaN HEMT is shown in Fig.3.16 (a). The drain bias was ramped from 0 V to 10 V for each of the gate biases. The peak current density reached was of V_{gs}= +2 V, V_{ds}= +10 V at 300 K with a current density of 0.84 A/mm. We observed a reduction in I_{ds} (≈ 52%) with an increase in temperature from 300 K to 600 K. The high current density could be attributed to the extremely high charge that was accumulated in the channel due to the polarization effects and the high saturation and peak velocity of electrons in GaN. The maximum drain current was reduced whereas temperature rose from 300 to 600 K.

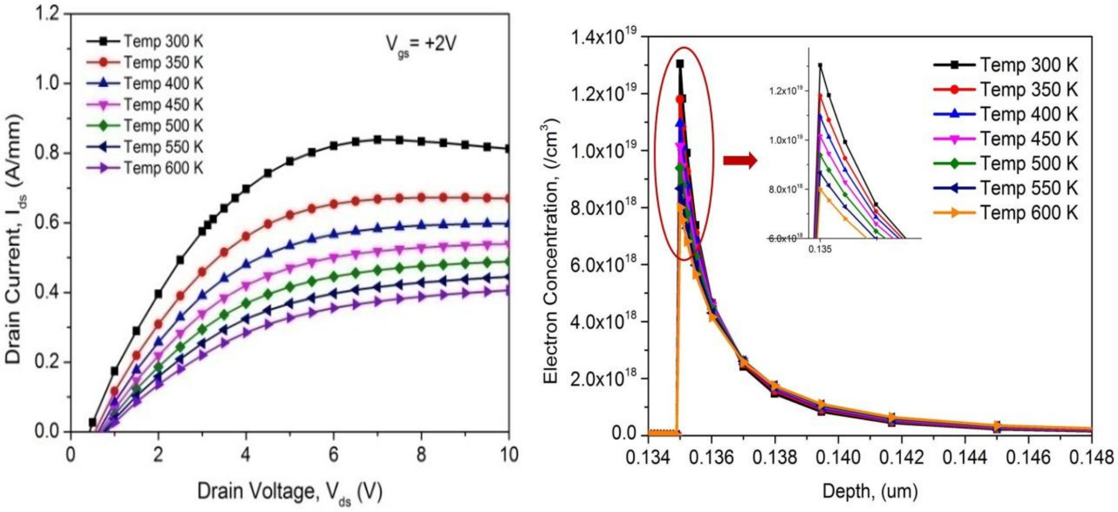

(a) **(b)**

Figure 3.16: Comparison of (a) drain current and (b) electron concentration at different temperature

To understand the reason behind this, we checked for various parameters such as carrier concentration and electron mobility as shown in Fig. 16 (b). Peak electron concentration alongside of the channel was about 1.3x10^{19} /cm^3 at 300 K corresponding to the highest I_{ds}=0.84 A/mm when the device was turned on. Because of phonon-scattering-induced mobility degradation, the magnitude of I_{ds} in both linear and saturation regions went down at higher temperatures [166]. Fig. 3.17 (a) illustrates that the transconductance, g_m versus gate-source voltage, V_{gs} of AlGaN/GaN HEMT at various ambient temperatures between 300 K and 600 K.

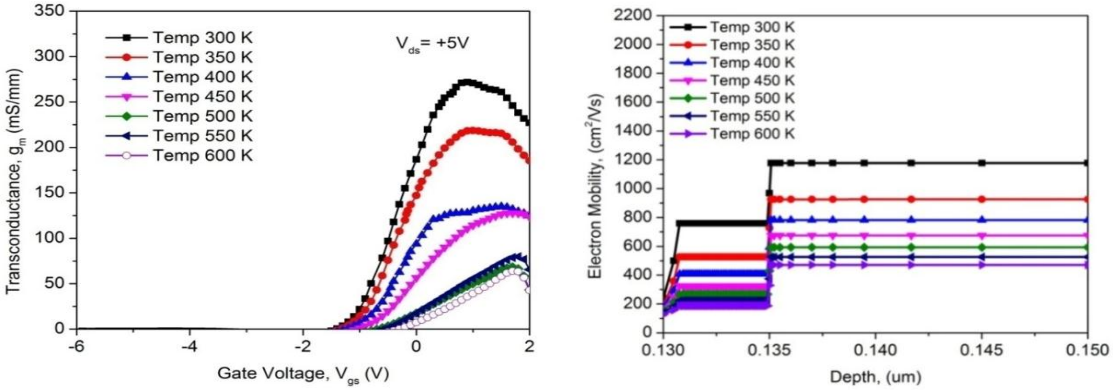

(a) **(b)**

Figure. 3. 17: Comparison of (a) transconductance and (b) electron mobility at different temperature

By increasing temperature calculated transconductance at V_{ds}= +5 V decreased from g_m= 270 mS/mm at 300 K to g_m= 80 mS/mm at 600K. Such effect could be explained by, looking at the differences between the electron mobility values at different temperatures as depicted in Fig. 3.17 (b). The electron mobility in the channel was 1181 cm^2/Vs at 300 K. When the temperature was increased electron mobility degraded along with the channel as a result of phonon and impurity scattering.

3.5 Trapping Effects on Leakage and Current Collapse in AlGaN/GaN HEMTs

The performances of these devices can be constrained by the presence of structural imperfection, dislocations, and trap related phenomenon in HEMT structures [39], [167]. Trapping effect related issues like current collapse, high leakage current through the buffer layer, and the reduced breakdown voltage needs to be enhanced to get long term reliability of the HEMT structures [168], [169]. These traps/deformity levels can be generated during the material growth or device processing and introduced deep level acceptors. The acceptor type traps in the GaN buffer and AlGaN barrier layers are necessary for device working, but the appropriate combination of trap density and energy level can suppress leakage current. Herein, it is exhibited that the density of acceptor type trap in the buffer/barrier layer and the trapping energy levels also play a crucial role in governing the current collapse and leakage current in the HEMT devices. Current collapse is a mutual effect of gate and drain lag, in which the deliberated output RF power, is always lesser than anticipated from dc operation [170]. Charge carriers get trapped at these defects levels which reduce the concentration of charge carrier accessible for the conduction of current. Consequently, the drain current gets reduced. As the buffer/barrier trap density or energy level rises, the current collapse became additionally dominating whereas leakage current became drastically diminish. Moreover, the acceptor type traps in the buffer and barrier have been anticipated to reduce current collapse during persist in the leakage current minimal. The physical properties and input model parameters of AlGaN and GaN employed in our modelling are concise in Table 3.5.

Table 3. 5: Input of material parameters for AlGaN and GaN used in the simulations

Parameter	**$Al_{0.25}Ga_{0.75}N$**	**GaN**
Band gap (eV)	3.96	3.4
Permittivity	9.5	9.5
N_C300 (cm^{-3})	$3.3x10^{18}$	$2.3x10^{18}$
N_V300 (cm^{-3})	$1.5x10^{20}$	$0.4x10^{20}$
Thermal Conductivity (W/cm.K)	2.85	1.5
v_{sat} for electrons ($cm.s^{-1}$)	$1x10^7$	$1x10^7$
B	2	2
Piezoelectric Constant (c/m^2)	-0.729	-1.0

1. Poisson's Equation

Poisson's Equation is part of Maxwell's equations. These equations can be correlated by electric field towards the space charge distribution specified by [69]

$$\text{div}\ (\varepsilon \nabla \psi) = -\rho \tag{3.5}$$

where, ψ is the electrostatic potential, ε is local electrical permittivity, and ρ is the local space charge density. The reference potential for ATLAS is always the intrinsic Fermi potential ψ_i. The space charge density in a semiconductor is given in the general case by [69]

$$\rho = +q\,[p + N_D^+ - n - N_A^-] - \rho_{Trap} \tag{3.6}$$

where, n and p are the electron and hole densities and N_D^+ and N_A^- are the donor and acceptor ion densities, ρ_{Trap} is the charge density contributed by the traps and fixed charges, all of which are, in general, a function of space and time at each node in the device structure.

2. Mobility Model

The temperature, doping, composition and field dependent electron mobility models were employed within this work. The doping-dependent electron mobility can be modeled as [165]:

$$\mu_o(T,N) = \mu_{min}\left(\frac{T}{300}\right)^{\beta_1} + \frac{(\mu_{max}-\mu_{min})\left(\frac{T}{300}\right)^{\beta_2}}{1+\left[\frac{N}{N_{ref}\left(\frac{T}{300}\right)^{\beta_3}}\right]^{\alpha\left(\frac{T}{300}\right)^{\beta_4}}} \tag{3.7}$$

where, T is the temperature, N is the total doping density, and α, β_1, β_2, β_3, β_4, μ_{min}, μ_{max}, N_{ref} are the parameters which were interpreted by Monte Carlo simulation.

Since the charge carriers gets accelerated in the applied electric field, at that instance, their velocity goes into saturation and the electric field turns out to be more substantial. This impact could be used as a decrement of the mobility because the extent of the drift velocity is the combined effect of mobility and electric field in the course of the current flow. The parallel field dependent electron mobility model to compute velocity saturation is shown below [165]:

$$\mu = \frac{\mu_o(T,N)+V_{sat}\frac{E^{n_1-1}}{E_c^{n_1}}}{1+a\left(\frac{E}{E_c}\right)^{n_2}+\left(\frac{E}{E_c}\right)^{n_2}} \tag{3.8}$$

where $\mu_o(T, N)$ is the doping dependent mobility, communicated in (3). The parameters, v_{sat}, E_c, a, n_1 and n_2 are calculated by least squares fit to the outcome obtained by Monte Carlo simulation. The estimation of these parameters obtained for both ternary compounds with two bracketing cases of alloy scattering.

3. Shockley-Read-Hall (SRH) Recombination

The recombination in the presence of traps in the forbidden gap is explained by the Shockley–Read–Hall (SRH) recombination model. Shockley-Read-Hall recombination is given by [69]:

$$R_{SH} = \frac{pn - n_{ie}^2}{\tau_{p0}[n+n_x] + \tau_{n0}[p+p_x]} \tag{3.9}$$

$$n_x = n_{ie} e^{\left(\frac{E_{Trap}}{kT_L}\right)} \tag{3.10}$$

$$p_x = n_{ie} e^{-\left(\frac{E_{Trap}}{kT_L}\right)} \tag{3.11}$$

where, E_{Trap} is the change in the trap energy level from the intrinsic Fermi level, where n_{ie} is the effective intrinsic density, T_L is the lattice temperature in Kelvin and τ_{no} and τ_{po} are the electrons and hole lifetimes. To investigate the impacts of deep level acceptor traps, physics based numerical simulations of AlGaN/GaN HEMT with different trap density for buffer ($N_{T,buffer}$), trap density for barrier ($N_{T,barrier}$), trap energy for buffer ($E_{T,buffer}$) and trap energy for barrier ($E_{T,barrier}$) were taken into consideration. A systematic examination of the effect of buffer and barrier trapping energies and densities on current collapse and leakage current were summarized in the next sections.

3.5.1 Trapping Effects with Various Trap Densities

A) Buffer Trapping Effects

The Buffer trap density ($N_{T,buffer}$) was varied at the range of $5\text{x}10^{15}$ ~$5\text{x}10^{18}$ cm^{-3}. The trap energy level ($E_{T,buffer}$) was kept constant at 0.75 eV. Besides this, we included donor doping of $5\text{x}10^{14}$ cm^{-3} in the GaN buffer layer which is accounted as a background carrier. It should be noted that in this section, only traps in buffer layer were considered. Fig. 3.18 shows the results of current collapse depending on the traps in the buffer and barrier layers. The observed increase of current collapse, 6% to 89.8% in the buffer and 0.3% to 17.5% in the barrier layers has been attributed to an increased trap density.

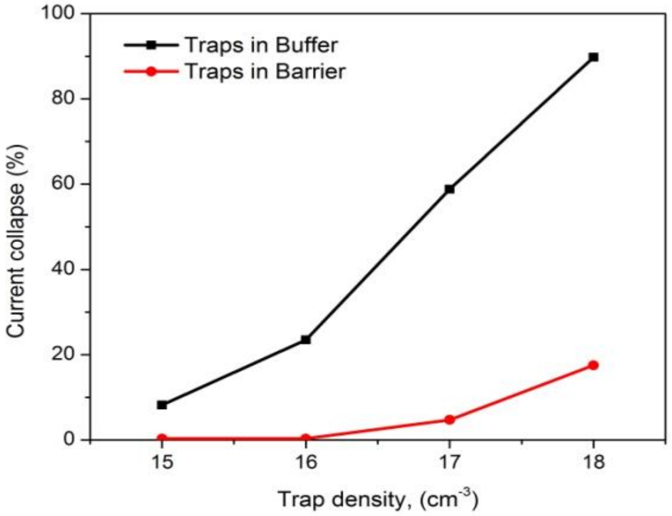

Figure 3.18: Current collapses depending on the variation in trap density of buffer and barrier layer ranging from 5x10^{15} ~5x10^{18} cm^{-3}

Fig. 3.19 (a) shows the DC current-voltage characteristics with deep trap energy, $E_{T,buffer}$ = 0.75 eV and $N_{T,buffer}$ varies from 5x10^{15} ~ 5x10^{18} cm^{-3}.

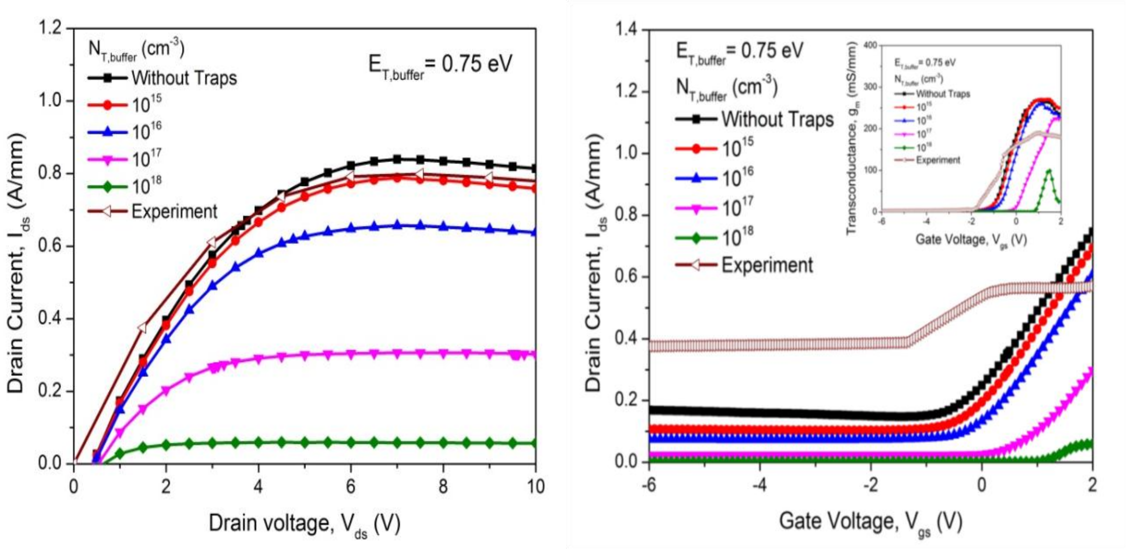

(a) (b)

Figure 3.19: (a) DC I-V characteristics of GaN HEMTs at V_{gs}= +2 V, (b) Transfer characteristics at V_{ds}= +5 V at trap energy ($E_{T,buffer}$= 0.75 eV) with variation in trap density of buffer layer ($N_{T,buffer}$) ranging from 5x10^{15} ~5x10^{18} cm^{-3}

The maximum drain current, I_{ds}=0.75 mA/mm at V_{gs}= 2 V and V_{ds}= 10 V, was obtained for the $N_{T,buffer=}$ 5x10^{15} cm^{-3} and provides approximate fit with the experimental data as depicted in Fig. 3.19 (a). The peak transconductance of 250 mS/mm at V_{ds}= 5 V was also recorded for the $N_{T,buffer=}$ 5x10^{15} cm^{-3}. The threshold voltage of the device was about 1 V for enhancement-mode operation. The collapse could be analysed clearly from Fig. 3.19 in which output drain current and transconductance was decreased with the increase in trap density. The off state leakage current, I_g is shown in Fig. 3.20. As discussed above, the current collapse was dominating for HEMTs having higher trapping densities; though, leakage current I_g was much less for these devices, leakage current falls drastically from 80.2% to 1.76%. The peak transconductance value for the $N_{T,buffer=}$ 5x10^{15} cm^{-3} is not in accordance with the experimental data because of the presence of off state leakage current in the devices.

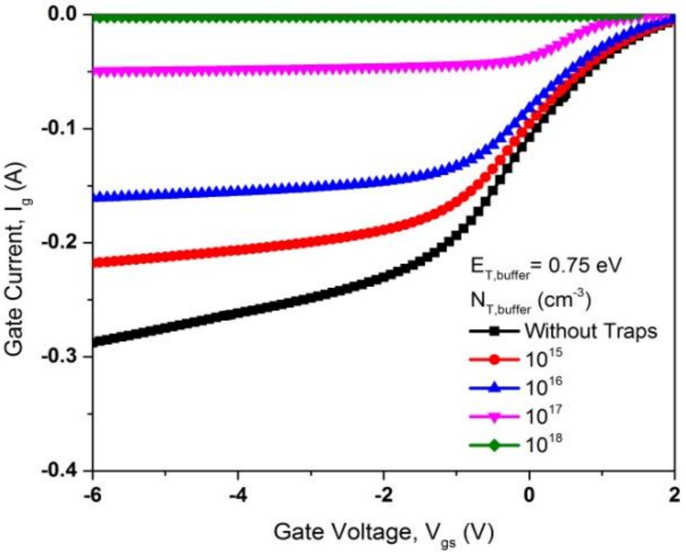

Figure 3.20: Leakage current (I_g) with variation in trap density of buffer layer ($N_{T,buffer}$) ranging from 5x10^{15} ~5x10^{18} cm^{-3} and trap energy, $E_{T,buffer}$= 0.75 eV at V_{ds}= +5 V.

As the $N_{T,buffer}$ intensifies, more electrons would be able to be confined in the trapping sites. These trapping sites get more ionized. The ionized traps create negative bias and block additional electrons overflow. These results provide improved electron confinement and a smaller amount of leakage current [168]. To describe the above occurrence, ionized acceptor trapping densities for different $N_{T,buffer,}$ and $E_{T,buffer}$ = 0.75 eV are also studied.

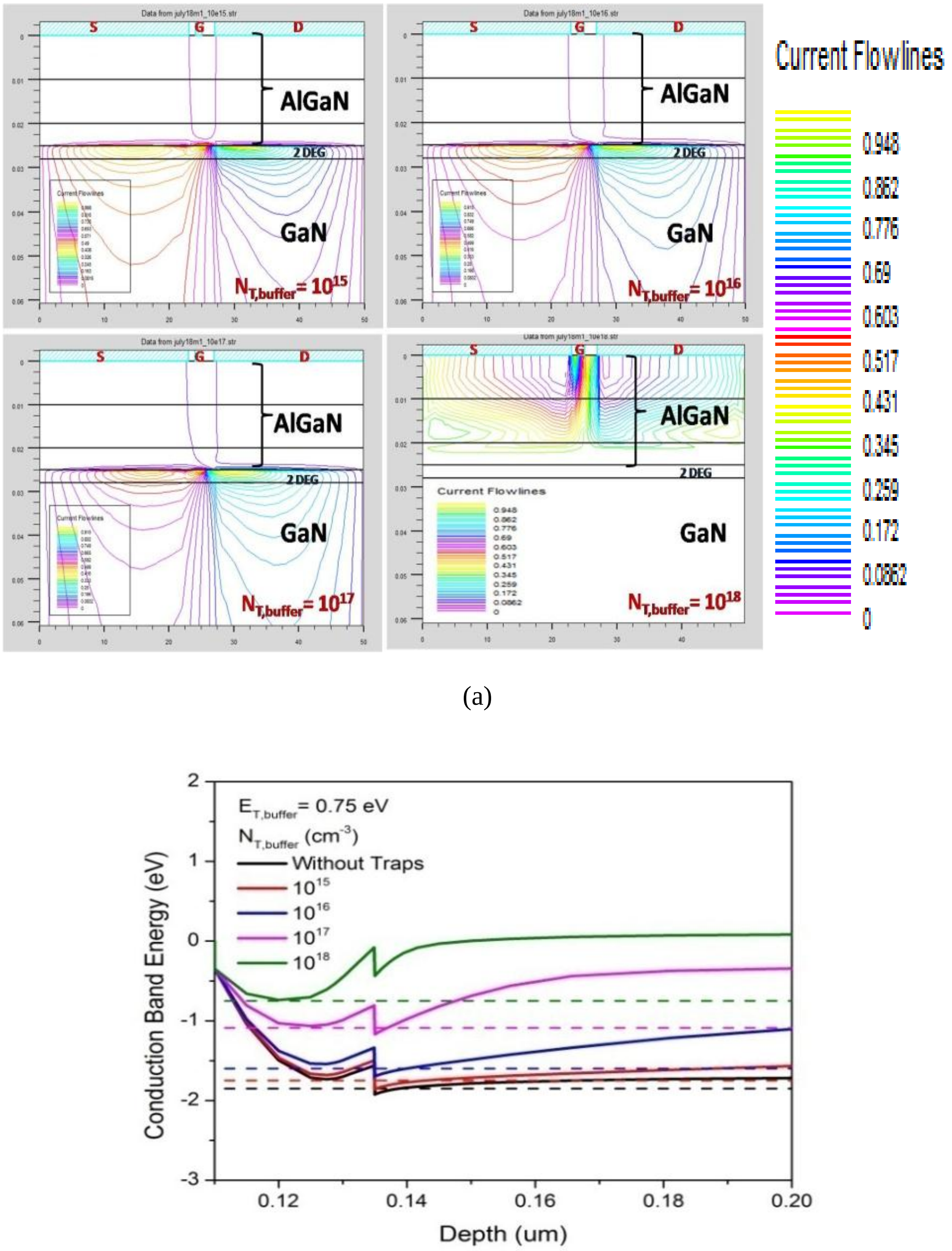

(a)

(b)

Fig.ure 3.21: (a) Current flow lines (b) Energy band diagrams with variation in trap density of buffer ($N_{T,buffer}$) ranging from $5x10^{15}$ ~$5x10^{18}$ cm^{-3} and trap energy, $E_{T,buffer}$= 0.75 eV.

It reveals that the increased acceptor ionized trap density distribution was more dense in the buffer layer for $N_{T,buffer}$ = 5x10^{15} in comparison to high trapping buffer density. The more acceptor ionized traps show that introduction of additional electrons commence more confined channel area. This results in the depletion of 2DEG density in channel area and a consequent decline in the output drain current. Hence, the ionized trap density towards 2 DEG acts as a more of a negative bias in the case of $N_{T,buffer}$ = 5x10^{18}. From the above outcomes and discussions, we observed that buffer leakage current abruptly decreases as the trap density increased and high ionized acceptor trap density results in reduced 2DEG density. Now, Fig. 3.21(a) is a graphical representation of current flow lines with various trap densities. The cutline is drawn in the middle of the gate contact. The simulation results for the current flow-lines were taken at biasing condition V_{gs}= 2 V and V_{ds}= 10 V. The current flow path in the 2DEG of HEMTs with $N_{T,buffer}$= 5x10^{15}, 5x10^{16} and 5x10^{17} cm^{-3} tends to be likely spill over through the GaN buffer layer. This outflow of electron results in decrease in the output current and transconductance. However, $N_{T,buffer}$= 5x10^{18} showed a significant reduction in leakage current and current flow lines were limited in the AlGaN and 2DEG region. Furthermore, to affirm that electron confinement could be obtained by improving trapping density within buffer layer. This phenomenon could be clearly seen by evaluating band diagrams with various trap densities in Fig. 3.21(b), where, 2DEG was completely disturbed at the critical value of 10^{18}. According to above discussion, in the case of buffer trap density, $N_{T,buffer}$= 5x10^{16} cm^{-3} showed a good balance between current collapse (20.3 %) and leakage current.

B) **Barrier Trapping Effects**

Next, we investigated current collapse and leakage current dependency on the trapping densities in the AlGaN barrier. The trapping density was varied for the range of 5x10^{15} ~5x10^{18} cm^{-3}. The energy level of the traps in barrier layer kept constant at 1.12 eV [171]. Fig. 3.22 demonstrates the simulated DC current-voltage characteristics (I_{ds}-V_{ds}) for V_{gs}= 2 V and V_{ds}= 10 V. It can be observed that as the trap density goes high in AlGaN barrier layer, the collapse raised from 0.3% to 17.5%. The current collapse was less pronounced in the case of presence of traps in barrier due to a separation between 2DEG and AlGaN barrier layer.

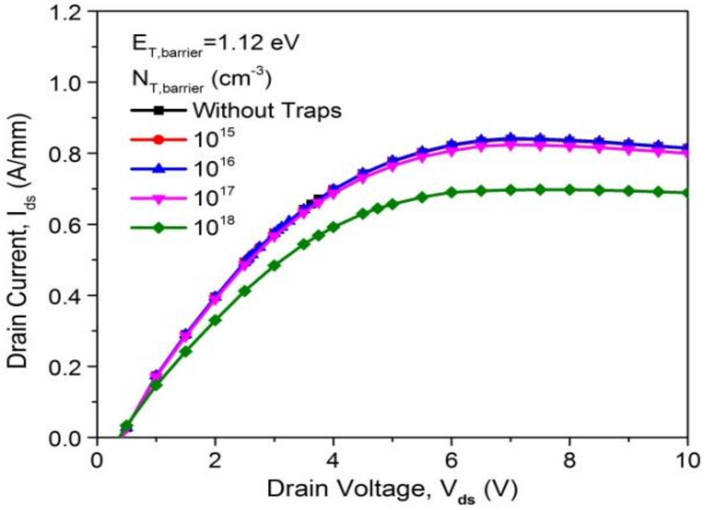

Figure 3.22: I_D-V_D characteristics at V_{gs}= +2 V, at trap energy ($E_{T,barrier}$= 1.12 eV) with variation in trap density of barrier ($N_{T,barrier}$) ranging from 5x10^{15} ~5x10^{18} cm^{-3}.

On the other hand, leakage current falls drastically from 95% to 12.6% as shown in Fig. 3.23. The reason behind this reduction was alike in the case of traps in buffer.

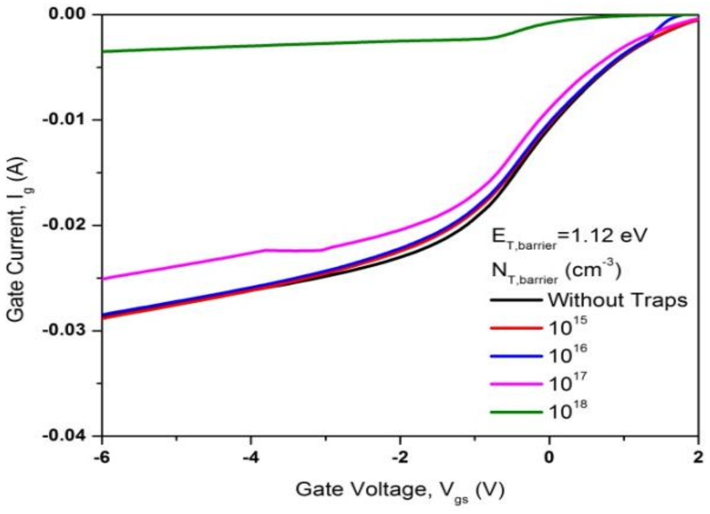

Figure 3.23: Leakage current at trap energy ($E_{T,barrier}$= 1.12 eV) with variation in trap density of barrier layer ($N_{T,barrier}$) ranges from 5x10^{15} ~5x10^{18} cm^{-3} at V_{ds}= +5 V.

Ionized acceptor barrier trap density was observed in barrier layer only. These traps accomplished negative biasing, which provided improved electron confinement. This negative bias was not much affected to 2DEG because of the separation between 2DEG and barrier layer. By analyzing current flow lines, it affirms that electron accumulation could be acquired implementing higher trapping density in barrier. Fig. 3.24 shows graphical representation of current flow lines. Also, the increase in ionized trap density acted as a negative bias, repels the current flow lines. According to our analysis in the case of barrier trap density, 10^{18} showed a good balance between current collapse (17.5%) and leakage current.

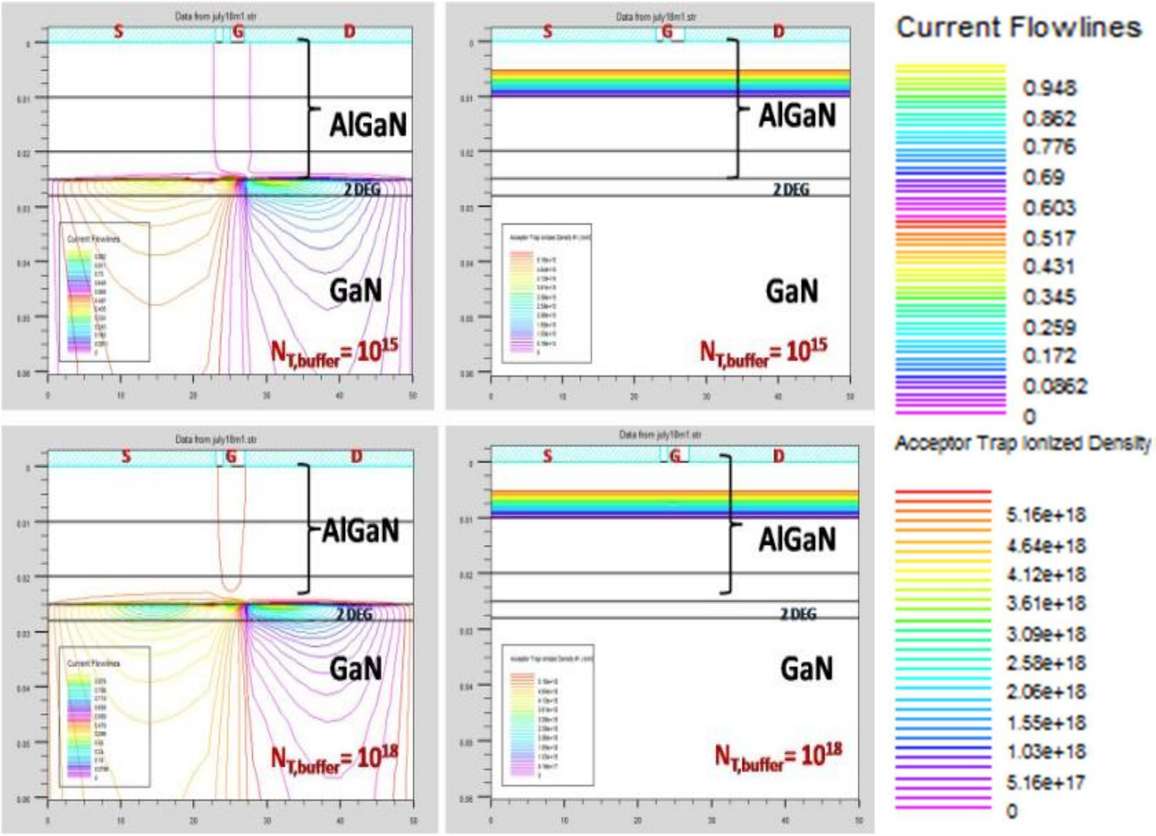

Figure 3. 24: Current flow line and ionized acceptor trap density at trap energy ($E_{T,barrier}$= 1.12 eV) with variation in trap density of barrier layer $N_{T,barrier}$= $5x10^{15}$ and $5x10^{18}$ cm^{-3}

3.5.2 Trapping Effect Depending on Different Trap Energy Level

In this section, various energy levels of the acceptor traps in the GaN buffer layer 0.75, 1.8 and 2.85 eV were studied. These trapping energy levels were taken from the literature by P. B. Klein and co-author's [172]. We observed deep level traps in these energy levels by a spectroscopic technique which caused current collapse. The $N_{T,buffer}$ kept constant at 10^{16} cm^{-3} that were chosen from the analysis of different trap densities as discussed in section 1. Output drain current reduces with an increment in the energy level of traps as shown in Fig. 3.25. The high drain current of 0.81 A/mm was recorded when traps were not present in the buffer layer.

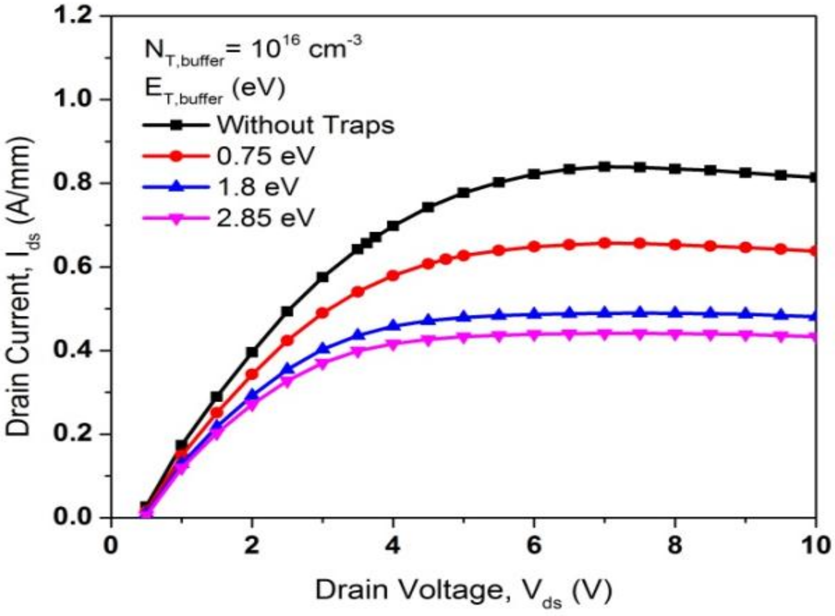

Figure 3.25: DC I_D-V_D characteristics of GaN HEMTs at V_{gs}= +2 V, at trap density of buffer layer ($N_{T,buffer}$= 5x10^{16} cm^{-3}) with variation in trap energy level, $E_{T,barrier}$ 0.75, 1.8 and 2.85 eV

As we considered traps in buffer with $N_{T,buffer}$= 5x10^{16} $cm^{-3\ and}$ $E_{T,barrier}$= 0.75 eV current fall down to 0.63A/mm and it was lowest for the combination of $N_{T,buffer}$= 5x10^{16} $cm^{-3\ and}$ $E_{T,barrier}$= 2.85 eV for the Current collapse increases from 22% to 47% with increased trap energy level. Fig. 3.26 presents that increment in trapping energy from 0.75 to 2.85 eV, the leakage current reduced from 58% to 3.8%. Higher trapping energy level shows further electrons infusion in channel area. These extra added electrons caught by the buffer traps, following decrease in 2DEG thickness in the channel area and a consequent reduction of the drain current.

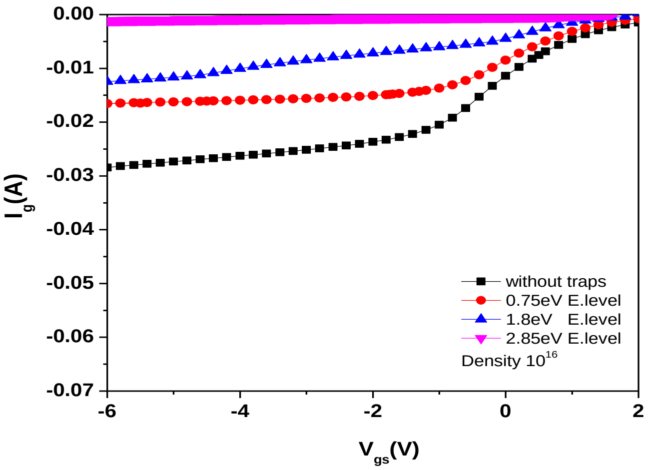

Figure 3.26: Leakage current at trap density of buffer layer ($N_{T,buffer}$= 5x10^{16} cm^{-3}) with variation in trap energy level, $E_{T,barrier}$ 0.75, 1.8 and 2.85 eV

The ionized acceptor traps of high trapping energy level, ($E_{T,buffer}$ = 2.85 eV) in the GaN buffer layer raise the conduction band energy of the GaN buffer layer and the electrons in the 2DEG to enhance confinement as depicted in Fig. 3.27.

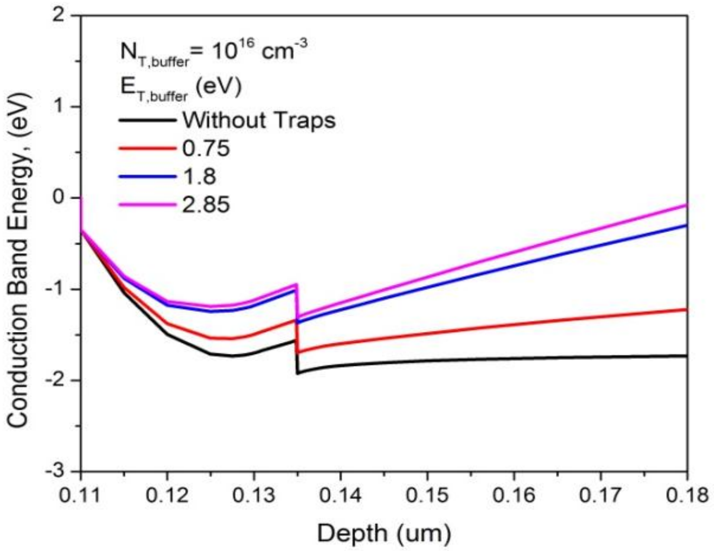

Figure 3.27: Energy band diagrams at trap density of buffer layer ($N_{T,buffer}$= 5x10^{16} cm^{-3}) with variation in trap energy level, $E_{T,barrier}$ =0.75, 1.8 and 2.85 eV. The cutline is drawn in the middle of gate contact

Consequently, electron brim over to the buffer layer was effectively underlying, and the trapping effect was drive down more at the higher energy. We also investigated the effect of trap energy level on the ionized acceptor density and electron distribution. Ionized acceptor traps density and electron distribution further confirm that the higher energy levels confinement became intensified and promoted a smaller amount of electron spill-over and hence reduced the leakage current. In the case of buffer trap energy level, 0.75 showed a good balance between current collapse (22%) and leakage current. The effect of acceptor traps on current collapse and leakage current has been examined by employing device simulator SILVACO ATLAS. Current collapse and leakage dependency on the density and energy level of the acceptor like traps in buffer and barrier layer were studied. Traps in buffer and barrier layer are necessary to prevent the dissemination of buffer leakage and reduction in current collapse.

We demonstrated the effect of trap density and trap energy level in the buffer and barrier layer on the DC characteristics and leakage current of the AlGaN/GaN HEMT. It is observed that higher the trap density in the buffer layer, the higher the current collapse and less leakage current. Trapping density, $N_{T,buffer}$ was changed from $5x10^{15}$ cm^{-3} onwards to reach to the critical value $5x10^{18}$ cm^{-3} at $E_{T,buffer} = 0.75$ eV. As a result, we achieved a maximum drain current I_{ds}= 0.758 A/mm and a peak transconductance, g_m = 250 mS/mm from the combination of $E_{T,buffer} = 0.75$ eV and $N_{T,buffer} = 5x10^{15}$ cm^{-3}. Since, trapping density lifted up, leakage current dropped abruptly from 80.2% to 1.76%. However, current collapse increased from 6% to 89.8% with the trap density in the buffer. These results indicate that balancing the trade-off amid diminishing current collapse and minimizing buffer leakage current is necessary. We have perceived that higher the buffer trapping energy, lesser the magnitude of leakage current. Finally, our observation concludes that the trap density $5x10^{16}$ cm^{-3} shows a good agreement concerning reduction in current collapse 22% and lowering leakage 58%. We also observed that higher the buffer trapping energy at constant $N_{T,buffer}$= $5x10^{16}$ cm^{-3} lowers the leakage current. The current collapse increases from 22% to 47% with the higher energy level of buffer traps but leakage current fell down from 58% to 3.8%.

In addition traps in barrier layer are also considered. As the trap density increases $N_{T,buffer}$= 5x10^{15}~5x10^{18} cm^{-3} at $E_{T,buffer}$ = 1.12 eV , current collapse raised from 0.3% to 17.5% and leakage current decrease from 100% to 12.6%. Barrier collapses percentage is not much pronounced in comparison to buffer traps. Finally, an optimum values of current collapse 17.5% and leakage 12.6% with trap density 10^{18} was observed.

3.6 Summary and Concluding Remarks

In summary, we performed an extensive study of the AlGaN/GaN and GaN/AlGaN/GaN heterostructures. The results of this study indicates that the inclusion of a GaN capping layer in AlGaN/ GaN heterostructures increases the peak electron concentration and decreases the 2D-electron mobility. A device with a GaN cap layer does not exhibit gate leakage current. Devices with 10 nm GaN Cap layer gave moderate electron mobility1050 cm^2/Vs, moderate drain current 1.56 A/mm and peak electron concentration 1.3 x 10^{19} cm^{-3} at the AlGaN/GaN surface. Thin AlGaN layers give lower value of drain current together with lower value of leakage currents. Thick AlGaN layers exhibit high drain current and the leakage current become prominent. But this layer should be thick enough to eliminate a pure tunneling process from the channel area in the surface states. AlGaN layer with 25nm thickness gives good drain current, electron mobility, and peak electron concentration.

Analytical analysis and simulated study of various electrical parameters such as output current, transconductance, electron mobility, and electron concentration have been done and the results have been obtained by solving appropriate energy balance equations using Silvaco-ATLAS tool. The set was validated against analytical data from a real device in a wide temperature range. Good predictive results for the DC characteristics of various devices were obtained. The calibrated simulation tool allows for the study, design and optimization of down-scaled and gate recess structures for high-temperature operation.

The effect of acceptor traps on current collapse and leakage current has also been analyzed. Current collapse and leakage dependency on the density and energy level of the acceptor like traps in buffer and barrier layer were studied. Traps in buffer and barrier layer are necessary to prevent the dissemination of buffer leakage and reduction in current collapse. AlGaN layer with 25nm thickness gives good drain current, electron mobility, and peak electron concentration. Configuration L_{SD}7µm_L_G1µm_L_{SG}1µm was chosen as the best combination due to highest attainable value of g_m (211 mS/mm) and I_{ds} (1.01 A/mm). We have fabricated the above mentioned optimised simulated HEMT structure (AlGaN Layer 18 to 25 nm and L_{SD}7µm_L_G1µm_L_{SG}1µm) with some other sets of device dimensions for the experimental work. We have presented detail information about the device structure and dimensions in the Chapter 4.

CHAPTER 4

Fabrication and Characterization of AlGaN/GaN HEMTs

In this chapter, we are reporting on the fabrication and characterization of AlGaN/GaN HEMT devices.

4.1 Introduction

AlGaN/ GaN high electron mobility transistor (HEMT) devices are the remarkable contenders for the cutting edge power, voltage, microwave, optoelectronics, and biosensing devices due to the ideal composite of large band-gap, high electron mobility, high carrier concentration and high saturation velocity with high electric field value [173]–[176].

Epitaxial growth of AlGaN/GaN HEMTs structure encounters many problems. AlGaN/GaN HEMT devices are generally hetero-epitaxially grown on foreign substrate materials like Sapphire [177], [178] or Silicon Carbide (SiC) [179] or Si [180] because of insufficiency of the native substrate. High crystal quality GaN epitaxial layers on such substrates are obtained by using Metal Organic Chemical Vapor Deposition (MOCVD) growth technique. Outstanding development in epitaxial material quality is reported by implementing annealing of the substrate in Nitrogen, Fe doping [181], delta doping [182] etc. The characteristic and quality of epitaxial growth of GaN are additionally investigated on low-cost SiC substrates [183] and on the Diamond substrates [184]. It is complicated to obtain crack-free AlGaN/GaN epitaxial structure along with high Al composition [185]. There are a lot of efforts, for example, using interlayer [186]or super lattices [187], to enlarge the crack free thickness of an active layer. The accurate determination of strain and Al composition in AlGaN/GaN epitaxial structure is essential for high power and frequency applications. Nevertheless, in order to get proficient usage of the distinct III-Nitride hetero structure properties in HEMT technology, various device processing steps must be expounded.

In this chapter, HEMT structures have been fabricated over AlGaN/GaN epitaxial structure grown MOCVD technique. The sapphire substrates were favored due to high crystal quality and its accessibility at the generally minimal expense contrasted SiC or GaN substrates. In case of biosensors, precision and chemical stability are the foremost decisive factors of substrate selection. Last of all sapphire is the majorly considered substrate for group III nitrides because the growth techniques are well established for sapphire [15]. Finally, AlGaN/GaN HEMTs are fabricated and tested by I-V measurements.

4.2 Device Processing

To fabricate AlGaN/GaN heterostructure limiting the channel area into an electrochemical sensor device, the technologies which are accessible at CEERI, Pilani is utilized. Now, the HEMT structures comprised of a 2.3 μm thick unintentionally doped GaN buffer and 18 nm thick *n*-type $Al_{0.25}Ga_{0.75}N$ layer. The epi-layers were deposited on sapphire substrate by MOCVD growth technique on GaN buffers deposited on sapphire substrates. Processing steps for the fabrication of AlGaN/GaN HEMT on Sapphire are expressed in Fig. 4.1.

4.2.1 Photolithography

Photolithography is a very crucial stride in the fabrication process of GaN HEMTs. To fabricate the AlGaN/GaN HEMT devices, chrome plated mask of size 3" x 3" is utilized. Shipley-1818 a positive photoresist was being used for the pattern transfer. At first, samples were mounted on the glass plate by spinning the photoresist at 1000 rpm for 10 sec. After mounting, samples were baked at 90°C for 25 min. The photoresist was coated on the specimen by spinning the sample at 4000 rpm for 40 sec. The thickness of the photoresist is ~ 2 μm. Optical Mask Aligner (Karl Suss MJB3 UV/VIS) has been utilized for the exposure to UV rays

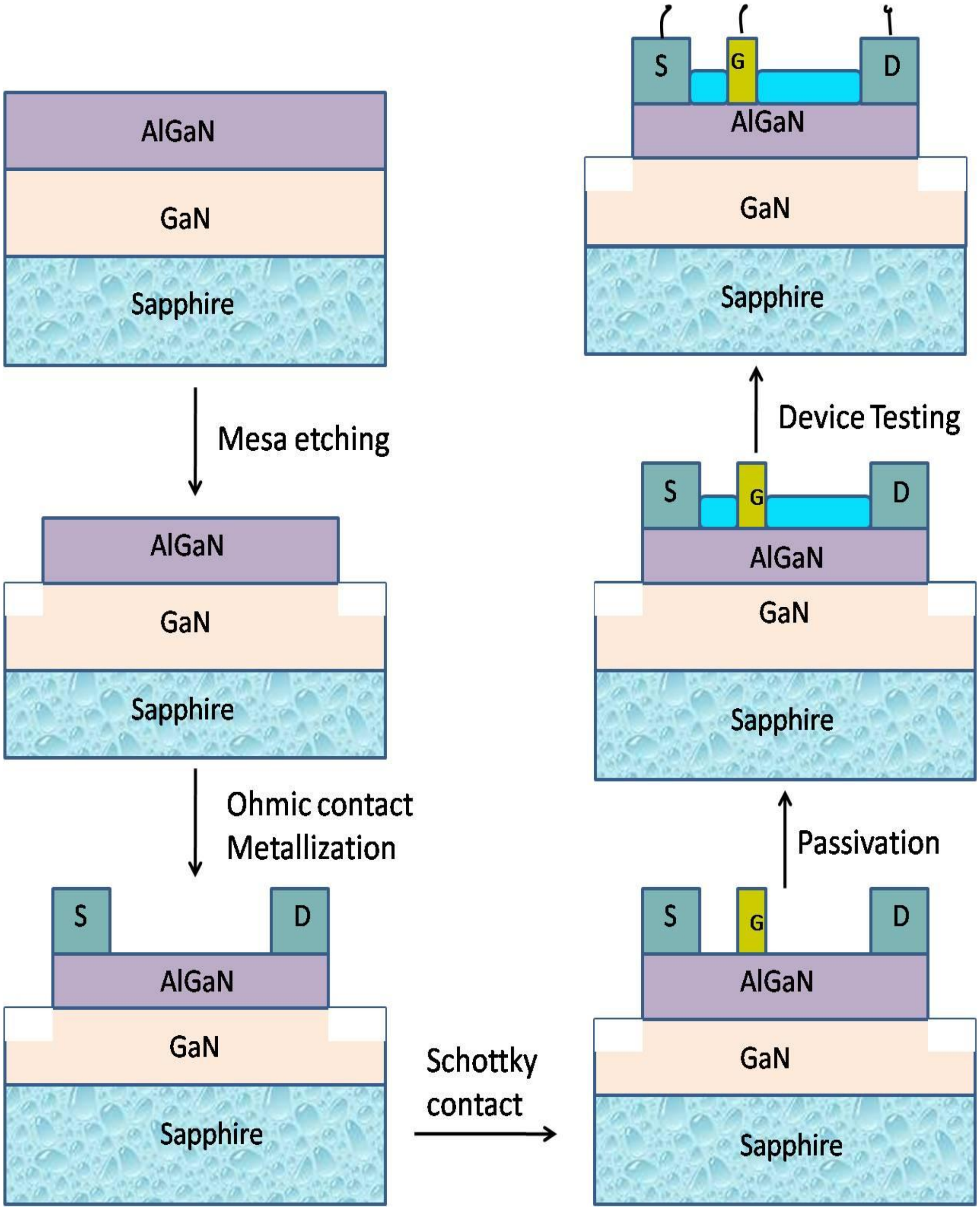

Figure 4.1: Schematic diagram of processing steps involved in the fabrication of AlGaN/GaN HEMT on Sapphire.

Optical aligner, limits the dimension of the features which might be processed about 1 µm caused by wavelength of the lamp source utilized (an ultraviolet lamp having wavelength 365 nm). The resolution of UV lamp was within acceptable limits for AlGaN/GaN HEMT sensors, however for smaller feature sizes, electron beam lithography have to employ. Exposure time was optimized to 20 sec. The subsequent step was developing the structures and regulating them through optical microscopy. The development time was 60 sec in developer solution (MFCD 26). After the development process, the samples were flushed in DI water and hard baked at 90°C for 50 minutes. Preceding any processing step, the specimens were treated with plasma ashing process. The samples were then exposed to oxygen plasma for 1 to 2 min, to expel the traces of photoresist from the active/exposed area. This step was recurred for following metallic layers and dry etches, which were requisite to develop a entire device.

4.2.2 Device Isolation

Device isolation was one of the most crucial process step attained by using mesa etching or ion implantation technique [188]. The first lithographic step is to make an isolated area between the adjacent devices, following the completion of organic and acid cleaning. In this case, 18 nm of AlGaN layer and some parts of the GaN layers are etched by different isolation techniques. Inter-device isolation in GaN HEMT was mostly exercised by creating mesa structures utilizing dry etch process. Lamentably, the chemical inertness of nitride material diminishes the etch rates. Due to which, the ratio combination of chemical radicals with ions utilized as a part of dry etching technique (RIE) was by all accounts feasible innovation to evacuate materials faster than conventional wet etching process. Drawbacks of these mesa processes are related to mesa sidewall. This sidewall may prompt to additional gate leakage current and least breakdown voltages [189]. Various methodologies were addressed to take out issues related to the mesa sidewall. Authors in [190] revealed a configuration of isolation using oxide layer to cover the mesa edge and diminish related gate leakage current [191]. Besides, planar ion implantation (I.I) approaches to avoid the mesa sidewall and lessen step coverage problem in the gate at mesa edge, thus reduced the gate leakage current and improved the yield and uniformity [192]. Implant isolations can be accomplished in GaN utilizing H^+, He^+, N^+, F^+, Mg^+, and Ar^+ ions [193]–[198]. The heavy Ion mass (Ar^+) isolation implantation created the displacements at the shallower location with a higher concentration compared to light atomic mass ions (i.e., H^+, He^+ or N^+). A heavy ion is anticipated to cause additional lattice damage and disorders. Hence it is able to endure successive high temperature processes. The lesser amount of implantation incident energy diminishes the likelihood of surface destruction of the device. The multiple incident ion energy and multiple ion dosage for two different ion masses were used and compared to make sure qualitative isolation in both AlGaN and GaN buffer layers with proficient thermal stability. To the best of author's knowledge till date, the previous writings offer no such direct multi-parametric performance evaluation involving these device isolation techniques. This section addresses comparative investigation of device performance on fabricated HEMTs by the mesa etch and ion implantation.

Firstly exhibits the device isolation using ion implantation technique. Two different ion species (Ar^+ and N^+) with multiple-energy and multi-dosage are employed in this process. Furthermore, we gave an account of electrical studies made on AlGaN/GaN HEMTs utilizing RIE (Model: 591, Sentech, Germany) for mesa etching. Ar^+ based chemistry was used in single and double step RIE process for Mesa isolation. The AlGaN/GaN HEMTs structure used for the experiment consist of 2 nm AlN nucleation layer along with 2.3 µm unintentionally doped GaN buffer layer and 18nm thick *n*-type $Al_{0.25}Ga_{0.75}N$ layer. The epitaxial layers were deposited MOCVD growth technique on GaN buffers deposited on sapphire substrates. Device fabrication includes ohmic contacts formation after device isolation. Drain and source ohmic contacts with a metal stack of Ti/Al/Ni/Au were obtained using e-beam metallization technique and then annealed in nitrogen ambient. Ni-based Schottky contact was used as a gate finger. Ion implantation and dry etch processes were used for the device isolation. Devices were interconnected using Au interconnects. The 2DEG carrier mobility is 1300 cm^2/Vs and sheet carrier density is 10^{13} cm^{-2}. Hall measured sheet resistance value is 550 ohm/square. Transmission line measurement (TLM) and meander structures were used to study the sheet resistance, contact resistance and isolation resistance. The fabricated meander structure after isolation is depicted in Fig. 4.2 to measure isolation resistance. Output characteristics were measured on unit gate devices having an L_{SD} = 50.0 µm explicitly used for the sensing applications.

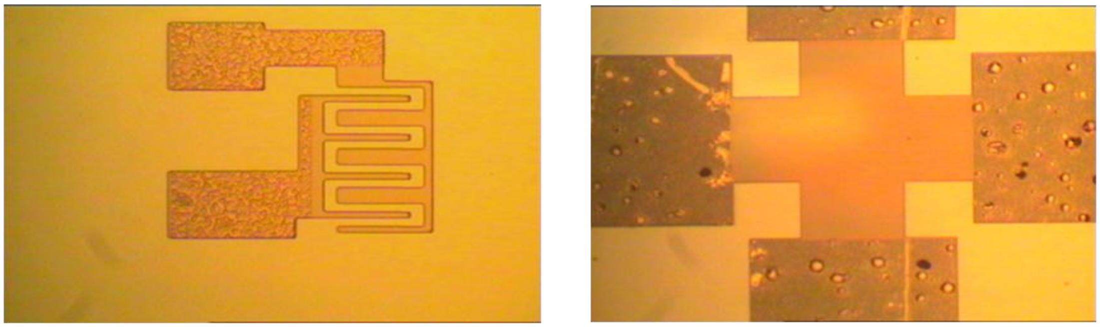

Figure 4.2: (a) Meander Structure after Isolation (b) Vander Pauw after Isolation

Fig. 4.3 demonstrates the schematic cross-section of the fabricated HEMT devices on (a) Ion-implanted (b) mesa-isolated samples.

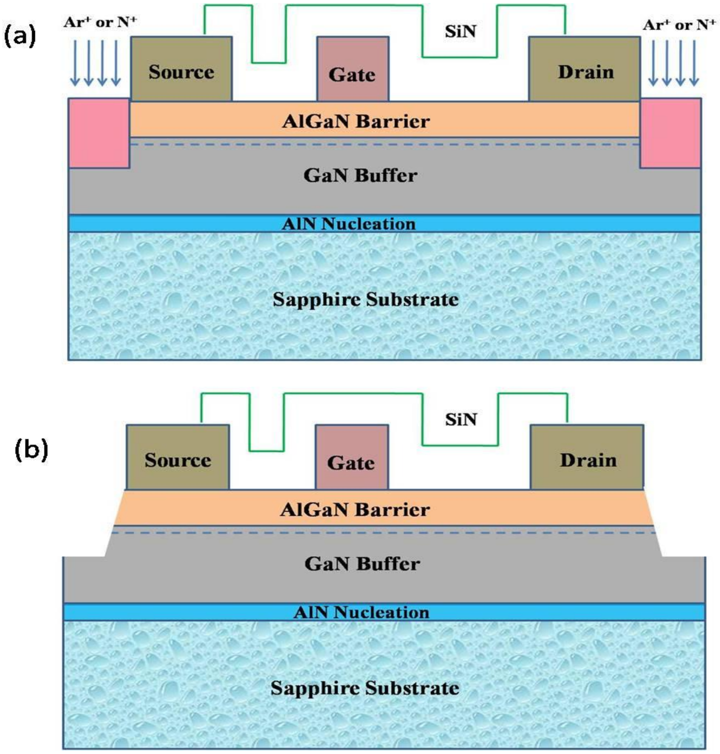

Figure 4.3: Schematic cross-section of AlGaN/GaN HEMTs fabricated on (a) ion implanted and (b) mesa-isolated samples

At first, different samples were implanted with multi-energy and multi-dose to produce an effective damage depth. Parameters used for ion implantation (I.I) are listed in Table 4.1.

To make a highly resistive isolation region, devices were pushed to undergo to Ar^+/N^+ ion implantation including three and four energies (3 E & 4 E) of (20/35/65 keV & 20/35/65/ 160 keV), and doses of ($4.2 \times 10^{12}/6.3 \times 10^{12} /1.11 \times 10^{13}$ cm^{-2} & $4.2 \times 10^{12}/6.3 \times 10^{12} /1.11 \times 10^{13}/ 1.11 \times 10^{13}$ cm^{-2}) respectively. These energies produced an effective damage depth of 255 nm. The transport of ions in matter (TRIM) software was employed to compute ion ranges in GaN HEMT structures [199]. Fig. 4.4 shows the displacement profiles in AlGaN/GaN by $^{14}N^+$ and $^{40}Ar^+$ ions for successive 3 E and 4 E calculated using TRIM code

Table 4. 1: Parameters used for multiple-energy and multi-dose ion implant

Recipe	Ion Energy (keV) and Doses (/cm^2)				Source Gas
3 Energy	20	35	65		Ar^+/N^+
	4.2×10^{12}	6.3×10^{12}	1.11×10^{13}		
4 Energy	20	35	65	160	Ar^+/N^+
	4.2×10^{12}	6.3×10^{12}	1.11×10^{13}	1.11×10^{13}	

Secondly, Reactive ion etching (RIE) method was employed as a dry etch technique employing single step and dual step etch processes. For optimization, different ratio combinations of the flow rate of reacting gases ($BCl_3/Cl_2/Ar$), RF power and pressure were varied and investigated the impact of different mesa recipe/condition over the electrical performance of AlGaN/GaN HEMTs. The conventional single step BCl_3: Cl_2 based plasma chemistry (Recipe 1) with a specific combination of gas flow (3:1), RF power 75 W and pressure of 5 Pa was used for the mesa etching. Recipe 2 was generated by directly adding argon (Ar) in the single step Recipe 1. Next, the Double Step Recipe (Recipe 3) was created in which; the samples were pre-treated in BCl_3: Ar (2:1) plasma in the first step at 100 W and pressure of 1 Pa.

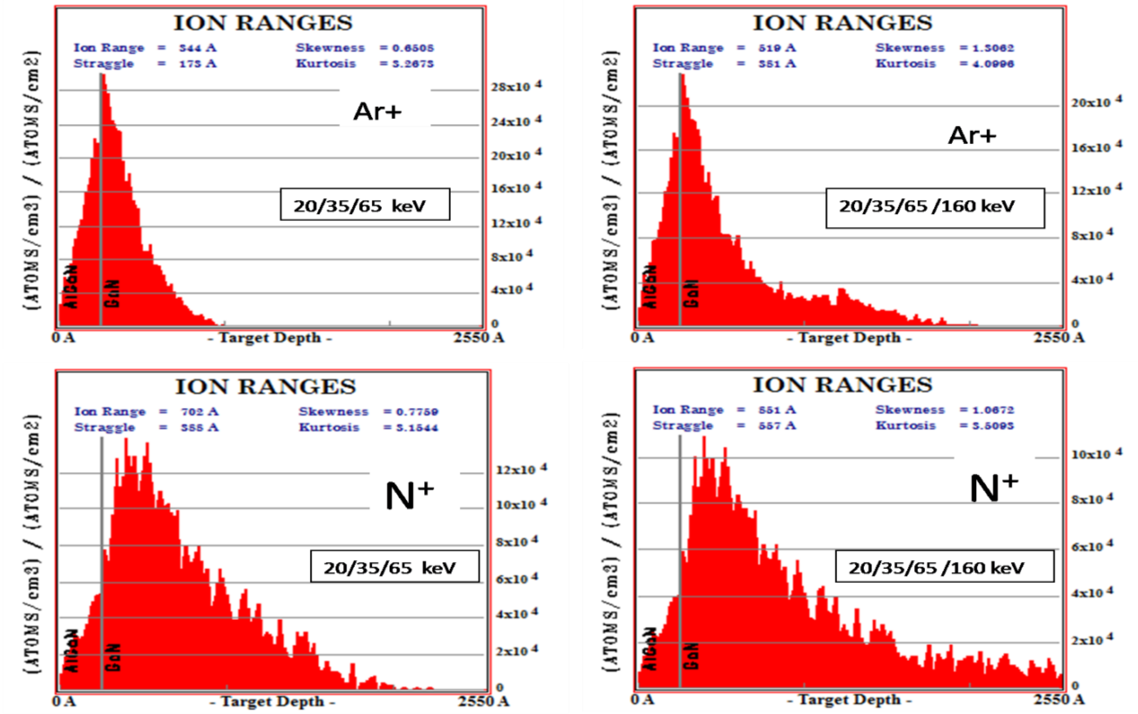

Figure 4. 4: Simulated depth profiles of vacancy and ion for successive Ar^+ and N^+ ion implantation for 3 and 4 Energies (20/35/65 keV and 20/35/65/160 keV) in AlGaN/GaN HEMT structure by TRIM Simulator

In the second step, the sample was etched using BCl_3: Cl_2: Ar (3:1:1) plasma chemistry. Recipe 4 was generated by reducing the power in Recipe 3. Table 4.2 gives the typical values of different experimental conditions, the ratio of flow rates of reacting gases, chamber pressure, and RF powers.

4.2.2.1 Isolation Using Ion Implantation Technique

This work reports on the use of multiple incident ion energies and multiple ion doses to ensure highly resistive isolated region in AlGaN and GaN buffer. For comparison, three energy and four energy Ar^+ ions with ion energies (20/35/65 keV & 20/35/65/ 160 keV), and doses of (4.2×10^{12}/6.3×10^{12} /1.11×10^{13} cm^{-2} & 4.2×10^{12}/6.3×10^{12} /1.11×10^{13}/ 1.11×10^{13} cm^{-2}) respectively were used for implant-isolation.

Table 4. 2: List of dry etching conditions in the RIE system to examine the effect of flow rate of reacting gases, RF power and chamber pressure on the electrical properties of the dry-etched surface in AlGaN/GaN heterostructures

Recipe	**Flow rate of ($BCl_3/Cl_2/Ar$) RF Power and Pressure** **Step 1**	**Flow rate of ($BCl_3/Cl_2/Ar$) RF Power and Pressure** **Step 2**
1 (Single Step)	BCl_3: Cl_2 = 3:1 @ 75 W, 5 Pa	---
2 (Single Step)	BCl_3: Cl_2: Ar = 3:1:1 @ 75W, 5 Pa	---
3 (Dual Step)	BCl_3: Ar = 2:1 @ 100W, 1 Pa	BCl_3: Cl_2: Ar = 3:1:1 @ 100W, 1 Pa
4 (Dual Step)	BCl_3: Ar = 2:1 @80W, 1 Pa	BCl_3: Cl_2: Ar = 5:1:1 @ 80 W, 1 Pa

To examine electrical parameters associated with isolated regions, we analyzed I–V characteristics of TLM structures. Isolation resistance was measured by meander structures. The recorded magnitudes of isolation resistance, specific contact resistance and sheet resistance after Ion implantation is listed in Table 4.3. The reference test sample which is not implanted showed a resistance approximately equals to ~200 Ω. After implantation, the isolation resistance increased for both the energies (3 E and 4 E). In these AlGaN/GaN devices, use of 3 E and 4 E resulted in a slight change in the isolation resistance. The maximum isolation resistance value of 0.11×10^6 Ω was recorded for 4 E. Use of 3 E in this instance probably generated more defects near to the 2DEG area which created leakage paths and hence the isolation resistance reduced. Sheet resistance was increased after 3 E and 4 E ion-implantation. Ion implant with 4 E has shown low sheet resistance 579.5 Ω/square as compared to 3 E. Device isolation current measured from meander structure for 3 E and 4E Ar^+ implant is 1.1 µA and 0.3 µA respectively.

Table 4. 3: Comparison of Isolation resistance and Sheet resistance obtained by 3 energy and 4 energy Ar^+ ion implant sequences

Isolation Resistance (MΩ)		**Sheet Resistance (Ω/Square)**		**Specific Contact Resistance (Ω/cm^2)**	
3 Energy	4 Energy	3 Energy	4 Energy	3 Energy	4 Energy
0.08	0.11	623.8	579.5	$6.2\text{x}10^{-5}$	$6.7\ \text{x}10^{-6}$

Fig. 4.5 presents the recorded output characteristics treated by both the sequences of ion implant with the source to drain length, L_{SD} = 50 µm. We can see that the output drain-current was I_{ds}= 0.37 A/mm for the samples treated with 4 E ion implantation and 0.22 A/mm for the samples treated with 3E ion implantation technique at V_{gs}= 2 V and V_{ds}= 25 V.

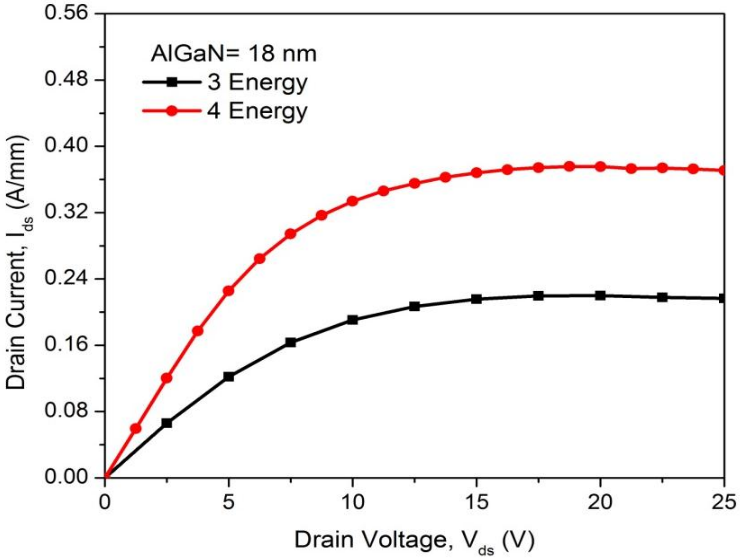

Figure 4.5: Comparison of Output drain current obtained by 3 energy, 4 energy Ar^+ ion-implant sequences for unit gate width devices with L_{SD} = 50 µm

Lowest specific contact resistance $\rho = 6.7\text{x}10^{-6}\ \Omega cm^2$ and contact resistance, R_c = 0.6 Ω.mm was recorded on the AlGaN HEMT treated with 4 energy Ar^+ implant. Hence, output current, I_{ds} = 0.37 A/mm was also recorded highest for this combination. These outcomes demonstrated the remarkable device isolation attained using 4E Ar^+ based ion implantation technique.

4.2.2.2 Isolation Using Mesa Etch Technique

The impact of different ratio combinations of the flow rate of reacting gases ($BCl_3/Cl_2/Ar$), RF power and pressure on mesa isolation was investigated in view of electrical performance in AlGaN/GaN HEMTs. Different AlGaN/ GaN HEMT devices were treated with the four recipes of RIE as mentioned in Table 4.2 and compared the etch rate obtained by employing above dry etch recipes. An etch rate of around 50 nm/min and 100 nm/min was recorded on the samples etched using Recipe 1 and Recipe 3 respectively. The mix of Cl_2 and BCl_3 additionally incremented the etch rate of GaN because of reactivity of chlorine. Fig.4.6 illustrates the scanning electron microscopy (SEM) image of Mesa etched AlGaN/GaN HEMTs.

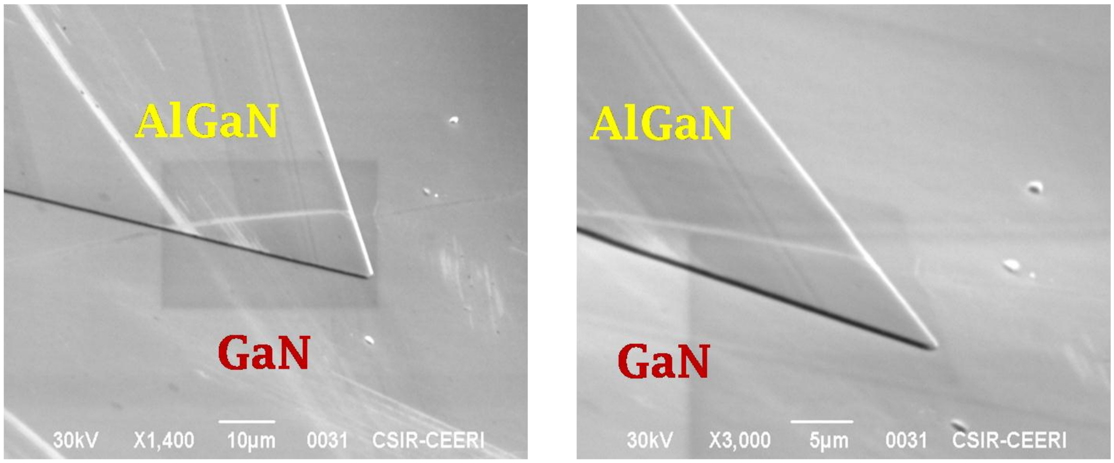

Figure 4.6: Scanning electron microscopy (SEM) image of Mesa etched AlGaN/GaN HEMTs

In addition, the additive gases like Ar added to BCl_3, and BCl_3/Cl_2 plasma again improved the etch rate. Apparently the Ar plasma helped in oxide removal in combination with BCl_3 which is a slow etchant of AlGaN and it was expected to help in sputter desorption of the etched product. These two recipes were then tested and compared to the other HEMT structure having a thin 18 nm AlGaN layer.

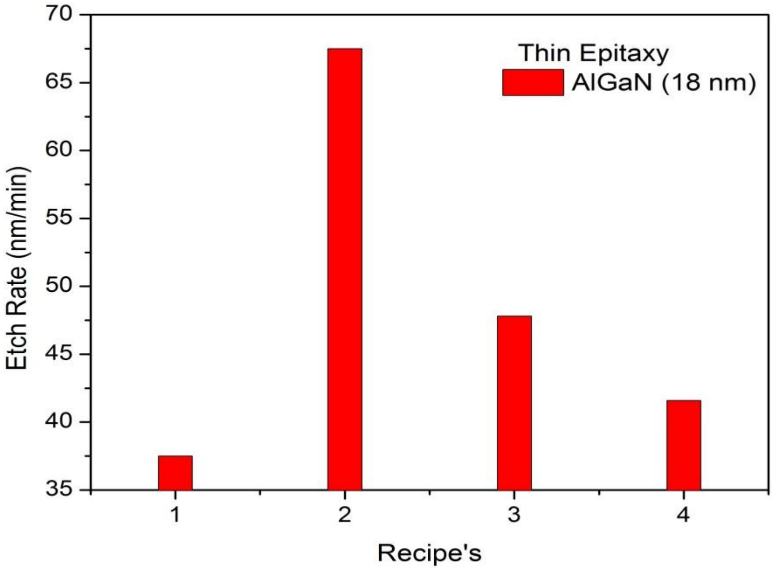

Figure 4.7: Comparisons of different mesa etching recipes Vs etch rates

In order to increase the etch rates in these devices; Recipe 2 was generated in which the Ar^+ was added in the Single Step Recipe 1. Fig. 4.7 compares the etch rate of different mesa etching recipes on thin AlGaN (18 nm) HEMT structure. The etch rate increased dramatically by 47 % after mixing Ar gas directly in BCl_3: Cl_2 combination. By reducing the RF power in double step etching (Recipe 4) reduced the etch rates from 47.8 nm/min to 41.6 nm/min. Hence, the Ar addition in the single step etching or recipe 2 proved much more beneficial as compared to the double step etching.

4.2.2.3 Comparison of Different Isolation Techniques

Further, we compared four different isolation techniques used for inter-device isolation on the AlGaN (18 nm) HEMT structure as a thin barrier and which is most suitable for biosensing application. These isolation techniques included four energy ion implantation using Ar^+, 4 energy N^+ implantation, single step BCl_3: Cl_2: Ar (3:1:1) at 75 W and pressure of 5 Pa (Recipe 2), and samples were treated with both the technique mesa etch and four energy N^+ implantation simultaneously. After employing these isolation techniques, isolation resistance and sheet resistance was measured for all the four methods (see Fig. 4.8). The highest isolation resistance value of around $0.56\text{x}10^6$ Ω was recorded for RIE, whereas 4 energy Ar^+ implantation results in lowest isolation resistance 0.11 $\times 10^6$ Ω. Sheet resistance value obtained for 4 E Ar^+ implant was 580 Ω/square. For 4 E N^+ implantation, the sheet resistance value decreased abruptly to the value 515 Ω/square. This value was highest (970 Ω/square) for isolation using the 4E N^+ implant with RIE. Isolation technique involving RIE as well as 4 E N^+ ion implantation provided better isolation. This could be the result of incorporation of deep states in GaN [12] suppressed by free carrier concentration and large lattice damage disorder created by N^+ -ions.

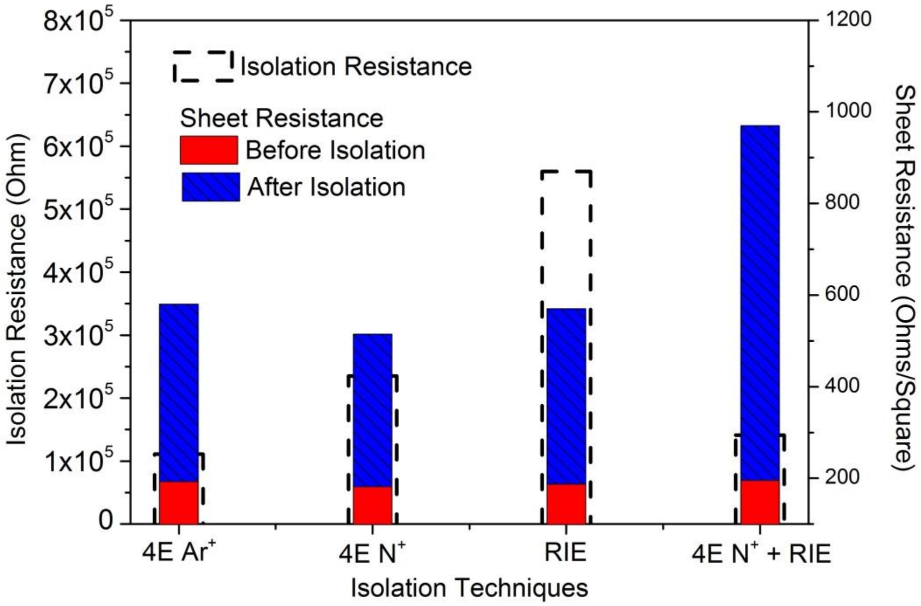

Figure 4.8: Comparison of Isolation resistance and Sheet resistance for four different isolation techniques includes 4 energy Ar^+ implant and 4 energy N^+ implant, RIE and 4 energy N^+ implant together with RIE.

The increment in sheet resistivity provided decrement in carrier concentration and mobility which will affect the output drain current. The calculated isolation current from meander structure for 4 E Ar^+, 4 E N^+ implant, $BCl_3/Cl_2/Ar$ plasma etching and 4 E N^++ RIE are 0.3 µA, 0.3 µA, 0.25 µA and 1 µA respectively. Fig. 4.9 presents the evolution of the specific contact resistance value and output characteristics treated by all four isolation methods.

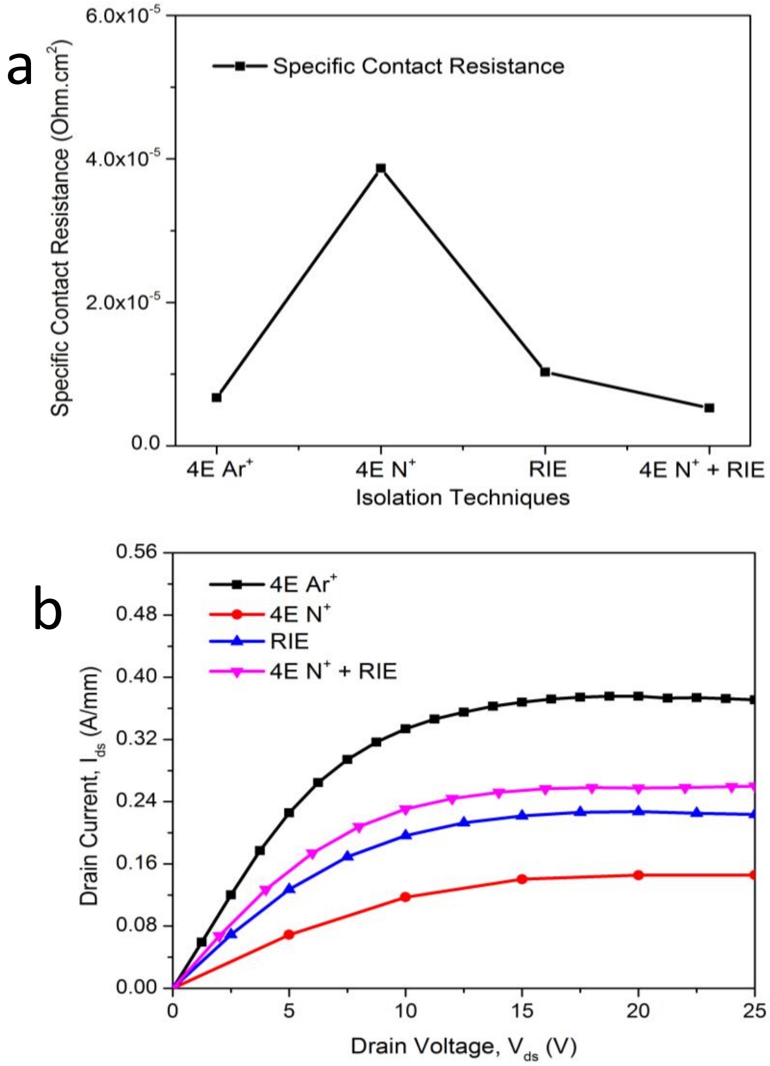

Figure 4.9: Comparison of (a) specific contact resistance and (b) output drain current (I_{ds}) for four different isolation techniques include 4 energy Ar$^+$ implant and 4 energy N$^+$ implant, RIE and 4 energy N$^+$ implant together with RIE on the unit gate width devices with L_{SD} = 50 µm

Specific contact resistance was 6.71x10^{-6} ohm-cm^2 for 4E Ar$^+$ implant and 5.26x10^{-6} ohm-cm^2 for 4E N$^+$ implant with RIE. As a result of which output drain current (0.37 A/mm) was highest for 4E Ar$^+$ isolation method. Isolation using 4 energy N$^+$ implants resulted in an increased value of specific contact resistance 3.87x10^{-5} ohm-cm^2 and which will lower the output drain current. Ar$^+$ based ion implantation and Ar based RIE proved to be an improved technology for device isolation. Ion implantation using 4 energy resulted in increased isolation resistance $0.11x10^6$ Ω as compared to 3 energy. Minimum specific contact resistance ρ= $6.7x10^{-6}$ $\Omega.cm^2$ and contact resistance, R_c =0.6 Ω.mm values were measured on the AlGaN HEMT devices treated with 4 energy. Consequently, output current, I_{ds} = 0.37 A/mm was likewise highest for this combination. In the case of RIE, mixing of Ar in BCl_3: Cl_2 gave higher etch rate. Therefore, the Ar addition in the single step etching proved better technique as compared to the double step etching process.

4.2.3 Formation of Ohmic Contact

After device isolation, the second lithographic step was done to realize Ohmic contacts for source and drain terminals.

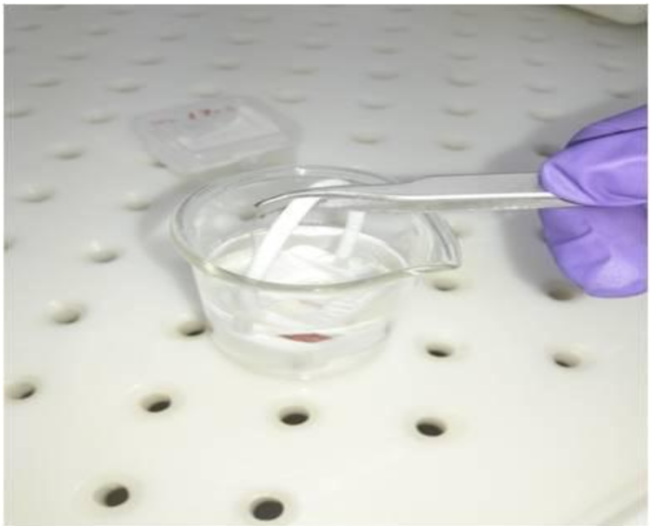

Figure 4.10: HCl: DI Pre-metalization etch

Prior to metallization, the samples were treated with HCl: DI water for 30 sec to perform pre-metallization etches (shown in Fig. 4.10), then rinsed in DI water and dry with N_2 flux. Fig.4.11 shows the ohmic contact with metal stack Ti/Al/Ni/Au deposited on the AlGaN layer and growned TLM structures after Ohmic Contact Metallization. The samples were again cleaned before the second lithography. Subsequent to the lithographic step, Ashing was done to remove the traces of photoresist.

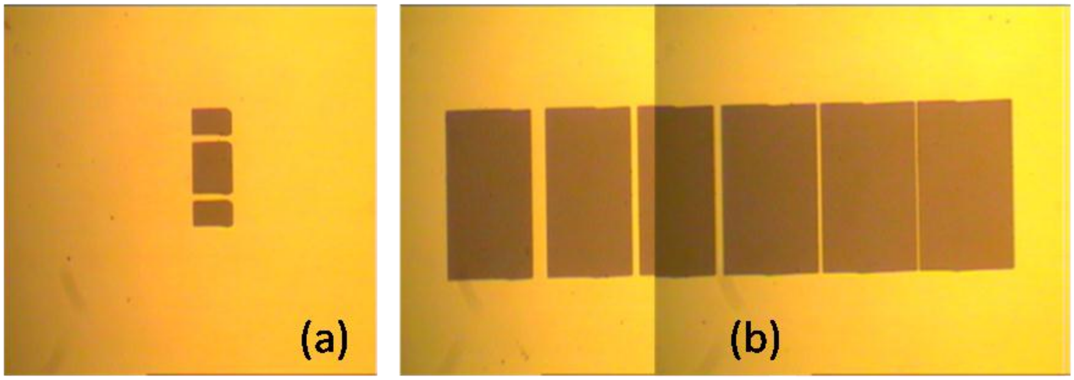

Figure 4. 11: Ti/Al/Ni/Au deposited on sample for Ohmic contact (a) unit gate width device (2 finger device), (b) TLM structures after Ohmic Contact Metallization

A comparison of specific contact resistance (ρ_c) and surface morphology for Ni, Pt, and Cr-based stacks is shown in Fig.4.12 and 4.13 respectively. The specific contact resistivity and other related parameters of the ohmic contact can be evaluated by transmission line model (TLM) between them.

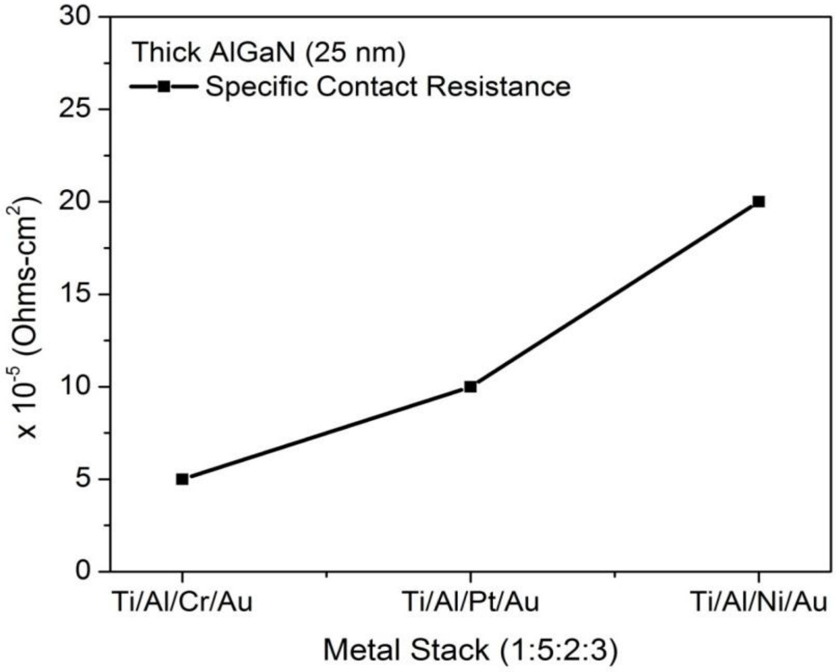

Figure 4.12: Comparison of specific contact resistance (ρ_c) for different metal stacks Ti/Al/Cr/Au, Ti/Al/Pt/Au and Ti/Al/Ni/Au

The aggregate resistance between the contacts is calculated by the four-point method and represented as a component of the contact spacing. It is fitted by utilizing linear regression as described in the given equation:

$$R_{meas} = 2R_k W + dR_s W \tag{4.1}$$

Where, R_{meas} is the total calculated resistance between two contacts in (Ω), R_k is the contact resistance in mm, R_s is the resistance of layer structure in the square, W is the width of the contact and d is the spacing between contacts.

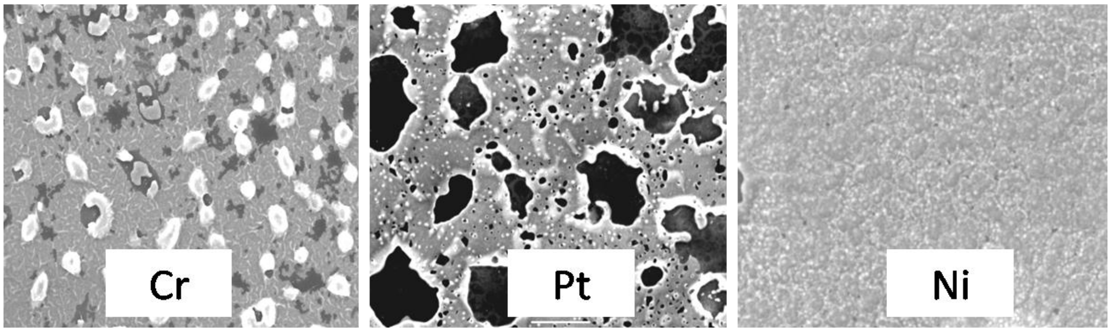

Figure 4.13: Ohmic contact (Ti/Al/x/Au) surface morphology SEM images where x metal layer is replaced by Cr, Pt, and Ni metals

The lowest $\rho_c$value of 5×10^{-5} Ω-cm^2 was measured on Cr samples. On the Pt and Ni samples, this value increased by 2 and 4 times respectively. However, the surface morphology of Ni was found to be better than Pt and Cr. The surface of Ni metal contact was smooth even after annealing, and the deep protrusion of the metal was not observed. On the contrary, the Pt and Cr surface have shown pits and hillocks. To improve the ρ_c of Ni contacts, the ratio of each metal in the Ti/Al/Ni/Au stack was changed. Initially a ratio of 1:5:4:3 was used that gave a ρ_c value of 25×10^{-5} Ω-cm^2. As the Ni content ratio is reduced to half, the ρ_c reduced. It decreased further with a diminishment in the amount of Au as appeared in Fig. 4.14. This could be due to the reduced Ni-Au phase [200]. The stack ratio of 1:5:2:2.5 delivered a very low ρ_c of 6×10^{-6} ohm-cm^2. As the Al and Au ratios were increased, the ρ_c ramped up again. At high annealing temperature, it became difficult for Ni to block the Au [201] to get mixed into the Al to form highly resistive purple plaque.

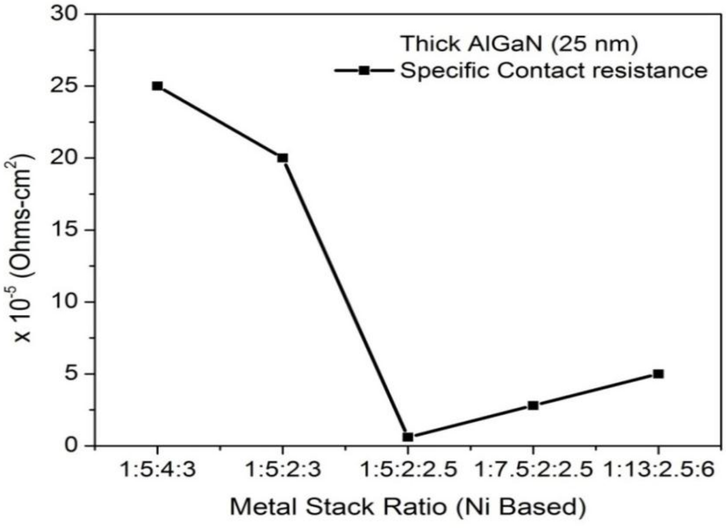

Figure 4.14: Effect of metal stack ratio variation on specific contact resistance in Ni-based recipe

The presence of Al and Au contents in the amount higher than the optimized value brightened up the possibility of intermixing. Thus, the ρ_c value increased. Different Ni-based stacks were then deposited, annealed and compared on thin and thick AlGaN/GaN HEMTs structures. For low Ni contents in the stack, the recorded ρ_c value did not differ much in thick and thin structures (shown in Fig.4.15).

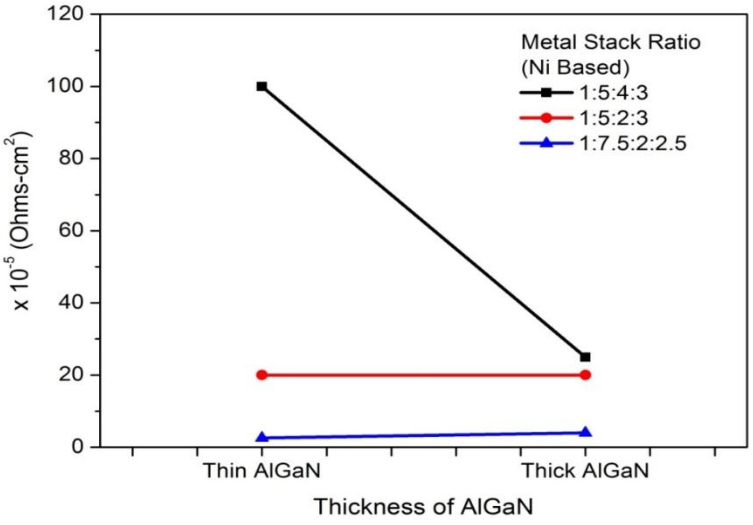

Figure 4.15: Comparison of ρ_c for different ratio of Ni-based ohmic contacts (1:5:4:3, 1:5:2:3 and 1:7.5:2:2.5) over thin and thick AlGaN structures

As the Ni content was doubled, the ρc $\rho_c$increased in both thick and thin AlGaN/GaN HEMTs structures. However, this increase was much more pronounced and dramatic in the case of thin AlGaN/GaN structures. We believe that it was because of an increase in the barrier height due to excessive Ni flow inward and towards AlGaN and its accumulation over the AlGaN layer. Thin structures suffered more due to the availability of less free charge carriers for tunneling as compared to the thick structures. Pre metallization surface treatments were also compared for both thick and thin structures. In this series, at first, the surface of thick structures were etched before metal deposition using HCl: DI, HNO_3: HCl and buffer oxide etchant (BOE). Fig. 4.16 shows the effect of these treatments on ρ_c. Best result was obtained on HCl:DI treated sample. The HNO_3: HCl treated samples spoiled the surface badly with an increased value of ρ_c. The buffer oxide etchant (BOE) treatment retained the smooth surface morphology but the ρc value obtained was very high as compared to HCl: DI treated sample.

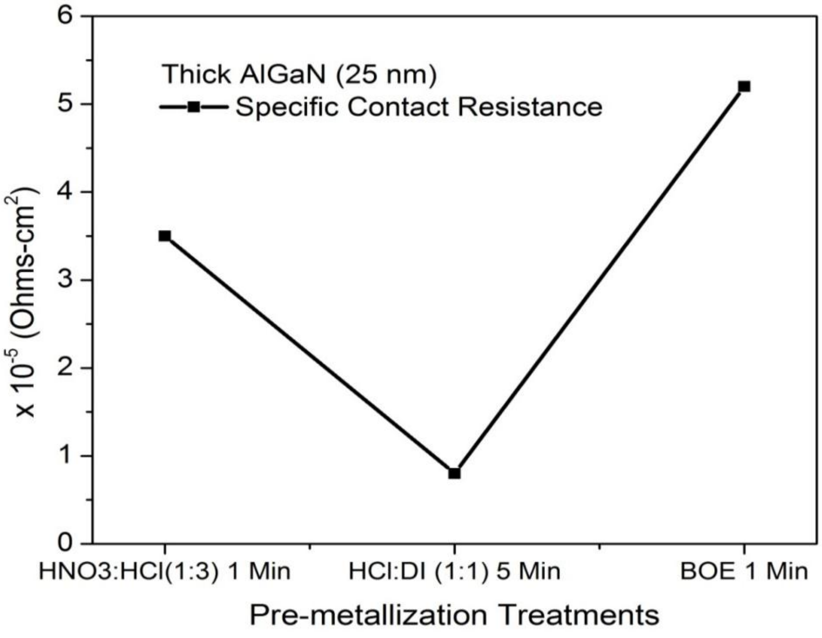

Figure 4.16: Effect of different pre-metallization surface treatments on ρc over thick AlGaN structures

An effect of BOE and HCl: DI were compared on both the thick and thin structures as shown in Fig. 4.17.

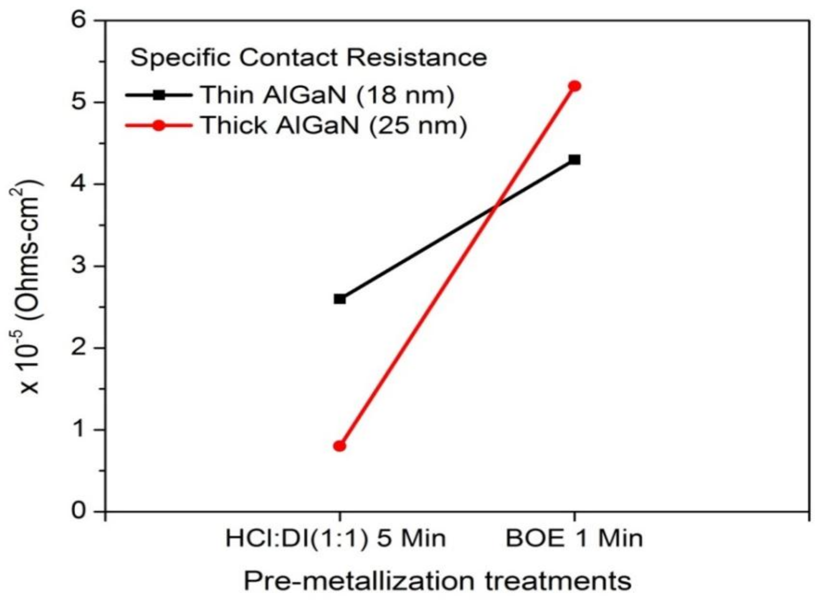

Figure 4.17: Effect of different Pre-metallization surface treatments on ρ_c over thick and thin AlGaN structures

Irrespective of the type of epitaxial structure, HCl: DI treatment was found to be the best for native oxide removal. The ohmic contact performance may also depend on isolation technique used. To obtain good device electrical characteristics, a good isolation between the adjacent devices are required. Device isolation was obtained by the dry etching process and ion implantation. Both the thin (18 nm) and thick (25 nm) epitaxial designs were treated with the reactive ion etch (RIE) and ion implantation. Thick epitaxy treated with RIE gave better contact resistance, R_c= 0.6 Ω-mm, and specific contact resistance, ρ_c ρ_c= 6.8×10^{-6} Ω-cm^2 whereas thin epitaxy treated with ion implantation gave better contact performance. Hence, the isolation process utilizing RIE is recommended for thick AlGaN and ion implant for thin AlGaN layers.

4.2.4 Formation of Schottky Contact

The third lithography step have used for making gate contact. For a typical HEMT design with the gate finger in between source and drain contacts, a Schottky metal gate contact was deposited. To establish an efficient Schottky contact a metal stack would be preferred which has the following attributes:

1. Good adhesion to the surface of the material.
2. High enough work function so that leakage currents are kept to a minimum.
3. Thermally and mechanically stable while operating under high biasing voltages.

Ni and Ti provide the best adhesive properties to create schottky contact for AlGaN/GaN HEMT devices. Ni has higher work function (5.15 eV) compared to Ti metal (4.33 eV). So we chose Ni as a metal layer for gate contact over Ti. The Au layer was used to prevent oxidation of the underlying Ni and improve conductivity during operation.

The gate length for the transistors was about 1-5 μm. The resolution for the above range of gate length 1-5 μm was realizable using optical contact photolithography. Oxygen plasma Ashing was done on this sample to eliminate the traces of photoresist from the active area of the device. No post-annealing step for Schottky contact has been done after the metallization. The samples after Schottky metallization are shown in Fig. 4.18.

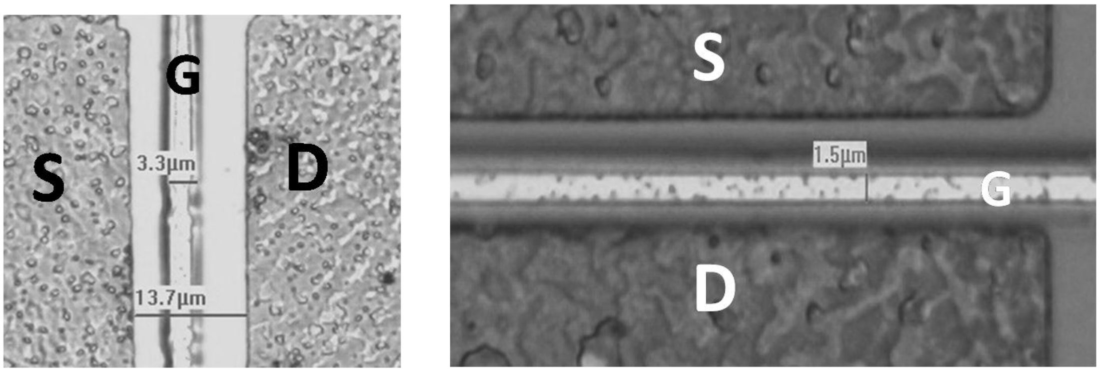

Figure 4.18: $L_{SD} \approx 14.0$ μm, $L_G \approx 3.0$ μm, $L_{SD} \approx 5.0$ μm, $L_G \approx 1.5$ μm

4.2.5 Metal Interconnects

Two or multi finger devices were connected using interconnection pads. These pads should be adaptable with the measurements apparatus. The contact pads could play a crucial role as the parasitic induced by them may influence the device performance. Interconnects should be stable and mechanically resistant at higher temperatures. In this work, we fabricated interconnection pads with area 50×50 µm^2 and spacing 150 µm. Ti/Au metal stacks have been used (shown in Fig. 4.19 and 4.20).

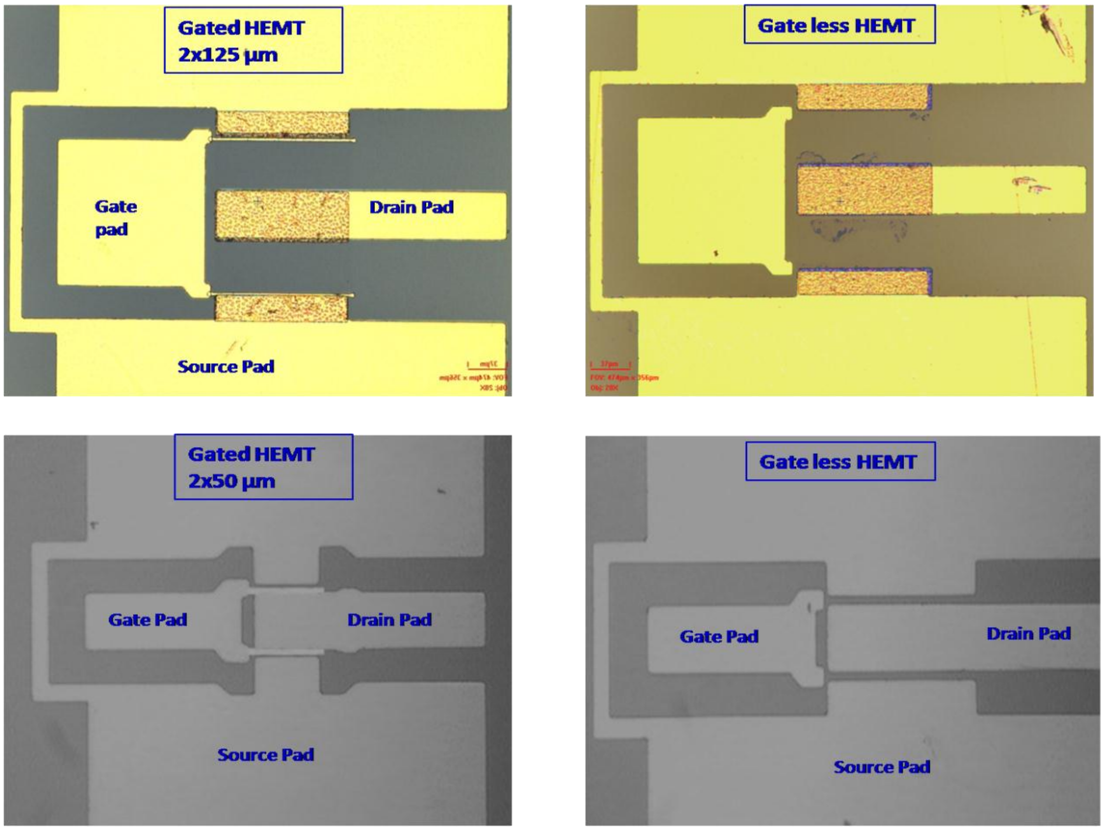

Figure 4.19: Fabricated samples after interconnection pads for gateless and gated HEMTs

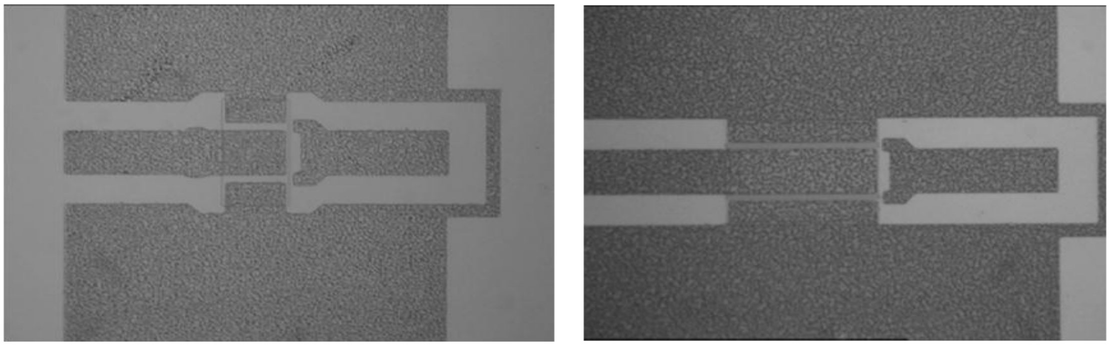

Figure 4.20: Fabricated HEMT devices after interconnection pads for different gate widths

4.2.6 Passivation

Surface passivation is the practice of depositing a thin inert film onto the surface of microelectronic devices to significantly improve its electrical characteristics. It helps in enhancing the performance of semiconductor devices which are susceptible to surface area effects. Passivation reduces the various defects on the surface of the device like surface leakage current, the inversion layer, and interfacial traps [202]. Passivation is also utilized to protect a device from the outside world.

The passivation of the sensor structure is a significant aspect of attaining stability and reproducibility of the device in liquids such as electrolytes. The passivation layer reduces the probable electrochemical reactions among contact fingers and electrolyte. Thus the passivation must be mechanically and chemically stable in both acidic and alkaline solutions. Additionally, for biosensors the layer biocompatibility is a necessary requirement. Among the various chemical vapor deposition methods, we used plasma enhanced chemical vapor deposition (PECVD) method to passivate the HEMTs surface with dielectrics such as SiO_2, Si_3N_4. These dielectric films were patterned using Reactive ion etching (RIE) as shown in Fig.4.21.

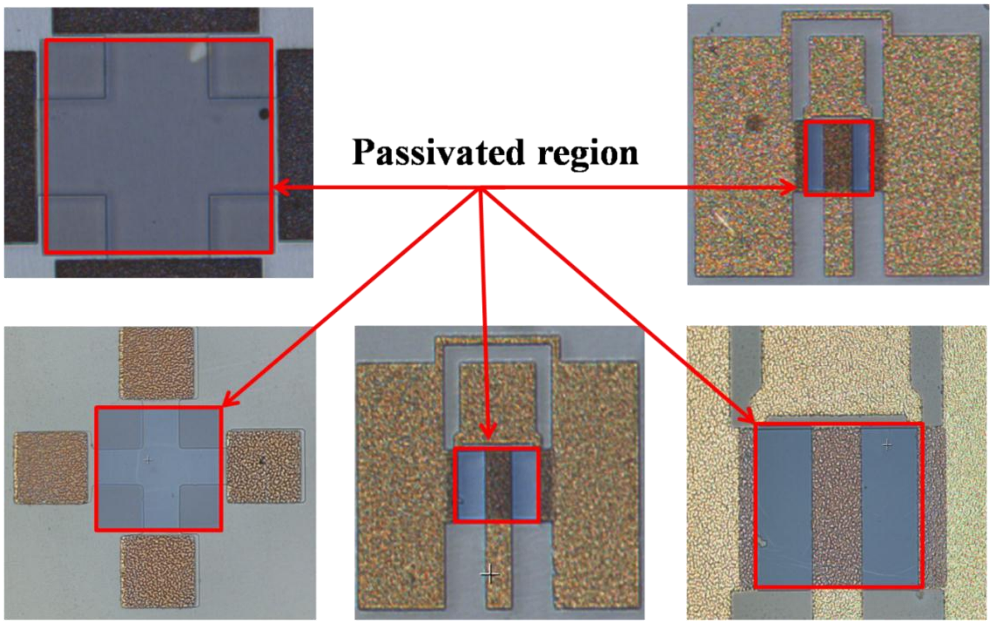

Figure 4.21: Fabricated samples after Si_3N_4 passivation

We performed a comparative investigation on AlGaN/GaN unpassivated HEMTs and passivated HEMTs with two different dielectrics, SiO_2 and Si_3N_4 were fabricated with identical device dimensions, on the same epi-layer structures and using the same fabrication technologies.

(A) Deposition of SiO_2 Layer for Passivation

In the first set of fabrication, we have deposited a SiO_2 layer of thicknesses 100 and150 nm over AlGaN/GaN HEMTs by Silane: N_2O based PECVD at 300°C. Then this film was etched using RIE technique by CF_4: O_2 plasma under a chamber holding 80 m torr pressure and 100 W power. Parameters used for the passivation of SiO_2 and Si_3N_4 dielectric layer are detailed in Table 4.4.

(B) Deposition of Si_3N_4 Layer for Passivation

In the next set of fabrication, samples were passivated with 100 and 150 nm-thick SiN_3H_4 layers utilizing Silane: NH_3 based PECVD at 300 °C. The Si_3N_4 was etched by CF_4: O_2 plasma under a chamber pressure of 80 m Torr and power of 100 W. Fig. 4.22 shows measured output characteristics of AlGaN/GaN HEMT before and after passivation of SiO_2 and Si_3N_4 of 100 nm and 150 nm thicknesses.

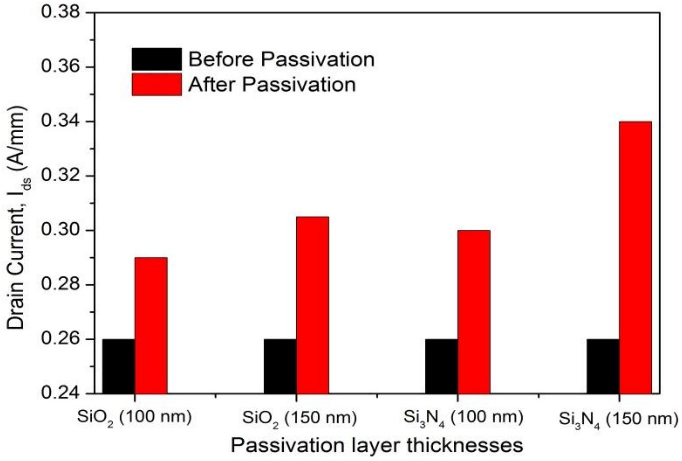

Figure 4.22: Output characteristics of SiO_2 and Si_3N_4 passivated AlGaN/GaN HEMT devices of dimension L_{SD}= 50 µm for 100 nm and 150 nm thickness

Table 4. 4: Parameters used for the passivation of SiO_2 and Si_3N_4 layer

	#Sample 1	**#Sample 2**
Passivation Material	PECVD SiO_2	PECVD SiNx
Deposition parameters	Power: 80 W (RF) Pressure: 0.3 Torr Flow SiH_4: 2.5 sccm Flow N_2O: 180 sccm Flow N_2: 300 sccm Flow Ar: 550 sccm Temp.: 300 ºC Rate: 60-70 nm/min.	Power: 120 W (RF) Pressure: 40 Pa (300 m Torr) Flow SiH_4: 7.2 sccm Flow NH_3: 180 sccm Flow N_2: 300 sccm Flow Ar: 550 sccm Temp.: 300 ºC Rate: 13-15 nm/min.
Deposition Time	2.30 min.	11 min.
Lithography	ok	ok
Thickness required	150 nm	150 nm
Thickness measured (step profiler)	130 nm	145 nm
Etching	Flow CF4: 35 sccm, Flow O2: 2sccm Power: 100 W, Pressure: 10 Pa (80m torr) Time: 4 min Etch rate: 45 nm/min	Flow CF4: 35 sccm, Flow O_2: 2sccm Power: 100 W, Pressure: 10 Pa (80m torr) Time: 2.30 min. Etch rate: 60 nm/min.

The observed drain current of SiO_2 passivated HEMT devices were improved because of increment in charge carrier presence in the 2DEG layer [203]. This was the result of the deposited passivation layer that stops the introduction of electrons into the surface trap and hence amplifies the 2DEG channel concentration. Before passivation, we observed 0.26 A/mm of drain current and this current was increased 0.29 A/mm after passivation. Total 12 % change in drain current after passivation at V_{ds}= 10 V was recorded. Because the use of SiO_2 passivation layer we can restore the lost current (current collapse). And the increased drain current directly influences the output power. For the case of 150 nm SiO_2 layers, the I_{ds} improved by 15 % respectively. Drain current response deteriorated slightly because of increase in the Oxide thickness.

All the details of processing parameters are given in Table 4.4. Deposition of 150 nm SiN_3H_4 layer resulted in the 24 % improvement in I_{ds} at 10 V. As the Nitride thickness reduced to 100 nm, the percentage change in the drain current degrades to 13%. Therefore, an increase in the Nitride thickness improved the device performance. When comparing the performance of 100 nm SiO_2 and Si_3N_4 layers, the SiO_2 showed better current recovery. On the other hand, for 150 nm of dielectric thickness, the Si_3N_4 proved to be a better dielectric material than the SiO_2. The results of different dielectric constant and thicknesses along with H passivation effects are the possible reason behind change in fringe capacitance and electric fields. This enhancement in drain current was because of the increment in sheet charge in the two-dimensional electron gas (2DEG) layer, explicitly examined while a passivation of the thin film was realized over the top of HEMT structure. The AlGaN/GaN heterostructure comprises a negative polarization charge over the AlGaN surface which initiates depletion of the 2DEG. The rise in sheet charge could be elucidated by the accomplishment of the passivating layer in trapping positive charge at the interface with the AlGaN barrier thus counterbalancing the net negative charge at the surface. Therefore, the passivation layer could eradicate the depletion of the underlying 2DEG.

4.3 Electrical Characterization of Fabricated HEMT Device

After fabrication, the AlGaN/GaN heterostructures were characterized to calculate its electrical characteristics and surface properties. Foremost techniques for the surface analysis have been atomic force microscopy (AFM) and scanning electron microscopy (SEM). The IV measurements were used to characterize electrical properties. TLM was employed to examine the metal contacts to the group III nitride heterostructures. In this chapter, the electrical investigation of the AlGaN/GaN heterostructures by TLM and I-V measurements will be presented in more detail and the outcomes will be discussed. Electrical testing of the device was done by Keithley 4200-SCS Semiconductor Characterization System. The information extracted from the DC measurements of AlGaN/GaN HEMT was exercised to calculate the contact resistance, maximum channel current, threshold voltage and transconductance.

4.3.1 Transmission Line Method (TLM)

The sheet resistance, specific contact resistance for the structuring of Ohmic contacts could be measured, using transmission line method (TLM) on 100 x 100 μm^2 pads as shown in Fig. 4.23 with the interspacing of 10, 20, 30, 40 and 50 μm respectively.

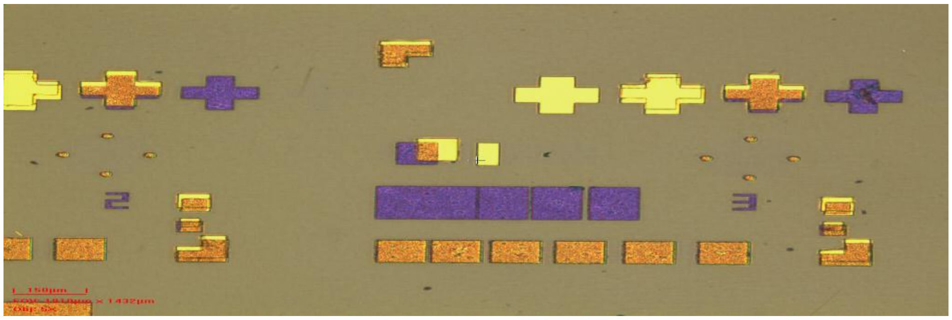

Figure 4.23: TLM Pads on the fabricated AlGaN/GaN sample

At first, a graph was drawn between the resistances generated between two consecutive pads versus distance between the pads (in microns) as shown in Fig. 4.24. In TLM, resistance between pads is given by [204],

$$R(L) = (L + 2L_T)\frac{R_{sh}}{W} \tag{4.2}$$

Where R(L) is resistance between pads, R_{sh} is the sheet resistance, L is spacing between pads, L_T is transfer length and W is the width of the pad.

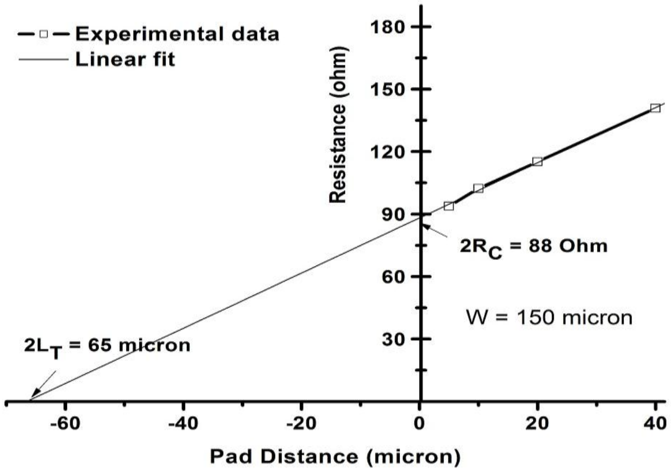

Figure 4. 24: Resistance versus TLM pads spacing

At L=0

$$R(0) = 2R_c = 2L \quad \frac{R_{sh}}{W} \tag{4.3}$$

where R_c is the contact resistance, the above equation can be written as,

$$R_{sh} = \frac{R_c W}{L_T} \tag{4.4}$$

Specific contact resistance, ρ_c of contact is written as,

$$\rho_c = R_{sh} L_T^2 \tag{4.5}$$

By putting the value of R_{sh} from Eq. 4.4 we get,

$$\rho_c = R_c W L \tag{4.6}$$

Using the method of least square, a linear fit to the experimental data is plotted, as shown in Fig. 4.24. This gives a slope (m), intercept (c) of the line on the y axis and intercept on the x axis. These slopes and intercepts values were used to calculate the sheet resistance, contact resistance and transfer length as,

$$R_{sh} = m \times W, R_c = \frac{c}{2}\Omega \tag{4.7}$$

$$L_T = \frac{1}{2}.Interceptonx - axis \tag{4.8}$$

The measured values of sheet resistance (R_{sh}) are 203 Ω per square, contact resistance (R_c) is 44Ω, transfer length (L_T) is 32.5 µm and the specific contact resistivity (ρ_c) for the source and drain Ohmic contact pads is 2.15 x 10^{-3} Ω cm^2.

4.3.2 DC Measurements

Output characteristics of HEMT devices were measured on the samples having unit gate width (2 gate finger and 50 and 125 µm gate width) as shown in Fig. 4.25.

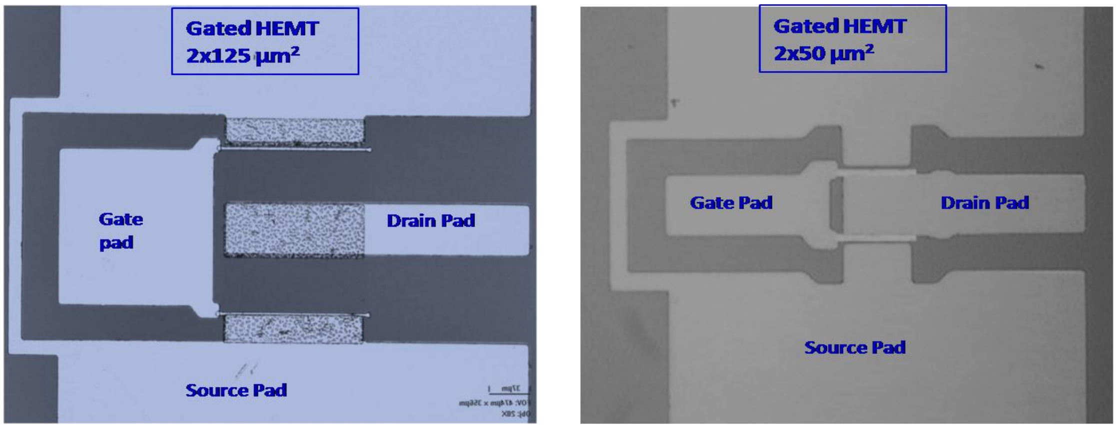

Figure 4. 25: Fabricated double gate (W_g= 125 µm, L_{SD}= 50 µm, L_G= 1 µm, and W_g= 50 µm L_{SD}= 6 µm, L_G= 4 µm) AlGaN/GaN HEMTs

The maximum output drain current (I_{ds}) of 0.53 A/mm was obtained for AlGaN/GaN HEMT at L_{SD}= 6 µm, L_G= 1 µm, unit gate width and V_{gs} = 0 V. As the source to drain length (L_{SD}) increases, drain current start decreasing and we obtained 0.21 A/mm current for L_{SD}= 50 µm, L_G= 1 µm and V_{gs} = 0 (shown in Fig. 4.26). Fig. 4.26 revealed the fact that reduction in drain current with L_{SD} variation was due to the decrease in electron concentration (n_s). A reduction in L_{SD} led to the decrease in the on-resistance (R_{on}) and hence current increased [205].

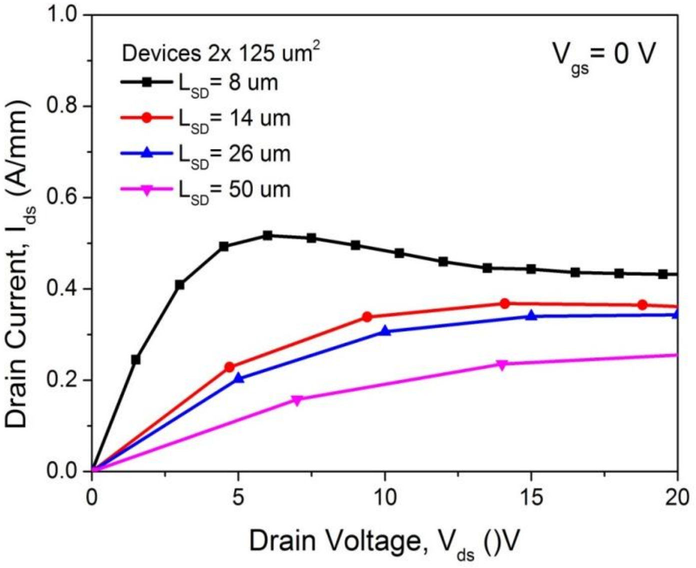

Figure 4.26: Output characteristics of AlGaN/GaN HEMT (Unit gate width, L_G= 1 µm)

Fig. 4.27 explains variation in drain current for the two finger devices with different gate width (W_g= 50 and 125 µm), source to drain length L_{SD}= 8 µm and gate length L_G= 1 µm. Devices having smaller gate width produce high drain current 0.651 A/mm in comparison to larger gate width 0.512 A/mm.

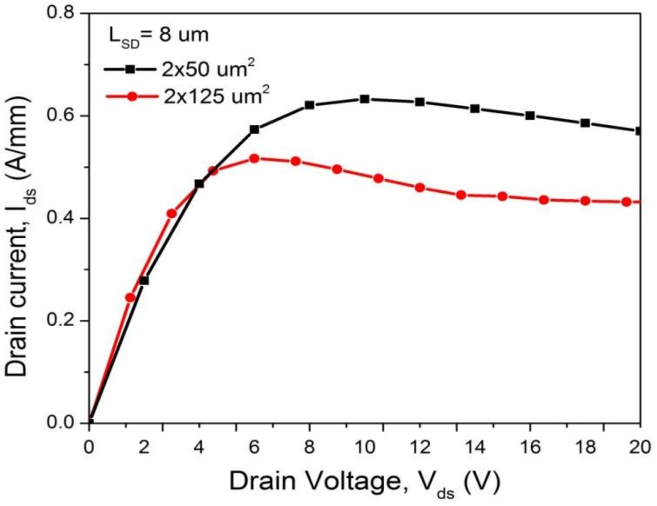

Figure 4.27: DC Transistor characteristics of AlGaN/GaN for two different device gate width at L_{SD}= 8 µm and L_G= 1 µm

The transfer characteristic of the device is shown in Fig. 4.28. The channel current was normalized with respect to gate width which is given in terms of mA/mm gate width.

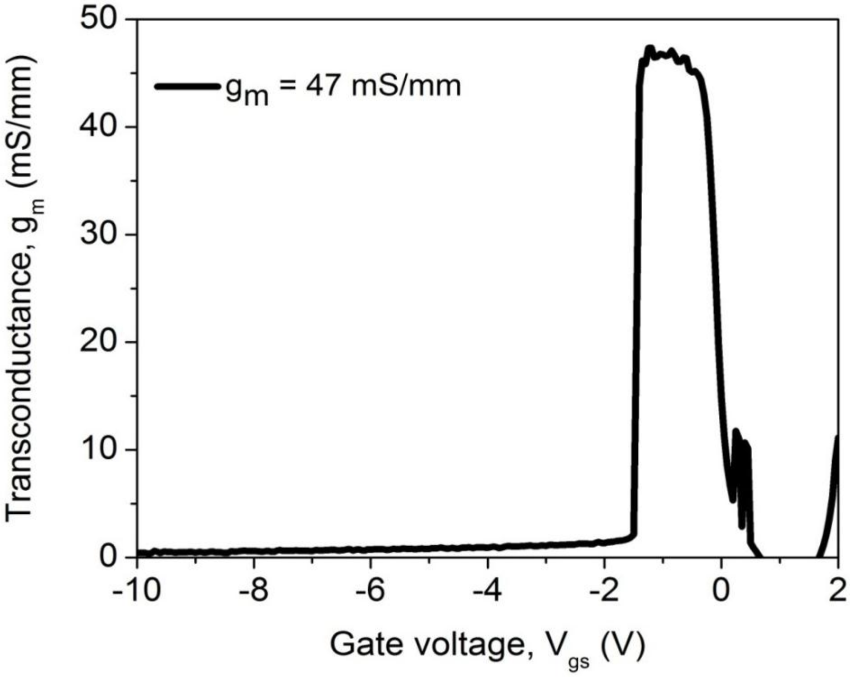

Figure 4.28: Transconductance of AlGaN/GaN HEMT (W_g= 125 μm device)

The maximum transconductance (g_m) of 47 mS/mm was obtained for the device dimension (L_{SD}= 50 μm, L_G= 1 μm, unit gate width) at V_{ds}= 0 V. When the transconductance of the device approached zero, the channel was completely pinched off because the electric field below the gate had completely depleted the channel. The pinch-off voltage of the device (V_p) is – 1.7 V.

Next, we have compared the experimental data with the simulated data for output current and transconductance at L_{SD}= 6 μm, L_G= 1 μm, unit gate width and V_{gs} = 0 V which is demonstrated in Fig. 4.29. The values obtained for output drain current and transconductance from experimental data (0.76 A/mm and 250 mS/mm) has also shown good aggrement with simulation data (0.81 A/mm and 275 mS/mm).

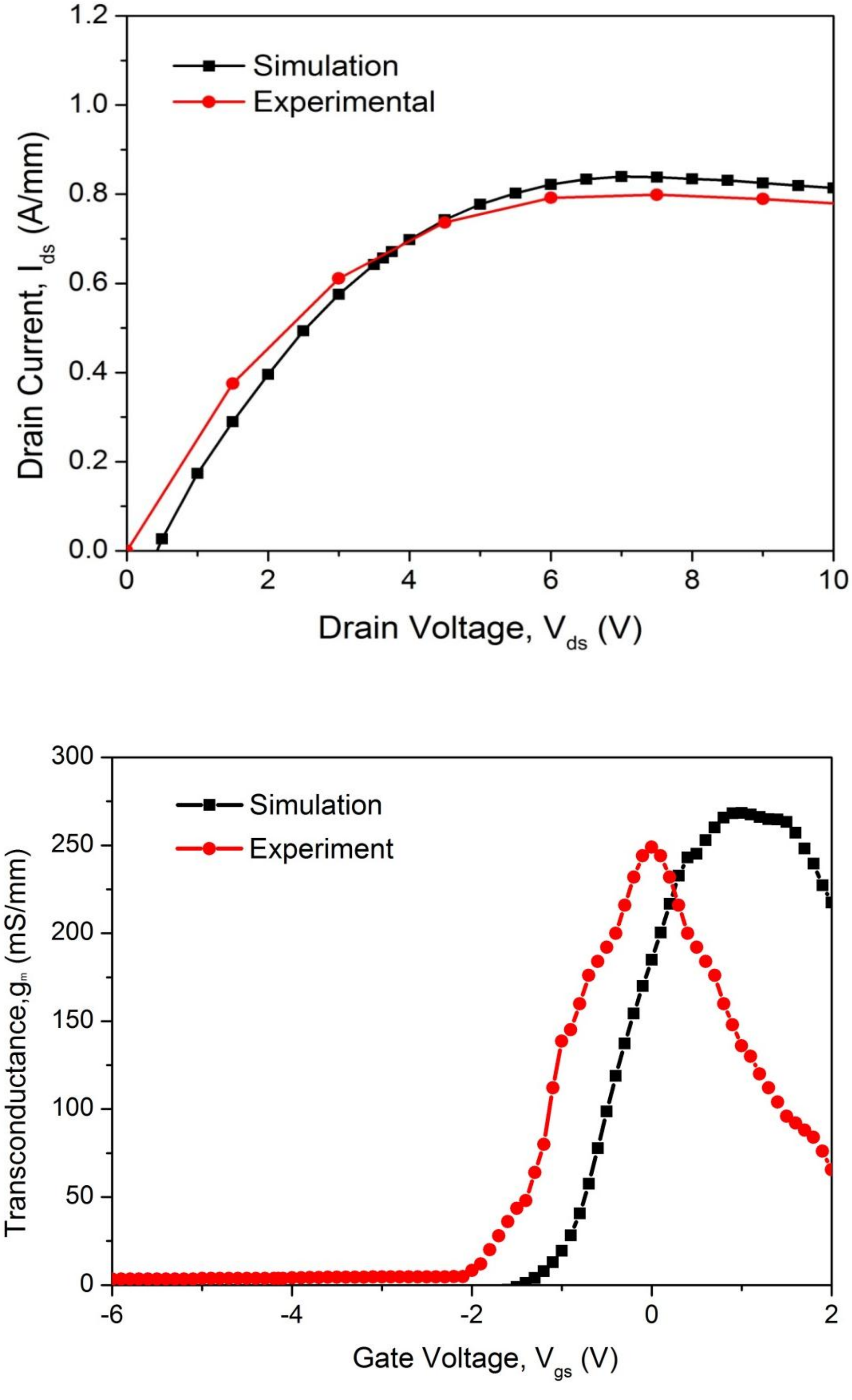

Figure 4.29: Drain Current and Transconductsnce for L_{SD}= 6 µm, L_G= 1 µm for unit gate width devices

4.4 Summary and Concluding Remarks

The AlGaN/GaN structures grown by MOCVD technique were used for the fabrication of AlGaN/GaN HEMT. The active region of the device was defined by two techniques. First was mesa etching by using different ratio combination of BCl_3/Cl_2/Ar gases based RIE. The second technique was the isolation using ion implantation by damaging the region using 3 and 4 energies with different ion dosage. The optimized value of sheet resistance was highest (970 Ω/square) for isolation using the 4E N^+ implant with RIE. Isolation technique involving RIE as well as 4 E N^+ ion implantation provided better isolation. For both 18 nm and 25 nm AlGaN structures, pre-metallization surface treatments using HCl:DI (1:1) for 5 min and BOE for 1 min were performed. Specific contact resistance (r_c) values of 2.6×10^5 Ω-cm^2 for HCl: DI and 4.3×10^5 Ω-cm^2 for BOE were obtained for 18 nm AlGaN structures. For 25 nmAlGaN structures, Specific contact resistance (r_c) values of 0.8×10^5 Ω-cm^2 for HCl: DI and 5.2×10^5 Ω-cm^2 for BOE were achieved. Pre metallization surface treatment done using HCl: DI gave the lowest specific contact resistance for both the AlGaN structures. After isolation, the Ohmic contacts are formed by evaporating Ti/Al/Ni/Au metal layers followed by annealing at 830 °C for 30 sec in RTA. The ohmic contact stack ratio of Ti/Al/Ni/Au (1:5:2:2.5) delivered a very low ρ_c of 6×10^{-6} Ω-cm^2. Irrespective of the type of epitaxial structure, HCl: DI treatment was found to be the best for native oxide removal. The Ni/Ti/Au mettal stack have been used for the deposition of schottky gate contacts with length L_G= 1-5 μm. Interconnection pads were formed using of Ti/Au metal layers. Devices were passivated using SiO_2 and Si_3N_4 dielectric layers of thickness 100 and 150 nm. The Si_3N_4 (150 nm) proved to be a better dielectric material than the SiO_2.

The maximum drain current of 0.53 A/mm was obtained for the device with dimensions L_{SD}= 6 μm, L_G= 1 μm and at $V_{gs} = 0$ V for the unit gate width device with gate length of ~1 μm and source to drain spacing of 6 μm. The pinch-off voltage of the device is – 1.7 V. The transconductance value of 47 mS/mm was obtained for the device (L_{SD}= 50 μm, L_G= 2 μm, unit gate width).

CHAPTER 5

GaN HEMT based Electrochemical Biosensor

In this chapter, we are reporting the fabrication and characterization of AlGaN/GaN HEMT based pH and salinity sensor.

5.1 Introduction

AlGaN/GaN HEMTs has been enormously proficient for chemical, gas, liquid and biosensing application [6]–[8], [100], [206] because of its remarkable properties like low toxicity, chemical stability, and superior conductivity on account of the high saturation velocity and high sheet carrier concentration of the two-dimensional electron gas (2DEG) layer in the AlGaN/GaN heterostructure [9]–[12]. GaN-based wide band semiconductors can be activated at elevated temperature (750^o C) without degradation in performance. These devices have an ability to detect low current levels than conventional Si-based devices. The adequacy of high-temperature operations empowers the devices to be advantageous in the applications in harsh environments [150]. A variety of chemical, gas, and biosensor in perspective of HEMT technology has been worked at elevated temperatures [151]–[153], [207]. For the gas sensor, long-term stability and high-temperature operation are the prime necessities. For example, in a hydrogen gas sensor hydrocarbons are dissociated by synergist metals barely at raised temperatures. The Si-based gas sensor has a state of control to be worked underneath 250 ^oC, restricting them from being utilized as hydrocarbon finders or for different usage involving working at high-temperature. In this way, semiconductor devices in light of AlGaN/GaN heterostructures have incredible potential for sensor application in extreme environments.

Moreover, electrochemical biosensors fabricated from the GaN material are mainly of great importance in various biomedical applications where pure DI and salt free water is required [13]. Even in the space applications where recycled water is used, these devices become very promising and conceivable to discriminate between fluids with dissimilar polarities. A standout amid the most used pH measurement electrochemical sensor is the ISFET based sensor [4]. These devices contrast with the conventional FET in the absence of the gate electrode. In ISFETs, the gate region is sensitive to charging effects, and a reference electrode is needed to bias the gate region above the threshold voltage to let the carriers to flow across the channel area. On the other hand, HEMTs do not require a gate voltage to turn ON and thus no reference electrode is needed, which becomes a substantial advantage over ISFETs in addition to higher chemical and thermal stability of HEMTs. The examination of the pH reactions over the AlGaN surfaces was recounted by authors in [208], using three-terminal open-gated structure. The likelihood of pH and polar liquid detection using 2 terminal undoped AlGaN/GaN HEMT was also conveyed [209], [210]. The undoped-AlGaN/GaN open-gate HEMT devices are capable of substantial functioning in electrolytes and demonstrate linear sensitivity underneath light conditions [211]. Although, to the best of author’s knowledge, a systematic investigation of the sensing performance of pH response for different pH values and the various molar concentrations of salty liquids on AlGaN/GaN HEMT devices is not much explored yet.

In this chapter, we are presenting the development of the gated AlGaN/GaN HEMTs based pH sensor and salinity sensor. We observe the linear change of current when devices are exposed to the PBS solution of different pH values and the aqueous salt solution of NaCl + DI. The sensitivity of GaN HEMT in different pH solutions and various molar concentrations of aqueous solution have been investigated. On the basis of obtained outcomes, we proposed a model of surface chemical reaction associated with the difference in H^+ and OH^+ ions concentration and their interaction with AlGaN surface.

5.2. Sensor Structure and Fabrication Process

The AlGaN/GaN HEMTs devices were employed for the experiment with an Al composition 0.25 consisted of 2 nm AlN nucleation layer followed by unintentionally doped GaN buffer layer of thickness 2.3 μm, and finally followed by a 18 nm thick layer of n-type $Al_{0.25}Ga_{0.75}N$.

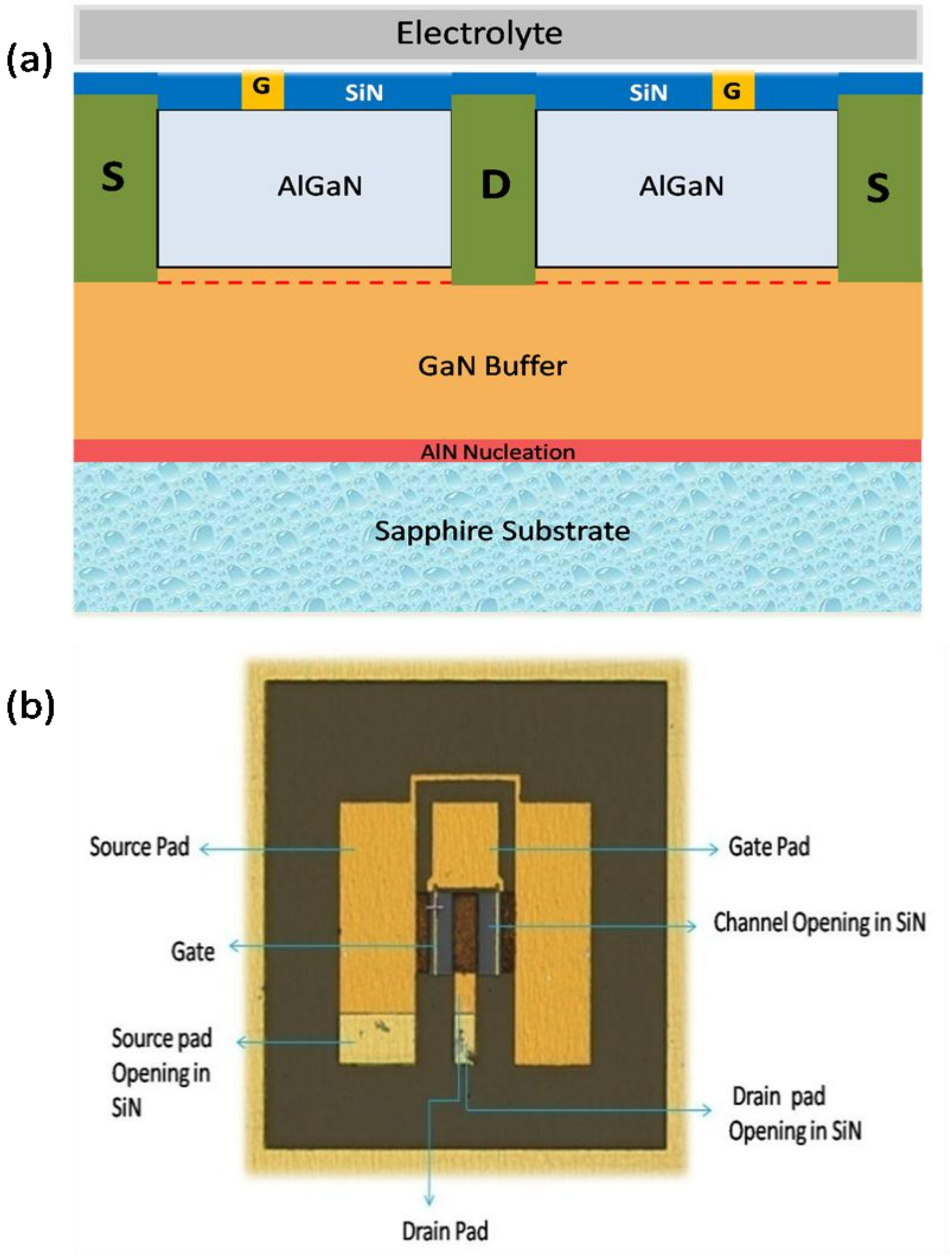

Figure 5. 1: (a) Cross-sectional Schematic illustration of AlGaN/GaN HEMT. The Au-coated gate area was exposed to the electrolyte. (b) Image of fabricated device with given device dimensions W_G= 125 μm, L_G= 1 μm, Source-drain length (L_{SD}=50 μm) and including a 5 nm Au layer in the gate region

The epitaxial layers were deposited by MOCVD growth technique on GaN buffers deposited on sapphire substrates. The device fabrication process started with the device isolation using multi-energy ion implantation technique. The drain and source ohmic contacts were obtained by a photolithography process followed by e-beam metallization Ti/Al/Ni/Au and conventional lift-off techniques [212]. The ohmic characteristics have been achieved by annealing at 830°C in N_2 ambient for 30 sec. Ni-based Schottky contacts with Au as a top layer were used for gate contact. Devices were interconnected using Ti/Au connection lines. The SiN passivation layer using plasma-enhanced chemical vapor deposition (PECVD) of 400 nm thicknesses were deposited to encapsulate the source and drain regions. A small opening for biasing was formed on source-drain pads. Gate and channel region were opened to allow the liquid solutions to cross the surface. A schematic cross-sectional view of the device is demonstrated in Fig. 5.1 (a), though a plan view of the fabricated device layout is depicted in Fig. 5.1 (b).

5.3 AlGaN/GaN HEMT based pH Sensor

To examine the ion concentration and flux density in the cellular fluid are the important errand for biosensors. In the fluids, the more significant part of the electrical procedures could be explained by calculating the change in the H^+ concentration which results in the variation of pH value. Consequently, the pH sensors proved to be a reliable basis for biosensors to facilitate the detection of various reactions occurs in vitro or in vivo.

5.3.1 pH and pH scale

A pH is a unit of measure which illustrates the degree of acidity or alkalinity of a solution. In this solution, solvated protons (H^+) come into view as hydronium ions H_3O^+. The concentration of these ions can alter in a broad range – mostly with magnitudes in between 1 M and 14 M. In some exceptional cases, even higher and lower concentrations can be obtained. The formal definition of pH is the negative logarithm of Hydrogen ion activity. $[H^+]$:

$$pH = -\log([H_3O^+]) \tag{5.1}$$

The pH described like this can be employed to determine pH for diluted solutions of acids and bases in water. For the much-diluted solutions like below 0.001 M, the difference between concentration and activity could be neglected. For highly concentrated solutions, it has to be taken into account and then the pH can be outlined as:

$$pH = -\log(a_{H_3O^+}) \tag{5.2}$$

The so characterized pH is described “thermodynamic pH” rather than “concentration pH” (equation 5.1) and all pH meters measure it as consequence of the Nernst equation. To obtain a better understanding to the pH scale, it is meaningful to keep in mind few pH magnitudes (Table 5.1). The pH definition empowers to set up the pH scale. In water solutions, the pH is constrained in the scale 0 – 14, whereas in different solvents pH values can be negative or higher than 14. Aqueous solutions always restrain H_3O^+ and OH^- ions, either from water dissociation or presented bases or acids. In unadulterated water at 25°C, equal numbers of H^+ and OH^- ions are present; the pH is classified as neutral and corresponds to magnitude 7. Solutions having more H^+ ion concentration than OH^- ions have pH value lower than 7 and are identified as acids. A solution containing higher concentration of OH^- ions from those of H^+ has pH value greater than 7 and is known as the base. The pH calculation of a solution is generally attained by comparing unknown solutions to those of known pH. Generally, solutions comprising various ions are in a state of equilibrium – all concentrations are invariable and not altering in time. This equilibrium is dynamic, which signifies that the reaction in forward and reverse direction have the similar rate. The equilibrium in the solution is a mixture of water, acid and base can be calculated by employing conventional chemical calculation. Determining such equilibrium forms the basis of pH estimation and from the pH value, the concentration of all other ions in the solution may be found.

Let's assume the acid HA, a base B and their analytical concentrations are C_a and C_b respectively. For the acid ionization reaction

$$HA + H_2O \leftrightarrow H_3O^+ + A^- \tag{5.3}$$

$$K_a = \frac{[H_3O^+][A^-]}{[HA]} \tag{5.4}$$

Table 5. 1: pH values of common substances

Fluids	**pH**
Stomach acid	1.5 to 3.5
Vinegar	2.4
Beer and Wine	4
Black Coffee	5
Milk	6.5
DI Water	7
Blood Plasma	7.34 – 7.45
Secretion of pancreas	8.1
Hand soap	9-10
Household Ammonia	11.6
Bleach	12
Caustic Soda	13

the equilibrium is expressed by the acid ionization constant described as:

For the base ionization reaction

$$B + H_2O \leftrightarrow BH^+ + OH^- \tag{5.5}$$

the base ionization constant is described as

$$K_b = \frac{[BH^+][OH^-]}{[B]} \tag{5.6}$$

Further, frequently utilized parameter to express dissociation, where a dissociation fraction is defined as the ratio of the concentration of dissociated molecules to the concentration of all molecules in the solution

$$f_p = \frac{[A^-]}{C_a} \tag{5.7}$$

It is usually assumed that strong acids and strong bases are fully dissociated. For the majority of practical objectives this is applicable however, due to their finite dissociation constants, in some cases partial dissociation can be observed. All chemical reactions are considered to occur in water and the water itself dissociates into H_3O^+ and OH^- ions

$$H_2O + H_2O \leftrightarrow H_3O^+ + OH^- \tag{5.8}$$

This reaction relates dynamic equilibrium among hydronium ions, hydroxide ions and water molecules. The equilibrium constant for this proton transfer reaction is called water equilibrium constant K_W defined as:

$$K_w = [H_3O^+][OH^-] \tag{5.9}$$

Taking the logarithm of both sides of equation (5.9):

$$\log(K_w) = \log([H_3O^+]) + log([OH^-]) \tag{5.10}$$

or, using the definition of equation (5.1) in “p” notation:

$$pK_w = pH + pOH \tag{5.11}$$

5.3.2 Nernst Law

As stated above, the thermodynamic pH could be determined, and this is a straight outcome of the Nernst law. The Nernst equation illustrates the potential in an electrochemical cell as a function of concentrations of ions taking part in the reactions:

$$E = E_o - \frac{RT}{nF}\ln(Q) \tag{5.12}$$

Where, Q is the concentration or activity quotient, n is the number of exchanged electrons, and F is the Faraday constant. For a given temperature, the expression RT/F has a constant value. To make the calculations more straightforward, it was often combined with a conversion factor between natural logarithm (ln) and decimal logarithm (log) resulting in a value of 0.0591 for 25°C.

Most ion sensors are potentiometric sensors that are the electrical potential difference $\Delta\phi$ at a solid/liquid interface as a function of the ion concentration is measured. In this case, the Nernst equation can be written:

$$\Delta\emptyset = \frac{RT}{F}\ln(a_{Me^+}) \tag{5.13}$$

Where, a_{Me} is the activity of one type of ions. In this case, the maximal potential difference for a pH electrode is 59 mV/pH [213], [214].

5.3.3 Buffer Solution

A solution capable of maintaining constant pH in spite of small measures of acid (H^+ ions) or base (OH^- ions) added are called buffers. It can likewise be characterized as a solution of reserve acidity or alkalinity which opposes the difference in pH upon the expansion of the small measure of acid or alkali. Their resistance to alteration in pH formulates buffer solutions exceptionally valuable for many biochemical procedures. The standard buffer for a specific pH has a pKa equivalent to the pH required, while a solution of this buffer would hold equal amounts of acid and base and remain in the middle of the range of buffering capability. Buffer solutions are essential to keep the accurate pH of enzymes in various being to work. Several enzymes only operate under very precise conditions; if the pH drifts too far out of the periphery, the enzymes get sluggish or quit functioning and can denature, consequently permanently hinder its catalytic action. A buffer solution of carbonic acid (H_2CO_3) and bicarbonate (HCO_3^-) is imparted in blood plasma, to sustain a pH between 7.35 and 7.45. Scientifically, buffer solutions are employed as a part of fermentation progression and in aligning the precise requirements for dyes utilized as a part of shading textures. They are additionally utilized as a part of chemical investigation and calibration of pH electrodes or sensors.

Conventional buffers include solutions of weak acids and its conjugated bases being foremost species. Slight extra measures of acids or bases addition are consumed by the buffer and the pH variations just marginally. If there should be an occurrence of high or low pH, only solutions of strong acids or bases are used. For instance, if there should arise an occurrence of pH = 1, the acid concentration is reasonably high (0.1 M) and minute accumulation of acid or base cannot modify the pH of such solution considerably. To determine the pH of buffer solutions containing together with acids and conjugated bases, the acid ionization constant marked out in equation (5.4) is used in the logarithmic form:

$$log\ k_a = log[H_3O^+] + log\left\{\frac{[A^-]}{[HA]}\right\} \tag{5.14}$$

Multiplying both sides of the equation by -1 allows the use of pKa and pH instead of log Ka and log [H3O$^+$] and equation (5.14) can be rewritten as:

$$pk_a = pH - log\left\{\frac{[A^-]}{[HA]}\right\} \tag{5.15}$$

This equation is known as Henderson-Hasselbalch equation (or buffer equation) which can be utilized to compute the pH of solutions having pairs of acids and conjugate bases, for example HA/A^-, HA^-/A^{2-} or B^+/BOH. The Henderson- Hasselbalch equation is generally used to evaluate the pH of the solution produced by incorporating known measures of acids and conjugate bases or by neutralizing acids along with strong bases.

Phosphate buffered saline (abbreviated as PBS) is a buffer solution frequently employed in biological research and experiments. It’s a salty solution restraining sodium chloride, sodium phosphate, and (in a few formulations) potassium chloride and potassium phosphate. The buffer facilitates to sustain an invariable pH. The osmolarity and ion concentrations of the solution generally coordinate to those of the human body (isotonic). PBS has several uses since it is isotonic and non-toxic to cells. It can be utilized to dilute substances. It is employed to rinse containers holding cells. PBS can be used as a diluent in techniques to dehydrated biomolecules, as water molecules surrounded by it will be constructed around the substance (protein, for instance) to be ‘dried’ and immobilized to a solid surface. The thin film of water that ties to the substance counteracts denaturation or other conformational transformations. Carbonate buffers might be utilized for the similar reason yet with fewer adequacies. PBS can be used to take a reference spectrum when evaluating the protein adsorption in ellipsometry. There are a wide range of methodologies to formulate PBS. A few methods exclude potassium, whereas others contain calcium or magnesium. A standout among the most well-known preparations is portrayed underneath.

To prepare 1 liter of 1X PBS, follow the given steps:

1. Take 800 ml of distilled water
2. Add 8 g of NaCl
3. Add 0.2 g of KCl
4. Add 1.44 g of Na_2HPO_4
5. Add 0.24 g of KH_2PO_4
6. Adjust the pH to 7.4 with HCl
7. Add distilled water to a total volume of 1 liter

Finally, a standard buffer solution from which fixed pH of 4, 7, and 10 was exercised for the characterization and calibration of the AlGaN/GaN HEMT sensors. These buffer solutions with known settled pH counts are the base for the characterization and the calibration of the sensors.

5.4 Measurement Setup for Sensor Characterization

Fig. 5.2 demonstrates an electrochemical measurement circuit comprising a Keithley IV characterization system, micropipette and a packaged HEMT device.

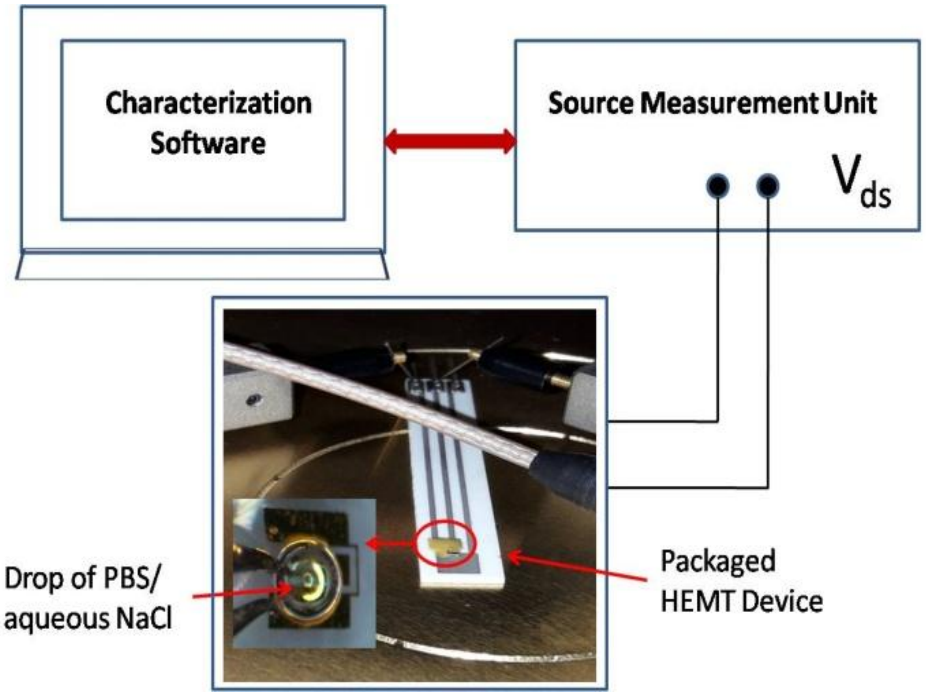

Figure 5.2: Schematic of the measurement setup, drain and source terminals are connected to the I-V measurement system

The GaN HEMT devices were exposed to a drop of the electrolyte on the gate and channel area using 2 µL micropipette. This device was passivated for the sensing purpose applying the dielectric material. Source-drain pads and channel areas were structured in the passivation layer for sensing**.** All these measurements were performed at a constant temperature. For *p*H-sensing measurements, we used phosphate buffer saline (PBS) of different pH values as an electrolyte. The *p*H values in solutions were measured using a digital *p*H meter. For salinity sensing, we used de-ionized (DI) water and molar concentrations (1 M to 1 fM) of NaCl. All measurements in solutions were performed at room temperature.

5.4.1 I-V Characteristics of HEMT Devices in De-Ionized Water

Fig. 5.3 shows typical drain *I-V* characteristics of the HEMT device exposed to air and in the DI water. A minor change in the output drain current was recorded when HEMT device was exposed to DI water. Ionic constituents were not present in the DI water, but even if we started with deionized water, it could pick up a few ions from a container or environment.

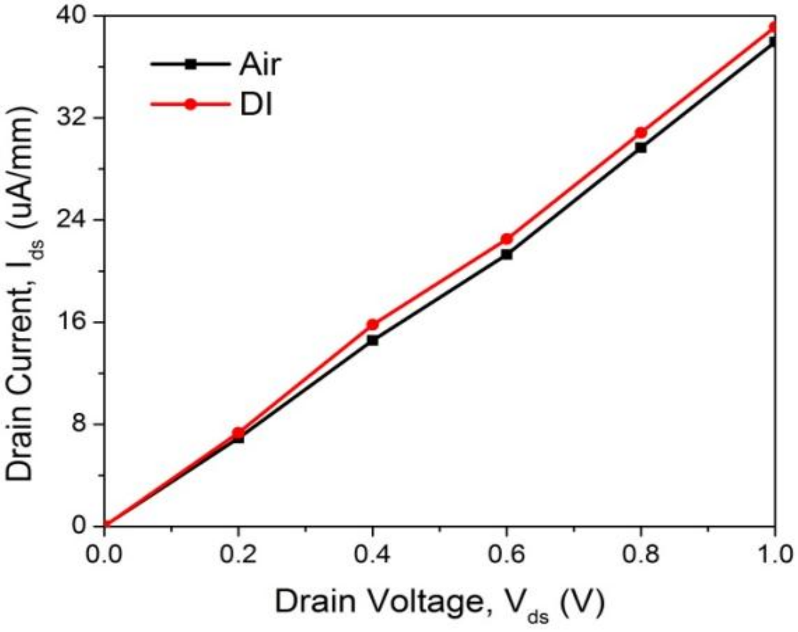

Figure 5.3: Output I–V characteristic of HEMT structures exposed to air and DI at V_{ds}= +1 V and V_g= 0 V for unit gate width devices with L_{SD} = 50 µm

The polarity of the charge depends on whether that particular surface mainly gives off negative or positive ions. Thus, there was being variation in the magnitude of drain current.

5.5 AlGaN/GaN HEMT pH Sensor Characterization

The top layer (Au) gate contact acts as a functionalization layer for AlGaN surface. In this case, the potential barrier between AlGaN and electrolyte was significantly reduced as compared to the potential barrier between Gold and electrolyte, as appeared in Fig. 5.4.

This prompts higher sensitivity of gate potential relating to change in pH of the electrolyte. At a specific pH value, the variation in the potential for the case with gold and electrolyte layer was higher than the variation in the potential for the case without the electrolyte layer.

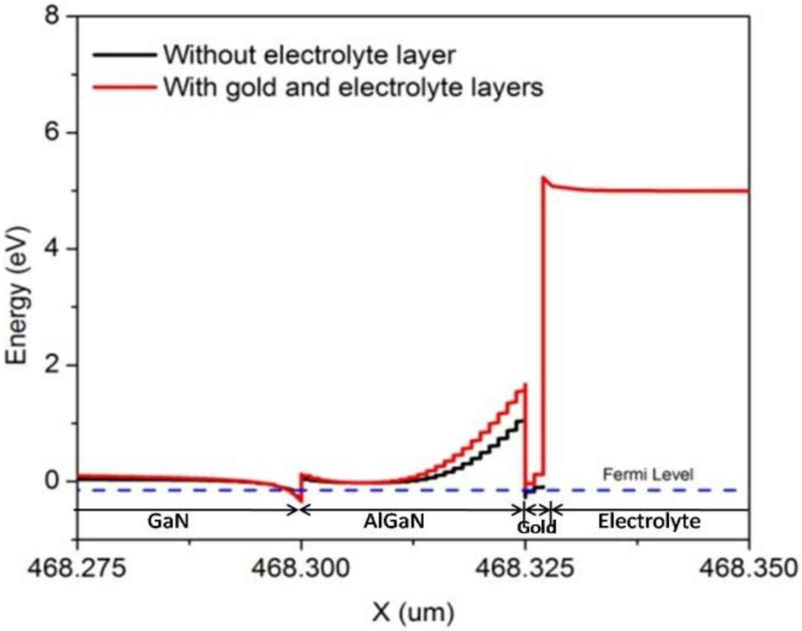

Figure 5. 4: Conduction band energies for two cases – with Gold + electrolyte layer and without electrolyte layer Vs depth (µm) showing variation in energy level

pH is a degree of acidity or alkalinity of a solution despite the fact that through definition it's a selective estimation of H^+ ion movement. In the acidic zone, the lesser pH values demonstrate elevated H^+ concentration whereas, in the basic zone, the increased pH indicates higher OH^- level. In this investigation, a phosphate buffer saline (PBS) was employed as an electrolyte. The pH of this solution was adjusting to specific pH values within the range of 4 to 10, verified by means of digital pH meter.

Fig. 5.5 demonstrates the change in drain current (I_{ds}) versus drain voltage (V_{ds}) for pH 4, 7 and 10. These characteristics were drawn at the biasing condition drain to source voltage, V_{ds}= +1V and gate voltage, V_g= 0 V for 2 finger HEMT device of gate width, W_g= 125 µm with gate length, L_G= 1 µm and source to drain length, L_{SD}= 50 µm. It was examined that the drain current dropped off with pH values. We achieved a significant variation in the drain current.

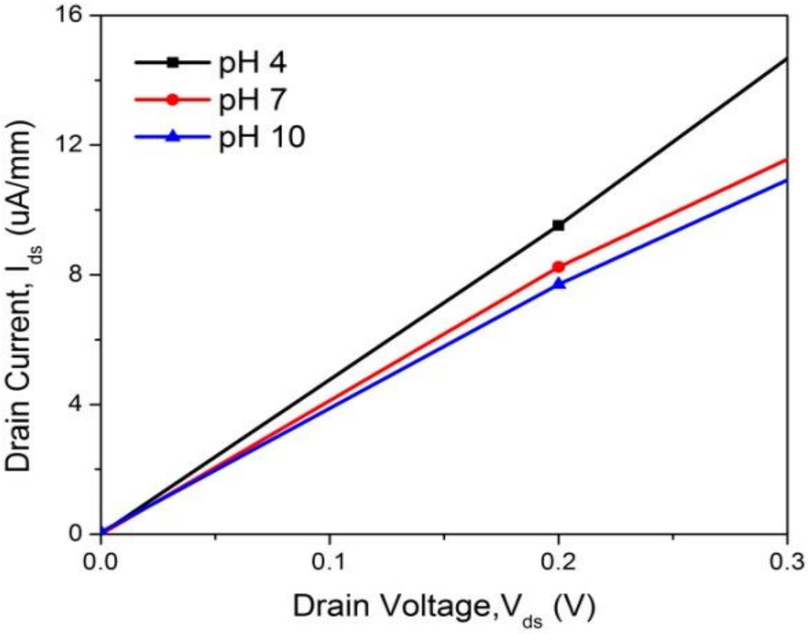

Figure 5.5: Output characteristics of the GaN HEMT in PBS of different pH values at V_{ds}= (0-0.3V) and V_g= 0 V for unit gate width devices with L_G=1 µm and L_{SD} = 50 µm

The possible mechanism of which change in potential at AlGaN/Au and Au/electrolyte surface related with H^+ concentration could be demonstrated by the site binding model developed by Yates et al. [215], [216]. As stated by this model, hydroxyl groups (MOH: M represents Si or metals) at the surface behaved as amphoters. They could be dissociated to or unite with H^+ ions be dependent on the H^+ concentration and the equilibrium constants for the related reactions, in this way.

$$MOH \leftrightarrow MO^- + H^+ \tag{5.16}$$

$$MOH + H^+ \leftrightarrow MOH_2^+ \tag{5.17}$$

Increasing H^+ concentration surface tends to be more positively charged at the surface because of protonized hydroxyls (MOH_2^+) formation, and 2DEG concentration increases with the intention of balance the induced positive charge on the surface. Fig. 5.6

demonstrates the change in drain current (I_{ds}) versus pH for pH 4, 7 and 10 at V_{ds}= +1 V and V_{ds}= + 0.3 V.

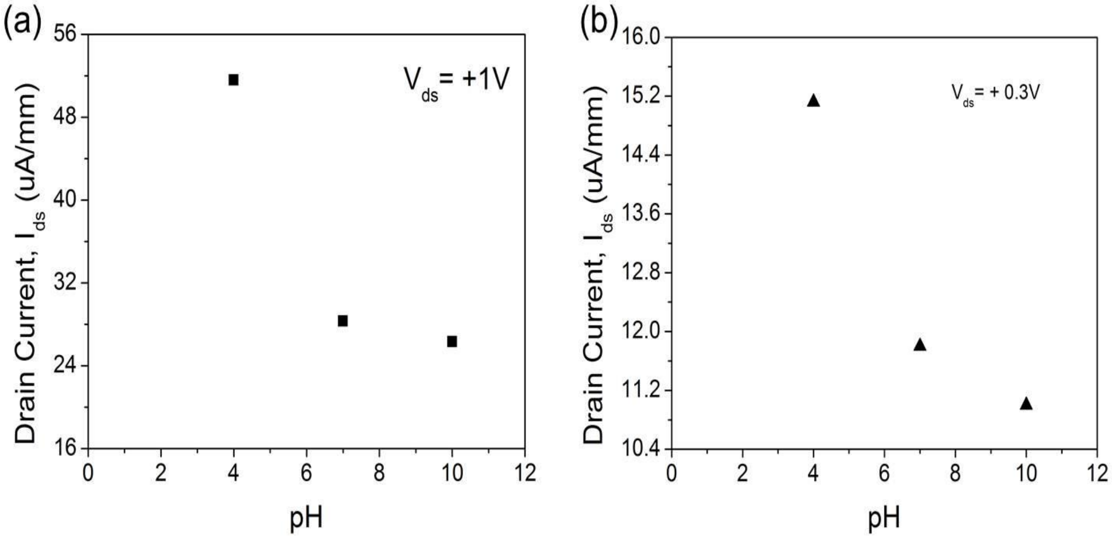

Figure 5. 6: Drain current measured under (a) V_g= 0 V and V_{ds}= +1 V as a function of the pH value (b) V_g= 0 V and V_{ds}= +0.3 V as a function of the pH value

The opposite situation happens by decreasing H^+ concentration. The H^+ concentration decreases in solution caused negative charges at the insulator surfaces owing to the deprotonized hydroxyls (MO^-). This would bring about the pH reliant net charge at the insulator surfaces and the liquid-solid interfacial potential thus abide by the Nernst equation.

5.5.1 Sensors Sensitivity

The crucial parameter for the characterization of AlGaN/GaN HEMT sensors is its sensitivity to the pH value. The GaN-based pH sensors were acknowledged and the high sensitivity to hydronium ions was reported [102]. As indicated by the reported outcomes, the sensor's sensitivity can be characterized as modification of the surface potential Ψ_0 in reliance to the concentration of hydronium ions in the electrolyte:

$$S = \frac{\Delta\varphi_0}{\Delta C_{H_3O^+}} \qquad (5.18)$$

To have the capacity to decide the pH sensitivity, it is essential to evaluate its output characteristic I_{ds} versus V_{ds} for no less than two dissimilar calibrated buffer solutions with already noted pH counts. In Fig. 5.6, the output characteristics in buffer solutions (pH 4, 7, 10) of a sensor with an active region of gate width W_g= 125 µm and L_{SD}= 50 µm (125 x 50 µm²) have appeared. At this point, the output characteristics are noted by a variation in drain-source current I_{ds} as an element of the open gate potential, whereas the source contact is coneected to ground. Accordingly, the concentration of ions describes the surface potential Ψ_0. The change in ion concentration in the buffer solution would reflect the difference in the surface potential. This regulates the sheet carrier concentration and hence, the current I_{ds}. The surface potential is comparable to a series voltage to the gate voltage. Thus, the drain characteristic is altered with the modulation in surface potential.

If the change in current upon pH value was recorded at a constant voltage the sensitivity could be explained as:

$$S_{pH} = \frac{\Delta I_{ds}}{\Delta pH} \tag{5.19}$$

The sensitivity (µA/mm-pH) of the HEMT devices was commonly described as the change in the drain current per pH unit ($\Delta I_{ds}/\Delta pH$). This sensitivity was measured at a single bias condition. The sensitivity parameter was subjected to the bias conditions of the device along with the device dimensions. Huang et al. [217] indicate experimental outcomes that exhibit an increased sensitivity of drain current upon increment in the drain bias. Utilizing above equations, the sensor's sensitivity whose drain characteristics are depicted in Fig. 5.5 and Fig. 5.6, is computed. Considering the case pH count from 4 to 7 sensitivity S_{pH} = 7.783 µA/mm.pH and for the run pH 7 to pH 10, S_{pH} = 0.66 µA/mm.pH at V_{ds}= 1 V was calculated. All the investigations were conducted at room temperature. For the similar sensor, the sensitivity was additionally analyzed for different V_{ds} (Fig. 5.7). Clearly, for this sensor the sensitivity in the acidic region was higher than in the basic locale. It is an extreme illustration, where acidic and alkaline solutions instigate effectively different sensitivities.

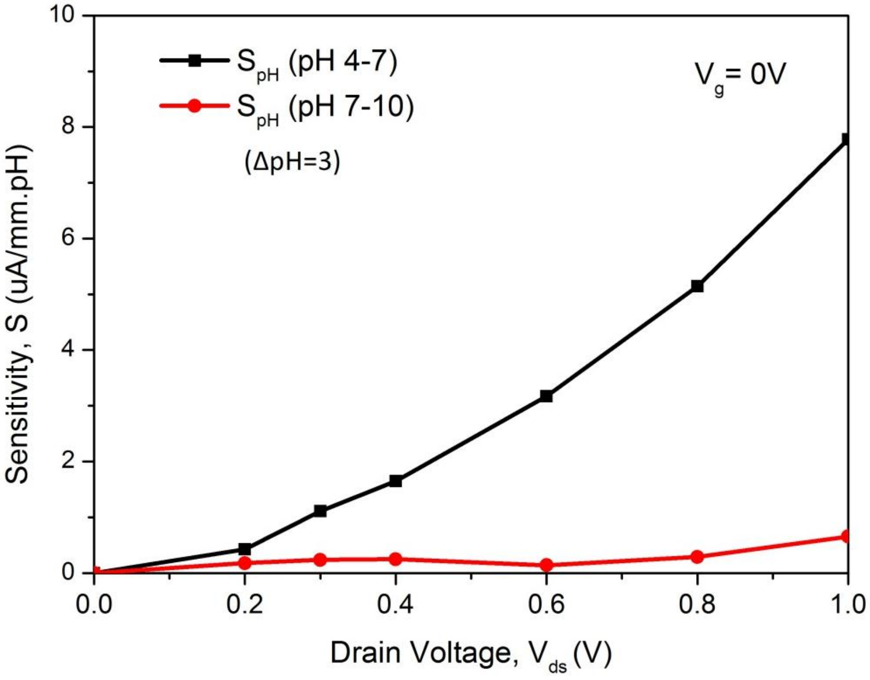

Figure 5.7: Sensitivities S_{pH} in µA/mm.pH at different V_{ds} for GaN HEMT sensor

It ought to be specified that the samples have diverse carrier densities in the confined 2DEG, and the consequent field in the barrier layer depending on the different pH level may influence the surface potential and, hence, the charge equilibrium. To calculate the sensor response of overall heterostructures and used geometry, a sensitivity of 4.32 µA/mm.pH was obtained for the GaN HEMT sensors.The general tendency of expanded sensitivity in steady voltage operation (Fig. 5.7) with rising V_{ds} was initiated by the ohmic conduct of the 2DEG channel. Isolating the sensitivity in µA/mm.pH by the respective V_{ds}, and a relative variation is also presented. Previous reports on the sensitivity of GaN HEMT devices were detailed in table.5.2. The experimental results of this work provided sensitivities of 0.7 µA/mm-pH at V_{ds}= 0.3 V and 4.32 µA/mm-pH at V_{ds}= 1 V, as illustrated in Fig. 5.6. The sensitivity we obtained is lower than the reported results. This particular structure which we used for the pH detection has Au layer over the gate region. Here we are then covering the Au gate with electrolyte, which appears to reduce the interactive with the H^+ and due to the large leakage current sensitivity couldn't be achieved as commonly reported in the literature. Suppression of current leakage by improving the device preparation and use of GaN cap layer to better trap H^+ at the surface is likely needed to improve the device performance. The sensitivity of saline sensor was analysed, indicating an efficient variation in potential at the AlGaN surface.

Table 5.2: Comparison of AlGaN/GaN HEMT based pH Sensor

S. No.	**Sensitivity (μA/mm-pH)**	**Gate Length, L_G (μm)**	**V_{DS} (V)**	**V_{GS} (V)**	**References**
1	123	1	0.25		[100]
2	80	10	0.2	-0.5	[208]
3	3880	40	5	0	[218]
4	4.32	1	1	0	Our Work
5	0.7	1	0.3	0	Our Work

It is clearly evident from the comparison that the fabricated GaN HEMT based pH sensor is proficient of steady operation in aqueous electrolytes and exhibits promising sensitivity compared with previously available reports and our device can be a potential candidate for future biomedical and space applications.

5.6 AlGaN/GaN HEMT based Salinity Sensor

Next, we investigated the sensitivity of GaN HEMT device to saline liquid. NaCl is a strong electrolyte compound, which is almost 100% dissociated in solution. This implies almost every sodium chloride equation unit based on sodium ions encompassed in water molecules and chloride particles surrounded by water atoms. We can express above phenomenon by given equation:

$$NaCl(s) \rightarrow Na^{+}(aq) + Cl^{-}(aq) \tag{5.20}$$

We prepared a solution with the various molar concentration of NaCl in DI water. The molar mass of NaCl is 55.44 g/mol. One molar (1 M) concentration indicates that the 0.58 g of NaCl per 10 ml of DI water. The output drain current in the linear bias region was measured for 1 M to the 1 fM concentration of aqueous NaCl. The percentage change in drain current was decreased with the decrease in molar concentration of salt in solution. At a drain bias of 1 V, there was variation in drain current of 0.76% in the DI water, 52.5% for 1 mM, 33.3% for 1 µM, 15.8% for 1 nM and 1.5% for 1 pM solution and 0.8% for 1 fM was obtained as shown in Fig. 5.8.

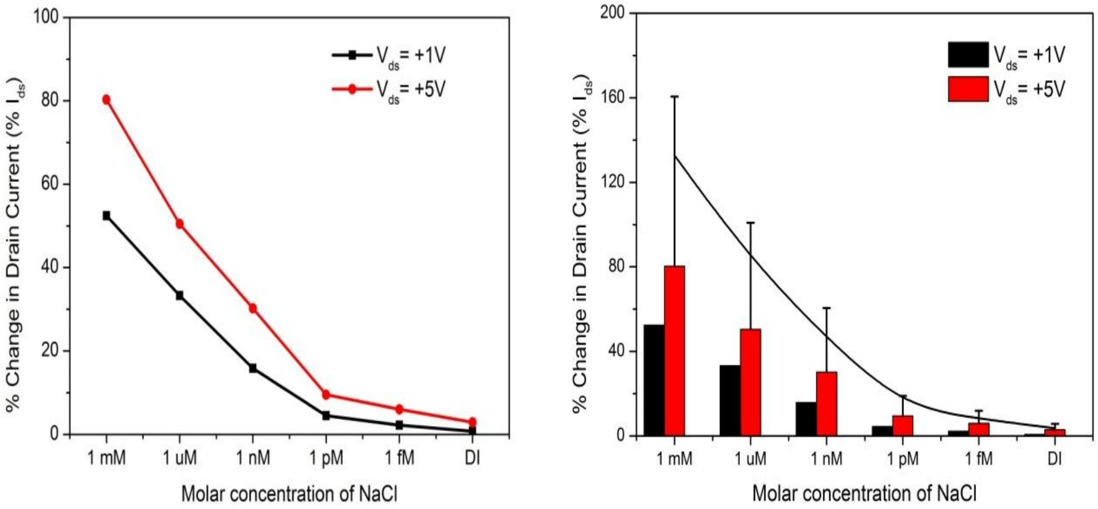

Figure 5.8: % Change in Drain current, ΔI_{ds} Vs different molar concentration Of NaCl at V_{ds}= + 1 V and V_{ds}= + 5 V

The possible mechanism for the drain current reduction related to the variation in molar concentration of salt in DI water or the polar liquid molecules on the AlGaN/GaN surface could be explained by equilibrium reactions of hydroxyls ions at the AlGaN surface concerning H^+ in a solution as represented in Fig. 5.9. It could be confirmed that these molecules were bonded by van der-Waals type of interactions and they may result in variation in the surface potential that was tempted by polarization in the AlGaN/GaN heterostructure. This advanced modification in the induced electron density in 2DEG that exists underneath the AlGaN/GaN interface. The amount of ionic constituents Na^+ and Cl^- ions was higher in case of 1 mM concentration.

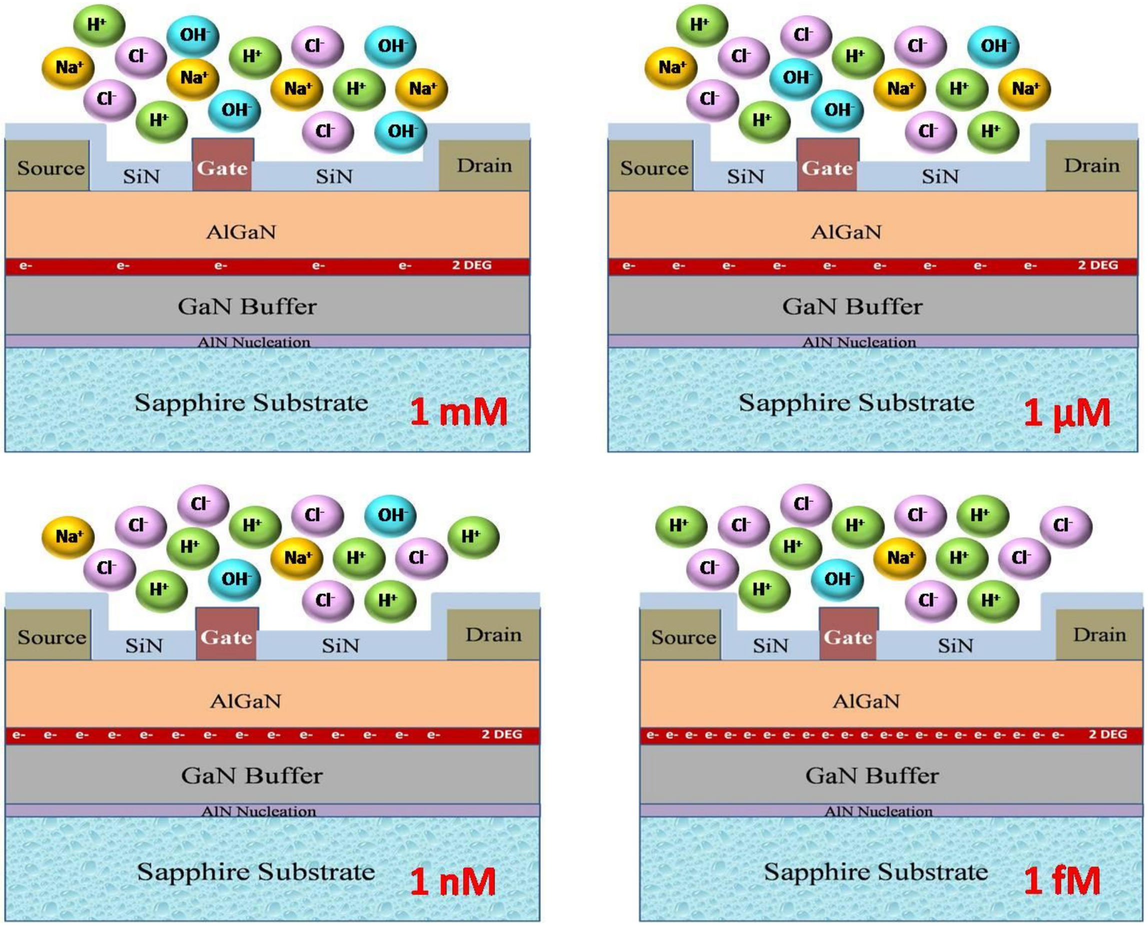

Figure 5.9: Effect of the presence of ions in electrolyte initiates the modifications to the net potential of devices.

The concentration of OH^- ion was dominant in this case. On the other side concentration of H^+ ions were high in 1 pM solution. Thus, the surface potential became positive and drain current was improved and channel resistance turned out to be down. Device Sensitivity 6.48 mA/mm-molar was recorded at $V_{ds}= +1$ V and $V_g= 0$ V for unit gate width devices with $L_{SD}= 50$ µm. These outcomes indicated the significant sensitivity of the HEMT structures to the comparatively minute difference in the concentration of the salt in a solution.

Another important parameter of the sensor was the response time, which marked out as the time needed to achieve 90% of the final value.

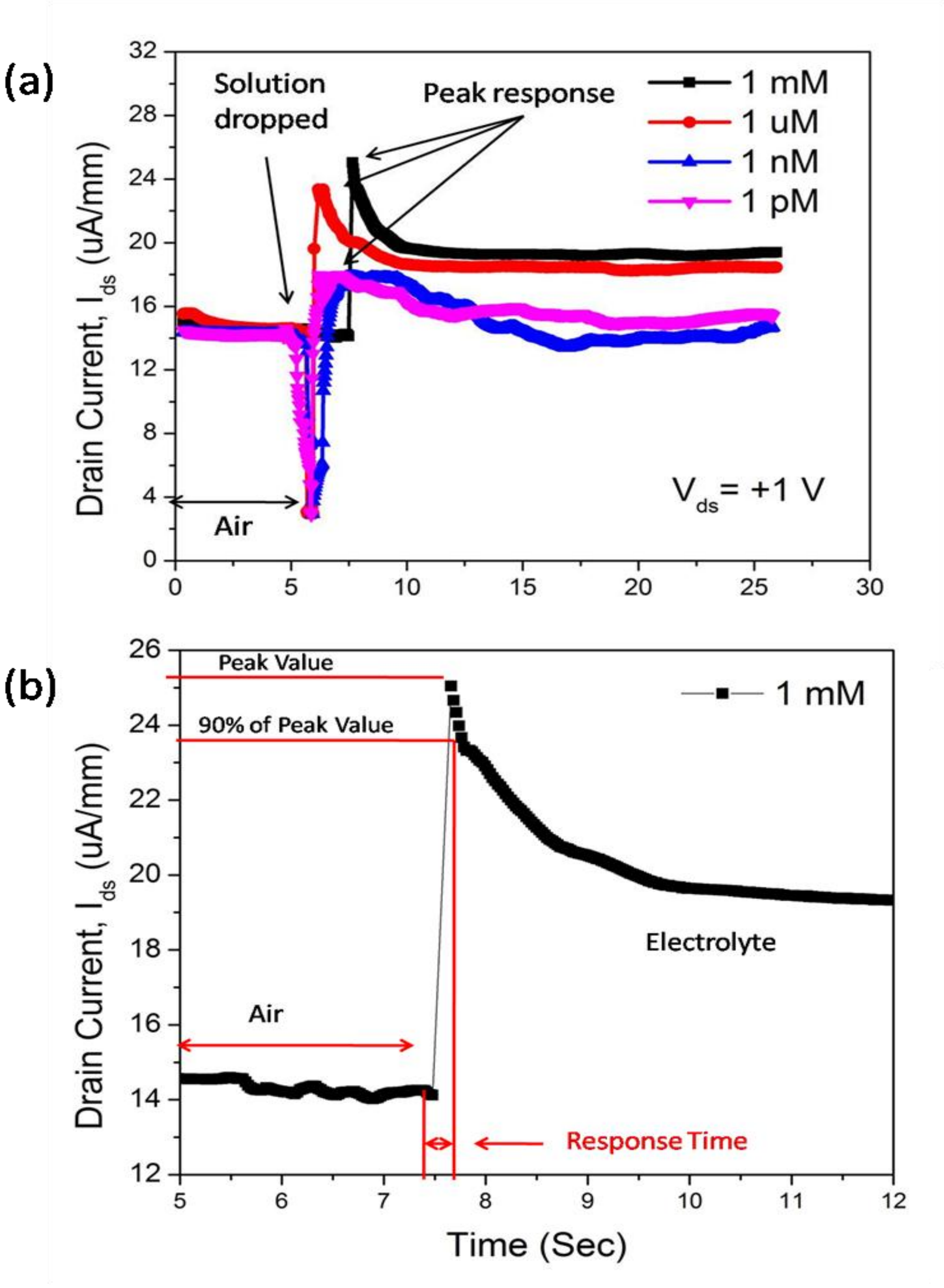

Figure 5.10: Transient response of drain current, (I_{ds}) as a function of the molar concentration value.

To explore the transient characteristics of the AlGaN/GaN HEMT, we carried out time-dependent measurements of I_{ds} under V_{gs}= 0 V and V_{ds}= 1 V (revealed in Fig. 5.10). The response time was estimated to be 250–350 ms which seems to be limited by the intrinsic device response changing from air to salt in solution.

5.7 Summary and Concluding Remarks

The realisation of reference free electrode measurements is extremely important to keep AlGaN/GaN FET devices small, robust and compatible with on-chip development; the objective is to replace existing glass electrode based pH and ion sensing. In this chapter, sensing characteristics of AlGaN/GaN HEMT structures were investigated in PBS of different pH and aqueous NaCl solution.

An optimised AlGaN/GaN HEMT structure which we discussed in chapter 4, AlGaN structures (18 nm) unity gate width, pre-metallization surface treatments using HCl:DI (1:1) for 5 min with isolation technique involving RIE as well as 4 E N^+ ion implantation, passivation layer Si_3N_4 (150 nm) and ohmic contact stack ratio of Ti/Al/Ni/Au (1:5:2:2.5) has been used for the sensing purpose.

In DI water, the GaN HEMT demonstrated competent drain I-V characteristics close to I-V characteristics of typical HEMTs when exposed to the air. These devices illustrate the dramatic variation in output drain-source current upon exposure to PBS in the gate region. The sensitivity of 4.32 µA/mmpH at V_{ds}= 1 V and Vg= 0 V was obtained which is smaller than the reported results. Due to the large leakage current sensitivity couldn't be achieved as commonly reported in the literature. Au layer over the gate region was used for the pH detection. Here we are then covering the Au gate with electrolyte which then seems less interactive with the H^+. This large leakage current may be caused by the technical factors rather than any characteristics of the devices. Although there are some imperfections in the device preparation and measurement, the fabricated HEMT devices perform very well in distinguishing the pH levels. Suppression of current leakage by improving the device preparation and use of GaN cap layer to better trap H^+ at the surface is likely needed to improve the device performance. The fabricated device is expected to be suitable for pH sensing applications.

Next, we also reported on the modification in the current with the various molar concentration of NaCl present in DI water. This additionally demonstrated a systematic potential change at the AlGaN surface consequently change in molar concentration of saline liquid is reported which results 6.48 mA/mm-molar sensitivity and response time 250 –350 ms. This fabricated saline sensor looks very promising to detect smaller (femtolevel) molar concentration of salt in the liquid.

CHAPTER 6

Conclusion and Future Work

In this chapter, we have summarized some major findings and outcomes of the thesis. Finally, the future scope of the work is outlined in the end.

6.1 Conclusion

Development of GaN based HEMTs have opened up the new and existing applications in the field of biosensing devices for space and biomedical applications. The realisation of reference free electrode measurements is extremely important to keep AlGaN/GaN FET devices small, robust and compatible with on-chip development; the objective is to replace existing glass electrode based pH and ion sensing.

In this thesis, a systematic study starting from simulation of GaN based HEMT devices to actual device fabrication have been presented. First, the various performance parameters for AlGaN/GaN HEMTs have been simulated using ATLAS simulator from silvaco international. These kinds of studies can be very helpful to optimize the various device parameters over the tool itself which can reduce the fabrication cost and efforts significantly. After completing tool based study, we moved towards actual fabrication of AlGaN/GaN HEMT devices with their applications in pH and salinity detection. The epitaxial layers were deposited by MOCVD growth technique on sapphire substrates. In order to ensure the enhancement in HEMT device performance, all the devices processing steps were optimized to its best. Various processing parameters such as AlGaN thickness, ohmic contact metal stack and its ratio thickness variation, annealing temperature, isolation parameters, RF power and gas flow rates have been optimized. A systematic investigation on how all these parameters affect electrical properties of GaN HEMT has been presented in detail. Sensitivity and response time of fabricated HEMT devices is also an important concern which is required to be addressed. So a detailed investigation on electrical and sensing characteristics of GaN HEMT sensor has also been done. The work presented in this thesis demonstrates that the fabricated HEMT devices devices illustrate the dramatic variation in output drain-source current upon exposure to PBS in the gate area. We also reported on the modification in the current with the various molar concentration of NaCl present in DI water. This additionally demonstrated a systematic potential change at the AlGaN surface thus changes in molar concentration of saline liquid. Finally, the potentiality of GaN HEMT based electrochemical biosensor various application has been tested. Results confirmed the pH and ion sensing capabilities of GaN based HEMT sensor that can be very useful in variety of space and biomedical applications.

Major Findings and Outcomes

A. Performance Analysis of AlGaN/GaN HEMT: A Simulation Study

In this work, simulation study and performance analysis of GaN based HEMTs have been presented. Different electrical parameters such as energy band diagram, electric field distribution, electron concentration, electron mobility, energy band diagram, output characteristics (I_{ds}-V_{ds}), transfer curve, transconductance (g_m) and gate leakage current (I_g) of AlGaN/GaN HEMTs have been simulated. A detailed simulation of GaN HEMT devices for the optimization of AlGaN and GaN Cap layer thicknesses, followed by an in-depth study of the high temperature and trapping effects on the device performance have been executed.

- For GaN Cap layer thickness variation from 1 nm to 100 nm, drain current was increments with GaN cap layer thicknesses, and eventually saturates at approximately 1.85 A/mm for capping layer thickness greater than 40 nm. The 2D-electron mobility, decrease monotonically with GaN capping layer thickness, and saturate at approximately 830 cm^2/Vs for capping layer thickness greater than ~40 nm. Devices with 10 nm GaN Cap layer gave moderate electron mobility 1050 cm^2/Vs, moderate drain current 1.56 A/mm and peak electron concentration 1.3×10^{19} cm^{-3} at the AlGaN/GaN surface could be recommended for electrochemical sensing purpose. The HEMT devices with a GaN cap layer didn't exhibit gate leakage current.

- For AlGaN layer thickness variation from 5 nm to 30 nm, carrier concentration was first decrease 1.03 x 10^{19}/cm^3 to 6.65 x 10^{18}/cm^3 with AlGaN layer thickness from 5 to 10 nm and after that it increases with the AlGaN layer thickness from 10 to 30 nm. The same trend was followed for electric field distributions. Electron mobility decreases monotonically with AlGaN layer thickness. Highest electron mobility 1354 cm^2/Vs were recorded for the AlGaN layer thickness of 5 nm. The extracted results were in good accord with published experimental data.
- Next, we investigated the effect of variations in gate length (1µm to 5µm) and source to gate length (1µm to 3µm) to choose the most suitable one for electrochemical sensing applications. Downscaling of gate length (L_G) and source to gate length (L_{SG}) enhanced the device characteristics, improving the drain-current (I_{ds}) and transconductance. Reduction in L_G was more effective than the reduction in L_{SG} to influence the biosensor performance. Configuration L_{SD}7µm_L_G1µm_L_{SG}1µm was chosen as the best combination due to highest attainable value of g_m (211 mS/mm) and I_{ds} (1.01 A/mm). That was the result of highest extracted value of C_{gs} (10.210 pF), mobility (1151.5 cm^2/Vs) and electric field (4.36 x 10^5 V/cm) with lowest value of gate leakage current among all these simulated designs. We have fabricated the above mentioned optimized simulated HEMT structure (AlGaN Layer 18 to 25 nm and L_{SD}7µm_L_G1µm_L_{SG}1µm) with some other sets of device dimensions for the experimental work.
- Also focused on 2D hydrodynamic computations of AlGaN/GaN HEMTs for temperatures ranges from 300 K to 600 K. A reduction in drain current, I_{ds} (≈ 52%) was noticed with the increment in temperature from 300 K to 600 K.
- In this work, we also investigated the impact of acceptor traps in the GaN buffer and AlGaN barrier layer on the leakage current and current collapse in the GaN HEMT. The dependency of current collapse and leakage current on the density and energy level of traps have been deliberately contemplated. With the trapping density increasing from 10^{15} cm^{-3} to 10^{18} cm^{-3}, the leakage current was significantly reduced from 80.2% to 1.76% in buffer layer and 95% to 12.6% in

barrier while current collapse increases from 6% to 89.8% in the buffer and 0.3% to 17.5% in the barrier layer. Effect of current collapse and leakage were more noticeable in the buffer layer in comparison to the barrier layer. Further, different energy level 0.75eV, 1.8eV, and 2.85eV of acceptor traps were likewise studied. It was demonstrated that high energy traps induced lower amount of leakage while current collapse was more. Finally, a balanced trade-off amid current collapse and the leakage current has been proposed.

B. Fabrication and Characterization of AlGaN/GaN HEMTs

- Ar^+ based ion implantation and Ar based RIE proved to be an improved technology for device isolation. Ion implantation using 4 energy resulted in increased isolation resistance 0.11×10^6 Ω as compared to 3 energy. Minimum specific contact resistance $\rho = 6.7 \times 10^{-6}$ $\Omega.cm^2$ and contact resistance, R_c =0.6 Ω.mm values were measured on the AlGaN HEMT devices treated with 4 energy. Consequently, output current, I_{ds} = 0.37 A/mm is likewise highest for this combination. In the case of RIE, mixing of Ar in BCl_3: Cl_2 gives higher etch rate. Isolation technique involving RIE as well as 4 E N^+ ion implantation provided better isolation with sheet resistance 970 Ω/square among all the processed combination. Therefore, the Ar addition in the single step etching together with 4 E N^+ ion implant-isolation proved better technique for isolation.
- Ohmic contacts using Ti/Al/x/Au, (x= Cr, Pt, Ni) metal stack were optimized and compared on two different AlGaN thickness 18 nm and 25 nm over GaN HEMTs structures. Ni based metal stack exhibits better surface morphology. Different ratios of thickness of metals (Ti, Al, Ni, Au) in the Ni-based stack were compared to obtain the lowest specific contact resistance (ρ_c) for 25 nm AlGaN structures.. Pre-metallization surface treatment done using HCl: DI gave the lowest specific contact resistance for both the AlGaN structures.

- When comparing the performance of 100 nm SiO_2 and Si_3N_4 layers, the SiO_2 showed better current recovery. On the other hand, for 150 nm of dielectric thickness, the Si_3N_4 proved to be a better dielectric material than the SiO_2.

C. Fabrication and Characterization of GaN HEMT based Electrochemical Biosensor

The sensing characteristics of AlGaN/GaN HEMT structures were investigated in PBS of different pH and aqueous NaCl solution. In DI water, the GaN HEMT demonstrated competent drain I-V characteristics close to I-V characteristics of typical HEMTs when exposed to the air. These devices illustrate dramatic variation in output drain source current upon exposure to PBS in the gate region. A high level of sensitivity 4.32 µA/mm-pH at V_{ds}= 1 V and V_g= 0 V was obtained which is smaller than the reported results. Due to the large leakage current sensitivity couldn’t be achieved as commonly reported in the literature. This large leakage current may be caused by the technical factors like epitaxial design issues and imperfection in the epitaxy. Desoite that fabricated HEMT devices perform well in distinguishing the pH levels at broader scale. Suppression of current leakage by improving the device preparation and focusing on epitaxial design issues are likely needed to improve the device performance. The fabricated device is expected to be suitable for pH sensing applications. Next, we also reported on the modification in the current with the various molar concentration of NaCl present in DI water. This additionally demonstrated a systematic potential change at the AlGaN surface as a result of change in molar concentration of saline liquid. A femto level molar concentration NaCl in DI was also detected by the fabricated GaN HEMT sensor. A minimal concentration of NaCl in DI (femto level molar concentration) was fairly distinguished by the fabricated GaN HEMT sensor. A high device sensitivity of 6.48 mA/mm-molar was recorded at V_{ds}= + 1 V and V_g= 0 V. We also performed transient response of the devices towards change in molar concentration. A quite good response time was retrieved 250 –350 ms. Finally, Table 1 compares various performance parameters of the fabricated AlGaN/GaN HEMT based pH sensor reported in past. It shows from the comparison that the fabricated pH sensor has exhibited good performance and it could become more efficient by focusing on epitaxial design issues. These devices can be a potential candidate with high level sensitivity pH and saline sensors for future biomedical and space applications.

6.2 Future Work

This thesis contributes to the development of AlGaN/GaN HEMT based sensor that can be used in biomedical applications. However, there are multiple problems that still remain to be directed before this device can be successfully commercialized.

- First there is more optimisation to be done and most amicable measure from an engineering perspective would be a scaling down and exhibit array assembly of sensors to operate measurements with high resolution. This progression ought to be trailed by proper pacakaging and passivation to certain the reliable operation of the chip. The advancements introduced in this postulation for reference electrode free, high sensitivity estimation, ought to be incorporated into the future outline elucidations to ensure sensor integration and miniaturization.
- Improved comprehension of the surface chemistry of the AlGaN/GaN compound in fluid media is required. This work just presented the ideas of processing and operation impact on the state of the sensor surface. Further XPS examinations are expected to realize every single conceivable impact of chemicals on the sensor surface. Proposed model of surface chemical response can be additionally supported through further investigation of sensor sensitivity to dipole atom.
- With the above enhancements, AlGaN/GaN electrochemical biosensor can be a reliable tool, particular to a large number of analytes and critical for research into cell culture and cell line functionalisation in addition to detection of different biomarkers.
- In the future one could see the benefits of a design that could consolidate multiple AlGaN/GaN HEMTs onto a single PCB that would empower the testing of various analytes in fluid utilizing some of the analyte-receptor methods.

Bibliography

[1] J. W. P Fromherz, A Offenhausser, and T Vetter, “A neuron-silicon junction: a Retzius cell of the leech on an insulated-gate field-effect transistor,” *Science*, vol. 252, no. 5010, pp. 1290–1293, 1991.

[2] P. Bergveld, “Development of an Ion-Sensitive Solid-State Device for Neurophysiological Measurements,” *IEEE Trans. Biomed. Eng.*, vol. 17, no. 1, 1970.

[3] L. Bousse, N. F. De Rooij, and P. Bergveld,“Operation of chemically sensitive field-effect sensors as a function of the insulator-electrolyte interface,” *IEEE Trans. Electron Devices*, vol. 30, no. 10, pp. 1263–1270, 1983.

[4] J. Chiang, Y. Chen, and J. Chou, “Simulation and Experimental Study of the pH-Sensing Property for AlN Thin Films,” *Jpn. J. Appl. Phys.*, vol. 40, no. 10, pp. 5900–5904, 2001.

[5] P. Bergveld, “Thirty years of ISFETOLOGY What happened in the past 30 years and what may happen in the next 30 years,” *Sensors Actuators B*, vol. 88, pp. 1–20, 2003.

[6] F. Ren, and S. J. Pearton, *Semiconductor Device-Based Sensors for Gas”, Chemical, and Biomedical Applications*. New York: Taylor and Francis Group, Boca Raton London New York, CRC Press, 2011.

[7] M. Stutzmann, G. Steinhoff, M. Eickhoff, O. Ambacher, C. E. Nebel, and J. Schalwig “GaN-based heterostructures for sensor applications,” *Diam. Relat. Mater.*, vol. 11, pp. 886–891, 2002.

[8] N. Sharma, D. Joshi, and N. Chaturvedi, “An impact of bias and structure dependent L $$_\mathrm{SD}$$ SD variation on the performance of GaN HEMTs based biosensor,” *J. Comput. Electron.*, vol. 13, no. 2, pp. 503–508, 2014.

[9] O. Ambacher, B. Foutz, J. Smart, J. R. Shealy, and N. G. Weimann, “Two dimensional electron gases induced by spontaneous and piezoelectric polarization in undoped and doped AlGaN / GaN heterostructures,” *J. Appl. Phys.*, vol. 87, no. 1, pp. 334–344, 2000.

[10] J. Osvald, “Polarization effects and energy band diagram in AlGaN / GaN heterostructure,” *Appl. Phys. A*, vol. 87, pp. 679–682, 2007.

[11] M. Farahmand, C. Garetto, E. Bellotti, K. F. Brennan, M. Goano, E. Ghillino, G. Ghione, J. D. Albrecht, and P. P. Ruden, “Monte Carlo Simulation of Electron Transport in the III-Nitride Wurtzite Phase Materials System : Binaries and Ternaries,” *IEEE Trans. Electron Devices*, vol. 48, no. 3, pp. 535–542, 2001.

[12] S. J. Pearton, J. C. Zolper, R. J. Shul, and F. Ren, “GaN : Processing , defects , and

devices," *J. Appl. Phys.*, vol. 86, no. 1, pp. 1–78, 1999.

[13] E. Caló and V. V Khutoryanskiy, "Biomedical applications of hydrogels : A review of patents and commercial products," *Eur. Polym. J.*, vol. 65, pp. 252–267, 2015.

[14] S. Strite and H. Morkoç, "GaN, AlN, and InN: A review," *J. Vac. Sci. Technol. B*, vol. 1237, no. 1992, pp. 1237–1266, 2016.

[15] O. Ambacher, "Growth and applications of Group III-nitrides," *J. Phys. D Appl. Phys.*, vol. 31, pp. 2653–2710, 1998.

[16] S. R. Choi, D. Kim, S. Choa, S. Lee,and J. Kim, "Thermal Conductivity of AlN and SiC Thin Films," *Int. J. Thermophys.*, vol. 27, no. 3, pp. 896–905, 2006.

[17] H. P. Maruska and J. J. Tietjen, "The preparation and properties of vapor deposited single crystalline GaN," *Appl. Phys. Lett.*, vol. 15, no. 10, pp. 327–329, 1969.

[18] P. Cantu, F. Wu, P. Waltereit, S. Keller, A. E. Romanov, S. P. Denbaars, J. S. Speck, "Role of inclined threading dislocations in stress relaxation in mismatched layers," *J. Appl. Phys.*, vol. 97, no. 2005, pp. 103534–1–103534–10, 2013.

[19] M. Grundmann, *The Physics of Semiconductors - 2006 An Introduction Including Devices and Nanophysics*. Germany: Springer.

[20] V. Potin, P. Ruterana and G. Nouet, "HREM study of stacking faults in GaN layers grown over sapphire substrate," *J. Phys. Condens. Matter*, vol. 12, pp. 10301–10306, 2000.

[21] S. Wei, X. Nie, I. G. Batyrev, and S. B. Zhang, "Breakdown of the band-gap-common-cation rule: The origin of the small band gap of InN," *Phys. Rev. B*, vol. 67, pp. 165209–1–165209–4, 2003.

[22] J. R. Waldrop, R. W. Grant, J. R. Waldrop, and R. W. Grant, "Measurement of AlN/GaN (0001) heterojunction band offsets by xray photoemission spectroscopy," *Appl. Phys. Lett.*, vol. 68, no. 20, pp. 2879–2881, 1996.

[23] I. J. Song, S. K. Lee, K. Lee, S. S. Park, and J. Y. Han, "Properties of Etched Ga- and N-Faces of Freestanding GaN Substrate Using Inductively Coupled Plasma-Reactive Ion Etching," *Jpn. J. Appl. Phys.*, vol. 41, pp. 317–319, 2002.

[24] Y. Wu, A. Hanlon, J. F. Kaeding, and R. Sharma, "Effect of nitridation on polarity , microstructure , and morphology of AlN films," *Appl. Phys. Lett.*, vol. 84, no. 6, p. 912-914, 2004.

[25] E. Monroy, E. Sarigiannidou, F. Fossard, N. Gogneau, and E. Bellet-amalric, "Growth kinetics of N-face polarity GaN by plasma-assisted molecular-beam epitaxy Growth kinetics of N-face polarity GaN by plasma-assisted," *Appl. Phys. Lett.*, vol. 84, no. 18, pp. 3684–3686, 2004.

[26] M. Seelmann-Eggebert, J. L. Weyher, H. Obloh, H. Zimmermann, A. Rar, and S. Porowski, “Polarity of (00.1) GaN epilayers grown on a (00.1) sapphire,” *Appl. Phys. Lett.*, vol. 71, no. 18, pp. 2635–2637, 1997.

[27] C. Wood, D. Jena, *Polarization effects in semiconductors: From ab initio theory to device applications*, Illustrate. Springer Science & Business Media, 2008.

[28] K. Shimada, T. Sota, and K. Suzuki, “First-principles study on electronic and elastic properties of BN , AlN , and First-principles study on electronic and elastic properties,” *J. Appl. Phys.*, vol. 84, no. 9, pp. 4951–4958, 1998.

[29] I. Lee, J. J. Lee, P. Kung, F. J. Sanchez, and M. Razeghi, “Band-gap narrowing and potential fluctuation in Si-doped GaN Band-gap narrowing and potential fluctuation in Si-doped GaN,” *Appl. Phys. Lett.*, vol. 74, no. 1, pp. 102–104, 1999.

[30] A. E. Yunovich, “A model of the ‘yellow band’ defect complex in GaN,” in *Electrochemical Society Proceedings*, vol. 97, 1998, pp. 258–259.

[31] J. P. Ibbetson, P. T. Fini, K. D. Ness, S. P. Denbaars, and J. S. Speck, “Polarization effects , surface states , and the source of electrons in AlGaN / GaN heterostructure field effect transistors,” *Appl. Phys. Lett.*, vol. 77, no. 2, pp. 250–252, 2000.

[32] I. P. Smorchkova, C. R. Elsass, J. P. Ibbetson, R. Vetury, and B. Heying, “Polarization-induced charge and electron mobility in AlGaN / GaN heterostructures grown by plasma-assisted molecular-beam epitaxy,” *J. Appl. Phys.*, vol. 86, no. 8, pp. 4520–4526, 1999.

[33] S. Taking and S. Taking, “AlN/GaN MOS-HEMTs Technology by A thesis submitted in fulfillment for the,” University of Glasgow, 2012.

[34] R. F. Pierret, *Semiconductor Device Fundamentals*, Ist. School of Electrical and Computer Engineering Purdue University, New York, 2006.

[35] M. Germain M. Leys, S. Boeykens, S. Degroote, Wi. Wang, Dominique Schreurs, W. Ruythooren, K-H Choi, B. V. Daele, G. V. Tendeloo and G. Borghs, “High electron mobility in AlGaN/GaN HEMT grown on sapphire: strain modification by means of AlN interlayers.,” *Mat. Res. Soc. Symp. Proc.*, vol. 798, pp. 1–6, 2004.

[36] J. Misiewicz, R. Kudrawiec, M. Syperek, and R. Paszkiewicz, “Investigations of AlGaN / GaN field-effect transistor structures by photoreflectance spectroscopy,” *Microelectronics J.*, vol. 36, pp. 442–445, 2005.

[37] E. Ogawa, T. Hashizume, S. Nakazawa, T. Ueda, and T. Tanaka, “Chemical and Potential-Bending Characteristics of SiN x / AlGaN Interfaces Prepared by In Situ Metal-Organic Chemical Vapor Deposition,” *Jpn. J. Appl. Phys.*, vol. 46, no. 24, pp. 590–592, 2007.

[38] R. Dingle, H. L. Störmer, A. C. Gossard, W. Wiegmann, “Electron mobilities in modulationdoped semiconductor heterojunction superlattices,” *Appl. Phys. Lett.*, vol. 33, no. 7, pp. 665–667, 1978.

[39] R. Vetury, N. Q. Zhang, S. Keller, and U. K. Mishra, “The Impact of Surface States on the DC and RF Characteristics of AlGaN / GaN HFETs,” *IEEE Trans. Electron Devices*, vol. 48, no. 3, pp. 560–566, 2001.

[40] A. P. F. Turner, *Biosensors Encyclopedia of Chemical Technology Concise*, 3-5th edn. New York: Wiley, 2007.

[41] S. Subrahmanyam, S. A. Piletsky, and A. P. F. Turner, “Application of Natural Receptors in Sensors and Assays,” *Anal. Chem.*, vol. 74, no. 16, pp. 3942–3951, 2002.

[42] R. S. Sethi, “Transducer aspects of biosensors,” *Biosens. Bioelectron*, vol. 9, pp. 243–264, 1994.

[43] P. Bergveld, D. R. TheÂvenot, *Advances in Biosensors*. London, UK: JAI Press, London, UK, 1993.

[44] P. S. Bisen, *Laboratory Protocols in Applied Life Sciences*. 2014.

[45] R. P. Buck and E. R. N. Lindneri, “Commission On Electroanalytical Chemistry * Recomendations For Nomenclature Of Ion-Selective Electrodes,” *Pure &App/. Chem.*, vol. 66, no. 12, pp. 2527–2536, 1994.

[46] J. Inczedy, T. Lengyel, A. M. Ure, *Compendium of Analytical Nomenclature*, Blackwell . 1998.

[47] E. P. E. Lindner, K. Toth, “Definition and determination of response time of ion selective electrodes,” *Pure Appl. Chem.*, vol. 58, no. 3, pp. 469–479, 1986.

[48] H. T. Wang, B. S. Kang, F. Ren, S. J. Pearton, J. W. Johnson, P. Rajagopal, J. C. Roberts, E. L. Piner, and K. J. Linthicum , “Electrical detection of kidney injury molecule-1 with AlGaN⁄GaN high electron mobility transistors,” *Appl. Phys. Lett.*, vol. 91, pp. 222101–1–3, 2007.

[49] R. Thapa, S. Alur, K. Kim, F.Tong, Y. Sharma, M. Kim, C. Ahyi, J. Dai, J. Wook H., M. Bozack, J. Williams, A. Son, A. Dabiran, and M Park, “Biofunctionalized AlGaN/GaN high electron mobility transistor for DNA hybridization detection,” *Appl. Phys. Lett*, vol. 100, pp. 232109-1–232109–4, 2012.

[50] M. S. Makowski, D. Y. Zemlyanov, J. Lindsey, J. C. Bernhard, E. Hagen, B. K. Chan, A. A. Petersohn, M. R. Medow, L. E. Wendel, D. Chen, J. M. Canter, A. Ivanisevic., “Covalent attachment of a peptide to the surface of gallium nitride,” *Surf. Sci.*, vol. 605, pp. 1466–1475, 2011.

[51] S. J. Wilkins, M. Greenough, C. Arellano, T. Paskova, and A. Ivanisevic, "In Situ Chemical Functionalization of Gallium Nitride with Phosphonic Acid Derivatives during Etching," *Am. Chem. Soc.*, vol. 30, p. 2038 − 2046, 2014.

[52] C. M. Foster, R. Collazo, Z. Sitar, and A. Ivanisevic, "Cell Behavior on Gallium Nitride Surfaces : Peptide A ffi nity Attachment versus Covalent Functionalization," *Am. Chem. Soc.*, vol. 29, p. 8377−8384, 2013.

[53] L. Liu, Chien-Fong Lo, Yuyin Xi, Fan Ren, Stephen J. Pearton, Oleg Laboutin, Yu Cao, J. Wayne Johnson, and Ivan I. Kravchenko, "Effect of buffer structures on AlGaN / GaN high electron mobility transistor reliability," *J. Vac. Sci. Technol. B*, vol. 31, no. 1, pp. 011805–1–011805–6, 2013.

[54] K. Gurnett and T. Adams, "GaN makes inroads in the wireless infrastructure," *III-Vs Rev. Adv. Semicond. Mag.*, vol. 19, no. 9, pp. 33–35, 2006.

[55] K. Wong, W. Tang, K. M. Lau, and K. J. Chen, "Surface acoustic wave device on AlGaN/GaN heterostructure using two-dimensional electron gas interdigital transducers," *Appl. Phys. Lett.*, vol. 90, pp. 213506–1213506–3, 2007.

[56] S. J. Pearton, B. S. Kang, S. Kim, F. Ren, B. P. Gila, C. R. Abernathy, J. Lin, and S. N. G. Chu, "GaN-based diodes and transistors for chemical, gas, biological and pressure sensing" *J. Phys. Condens. Matter*, vol. 16, pp. R961–R994, 2004.

[57] C. P. Wen, J. Wang, and Y. Hao, "Current Collapse, Memory Effect Free GaN HEMT," in *Microwave Symposium Digest*, 2010, pp. 149–152.

[58] Y. Mancuso, P. Gremillet, and P. Lacomme, "T/R- Modules Technological and Technical Trends for Phased Array Antennas," in *European Microwave Conference*, 2005, pp. 614–617.

[59] H. Hommel, H. Feldle, and E. D. Gmbh, "Current Status of Airborne Active Phased Array (AESA) Radar Systems and Future Trends," in *Current Status of Airborne Active Phased Array (AESA) Radar Systems and Future Trends*, 2005, no. October 2004, pp. 1449–1452.

[60] R. Kiehl, and T. G. Sollner, *High Speed Heterostructure Devices*, 1st ed. Academic Press, 1994.

[61] B. H. Chu, B. S. Kang, H. T. Wang, C. Y. Chang, Y. Tseng, A. Goh, A. Sciullo, W. S. Wu, J. N. Lin, B. P. Gila, and S. J. Pearton, "AlGaN/GaN HEMT And ZnO nanorod-based sensors for chemical and bio-applications," Proc. SPIE 7216, Gallium Nitride Materials and Devices IV, 72162A, 2009.

[62] M. Eickhoff, M., Schalwig, J., Steinhoff, G., Weidemann, O., Görgens, L., Neuberger, R., Hermann, M., Baur, B., Müller, G., Ambacher, O., and Stutzmann, "Hydrogen sensing with GaN-based Schottky diodes," *phys. stat. sol.*, pp. 1908–1918, 2003.

[63] Irina Nicoleta Cimalla, “AlGaN/GaN sensors for direct monitoring of fluids and bioreactions,” *phys. stat. sol*, p. 3767, 2003.

[64] T. Young and C. Chen, “Assessment of GaN chips for culturing cerebellar granule neurons,” *Biomaterials*, vol. 27, pp. 3361–3367, 2006.

[65] I. Cimalla *et al.*, “AlGaN / GaN biosensor — effect of device processing steps on the surface properties and biocompatibility,” *Sensors Actuators B*, vol. 123, pp. 740–748, 2007.

[66] G. Steinhoff, B. Baur, G. Wrobel, S. Ingebrandt, and A. Offenhäusser, A. Dadgar and A. Krost, M. Stutzmann and M. Eickhoffa, “Recording of cell action potentials with Al Ga N Ga N field-effect transistors,” *Appl. Phys. Lett*, vol. 86, pp. 033901–1–3, 2006.

[67] R. Neuberger, and G. Mu, “Rapid Research Note Ion-Induced Modulation of Channel Currents in AlGaN / GaN High-Electron-Mobility Transistors,” *phys. stat. sol.*, vol. 183, no. 2, pp. R10 – R12, 2001.

[68] B. G. Steinhoff, O. Purrucker, M. Tanaka, M. Stutzmann, and M. Eickhoff, “Alx Ga1±xN A New Material System for Biosensors,” *Adv. Funct. Mater.*, vol. 13, no. 11, pp. 841–846, 2003.

[69] *Silvaco- Int. ATLAS User’s Manual, Device Simul. Software, St. Clara, CA*, no. 408, pp. 567–1000, 2006.

[70] K. P. Eimers, “2-D modeling of GaN HEMTs incorporating the piezoelectric effect,” Naval Postgraduate School Monterey, California, 2001.

[71] K. L. Holmes, “Two-dimensional modeling of aluminum gallium nitride / gallium nitride high electron mobility transistor,” Naval Postgraduate School, Monterey , California, 2002.

[72] R. P. Salm, “Thermal modeling of GaN HEMTs on sapphire and diamond,” Naval Postgraduate School, 2005.

[73] J. D. Albrecht, P. P. Ruden, S. C. Binari, and M. G. Ancona, “AlGaN / GaN Heterostructure Field-Effect Transistor Model Including Thermal Effects,” vol. 47, no. 11, pp. 2031–2036, 2000.

[74] M. A. Littlejohn, J. R. Hauser, and T. H. Glisson, “Monte Carlo calculation of the velocityfield relationship for gallium nitride,” *Appl. Phys. Lett.*, vol. 26, pp. 625–627, 1975.

[75] S. Karmalkar and U. K. Mishra, “Enhancement of Breakdown Voltage in AlGaN / GaN High Electron Mobility Transistors Using a Field Plate,” *IEEE Trans. Electron Devices*, vol. 48, no. 8, pp. 1515–1521, 2001.

[76] A. W. Smith and K. F. Brennan, “Hydrodynamic Simulation Of Semiconductor Devices,” *Prog. Quant. Electr.*, vol. 21, no. 4, pp. 293–360, 1998.

[77] S. Russo and A. Di Carlo, “Influence of the Source–Gate Distance on the AlGaN/GaN HEMT Performance,” *IEEE Trans. Electron Devices*, vol. 54, no. 5, pp. 1071–1075, 2007.

[78] E. J. Miller, X. Z. Dang, and E. T. Yu, “Gate leakage current mechanisms in AlGaN / GaN heterostructure field-effect transistors,” *J. Appl. Phys.*, vol. 88, no. 10, pp. 5951–5958, 2000.

[79] A. Pérez-Tomás, A. Fontserè, S. Sánchez, M. R. Jennings, P. M. Gammon, and Y. Cordier, “Gate traps inducing band-bending fluctuations on AlGaN/GaN heterojunction transistors,” *Appl. Phys. Lett.*, vol. 102, pp. 023511–1–4, 2013.

[80] D. M. Sathaiya and S. Karmalkar, “Thermionic trap-assisted tunneling model and its application to leakage current in nitrided oxides and Al Ga N Ga N high electron mobility transistors,” *J. Appl. Phys.*, vol. 99, pp. 093701–1–6, 2006.

[81] S. Glasstone, r K. J. Laidle, and H. Eyring, *The Theory of Rate Processes*. New York: New York, McGraw-Hill, 1941.

[82] W. Kuang, “TCAD Simulation and Modeling of AlGaN/GaN HFETs,” North Carolina State University, 2008.

[83] M. A. Khan, J. N. Kuznia, A. R. Bhattarai, and D. T. Olson, “Metal semiconductor field effect transistor based on single crystal GaN field effect transistor ased on single crystal,” *Appl. Phys. Lett*, vol. 62, no. 15, pp. 1786–1787, 1993.

[84] M. A. Khan, J. N. Kuznia, J. M. Van Hove, N. Pan, and J. Carter, “Observation of a twodimensional electron gas in low pressure metalorganic chemical vapor deposited GaN/AlxGa1−xN heterojunctions,” *Appl. Phys. Lett*, vol. 60, no. 24, pp. 3027–3029, 1992.

[85] T. Egawa, G. Zhao, H. Ishikawa, M. Umeno, and T. Jimbo, “Characterizations of Recessed Gate AlGaN/GaN HEMTs on Sapphire,” *IEEE Trans. Electron Devices*, vol. 48, no. 3, pp. 603–608, 2001.

[86] W. Wang *et al.*, “Performance Enhancement by Using the n+ -GaN Cap Layer and Gate Recess Technology on the AlGaN–GaN HEMT Fabrication,” *IEEE Electron. Device Lett.*, vol. 26, no. 1, pp. 5–7, 2005.

[87] U.K. Mishra, Y.-F. Wu, B.P. Keller, S. Keller, and S. P. Denbaars “GaN Microwave Electronics,” in *Topical Symp. on Millimeter Waves*, 1998, pp. 35–39.

[88] I. A. V. Kumar, W. Lu, F. A. Khan, R. Schwindt, A. Kuliev, G. Simin, J. Yang, M. Asif Khan, “High performance 0.25 μm gate-length AlGaN/GaN HEMTs on sapphire with transconductance of over 400 mS/mm,” *Electron. Lett.*, vol. 38, no.

5, pp. 252–253, 2002.

[89] W. Lu, J. Yang, M. A. Khan, and I. Adesida, “AlGaN / GaN HEMTs on SiC with over 100 GHz f T and Low Microwave Noise,” *IEEE Trans. Electron Devices*, vol. 48, no. 3, pp. 581–585, 2001.

[90] Y. Han *et al.*, “Nonselective and smooth Nonselective and smooth etching of GaN/AlGaN heterostructures by Cl2/Ar/ BCl3 inductively coupled plasmas,” *J. Vac. Sci. Technol. A*, vol. 22, no. 2, pp. 407–412, 2004.

[91] G. T. and Y. L. Tong WU, Zhi-Biao HAO, “Dry Etching Characteristics of AlGaN/GaN Heterostructures Using Inductively Coupled H2/Cl2, Ar/Cl2 and BCl3/Cl2 Plasmas,” *Jpn. J. Appl. Phys.*, vol. 42, p. L 257–L 259, 2003.

[92] D. W. Jenkins and J. D. Dow, “Electronic structures and doping of InN, InxGa1-xN, and InxAl1-xN,” *Phys. Rev. B*, vol. 39, no. 5, pp. 3317–3329, 1989.

[93] K. O. Schweitz *et al.*, “V/Al/Pt/Au Ohmic contact to n-AlGaN/GaN heterostructures,” *Appl. Phys. Lett*, vol. 80, no. 11, pp. 1954–1956, 2002.

[94] S. Ruvimov *et al.*, “Microstructure of Ti/Al and Ti/Al/Ni/Au Ohmic contacts for nGaN,” *Appl. Phys. Lett*, vol. 69, no. 11, pp. 1556–1558, 1996.

[95] J. Hilsenbeck, G. Tra, and J. Wu, “AlGaN / GaN HFETs with New Ohmic and Schottky Contacts for Thermal Stability up to 400 C,” *phys. stat. sol.*, vol. 176, pp. 183–188, 1999.

[96] N. Chaturvedi, U. Zeimer, J. Wurfl, and G. Trankle, “Mechanism of ohmic contact formation in AlGaN/GaN high electron mobility transistors,” *Inst. Phys. Publ.*, vol. 21, pp. 175–179, 2006.

[97] R. Neuberger, G. Muller, O. Ambacher, and M. Stutzmann, “High-Electron-Mobility AlGaN/GaN Transistors (HEMTs) for Fluid Monitoring Applications,” *phys. stat. sol.*, vol. 185, no. 1, pp. 85–89, 2001.

[98] H. Wang *et al.*, “Fast electrical detection of Hg(II) ions with Al Ga N ∕ Ga N high electron mobility transistors,” *Appl. Phys. A*, vol. 91, pp. 042114–1–4, 2007.

[99] Y. Alifragis, A. Volosirakis, N. A. Chaniotakis, G. Konstantinidis, A. Adikimenakis, and A. Georgakilas, “Potassium selective chemically modified field effect transistors based on AlGaN/GaN two-dimensional electron gas heterostructures,” *Biosens. Bioelectron*, vol. 22, pp. 2796–2801, 2007.

[100] B. S. Kang *et al.*, “pH sensor using AlGaN∕Ga N high electron mobility transistors with Sc2O3 in the gate region,” *Appl. Phys. Lett.*, vol. 91, pp. 012110–1–012110–3, 2007.

[101] M. Shafinaz *et al.*, “Open-Gated pH Sensor Fabricated on an Undoped-

AlGaN/GaN HEMT Structure," *Sensors*, vol. 11, pp. 3067–3077, 2011.

[102] G. Steinhoff, M. Hermann, W. J. Schaff, L. F. Eastman, M. Stutzmann, and M. Eickhoff, "pH response of GaN surfaces and its application for pH-sensitive field-effect transistors," *Appl. Phys. Lett*, vol. 83, no. 1, pp. 177–179, 2003.

[103] Y. Alifragis, A. Volosirakis, N. A. Chaniotakis, G. Konstantinidis, and E. Iliopoulos, "AlGaN/GaN high electron mobility transistor sensor sensitive to ammonium ions," *phys. stat. sol.*, vol. 204, no. 6, pp. 2059–2063, 2007.

[104] Y. Wang *et al.*, "Oxygen gas sensing at low temperature using indium zinc oxide-gated AlGaN/GaN high electron mobility transistors," *J. Vac. Sci. Technol. B*, vol. 28, no. 2, pp. 376–379, 2010.

[105] S. Hung *et al.*, "SnO2-gated AlGaN/GaN high electron mobility transistors based oxygen sensors," *J. Vac. Sci. Technol. B*, vol. 30, no. 4, pp. 041214–1–4, 2012.

[106] M. Myers *et al.*, "Nitrate - selective gallium nitride transistor - based ion sensors with low detection limit," in *IMCS 2012 – The 14th International Meeting on Chemical Sensors*, 2012, no. D, pp. 671–673.

[107] C. Cheng *et al.*, "Pd-oxide- Al0.24Ga0.76As (MOS) High Electron Mobility Transistor (HEMT) -Based Hydrogen Sensor," *IEEE Sens. J.*, vol. 6, no. 2, pp. 287–292, 2006.

[108] S. Hung *et al.*, "SnO2 functionalized AlGaN/GaN high electron mobility transistor for hydrogen sensing applications," *Int. J. Hydrogen Energy*, vol. 37, no. 18, pp. 13783–13788, 2012.

[109] Z. Guo, L. Wang, Z. Hao, and Y. Luo, "Sensors and Actuators B : Chemical Modeling and experimental study on sensing response of an AlGaN/GaN HEMT-based hydrogen sensor," *Sensors Actuators B. Chem.*, vol. 176, pp. 241–247, 2013.

[110] K.-Ah Son, B. Yang, N. Prokopuk, J. S. Moon, A. Liao, T. M. Katona and M. A. Khan, "RF GaN HEMT Sensors for Detection of Caustic Chemicals," *IEEE Sens. J.*, vol. 11, no. 12, pp. 3476–3478, 2011.

[111] O. Yilmazogl, K. Mutamba, D. Pavlidis, and M. R. Mbarga, "Strain sensitivity of AlGaN/GaN HEMT structures for sensing applications," *IEICE Trans. Electron.*, vol. E89–C, no. 7, pp. 1037–1041, 2006.

[112] S. A. Eliza, S. K. Islam, S. Mostafa, and F. S. Tulip, "Modeling of AlGaN / GaN HEMT Based Stress Sensors," in *6th International Conference on Electrical and Computer Engineering ICECE 2010*, 2010, no. 6th, pp. 306–309.

[113] B. S. Kang *et al.*, "Capacitance pressure sensor based on GaN high-electron-mobility transistor-on-Si membrane," *Appl. Phys. A*, vol. 86, pp. 253502–1–3, 2005.

[114] S. C. Hung, B. H. Chou, C. Y. Chang, C. F. Lo, K. H. Chen, Y. L. Wang, S. J. Pearton, A. Dabiran, P. P. Chow, G. C. Chi, and F. Ren, “Minipressure sensor using AlGaN / GaN high electron mobility transistors,” *Appl. Phys. Lett*, vol. 94, pp. 043903–1–4, 2009.

[115] M. J. Edwards *et al.*, “Modelling and optimisation of a sapphire/GaN-based diaphragm structure for pressure sensing in harsh environments,” in *The 18th International Conference on Advanced Semiconductor Devices and Microsystems, ASDAM 2010*, 2010, no. 18th, pp. 127–130.

[116] V.-G. Dumitru, S.-Dan Costea, M. Brezeanu, and B.-C. Serban “Harsh environment pressure sensor,” EP2477019 A1, 2011.

[117] S Koide, H. Takahashi, A. Abderrahmane, I. Shibasaki, and A. Sandhu, “High Temperature Hall sensors using AlGaN / GaN HEMT Structures,” in *Asia-Pacific Inter disciplinary Research Conference2011(AP-IRC2011)*, 2012, pp. 1–4.

[118] J. Lü and M. S. Shur, “Terahertz detection by high-electron-mobility transistor : Enhancement by drain bias,” *Appl. Phys. Lett*, vol. 78, pp. 2587–2588, 2001.

[119] A. El Fatimy *et al.*, “Resonant and voltage-tunable terahertz detection in In Ga As ⁄ In P nanometer transistors,” *Appl. Phys. A*, vol. 89, pp. 131926–1–3, 2006.

[120] T. Watanabe *et al.*, “InP- and GaAs-Based Plasmonic Terahertz Sensing and Imaging,” *IEEE Sens. J.*, vol. 13, no. 1, pp. 89–99, 2013.

[121] N. N. Esfahani, R. E. Peale, W. R. Buchwald, J. R. Hendrickson and J. W. Cleary “Millimeter and terahertz detectors based on plasmon excitation in InGaAs/InP HEMT devices,” in *Proc. SPIE 8624, Terahertz, RF, Millimeter, and Submillimeter-Wave Technology and Applications VI, 86240Q*, 2013, vol. 1, no. 1, pp. 1–8.

[122] B. S. Kang *et al.*, “Prostate specific antigen detection using AlGaN⁄GaN high electron mobility transistors,” *Appl. Phys. Lett.*, vol. 91, pp. 112106–1–3, 2007.

[123] Y. Wang *et al.*, “Botulinum toxin detection using AlGaN⁄GaN high electron mobility transistors,” *Appl. Phys. Lett.*, vol. 93, pp. 262101–1–3, 2008.

[124] B. H. Chu *et al.*, “Enzyme-based lactic acid detection using AlGaN⁄GaN high electron mobility transistors with ZnO nanorods grown on the gate region,” *Appl. Phys. Lett*, vol. 93, pp. 042114–1–3, 2008.

[125] K. H. Chen *et al.*, “c-erbB-2 sensing using AlGaN⁄GaN high electron mobility transistors for breast cancer detection,” *Appl. Phys. Lett.*, vol. 92, pp. 192103–1–3, 2008.

[126] Y. Wang *et al.*, “Fast detection of a protozoan pathogen , Perkinsus marinus , using AlGaN / GaN high electron mobility transistors,” *Appl. Phys. Lett*, vol. 94, pp.

243901–1–3, 2009.

[127] B. H. Chu *et al.*, “Aluminum Gallium Nitride (GaN)/GaN High Electron Mobility Transistor-Based Sensors for Glucose Detection in Exhaled Breath Condensate,” *J. Diabetes Sci. Technol.*, vol. 4, no. 1, pp. 171–179, 2010.

[128] Y. Song, Y. Lei, X. Yan, Y. Zhang, and Y. Liu, “Biosensors of ZnO Nanotetrapods and HEMT for Detecting Uric Acid,” in *2012 38th Annual Northeast Bioengineering Conference (NEBEC 2012), Philadelphia, Pennsylvania, USA*, 2012, pp. 345–346.

[129] M. S. Makowski *et al.*, “Physisorption of functionalized gold nanoparticles on AlGaN/GaN high electron mobility transistors for sensing applications,” *Appl. Phys. Lett.*, vol. 102, pp. 074102–1–5, 2013.

[130] “Medici Two-Dimensional Device Simulation Program User Manual,” *Medici TCAD Ind. Process Device Simulators, Synopsis*, no. February, pp. 1–1204, 2003.

[131] “Sentaurus Device User Guide -,” *Sentaurus TCAD Ind. Process Device Simulators, Synopsis, Mt. View, CA, USA*, 2012.

[132] “ISE TCAD – User’s Manual,” *Release 6.0, Integr. Syst. Eng. AG, Zurich, Switzerland, DESIS-ISE, ISE TCAD*, 2004.

[133] “Macro, A. P. S. Y. S. "User’s Manual,” *ver. 2011. Crosslight Softw.*, 2011.

[134] “BIPOLE3 User’s Manual,” *Univ. Waterloo, Ontario, N6L 3G1 Canada*, 1993.

[135] “G-PISCES-2B,” *Univ. Waterloo, Ontario, N6L 3G1 Canada*, 1994.

[136] “PISCES-2ET and Its Application Subsystems,” *Integr. Circuits Lab. Stanford Univ. Stanford, Calif. 94305*, 1994.

[137] M. S. and M. T. C. Fischer, P. Habas, O. Heinreichsberger, H. Kosina, P. Lindorfer, P. Pichler, H. Potzl, C. Sala, A. Schutz, S. Selberherr, “MINIMOS User Guide,” *Inst. Mikroelektron. Tech. Univ. Wien, Austria*, 2002.

[138] Mark Law, “FLorida Object- Oriented Device Simulator (FLOODS),” *Univ. Florida*.

[139] “GALENE II User’s Guide,” *RWTH Aachen, Ger.*

[140] “NEXTNANO3 device simulator,” *Progr. is available www. wsi. tum. de/nextnano3 www.nextnano.de*, 2013.

[141] R. From and I. B. M. Journal, “Finite-Element analysis of Semiconductor Devices: The FIELDAY Program,” *IBM J. Res. Dev.*, vol. 44, no. 1/2, pp. 142–156, 2000.

[142] X. L. Wang, G. Jiao, J. P. Li, Y. P. Zeng, and J. M. Li, “Improved DC and RF performance of AlGaN/GaN HEMTs grown by MOCVD on sapphire substrates,” *Solid. State. Electron.*, vol. 49, pp. 1387–1390, 2005.

[143] A. A. Efremov *et al.*, “Effect of the Joule Heating on the Quantum Efficiency and Choice of Thermal Conditions for High-Power Blue InGaN/GaN LEDs,” *Semiconductors*, vol. 40, no. 5, pp. 605–610, 2006.

[144] E. Bahat-treidel, I. Khalil, O. Hilt, J. Würfl, and G. Tränkle, “Engineered linearity of GaN-based HEMTs power devices by tailoring transfer characteristics,” *Phys. Status Solidi C*, vol. 6, no. 6, pp. 1378–1381, 2009.

[145] E. W. Faraclas, R. T. Webster, and A. F. M. Anwar, “AlGaN/GaN HEMTs : Experiment and Simulation of DC Characteristics,” in *Semiconductor Device Research Symposium*, 2005, pp. 1–2.

[146] T. Grasser, T. Tang, H. Kosina, and S. Selberherr, “A Review of Hydrodynamic and Energy-Transport Models for Semiconductor Device Simulation,” *Proc. IEEE*, vol. 91, no. 2, pp. 251–274, 2003.

[147] S. Heikman, S. Keller, D. S. Green, S. P. Denbaars, and U. K. Mishra, “High conductivity modulation doped AlGaN/GaN multiple channel heterostructures,” *J. Appl. Phys.*, vol. 94, no. 8, pp. 5321–5325, 2003.

[148] T. Ide, M. Shimizu, A. Nakajima, M. Inada, S. Yagi, Y. Yano, N. Akutsu, H. Okumura, and K. ARAI, “Gate-Length Dependence of DC Characteristics in Submicron-Gate AlGaN / GaN High Electron Mobility Transistors,” *Jpn. J. Appl. Phys.*, vol. 46, no. 4B, pp. 2334–2337, 2007.

[149] G. Dambrine, A. Cappy, F. Heliodore, and E. Playez, “A new method for derermining the Small-Signal Equivalent Circuit,” *IEEE Trans. Microw. Theory Tech.*, vol. 36, no. 7, pp. 1151–1159, 1988.

[150] S. Vitanov, V. Palankovski, S. Maroldt, and R. Quay, “High-temperature modeling of AlGaN/GaN HEMTs,” *Solid State Electron.*, vol. 54, no. 10, pp. 1105–1112, 2010.

[151] B. P. Luther, S. D. Wolter, and S. E. Mohney, “High temperature Pt Schottky diode gas sensors on n-type GaN,” *Sensors Actuators B*, vol. 56, pp. 164–168, 1999.

[152] I. Rýger, G. Vanko, P. Kunzo, T. Lalinský, M. Vallo, and A. Plecenik, “AlGaN/GaN HEMT Based Hydrogen Sensors With Gate Absorption Layers Formed by High Temperature Oxidation,” *Procedia Eng.*, vol. 47, pp. 518–521, 2012.

[153] T. Lalinský *et al.*, “AlGaN/GaN based SAW-HEMT structures for chemical gas sensors,” *Procedia Eng.*, vol. 5, pp. 152–155, 2010.

[154] J. D. Albrecht, R. P. Wang, P. P. Ruden, M. Farahmand, and K. F. Brennan, "Electron transport characteristics of GaN for high temperature device modeling," *J. Appl. Phys.*, vol. 83, no. 9, pp. 4777–4781, 1998.

[155] Y. Cordier, M. Hugues, P. Lorenzini, F. Semond, F. Natali, and J. Massies, "Electron mobility and transfer characteristics in AlGaN/GaN HEMTs," *phys. stat. sol.*, vol. 2, no. 7, pp. 2720–2723, 2005.

[156] V. O. Turin, and A. A. Balandin, "Electrothermal simulation of the self-heating effects in GaN-based field-effect transistors," *J. Appl. Phys.*, vol. 100, pp. 054501–1–8, 2006.

[157] S. K. Islam and H. F. Huq, "Improved temperature model of AlGaN/GaN HEMT and device characteristics at variant temperature," *Int. J. Electron.*, vol. 94, no. 12, pp. 1099–1108, 2007.

[158] I. Vurgaftman, J. R. Meyer, and L. R. Ram-Mohan, "Band parameters for III – V compound semiconductors and their alloys," *J. Appl. Phys.*, vol. 89, no. 11, pp. 5815–5875, 2001.

[159] W. A. Gibson, "Comparison of Gallium Nitride High Electron Mobility Transistors modeling in two and three dimensions NAVAL POSTGRADUATE," Monterey California. Naval Postgraduate School, 2007.

[160] E.K.Siche, and J.I..Pankove, "Thermal conductivity of GaN, 25–360 K," *J. Phys. Chem. Solids*, vol. 38, no. 3, p. 330, 1977.

[161] C. Mion, J. F. Muth, E. A. Preble, and D. Hanser, "Thermal conductivity , dislocation density and GaN device design," *Superlattices Microstruct.*, vol. 40, pp. 338–342, 2006.

[162] A. Jacquot *et al.*, "Optical and thermal characterization of AlN thin films deposited by pulsed laser deposition," *Appl. Surf. Sci.*, vol. 186, pp. 507–512, 2002.

[163] Glen A.Slack, R.A.Tanziili, R.O.Pohl, and J.W.Vandersande, "The intrinsic thermal conductivity of AIN," *J. Phys. Chem. Solids*, vol. 48, no. 7, pp. 641–647, 1987.

[164] G. A. Slack, L. J. Schowalter, D. Morelli, and J. A. Freitas, "Some effects of oxygen impurities on AlN and GaN," *J. Cryst. Growth*, vol. 246, pp. 287–298, 2002.

[165] M. Farahmand *et al.*, "Monte Carlo Simulation of Electron Transport in the III-Nitride Wurtzite Phase Materials System : Binaries and Ternaries," *IEEE Trans. Electron Devices*, vol. 48, no. 3, pp. 535–542, 2001.

[166] M. Miczek, C. Mizue, T. Hashizume, and B. Adamowicz, "Effects of interface states and temperature on the C-V behavior of metal/insulator/AlGaN/GaN

heterostructure capacitors," *J. Appl. Phys.*, vol. 103, pp. 104510–1–11, 2008.

[167] T. Mizutani, S. Member, Y. Ohno, M. Akita, and S. Kishimoto, "A Study on Current Collapse in AlGaN/GaN HEMTs Induced by Bias Stress," *IEEE Trans. Electron Devices*, vol. 50, no. 10, pp. 2015–2020, 2003.

[168] M. J. Uren, J. Möreke, and M. Kuball, "Buffer Design to Minimize Current Collapse in GaN/AlGaN HFETs," *IEEE Trans. Electron Devices*, vol. 59, no. 12, pp. 3327–3333, 2012.

[169] W. Saito *et al.*, "Effect of Buffer Layer Structure on Drain Leakage Current and Current Collapse Phenomena in High-Voltage GaN-HEMTs," *IEEE Trans. Electron Devices*, vol. 56, no. 7, pp. 1371–1376, 2009.

[170] K. Horio and A. Nakajima, "Buffer-trap and surface-state effects on gate lag in AlGaN/GaN HEMTs," *P hys. Status Solidi C*, vol. 7, pp. 1931–1933, 2010.

[171] M. Gassoumi, O. Fathallah, C. Gaquiere, and H. Maaref, "Analysis of deep levels in AlGaN/GaN/Al2O3 heterostructures by CDLTS under a gate pulse," *Phys. B Phys. Condens. Matter*, vol. 405, no. 9, pp. 2337–2339, 2010.

[172] P. B. Klein, J. A. F. Jr, S. C. Binari, and A. E. Wickenden, "Observation of deep traps responsible for current collapse in GaN metal – semiconductor field-effect transistors," *Appl. Phys. Lett.*, vol. 75, no. 25, pp. 4016–4018, 1999.

[173] T. Ueda, Y. Uemoto, T. Tanaka, and D. Ueda, "GaN Transistors For Power Switching And Millimeter-Wave Applications," *Int. J. High Speed Electron. Syst.*, vol. 19, no. 1, pp. 145–152, 2009.

[174] H. Sun *et al.*, "Nanometric AlGaN/GaN HEMT Performance with Implant or Mesa Isolation," *IEEE Electron. Device Lett.*, vol. 32, no. 8, pp. 1056–1058, 2011.

[175] U. K. Mishra, L. Shen, T. E. Kazior, and Y. Wu, "GaN-Based RF Power Devices and Amplifiers," *Proc. IEEE*, vol. 96, no. 2, pp. 287–305, 2008.

[176] S. J. Pearton *et al.*, "Progress in Materials Science Recent advances in wide bandgap semiconductor biological and gas sensors," *Prog. Mater. Sci.*, vol. 55, no. 1, pp. 1–59, 2010.

[177] D. S. Wuu *et al.*, "Defect reduction and efficiency improvement of near-ultraviolet emitters via laterally overgrown GaN on a GaN/patterned sapphire template," *Appl. Phys. Lett.*, vol. 89, pp. 161105–1–161105–3, 2006.

[178] S. Raghavan and J. M. Redwing, "Growth stresses and cracking in GaN films on (111) Si grown by metal- organic chemical-vapor deposition. I.AlN buffer layers," *J. Appl. Phys.*, vol. 98, pp. 023514–1–023514–9, 2005.

[179] S. Rajan, P. Waltereit, C. Poblenz, S. J. Heikman, D. S. Green, J. S. Speck, and U.

K. Mishra., “Power Performance of AlGaN/GaN HEMTs Grown on SiC by Plasma-Assisted MBE,” *IEEE Electron. Device Lett.*, vol. 25, no. 5, pp. 247–249, 2004.

[180] C. Liang, K. Y. Chen, N. C. Chen, P. H. Chang, and C. Chang, “Al0.15Ga0.85N/ GaN high electron mobility transistor structures grown on p -type Si substrates,” *Appl. Phys. Lett.*, vol. 89, pp. 132107–1–132107–3, 2006.

[181] Y. C. Choi, M. Pophristic, H. Cha, B. Peres, M. G. Spencer, and L. F. Eastman, “The Effect of an Fe-doped GaN Buffer on OFF -State Breakdown Characteristics in AlGaN / GaN HEMTs on Si Substrate,” *IEEE Trans. Electron Devices*, vol. 53, no. 12, pp. 2926–2931, 2006.

[182] Y. B. Pan, Z. J. Yang, Z. T. Chen, Y. Lu, T. J. Yu, X. D. Hu, K. Xu, G. Y. Zhang, “Reduction of threading edge dislocation density in n-type GaN by Si delta-doping,” *J. Cryst. Growth*, vol. 286, pp. 255–258, 2006.

[183] G. Meneghesso, M. Meneghini, and E. Zanoni, “GaN-based power HEMTs , Parasitic , Reliability and high field issues,” in *224th ECS Meeting, © 2013 The Electrochemical Society*, 2012, p. 401.

[184] G. W. G. Van Dreumel, T. Bohnen, J. G. Buijnsters, W. J. P. van Enckevort, J. J. ter Meulen, P. R. Hageman, and E. Vlieg, “Comparison of GaN and AlN nucleation layers for the oriented growth of GaN on diamond substrates,” *Diam. Relat. Mater.*, vol. 19, pp. 437–440, 2010.

[185] D. Pavlidis, “III-V Nitride Electronics,” in *Indium Phosphide and Related Materials Conference*, 2002, pp. 443–446.

[186] R. Gaska, A. Osinsky, J. W. Yang, and M. S. Shur, “Self-Heating in High-Power AlGaN-GaN HFET’s,” *IEEE Electron. Device Lett.*, vol. 19, no. 3, pp. 89–91, 1998.

[187] S. Yngvesson, *Microwave semiconductor devices*, 134th ed. Kluwer Academic Publishers, Springer US, 1991.

[188] G. J. Wurfl, V. Abrosimova, J. Hilsenbeck, E. Nebauer, W. Rieger, and G. Trankle, “Reliability considerations of III-nitride microelectronic devices,” *Microelectron. Reliab.*, vol. 39, no. 12, pp. 1737–1757, 1999.

[189] N. A. Moser, J. K. Gillespie, G. D. Via, A. Crespo, and M. J. Yannuzzi, “Effects of surface treatments on isolation currents in AlGaN / GaN high- electron-mobility transistors,” *Appl. Phys. Lett.*, vol. 83, no. 20, pp. 4178–4180, 2003.

[190] Y. Lin, Y. Lain, and S. S. H. Hsu, “AlGaN/GaN HEMTs With Low Leakage Current and High On/Off Current Ratio,” *IEEE Electron. Device Lett.*, vol. 31, no. 2, pp. 102–104, 2010.

[191] S. Karmalkar, D. M. Sathaiya, and M. S. Shur, “Mechanism of the reverse gate leakage in AlGaN/GaN high electron mobility transistors,” *Appl. Phys. Lett.*, vol. 82, no. 22, pp. 3976–3978, 2003.

[192] J. W. Johnson, E.L. Piner, Andrei Vescan, R. Therrien, Pradeep Rajagopal, J. Roberts, J. D. Brown, Sameer Singhal, K.J. Linthicum, “12 W/mm AlGaN/GaN HFETs on Silicon Substrates,” *IEEE Electron. Device Lett.*, vol. 25, no. 7, pp. 459–461, 2004.

[193] S. C. Binari, H. B. Dietrich, G. Kelner, L. B. Rowland, K. Doverspike, and D. K. Wickenden, “H , He , and N implant isolation of n-type GaN,” *J. Appl. Phys.*, vol. 78, no. 5, pp. 3008–3011, 1995.

[194] S. J. Pearton, C. B. Vartuli, J. C. Zolper, C. Yuan, and R. A. Stall, “Ion implantation doping and isolation of GaN,” *Appl. Phys. Lett.*, vol. 67, no. 10, pp. 1435–1437, 1995.

[195] R. G. Wilson, C. B. Vartuli, C. R. Abernathy, S. J. Pearton, and J. M. Zavada, “Implantation and redistribution of dopants and isolation species in GaN and related compounds,” *Solid-Slate Electron.*, vol. 38, no. 7, pp. 1329–1333, 1995.

[196] J. C. Zolper, “Ion implantation in group III-nitride semiconductors: a tool for doping and defect studies,” *J. Cryst. Growth*, vol. 178, pp. 157–167, 1997.

[197] B. Boudart, Y. Guhel, J. C. Pesant, P. Dhamelincourt, and M. A. Poisson, “Raman characterization of Ar+ ion-implanted GaN,” *J. Raman Spectrosc.*, vol. 33, pp. 283–286, 2002.

[198] B. Boudart, Y. Guhel, J. C. Pesant, P. Dhamelincourt, and M. A. Poisson, “Raman characterization of Mg+ ion-implanted GaN,” *J. Phys. Condens. MATTER*, vol. 16, no. 2, pp. 49–55, 2004.

[199] J. P. Biersack, L.G. Haggmark, “A Monte Carlo Computer Program For The Transport Of Energetic Ions In Amorphous Targets,” *Nucl. Instruments Methods*, vol. 174, pp. 257–269, 1980.

[200] Z. Yang, D. J. Lichtenwalner, A. S. Morris, J. Krim, and A. I. Kingon, “Comparison of Au and Au-Ni alloys as contact materials for MEMS switches,” *J. Microelectro Mech. Syst.*, vol. 18, pp. 287–294, 2009.

[201] H. P. Xin, S. Poust, W. Sutton, D. Li, D. Lam, I. Smorchkova, R. Sandhu, B. Heying, J. Uyeda, M. Barsky, M. Wojtowicz, R. Lai, “Optimization of AlGaN / GaN HEMT Ohmic Contacts for Improved Surface Morphology with Low Contact Resistance,” in *CS MANTECH Conference, May 17th-20th, 2010, Portland, Oregon, USA,* 2010, pp. 149–152.

[202] W. Lu, V. Kumar, R. Schwindt, E. Piner, and I. Adesida, “A comparative study of surface passivation on AlGaN / GaN HEMTs,” *Solid. State. Electron.*, vol. 46, pp.

1441–1444, 2002.

[203] M. Ha, S. Lee, J. Park, J. Her, K. Seo, and M. Han, “Silicon Dioxide Passivation of AlGaN/GaN HEMTs for High Breakdown Voltage,” in *Proceedings of the 18th International Symposium on Power Semiconductor Devices & IC’s June 4-8, 2006 Naples, Italy,* 2006, pp. 4–7.

[204] N. Stavitski, M. J. H. Van Dal, R. A. M. Wolters, A. Y. Kovalgin, and J. Schmitz, “Specific Contact Resistance Measurements of Metal-Semiconductor Junctions,” in *Microelectronic Test Structures, 2006. ICMTS 2006. IEEE International Conference,* 2006, pp. 13–17.

[205] T. Ide, M. Shimizu, S. Yagi , M. Inada, G. Piao, Y. Yano, N. Akutsu, H. Okumura, K. Arai, “Low on-resistance AlGaN/GaN HEMTs by reducing gate length and source-gate length,” *phys. stat. sol.*, vol. 5, no. 6, pp. 1998–2000, 2008.

[206] J. Schalwig, G. Muller, M. Eickhoff, O. Ambacher, and M. Stutzmann “Gas sensitive GaN/AlGaN-heterostructures,” *Sensors Actuators B,* vol. 87, no. 2, pp. 425–430, 2002.

[207] N. Sharma, C. Periasamy, and N. Chaturvedi, “Investigation of High-Temperature Effects on the Performance of AlGaN/GaN High Electron Mobility Transistors,” *J. Nanoelectron. Optoelectron.*, vol. 11, no. 6, pp. 694–701, Dec. 2016.

[208] T. Kokawa, T. Sato, H. Hasegawa, and T. Hashizume, “Liquid-phase sensors using open-gate AlGaN/GaN high electron mobility transistor structure,” *J. Vac. Sci. Technol. B*, vol. 24, no. 4, pp. 1972–1976, 2006.

[209] R.Mehandru, B.Luo, B.S .Kang, J. Kim, F. Ren, S.J. Pearton, C.-C. Pan, G.-T. Chen, and J.-I. Chyi, “AlGaN/GaN HEMT based liquid sensors,” *Solid. State. Electron.,* vol. 48, pp. 351–353, 2004.

[210] J. Song and W. Lu, “Chemically gated AlGaN/GaN heterostructure field effect transistors for polar liquid sensing,” *Appl. Phys. Lett.*, vol. 89, pp. 223503–1–223503–3, 2006.

[211] B.S. Kang, H.T. Wang, F. Ren, M. Hlad, B.P. Gila, C.R. Abernathy, S.J. Pearton, C. Li, Z.N. Low, J. Lin, J.W. Johnson, P. Rajagopal, J.C. Roberts, E.L. Piner, and K.J. Linthicum, “Role of Gate Oxide in AlGaN / GaN High-Electron-Mobility Transistor pH Sensors,” *J. Electron. Mater.*, vol. 37, no. 5, pp. 550–553, 2008.

[212] S. Dhakad, N. Sharma, C. Periasamy, and N. Chaturvedi, “Superlattices and Microstructures Optimization of ohmic contacts on thick and thin AlGaN / GaN HEMTs structures,” *Superlattices Microstruct.*, vol. 111, pp. 922–926, 2017.

[213] G. M. Olmsted, J. III, and Williams, “Chemistry, The Molecular Science,” *J. Chem. Educ,* vol. 72, no. 5, 1997.

[214] P. Bergveld Em, “ISFET , Theory and Practice,” in *IEEE SENSOR CONFERENCE TORONTO, OCTOBER 2003*, 2003, no. October, pp. 1–26.

[215] D. E. Yates, S. Levine, and T. W. Healy, “Site-binding Model of the Electrical Double Layer at the Oxide / Water Interface,” *J. Chem. Soc., Faraday Trans. 1*, vol. 70, pp. 1807–1818, 1974.

[216] W. Monch, “Elementary calculation of the branch-point energy in the continuum of interface-induced gap states,” *Appl. Surf. Sci.*, vol. 118, pp. 380–387, 1997.

[217] H. Huang, C. Lin, and H. Chiu, “High Sensitivity pH Sensor Using AlXGa1-XN/ GaN HEMT Heterostructure Design,” in *2008 IEEE International Conference on Electron Devices and Solid-State Circuits, Hong Kong, China*, 2008, vol. 1, pp. 15–18.

[218] M. S. Z. Abidin, A. M. Hashim, M. E. Sharifabad,S. F. A.Rahman, and T. Sadoh, “Open-Gated pH Sensor Fabricated on an Undoped-AlGaN/GaN HEMT Structure,” *Sensors*, vol. 11, pp. 3067–3077, 2011.

List of Publication

Journals

1. N. Sharma, C.Periasamy and N. Chaturvedi ,"Performance Analysis of GaN Capping Layer Thickness on GaN/AlGaN/GaN HEMTs" , Journal of Nanoscience and Nanotechnology, American Scientific Publishers, Vol. 18, no. 7, pp. 4580-4587, July. 2018.

2. N. Sharma, C. Periasamy, and N. Chaturvedi, “Investigation of High-Temperature Effects on the Performance of AlGaN/GaN HEMTs”, Journal of Nanoelectronics and Optoelectronics, American Scientific Publishers, Vol. 11, no.6, pp. 694-701, Dec. 2016.

3. S. K. Dhakad, Niketa Sharma, C. Periasamy, and N. Chaturvedi, “Optimization of Ohmic Contacts on Thick and Thin AlGaN/GaN HEMTs Structures”, Superlattices and Microstructures, Elsevier, Vol. 111, pp. 922-926, July. 2017.

4. N. Sharma, S. Dhakad, C. Periasamy and N. Chaturvedi, “Refined Isolation techniques for GaN HEMTs”, Materials Science in Semiconductor Processing, Elsevier, Vol. 87, pp. 195-201, Nov. 2018.

5. N. Sharma, C. Periasamy and N. Chaturvedi, “Trapping effects on leakage and current collapse in AlGaN/GaN HEMTs”, Materials Express (Under Review).

6. N. Sharma, S. Dhakad, S. Mishra, K. Singh, N. Chaturvedi , A. Chauhan, C. Periasamy, D. K. Kharbanda, P. Parjapat, P. K. Khanna and N. Chaturvedi, “High Resolution Femto Level Salt Detection using AlGaN/GaN HEMT based Sensor for Biomedical and Space Applications” IEEE Transcation on Electron Devices (Under Review)

Conferences:

1. S. Mishra, S. Dhakad, N. Sharma, K. Singh, A. Chauhan, P. Prajapat and N. Chaturvedi, “Influence of High-k and Low-k dielectrics on drain current of GaN HEMTs” International Conference on Computational Mathematics in Nanoelectronics and Astrophysics, November 1-3, 2018, IIT Indore, M.P., India.

2. N. Sharma, S. Dhakad, K. Singh, N. Chaturvedi, A. Chauhan, C. Periasamy, N. Chaturvedi, “AlGaNGaN HEMTs based pH Sensor”, XIX International Workshop on The Physics of Semiconductor Devices (IWPSD 2017), 11-15 Dec 2017, IIT Delhi, New Delhi, India.

3. N. Sharma, S. Bhardwaj, S. Dhakad, C. Periasamy, and N. Chaturvedi "Ar^+ based Ion Implantation and Ar-RIE of thin and thick AlGaN/GaN HEMT, 40th WOCSDICE - Workshop on Compound Semiconductor Devices and Integrated Circuits held in Europe & 13th EXMATEC - Expert Evaluation and Control of Compound Semiconductor Materials and Technologies, 6-10 June 2016, Aveiro, Portugal.
4. N. Sharma, D. Joshi, C. Periasamy, N. Chaturvedi , "Buffer and barrier trapping effects on leakage and current collapse in AlGaNGaN HEMTs", National Conference on Semiconductor Materials and Devices, 4-6 March 2016, IIT Jodhpur, Rajasthan, India, pp. 24.

Brief CV

Niketa Sharma is doctoral candidate in Department of Electronics & Communication Engineering, Malaviya National Institute of Technology, Jaipur, Rajasthan, India. She received her M.Tech. in VLSI Design from Banasthali University, India and B.Tech. in Electronics & Communication Engineering from Govt. Engineering College, Ajmer, Rajasthan, India with Hons. in the year 2013 and 2010 respectively. She has published more than 13 papers in various peer-reviewed journals and conferences. Her current research interest covers modeling, simulation and fabrication of GaN-based HEMT devices for various applications.